U.S.NRC
United States Nuclear Regulatory Commission
Protecting People and the Environment

NUREG/CR-7122
PNNL-19497

An Evaluation of Ultrasonic Phased Array Testing for Cast Austenitic Stainless Steel Pressurizer Surge Line Piping Welds

Office of Nuclear Regulatory Research

AVAILABILITY OF REFERENCE MATERIALS IN NRC PUBLICATIONS

NRC Reference Material

As of November 1999, you may electronically access NUREG-series publications and other NRC records at NRC's Public Electronic Reading Room at http://www.nrc.gov/reading-rm.html. Publicly released records include, to name a few, NUREG-series publications; *Federal Register* notices; applicant, licensee, and vendor documents and correspondence; NRC correspondence and internal memoranda; bulletins and information notices; inspection and investigative reports; licensee event reports; and Commission papers and their attachments.

NRC publications in the NUREG series, NRC regulations, and *Title 10, Energy*, in the Code of *Federal Regulations* may also be purchased from one of these two sources.

1. The Superintendent of Documents
   U.S. Government Printing Office
   Mail Stop SSOP
   Washington, DC 20402–0001
   Internet: bookstore.gpo.gov
   Telephone: 202-512-1800
   Fax: 202-512-2250
2. The National Technical Information Service
   Springfield, VA 22161–0002
   www.ntis.gov
   1–800–553–6847 or, locally, 703–605–6000

A single copy of each NRC draft report for comment is available free, to the extent of supply, upon written request as follows:

Address: U.S. Nuclear Regulatory Commission
Office of Administration
Publications Branch
Washington, DC 20555-0001
E-mail: DISTRIBUTION.RESOURCE@NRC.GOV
Facsimile: 301–415–2289

Some publications in the NUREG series that are posted at NRC's Web site address http://www.nrc.gov/reading-rm/doc-collections/nuregs are updated periodically and may differ from the last printed version. Although references to material found on a Web site bear the date the material was accessed, the material available on the date cited may subsequently be removed from the site.

Non-NRC Reference Material

Documents available from public and special technical libraries include all open literature items, such as books, journal articles, and transactions, *Federal Register* notices, Federal and State legislation, and congressional reports. Such documents as theses, dissertations, foreign reports and translations, and non-NRC conference proceedings may be purchased from their sponsoring organization.

Copies of industry codes and standards used in a substantive manner in the NRC regulatory process are maintained at—

The NRC Technical Library
Two White Flint North
11545 Rockville Pike
Rockville, MD 20852–2738

These standards are available in the library for reference use by the public. Codes and standards are usually copyrighted and may be purchased from the originating organization or, if they are American National Standards, from—

American National Standards Institute
11 West 42nd Street
New York, NY 10036–8002
www.ansi.org
212–642–4900

Legally binding regulatory requirements are stated only in laws; NRC regulations; licenses, including technical specifications; or orders, not in NUREG-series publications. The views expressed in contractor-prepared publications in this series are not necessarily those of the NRC.

The NUREG series comprises (1) technical and administrative reports and books prepared by the staff (NUREG–XXXX) or agency contractors (NUREG/CR–XXXX), (2) proceedings of conferences (NUREG/CP–XXXX), (3) reports resulting from international agreements (NUREG/IA–XXXX), (4) brochures (NUREG/BR–XXXX), and (5) compilations of legal decisions and orders of the Commission and Atomic and Safety Licensing Boards and of Directors' decisions under Section 2.206 of NRC's regulations (NUREG–0750).

U.S.NRC
United States Nuclear Regulatory Commission
Protecting People and the Environment

NUREG/CR-7122
PNNL-19497

An Evaluation of Ultrasonic Phased Array Testing for Cast Austenitic Stainless Steel Pressurizer Surge Line Piping Welds

Manuscript Completed: December 2011
Date Published: March 2012

Prepared by:
A. A. Diaz, A. D. Cinson, S. L. Crawford, R. A. Mathews, T. L. Moran,
M. S. Prowant and M. T. Anderson

Pacific Northwest National Laboratory
P.O. Box 999
Richland, WA 99352

W. E., NRC Project Manager

NRC Job Code N6398

Office of Nuclear Regulatory Research

ABSTRACT

Confirmatory research is being conducted for the U.S. Nuclear Regulatory Commission at the Pacific Northwest National Laboratory to assess the effectiveness and reliability of advanced nondestructive examination methods for the inspection of primary system pressure boundary components and materials in light-water reactors. The work reported here provides a technical evaluation to assess the capabilities of phased-array (PA) ultrasonic testing (UT) methods as applied to the inspection of welds in cast austenitic stainless steel (CASS) pressurizer (PZR) surge line piping. A set of thermal fatigue cracks (TFCs) were implanted into CASS PZR surge-line specimens (pipe-to-elbow welds) salvaged from cancelled nuclear power plants that were fabricated of vintage materials formed in the 1970s. Responses from these cracks were used to evaluate detection and sizing performance of the PA-UT methods applied. Custom arrays, operating nominally at 800 kHz, 1.0 MHz, 1.5 MHz, and 2.0 MHz were employed. Raster and line-scan data were acquired as a function of probe frequency and angle from both the centrifugally and statically cast base materials adjacent to the welds.

All implanted TFCs were easily detected in these specimens. The results reported here show that longitudinal mode, transmit-receive matrix phased-array probes, over the applied frequency range, provides effective sound fields for detection and characterization of TFCs in CASS PZR surge line components. PA-UT results were compared against true-state data for all cracks, and root mean square error was computed as a metric for both length- and depth-sizing of these cracks. Signal-to-noise ratio measurements were documented and analyses made to quantify the potential impact of material-induced attenuation and redirection of the sound fields on crack detection and localization.

In addition to the implanted TFCs in the weld region, five in-situ grown TFCs were placed in parent pipe and elbow regions. Unlike implanted flaws, this cyclic induction heating process grows TFCs directly in the specimen material. The resultant crack morphology is a product of the specimen composition and microstructure. It is believed that certain characteristics of in-situ grown cracks, such as branching, surface facets, and local discontinuities, are more representative of service-induced cracks. All of these cracks, implanted and in-situ grown, were detected and accurately characterized at multiple frequencies.

Based upon the results of this work, state-of-the-art phased-array inspection approaches are shown to be rapidly evolving and the capability to detect cracks in CASS components where the wall thickness is generally less than 50 mm (2.0 in.) has been demonstrated. While additional questions remain to be answered, long-wavelength ultrasonic approaches coupled with advanced signal processing technologies are beginning to show signs of success toward addressing this challenging inspection issue.

In addition, to provide an external confirmatory data set, an inservice inspection (ISI) supplier was contracted to examine two of the CASS PZR specimens using Performance Demonstration Initiative (PDI) qualified procedures and equipment. Their crack detection and characterization results are also reported here.

FOREWORD

Cast stainless steel (CASS) material was used extensively in the primary pressure boundary of pressurized water reactors (PWRs) due to its relatively low cost and resistance to corrosion. However, the coarse-grained and anisotropic microstructure of CASS material makes it difficult to inspect CASS components and their associated welds. Similar problems exist for dissimilar metal welds and weld-overlay-repaired pipe joints. The large grain sizes of these materials strongly affect the propagation of ultrasound by causing severe attenuation, change in velocity, and scattering of ultrasonic energy. Thus, the signal patterns originating from flaws can be difficult to distinguish from scatter. In addition, redirection of the sound beam may result in some portions of the material not being examined.

Circa 2001, a literature search was conducted to discover if there were any active investigations regarding the inspection of CASS materials. Inquiries were made to national and international research organizations. No active research programs were found. Thermal aging embrittlement is a known degradation mechanism of CASS components in nuclear power plants and has been studied since the early 1990s (Chopra 1992). Given the lack of investigation into the unreliability of volumetric examination of CASS materials and considering thermal aging embrittlement, the NRC initiated a study at Pacific Northwest National Laboratory (PNNL).

The study has resulted in a number of findings documented in several reports. NUREG/CR-6929, *Assessment of Eddy Current Testing for the Detection of Cracks in Cast Stainless Steel Reactor Piping Components*, was published in February 2007. The report documented an assessment of eddy current testing for the detection of surface-breaking flaws in CASS reactor piping components from the inside diameter of the pipe wall. In March 2007, NUREG/CR-6933, *Assessment of Crack Detection in Heavy-Walled Cast Stainless Steel Piping Welds Using Advanced Low-Frequency Ultrasonic Methods*, was published. The report documents ultrasonic studies on vintage centrifugally cast stainless steel thick section primary piping conducted with low-frequency phased array technology. NUREG/CR-6984, *Field Evaluation of Low-Frequency SAFT-UT on Cast Stainless Steel and Dissimilar Metal Weld Components*, was published in 2008. The report is a compilation of the earlier work that led to the investigations documented in the 2007 NUREG/CR reports listed above. The study discussed in the 2008 report was semi-blind and thus thought to be a valuable source of information for future performance demonstration assessments. Moreover, the report addresses examinations of dissimilar metal welds for which only limited data have previously been published.

The investigation documented in the subject report assesses the capabilities of phased-array ultrasonic testing (UT) methods as applied to the inspection of welds in CASS pressurizer (PZR) surge line nuclear reactor piping. A study of the capabilities of inspection relative to PZR surge line piping was initiated in response to cracking discovered at several nuclear power plants; specifically PZR safety and relief nozzles, and surge line dissimilar metal welds, where the safe ends may be fabricated from centrifugally cast materials. The occurrences were summarized in NRC Information Notice 2004-11, “Cracking in Pressurizer Safety and Relief Nozzles and in Surge Line Nozzle,” published on May 6, 2004.

The wall thickness of PZR piping is typically about half that of the larger bore, primary loop piping. Pipe casting processes can produce varied metallurgical grain structures that introduce significant variations in the propagation and attenuation of ultrasonic sound fields. Accordingly, it was determined that, in addition to the thicker section piping previously studied, small section PZR piping should also be studied.

A set of thermal fatigue cracks (TFCs) were implanted and/or grown in-situ into CASS PZR surge-line specimens (pipe-to-elbow welds) salvaged from cancelled nuclear power plants (vintage materials formed in the 1970s). Since lower frequency phased arrays provided the best results relative to the inspection of thick section CASS piping, the flaw responses from the implanted PZR cracks were used to evaluate detection and sizing performance of phased arrays starting at 800 kHz. All of the TFCs introduced in these specimens were readily detected and accurately characterized.

Custom arrays, operating nominally at 1.0 MHz, 1.5 MHz, and 2.0 MHz were subsequently employed and again, all implanted flaws were readily detected. Based upon the results of this work, state-of-the-art phased-array inspection approaches are shown to be rapidly evolving and the capability to detect cracks in CASS components where the wall thickness is generally less than 50 mm (2.0 in.) has been demonstrated. Data and results from this study have been shared with the industry. A proposed Code Case was recently drafted and discussed with the cognizant Section XI committees, American Society of Mechanical Engineers.

CONTENTS

FIGURES

TABLES

EXECUTIVE SUMMARY

Research is being conducted for the U.S. Nuclear Regulatory Commission at the Pacific Northwest National Laboratory to assess the effectiveness and reliability of advanced nondestructive examination (NDE) methods for the inspection of light water reactor components. The scope of this research encompasses primary system pressure boundary materials including cast austenitic stainless steels (CASS), dissimilar metal welds, piping with corrosion-resistant cladding, weld overlays, inlays and onlays, and far-side examinations of austenitic piping welds. A primary objective of this work is to evaluate various NDE methods to assess their ability to detect, localize, and size cracks in coarse-grained steel components.

This report summarizes a technical evaluation to assess the capabilities of phased-array (PA) ultrasonic testing (UT) techniques as applied to the inspection of welds in CASS pressurizer (PZR) surge line nuclear reactor piping. A set of thermal fatigue cracks (TFCs) were implanted into three CASS PZR surge-line specimens (pipe-to-elbow welds) that were fabricated using vintage CASS materials formed in the 1970s. Acoustic responses from these cracks were used to evaluate detection and sizing performance of the PA-UT methods applied. This effort was comprised of multiple elements that included use of microstructural knowledge (dimensional analysis, grain orientation, and grain type) as well as sound field modeling to more effectively modify inspection parameters and enhance the inspection outcomes. Advanced probe design and sound field simulations were employed to enhance detection and characterization of circumferentially oriented flaws, and an assessment of lateral (circumferential) and axial flaw localization capability and performance was also conducted. An evaluation of flaw detection, length sizing, depth sizing, and signal-to-noise ratio was performed for all flaws in the subject specimens, as a function of various inspection parameters, and finally, measurements were made to quantify and assess baseline CASS material noise and attenuation, and the potential impact on flaw detection.

In addition to the implanted TFCs in the weld region, five in-situ grown TFCs were placed in parent pipe and elbow regions. Unlike implanted flaws, this cyclic induction heating process grows TFCs directly in the specimen material. The resultant crack morphology is a product of the specimen composition and microstructure. It is believed that certain characteristics of in-situ grown flaws, such as branching, surface facets, and local discontinuities, are more representative of service-induced cracks. All of these cracks, implanted and in-situ grown, were detected and accurately characterized at multiple frequencies.

Previous work has been focused on heavy-walled primary loop piping components with outer diameters (OD) ranging from 71.12 to 91.44 cm (28 to 36 in.). However, a variety of thinner cast piping welds, with OD measurements ranging from approximately 20.48 to 35.56 cm (12 to 14 in.) exist in pressurized water reactors, specifically in PZR surge lines and dissimilar metal safe ends at Combustion Engineering (CE) designed plants. These smaller diameter piping networks typically exhibit wall thicknesses ranging from 3.05 to 4.32 cm (1.2 to 1.7 in.), which is approximately half that of the larger bore, primary loop piping components. The specimens used in this study were fabricated from piping components salvaged from CE-designed units that were never brought to full operation.

This technical evaluation included examinations on implanted/fabricated and in-situ grown TFCs to evaluate detection, localization, and sizing performance at nominal inspection frequencies of 800 kHz, 1.0 MHz, 1.5 MHz, and 2.0 MHz. Data were acquired at varied inspection angles (30° to 70° in 1° increments) and from both sides of the weld. The data showed that all implanted TFCs were easily detected from both the centrifugally cast stainless steel (CCSS—the pipe) and the statically cast stainless steel (SCSS—the elbow) sides of the weld. Some of the grown in-situ cracks exhibited a significantly stronger signal response from one side of the crack than the opposite side, however, effective detection from either side was demonstrated. The results reported here show that longitudinal mode, transmit-receive matrix phased-array probes, over the applied frequency range, can provide effective sound fields for detection and characterization of TFCs in CASS PZR surge-line components. PA-UT results were compared against true-state data for all flaws, and root mean square error (RMSE) was computed as a metric for both length- and depth-sizing of the flaws. Also, signal-to-noise ratio (SNR) measurements were made and documented for all flaws and scanning scenarios.

The CASS PZR surge-line specimens were sliced, polished, and chemically etched to bring out the microstructures of both pipe and elbow segments. Microstructural analyses were conducted, and dimensional results provided insights into the inspection wavelength-to-grain diameter ratios. Grain diameters ranged from very small 0.5 mm (0.02 in.) to very large 41.0 mm (1.61 in.). Full circumferential PA scans were acquired from the corner trap (end of sample) at 800 kHz and 1.5 MHz on the CCSS pipe ends of the three surge-line specimens to assess baseline material noise and attenuation. In all specimens, the higher frequency resulted in more signal loss, as anticipated. The higher frequency (1.5 MHz) is more sensitive to attenuation and beam redirection as the wavelength relative to the average grain diameters found in these specimens is much smaller. The median length of the diminished signal was suggested as an indication of flaw length that could go undetected due to a loss of signal effect from the coarse material microstructure. With this assumption, the data show that a flaw less than 14.6 mm (0.57 in.) long could go undetected in this material as a worst-case scenario. This is only 1.4% of the circumference and exhibits acceptable detection capabilities. The results showed that lower frequency (800 kHz) was much more effective and consistent at detecting the corner response in all specimens.

The American Society of Mechanical Engineers Boiler and Pressure Vessel Code (ASME Code), Section XI, Appendix VIII acceptance criterion for length-sizing requires a RMSE less than 19.05 mm (0.75 in.), while depth-sizing must be less than 3.18 mm (0.125 in.) RMSE. The data show that length- and depth-sizing RMSE values fell within the ASME limits for both the implanted and grown in-situ flaws.

Signal-to-noise values were very good, further showing that flaw detection was not an issue. The data show that flaws are detectable at frequencies up to 2.0 MHz in these surge-line specimens, and that flaw-sizing performance is not degraded at these frequencies. The higher frequencies applied (especially the 2.0 MHz probe) provided specular and/or flaw tip-diffracted energy from the upper portion of the flaw, which allowed time-of-flight depth-sizing, with sizing error within the ASME Code-allowable limit. Specifically, raster data acquired on the implanted flaws from the CCSS side at 1.5 MHz showed an improvement in length-sizing over the line scan data as raster data better represents the flaw response. The crack depth-sizing was similar from both the CCSS and the SCSS sides for the implanted flaws over all frequencies

with an approximate 1.4-mm (0.05-in.) average error. Calculated SNR values were all very good for both the implanted and in-situ TFCs, indicating minimal attenuation effects on sound field propagation over the frequency range applied. Additionally, the ISI supplier results compared favorably to the PNNL data reported here.

The issue of beam redirection and the potential for circumferential error in the positional registration of flaw responses relative to their true position was also addressed. The measured localization data were compared to the true-state flaw position data on the specimens, and this information was plotted and analyzed to determine if beam skew and localization of the cracks were significantly affected by the microstructures. A limited flaw-mapping exercise was conducted and the data showed that potential lateral (circumferential) beam redirection was measured in 35% of the flaw end points and was as great as 18 mm (0.71 in.). Beam redirection in the axial direction was also addressed and found to be dependent on insonification angle. At a nominal 45 degrees, the average amount of axial beam skew was determined to be approximately 3 mm in the CCSS 9C-001 and 9C-002 specimens.

In conclusion, state-of-the-art phased-array inspection approaches are rapidly evolving and the capability to reliably detect and effectively characterize 10%–50% through wall TFCs in CASS components where the wall thickness is generally less than 50 mm (2.0 in.) has been demonstrated here. PA-UT data obtained using inspection frequencies ranging from 800 kHz to 2.0 MHz yielded strong SNRs and provided accurate length- and depth-sizing results. While additional questions remain to be answered, long-wavelength ultrasonic approaches coupled with advanced signal processing technologies are beginning to show signs of success toward addressing this challenging inspection issue.

ACKNOWLEDGMENTS

The work reported here was sponsored by the U.S. Nuclear Regulatory Commission (NRC) and conducted under NRC Job Code Number N6398. Wallace Norris is the NRC project manager. The Pacific Northwest National Laboratory (PNNL) would like to thank Mr. Norris for his guidance, technical direction, and attention to detail throughout the course of this effort.

In addition, the authors express their sincere gratitude to Guy Maes and Patrick Tremblay at ZETEC, Inc. for their willingness and ongoing engineering support with phased-array system functional and operational issues, as well as their guidance and input regarding phased-array probe design and manufacture.

The authors would like to thank the ISI supplier, LMT Inc., specifically Jeff Devers and Todd Blechinger, for their willingness to come to PNNL to participate in this NDE exercise and provide their professional expertise in assessing and evaluating these CASS specimens.

At PNNL, the authors wish to thank Dr. Stephen Cumblidge for his technical contributions and support of beam modeling and focal law development for phased-array inspection of CASS components. Also, the authors express their gratitude to Stan Owsley for designing the laboratory platform and peripheral mechanics for effective configuration of the piping segments for laboratory examination. The authors would like to thank Marino Morra for providing initial support to this effort in coordinating the cutting and machining of pipe segments for specimen fabrication. The authors are also grateful to Lori Bisping, Angie Dickson, and Earlene Prickett for their efforts in supporting program procurements, contractual issues, financial tracking, and various other administrative duties pertinent to this effort. Finally, the PNNL technical team would like to extend their thanks to Kay Hass for her ongoing support, attention to detail, and technical editing expertise in preparing and finalizing this document.

PNNL is operated by Battelle for the U.S. Department of Energy under Contract DE-AC05-76RL01830.

ACRONYMS AND ABBREVIATIONS

ASME	American Society of Mechanical Engineers
BW	bandwidth
CASS	cast austenitic stainless steel
CCSS	centrifugally cast stainless steel
COD	crack opening dimension
CWD	constant wedge delay
dB	decibels
DMW	dissimilar metal weld
EPRI	Electric Power Research Institute
ID	inner diameter
ISI	inservice inspection
LWR	light water reactor
NDE	nondestructive examination
NPP	nuclear power plant
NRC	U.S. Nuclear Regulatory Commission
OD	outer diameter
PA	phased array
PA-UT	phased array ultrasonic testing
PDI	performance demonstration initiative
PNNL	Pacific Northwest National Laboratory
PT	liquid penetrant testing
PWR	pressurized water reactor
PZR	pressurizer
RMSE	root mean square error
SAFT	synthetic aperture focusing technique
SCSS	statically cast stainless steel
SNR	signal-to-noise ratio
TFC	thermal fatigue crack
TLR	technical letter report
TRL	transmit-receive longitudinal
UT	ultrasonic testing
VWD	variable wedge delay
WSS	wrought stainless steel

1 INTRODUCTION

This report summarizes continuing laboratory evaluation of phased array (PA) ultrasonic testing (UT) on cast austenitic stainless steel (CASS) piping welds. Specifically, the work described herein was performed on pressurizer (PZR) surge line piping specimens at the Pacific Northwest National Laboratory (PNNL) in Richland, Washington. This work was conducted as part of a U.S. Nuclear Regulatory Commission (NRC) project at PNNL entitled, "Reliability of Nondestructive Examination for Nuclear Power Plant Inservice Inspection," under Task 2 of JCN N6398. This report is submitted as an Operating Plan Milestone deliverable.

The focus of the research is to determine the effectiveness and reliability of advanced nondestructive examination (NDE) methods on light water reactor (LWR) components containing cast austenitic stainless steel material and other coarse-grained components that encompass dissimilar metal welds (DMWs), piping with corrosion-resistant cladding, weld overlays, inlays and onlays, and far-side examinations of austenitic piping welds. A specific goal is to assess the capabilities of ultrasonic methods applied during inservice inspection to detect and characterize cracks, should these flaws be manifested, in weldments joining coarse-grained austenitic steels used in Class 1 primary pressure boundary piping at commercial light-water nuclear reactors. Flaw characterization includes length and depth sizing as well as a signal-to-noise determination.

The work described here was performed to provide insights for evaluating the utility of ultrasonic approaches for inspecting CASS PZR surge line, and similar small-bore, piping components. Section 2 of this report describes the project background and technical objectives. Section 3 provides a description of the scope of work as it pertains to this evaluation for PA inspection capability. Section 4 provides a discussion of the CASS inspection problem as it relates to the propagation of ultrasonic energy in coarse-grained microstructures, as well as information pertaining to a microstructural analysis of the various specimens used in this study. Section 5 describes the various probes and probe configurations used, modeling of the probe configurations to generate expected performance information, and issues associated with PA focal law development. Section 6 provides a description of the data acquisition set-up and experimental approach employed in this work, while Section 7 describes the various CASS specimens used in these laboratory studies, including details regarding flaw location, size, and true-state dimensions. Section 8 provides discussions of the data analysis process and results from PA examinations of the CASS PZR surge-line specimens. Section 9 includes a technical discussion and conclusions from the work presented here. Section 10 addresses unresolved issues and a description of work currently in progress, while Section 11 identifies references cited in this report.

2 BACKGROUND AND OBJECTIVES

Since 1977, PNNL has conducted research under NRC guidance to evaluate state-of-the-art technical approaches for inspecting coarse-grained steel reactor components (Taylor 1984; Diaz et al. 1998; Anderson et al. 2007). This work has recently focused on assessing the viability of phased-array ultrasonic NDE methods applied from the outside piping surface of welded components. Regarding ultrasonic methods, PNNL's strategy has been to evaluate low-frequency (500 kHz to 1.5 MHz) phased-array ultrasonic testing (PA-UT) methods to assess the viability in using long-wavelength inspection techniques that are inherently less sensitive to the effects of the coarse-grained microstructures, while maintaining suitable resolution, to effectively detect, localize, and size flaws in these materials (Anderson et al. 2003; Anderson et al. 2007).

The current work is being performed under Task 2 of Project JCN N6398, and is focused on assessing the effectiveness of advanced techniques that may allow consistent and reliable inspections in coarse-grained materials having complex geometrical conditions. A specific task involves determining whether certain NDE techniques (e.g., phased-array UT, synthetic aperture focusing technique [SAFT]-UT) can reliably detect and characterize flaws on the far side of austenitic similar and dissimilar metal welds in wrought piping materials, and on either side of CASS piping welds. This includes inspection of these components where corrosion-resistant cladding, weld overlays, inlays, and onlays have been applied. The NDE techniques should allow for discrimination between coherent ultrasonic energy scattered from grain boundaries (metallurgical or geometric reflectors) and cracks (e.g., discontinuities) in coarse-grained steel components.

Previously, the NRC published NUREG/CR-6933, *Assessment of Crack Detection in Heavy-Walled Cast Stainless Steel Piping Welds Using Advanced Low-Frequency Ultrasonic Methods* (Anderson et al. 2007), which provided a detailed description of the inspection challenges posed by CASS as it relates to the microstructures and component geometries of primary piping loop configurations. The NUREG/CR documented PNNL's initial results of using a new 500-kHz phased-array approach to examine Class 1 pressurized water reactor (PWR) primary coolant system piping welds. These welds are in cast piping of approximately 76.2-mm (3-in.) wall thickness, where low UT frequencies are typically necessary to allow adequate sound field penetration with reduced attenuation (scattering). However, piping welds in thinner cast materials exist in PWRs, such as on PZR surge lines and safe-ends in small-bore dissimilar metal welds (DMWs), where optimum ultrasonic frequencies and inspection parameters have yet to be established. Previously, PNNL submitted technical letter report PNNL-17698, entitled *Assessment of Ultrasonic Phased Array Testing for Cast Austenitic Stainless Steel Pressurizer Surge Line Piping Welds and Thick Section Primary System Cast Piping Welds* (Diaz et al. 2008), summarizing on-going assessments of lower-frequency PA inspection methods on both small and large bore CASS piping, including an initial ultrasonic experiment on machined reflectors to ascertain the optimal center frequency for sound propagation and crack detection in these materials, and providing insights into the application of a PA delta technique for detection of tip-diffracted energy in this piping. Since that time, probe design improvements, acquisition of additional PZR surge-line specimens, greater knowledge of the microstructures, and technological developments to the PA scanning/analysis system have allowed the acquisition of

new ultrasonic data. The resultant outcome was an improved detection and characterization capability for PA ultrasonic inspection of smaller bore CASS piping.

Part of the previous work focused on acquiring baseline PA-UT data using a 1.5-MHz transmit-receive longitudinal (TRL) wave probe to image the end-of-block on both the centrifugally cast stainless steel (CCSS) pipe-side and the statically cast stainless steel (SCSS) elbow side of a PZR surge-line weld obtained from a cancelled nuclear power plant. The pipe-to-elbow weld volume was also examined using this probe to obtain baseline PA-UT data prior to implantation of thermal fatigue cracks (TFCs). These data were used to evaluate the effectiveness of this frequency range for suitable penetration and resolution in these materials, and subsequently provided the basis for additional design and modeling of a more effective PA probe operating at a lower frequency (800 kHz). At the end of these studies, PNNL defined the specifications for implantation of a suite of TFCs in the austenitic weld of two additional CASS PZR surge lines for further evaluation of flaw detection, localization, and sizing capabilities with this technique. These flaws were specified to be implanted within the weld metal (with the exception of flaw 2 in specimen 7C-059) to minimize the potential for disturbing the CASS parent material or introducing implantation anomalies that might result in reflection of coherent sound energy.

The work reported here provides the results and conclusions from newly acquired ultrasonic PA data on all three PZR surge-line specimens using four discrete inspection frequencies—2.0 MHz, 1.5 MHz, 1.0 MHz, and 800 kHz, respectively. These data can be correlated with specific specimen microstructures and are compared against true-state data for all implanted and in-situ grown TFCs. As with the initial technical investigation, phased-array imaging of the entire end-of-block on the CCSS pipe sides of each of the three specimens were again obtained and analyzed to assess sound field continuity and signal strength through the parent material from the corner trap geometry, which essentially simulates a 100% through-wall flaw. This work is expected to provide insights and data to support development of ASME Code rules for improved inspections of CASS piping and allow performance demonstration processes for this coarse-grained material to be established.

3 SCOPE OF PA-UT EVALUATIONS

The scope of the work reported here was defined by NRC guidance and is focused toward evaluating UT inspection capabilities in CASS pressurizer surge-line piping welds. PNNL was tasked with acquisition and procurement of materials, fabrication of flawed specimens, and design and procurement of specialized PA probes, and conducting data acquisition and analysis on these specimens. The macrostructure determination of vintage PZR surge-line piping to determine grain size, shape, and orientation was performed in FY-2007. The material comprising these components include both centrifugally cast (pipe segments) and statically cast (elbows), with dimensions of approximately 30.5- to 35.5-cm (12- to 14-in.) outside diameter (OD) and approximately 33-mm (1.3-in.) wall thickness. This thickness is representative of typical PZR surge lines and various safe-ends in Combustion Engineering-designed plants. The technical evaluation reported here included PA-UT examinations on implanted/fabricated and in-situ grown TFCs to evaluate detection, localization, and sizing performance as a function of frequency and other critical inspection parameters.

The work consisted of design and sound field assessments for various PA probes, probe configurations, and wedges; development of specific PA focal laws; and use of a state-of-the-art data acquisition system (DYNARAY) for implementing examinations. The experimental parameters of the work reported here include:

- Multi-frequency PA-UT examination of CASS PZR surge-line components
  - As a function of inspection frequency (2.0 MHz, 1.5 MHz, 1.0 MHz, and 800 kHz)
  - As a function of inspection angle (30° to 70° in 1° increments)
  - From both sides of the weld (centrifugally cast pipe side and statically cast elbow side)
  - From both sides of the flaw (in-situ grown flaws are located in the parent material)
  - With ±10 degree beam skew on the in-situ grown flaws

During data analysis, microstructures (dimensional analyses, grain orientation, and grain type) of the piping specimens were evaluated, ultrasonic flaw detection and sizing performance was quantified against the true state, and assessments of the UT capabilities for flaw localization/positioning versus true state were conducted. In addition, an assessment of sound field continuity and signal strength (baseline material noise analysis) through the CCSS parent material was performed on all three specimens. Metrics used for the analyses included signal-to-noise ratio (SNR), root-mean-square error (RMSE), and true-state values for flaw length, depth, and axial and circumferential locations relative to the full penetration piping welds.

4 THE CASS INSPECTION CHALLENGE AND MICROSTRUCTURAL ANALYSIS OF PZR SURGE-LINE SPECIMENS

The relatively low cost and high-corrosion resistance of cast stainless steel has resulted in extensive use of this material in the primary coolant piping systems of Westinghouse-designed PWRs (Taylor 1984). Alloying elements and casting processes used in the fabrication of CASS materials are responsible for its corrosion resistance and strength, but also create complex and coarse-grained microstructures. This material is elastically anisotropic and inhomogeneous. The manufacturing process (vibration, pour rate, temperature, etc.) can result in the formation of columnar (dendritic) grain structures often several centimeters in length, with grain growth oriented along the direction of heat dissipation, typically normal to the surface. Additionally, during the cooling and solidification process, columnar, equiaxed (randomly speckled microstructure), or a mixed/layered structure can result, depending on chemical content, control of the cooling, and other variables in the casting process (Taylor 1984; Jeong 1987). The OD and inner-diameter (ID) surfaces of specimens used in the current study possess relatively smooth, machined conditions; this is a normal part of the fabrication method, performed to remove imperfections resulting from the casting process.

Piping welds are subject to periodic UT based on requirements found in the American Society of Mechanical Engineers (ASME) Boiler and Pressure Vessel Code, Section XI, *Rules for Inservice Inspection (ISI) of Nuclear Power Plant Components* (Examination Category B-J, Pressure Retaining Welds in Piping). For ISI to be successful, service-induced flaws must be detected and repaired prior to becoming of such size that the integrity of a component is compromised. Flaw detection is the initial priority, and for UT this is accomplished by analyzing ultrasonic echo waveforms from reflections within the volume of inspected material which could potentially be caused by service degradation. The large grain size found in CASS piping, relative to the acoustic pulse wavelength applied, can severely scatter and attenuate the interrogating sound field. These face-centered cubic materials are anisotropic, with significant changes in acoustic velocity being observed from grain-to-grain. This causes refraction and reflection of acoustic energy at the grain boundaries, effectively skewing and/or partitioning the sound field. As a result, flaws can be incorrectly identified, and specific volumes of material may not being adequately examined. To reduce the impact of the microstructure on the inspection technique, the work reported here focuses on low-frequency (800 kHz to 2.0 MHz) sound field propagation through the material as applied from the OD surface.

All specimens evaluated in this study were acquired from piping components salvaged from cancelled nuclear power plants (NPPs) that were only partially completed, thus never operated. As such, the microstructures comprising these specimens are considered vintage microstructures and representative of those that would be typically found in similar NPPs built in the 1970s. The three specimens were stamped with identification numbers. Specimen 7C-059 was the initial PZR surge-line specimen first acquired by PNNL and reported previously (Diaz et al. 2008). Figure 4.1 shows a side- and end-view of this specimen. The other two specimens, acquired more recently, were cut from the same surge-line piping component (but different casting heats) and were labeled as 9C-001 and 9C-002, respectively.

Figure 4.1 Photographs of the Side-View (left) and End-View (right) of the CASS PZR Ring Segment (specimen 7C-059)

The PZR surge-line specimens consist of a CCSS pipe segment welded to a SCSS elbow segment. Rings from both ends were cut, polished, and etched to show the microstructures of the pipe and elbow ends (centrifugally and statically cast microstructures, respectively) as illustrated in Figure 4.2 for specimen 7C-059. False colors have been added to Figure 4.2 to assist the viewer in judging microstructural transitions, variation and banding. Nominal wall thickness on the pipe side of specimen 7C-059 was 30 mm (1.2 in.) and on the elbow side, 39 mm (1.5 in.). Four circumferentially oriented TFCs were implanted in the weld region of this specimen.

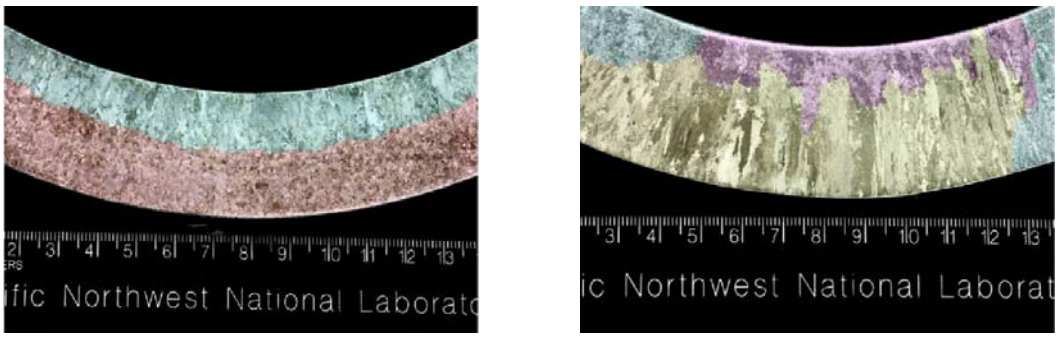

Figure 4.2 Photographs of Polished and Chemically Etched CASS PZR Ring Segment (specimen 7C-059) Showing the Pipe-Side (CCSS) Grain Microstructure (left) and the Elbow-Side (SCSS) Grain Microstructure (right)

An additional long segment of a surge line from Washington Nuclear Power Unit 3 (WNP-3) was obtained (see Figure 4.3). The foreground elbow was removed and cut in half to make two pipe-to-elbow specimens, 9C-001 and 9C-002. Again, rings from the two pipe sides and common elbow side were cut and the surfaces polished and chemically etched to display the microstructures. Figure 4.3 shows the microstructure from the two pipe rings, center and outside legs, and Figure 4.4 shows the elbow microstructure. Nominal wall thickness on the

pipe side was 33 mm (1.3 in.) and 34–44 mm (1.3–1.7 in.) on the elbow side. Three circumferentially oriented TFCs were implanted in each of these two specimens.

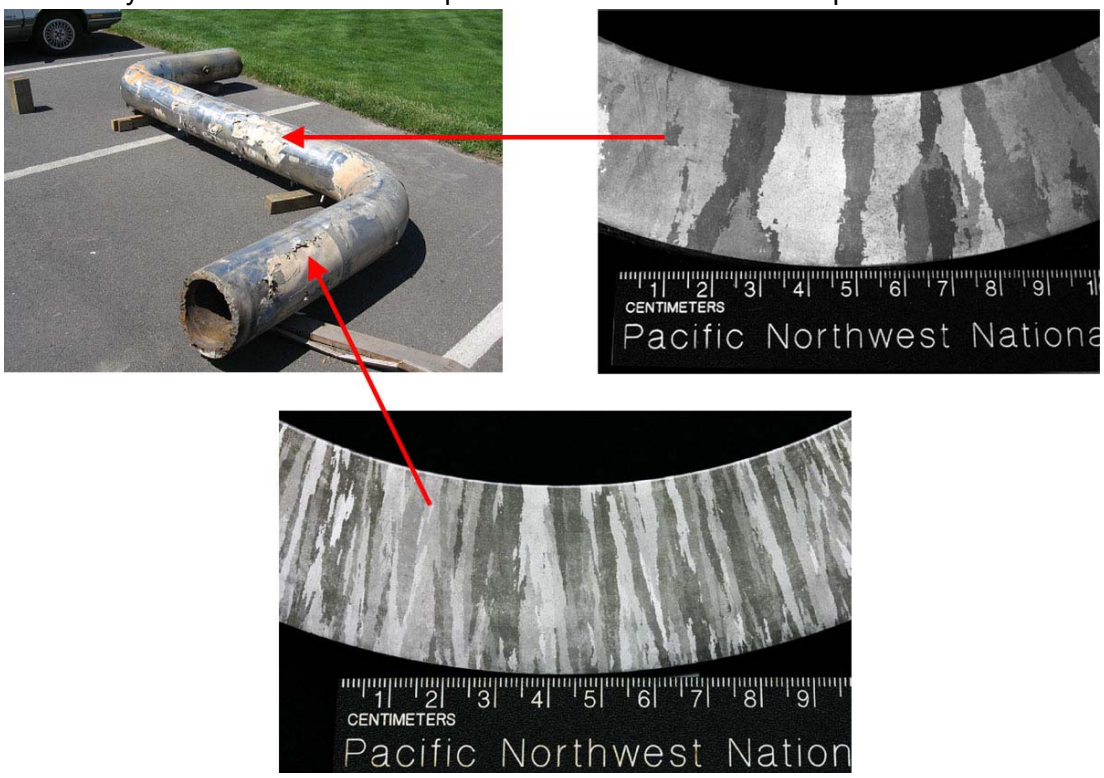

Figure 4.3 WNP-3 Surge Line Section Showing the Locations of the Pipe and Elbow Cuts to Produce Two Pipe-to-Elbow Specimens, 9C-001 and 9C-002. The centrifugally cast pipe microstructures are displayed for both specimens.

Figure 4.4 WNP-3 Surge Line Elbow Microstructure

The microstructures shown in Figures 4.2, 4.3, and 4.4, illustrate the variability and range of grain sizes that can be found in PZR surge-line components. Larger columnar grains that appear as “blocks of material” are evident on one side of the elbow, while thinner dendritic

grains make up the pipe's microstructure on the other side of the weld. In this case, it was anticipated that the average grain diameters and overall microstructures of these segments would provide a more challenging inspection scenario; however, this was not the case, as reported later in this report.

Typical grain diameters range in size from approximately 0.5 mm (0.04 in.) to over 40 mm (1.6 in.) or more as a function of depth or spatial position in the material. At a 1.5-MHz inspection frequency, the corresponding wavelength in the CASS PZR surge-line material is approximately 3.8 mm (0.15 in.). Thus, this wavelength (relative to the average grain diameters encountered) is expected to experience more scattering and attenuation as the sound field propagates through the material. In contrast, at an 800-kHz inspection frequency, the wavelength in the material is approximately 7.1 mm (0.28 in.). The sound field for the lower inspection frequency is generally less sensitive to the effects of grain boundary scattering and attenuation as the wavelength is slightly larger than the median grain size found in the microstructure of these specimens.

The grain-size diameters were measured at a mid-wall line in each of the specimens. Table 4.1 shows the average grain size and range from each of the surge-line specimens. The first surge-line specimen has a smaller-grained microstructure on both the pipe and elbow sides, with average grain diameters of 1.9 mm (0.07 in.) and 2.6 mm (0.10 in.), respectively.

Table 4.1 Grain Diameter Measurements from the Three PZR Surge-line Specimens

	Surge Line 1 Grain Diameter (7C-059), mm (in.)		WNP3 Surge Line Grain Diameter (9C-001 and 9C-002), mm (in.)		
	Elbow	**Pipe**	**Elbow**	**Pipe Center**	**Pipe Outside**
Average	2.6 (0.10)	1.9 (0.07)	10.3 (0.41)	6.6 (0.26)	3.5 (0.14)
Minimum	0.5 (0.02)	0.6 (0.02)	2.6 (0.10)	1.3 (0.05)	0.8 (0.03)
Maximum	6.3 (0.25)	6.7 (0.26)	41.0 (1.61)	25.6 (1.01)	13.9 (0.55)

The WNP-3 specimens' average grain sizes are 10.3 mm (0.41 in.) in the elbow and 3.5 mm (0.14 in.) or 6.6 mm (0.26 in.) in the pipe legs. Maximum grain diameters reached 41.0 mm (1.61 in.) on the elbow and 25.6 mm (1.01 in.) on the pipe side of the WNP-3 specimens. With these larger grains in the material, one would expect more scattering and attenuation as the sound field propagates through the material, possibly leading to a more challenging inspection.

5 PHASED ARRAY PROBES AND FOCAL LAW DEVELOPMENT

5.1 Ultrasonic Probe Details

The samples were examined using four phased-array probes: a 2.0-MHz transmit-receive longitudinal (TRL) arrangement, a 1.5-MHz TRL probe, a 1.0 MHz TRL probe, and an 800-kHz TRL probe. The 1.5-MHz transducer was chosen based on frequencies commonly used in reactor inspections of stainless steels. The 800-kHz transducer was developed by PNNL to be able to detect flaws in 25 to 50-mm (1 to 2-in.) thick CASS specimens based on previous PNNL experience in examining similar components. The additional 1.0- and 2.0-MHz probes were employed to more fully evaluate the entire frequency spectrum and provide data to better assess higher frequency limits for inspecting CASS PZR surge-line components. A set of custom wedges were fabricated for use in this study. Each set of wedges was curved to match the approximate 318-mm (12.5-in.) diameter of the surge-line specimens. General specifications for the four models of transducers are described in Table 5.1.

Table 5.1 Ultrasonic Transducer Physical Specifications

Probe	0.8-MHz TRL, mm (in.)	1.0-MHz TRL, mm (in.)	1.5-MHz TRL, mm (in.)	2.0-MHz TRL, mm (in.)
Active Aperture	44 (1.7)	40 (1.6)	35 (1.4)	22 (0.9)
Passive Aperture	22 (0.9)	20 (0.8)	17.5 (0.7)	11 (0.4)
Active Aperture Elements	10	10	10	10
Passive Aperture Elements	5	5	3	5

5.2 Focal Law Development

Before a phased-array probe can be used to perform an examination, a set of focal laws must be produced to control the firing of individual elements. The focal laws are inputs to the UltraVision control software, which determines specific elements to excite at specific times to allow for proper beam-forming in the material to be examined. The focal laws also contain details about the angles being generated, the focal point of the sound field, the delays associated with the wedge and electronics, and the orientation of the probe. PNNL uses a software package contained in the UltraVision 3.1R4 software program for producing focal laws known as the “ZETEC Advanced Focal Law Calculator.” The software package performs two functions: 1) focal law generation and 2) simulation of the ultrasonic field produced by the probe when using the generated laws. The user enters the physical information about the PA probe, such as the number of elements and the sizes of the elements, and the wedge information, such as the wedge angle and the wedge size, into the program. The desired angles and focal distances are then entered, and the software generates the needed delays for each element to produce the desired beam steering and focusing in the material. The software beam simulation produces a simple image of the probe on the wedge, ray-tracing to show the focal depth and

steering desired, and density mapping to enable the viewer to see how well the sound field responds for a particular angle and whether grating lobes exist that may be detrimental to the examination. Figure 5.1 shows an example of the ray tracing for a probe on the left with the sound field density mapping on the right. It should be noted that this simulation is performed in isotropic material; that is, the velocity of sound is maintained throughout any angle for a particular wave mode, which is not really the true state for CASS, but enables the user to estimate sound field parameters and transducer performance for optimal array design and focal law development.

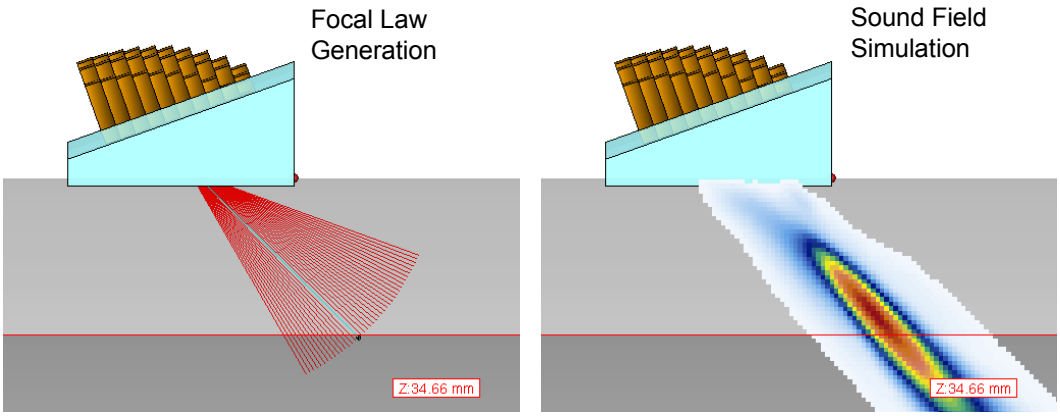

Figure 5.1 The ZETEC Advanced Phased Array Calculator is Useful for Generating Focal Laws (left) and Simulating the Sound Field for the Focal Law (right) to Determine Beam Characteristics

5.3 2.0-MHz TRL Probe

The 2-MHz TRL array was originally designed for evaluating inspection effectiveness of PA methods on components with inlays, onlays, and overlays (Figure 5.2). It consists of two, 5-element by 10-element matrix arrays. One array is used for transmitting, the other for receiving ultrasonic signals. This probe has a 62% bandwidth (BW) at −6 decibels (dB) and an approximately 30-mm^2 (1.2-$in.^2$) footprint with a customized wedge for data collection in tight geometrical configurations. The probes were designed at PNNL and built by Imasonic. The probe's nominal wavelength in stainless steel is 2.92 mm (0.11 in.) at its average center frequency of 2.0 MHz. Skew angles of ±20 degrees were possible with this array.

Specific focal laws were generated for the PZR surge-line specimens based on the thickness of each specimen and the width of the welds in each specimen. While a frequency of 2.0 MHz would normally be considered too high for use on CASS specimens, inspection work at 1.5 MHz indicated that even at higher frequencies, detection and sizing of flaws in smaller bore piping (e.g., CASS PZR surge-line piping) could be achieved. The 2.0-MHz probe produces a wavelength that is generally smaller than the majority of average grain diameters in all three of the PZR surge-line specimens evaluated in this study. However, to push the detection limits and determine whether microstructurally induced attenuation would dominate, this 2.0-MHz

probe was employed, which is a higher frequency than one would normally use for this material. Example simulations of the 2.0-MHz beam using one set of focal laws are shown in Figure 5.3.

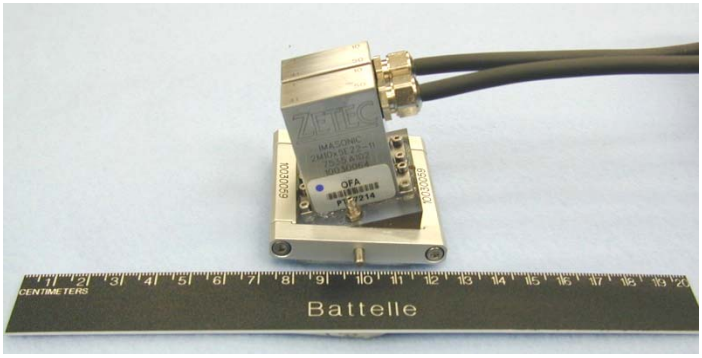

Figure 5.2 2.0 MHz, Phased-Array Probe, Originally Developed for Inlays, Onlays, and Overlays

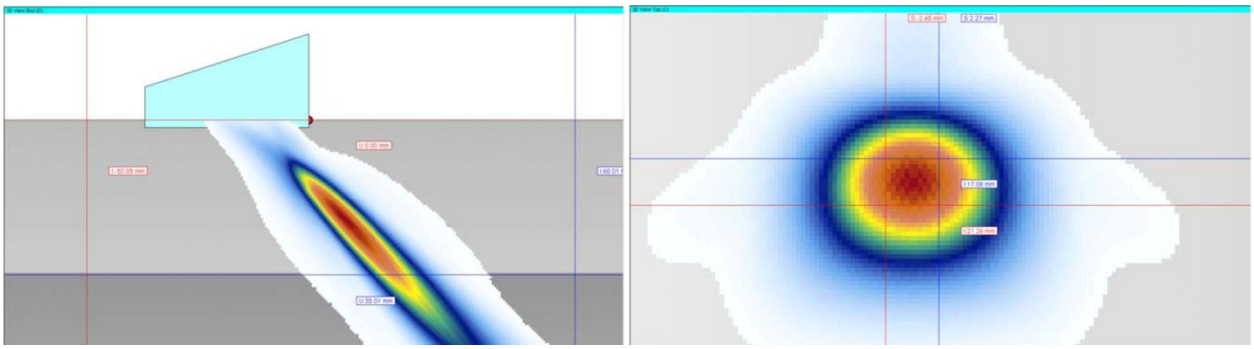

Figure 5.3 Un-normalized Beam Simulations for the 2.0-MHz PA Probe at 45° Incidence in the Cast PZR Surge-Line Specimen, Using a Half-Path Focus at 50 mm (1.97 in.). Top: side-view of focused sound field at 45° incident angle in the part. Bottom: cross-sectional view of sound field at the focal spot, where cursors mark the −3 dB points.

The 2.0-MHz probe was found to produce a beam with a horizontal width of 4.72 mm (0.19 in.) by vertical width of 4.18 mm (0.16 in.) at 45° at the −3 dB points. This probe is able to provide an effective sound field at distances from almost directly under the probe to a distance approximately 45 mm (1.8 in.) in front of the wedge. As with the 1.5-MHz probe, the ability of the probe to accurately measure crack width and depth improves with proximity between the probe focal spot and the flaw, as this is the location of tightest focusing and highest sensitivity.

5.4 1.5-MHz TRL Probe

This 1.5-MHz TRL probe was originally designed by PNNL for examinations of wrought stainless steels (WSS), and consists of two 1.5-MHz PA transducers mounted side-by-side on a Rexolite wedge. The 1.5-MHz probes operated in the pitch-catch mode with wedges held

together by an aluminum frame. The wedge dimensions are 49 × 50 mm (1.93 × 1.97 in.). Both transmit and receive probes were identical in design with a 3×10 element array, an active area of 35 × 17.5 mm (1.38 × 0.69 in.) and a greater than 60% bandwidth at −6 dB. The 1.5-MHz probe has been used in previous examinations of flaws on the near and far sides of austenitic welds in WSS. Similar to the 2.0-MHz array, 1.5 MHz is generally considered to be too high in frequency for examining CASS components which have larger and more complex grain structures than WSS. The 1.5-MHz TRL probe was included in this study because the probe has proven effective in examining materials of similar thickness to the surge line and provides a point of comparison for the other techniques. Skew angles of ±10 degrees were possible with this array. The probe is shown in Figure 5.4.

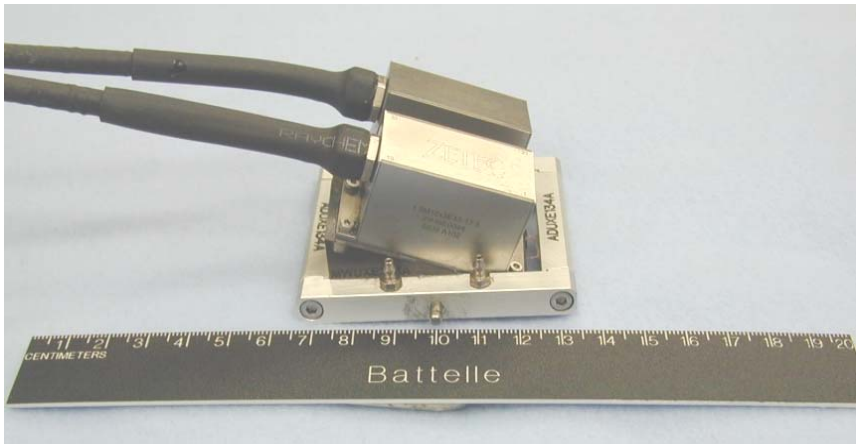

Figure 5.4 1.5-MHz TRL Probe Originally Designed for Wrought Stainless Steel Welds

Specific focal laws were generated for the surge line based on the thickness of the piping and the width of the weld in the surge line pipe-to-elbow specimens. The sound field simulations indicated that the 1.5-MHz probe would be able to produce a well-focused beam at distances from directly below the probe to approximately 45 mm (1.8 in.) in front of the wedge. Multiple focal laws were used in the examinations to obtain optimal results. Example simulations of the 1.5-MHz probe steered to 30°, 45°, and 60°, focused at a depth of 36 mm (1.4 in.), is shown in Figure 5.5. The wavelength for a 1.5-MHz probe is 3.8 mm (0.15 in.). From Figure 5.6, the 1.5-MHz probe was found to produce a beam with a horizontal width of 5.01 mm (0.20 in.) by vertical width of 3.81 mm (0.15 in.) at 45° at the −3 dB points.

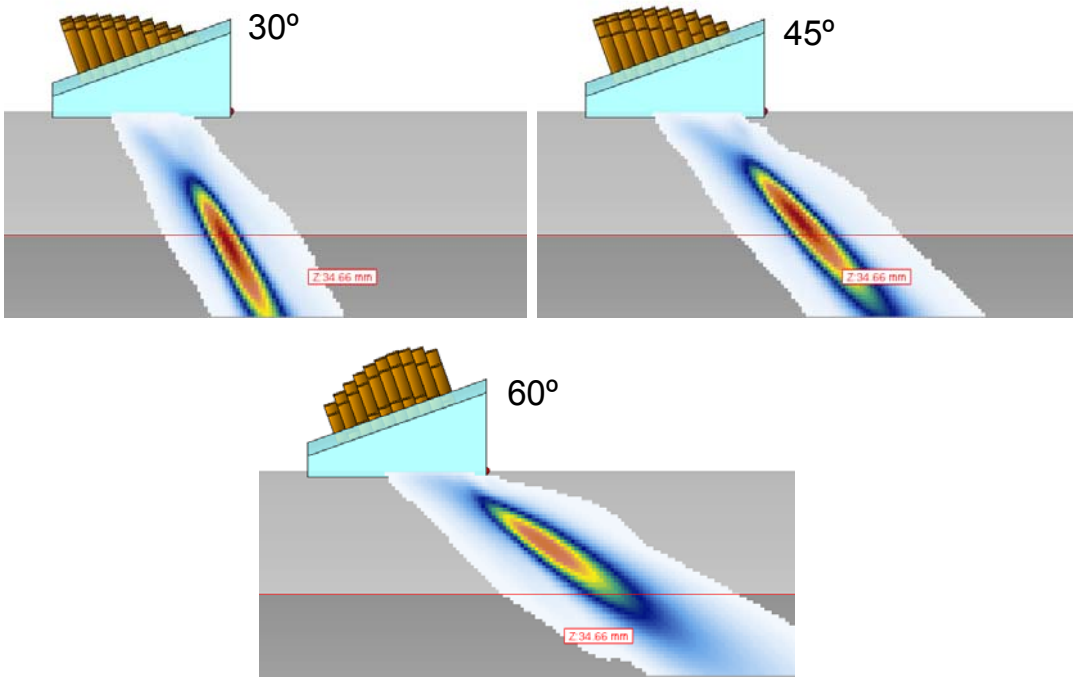

Figure 5.5 Simulations of the Beams Created by the 1.5-MHz TRL Arrangement for 30°, 45°, and 60°

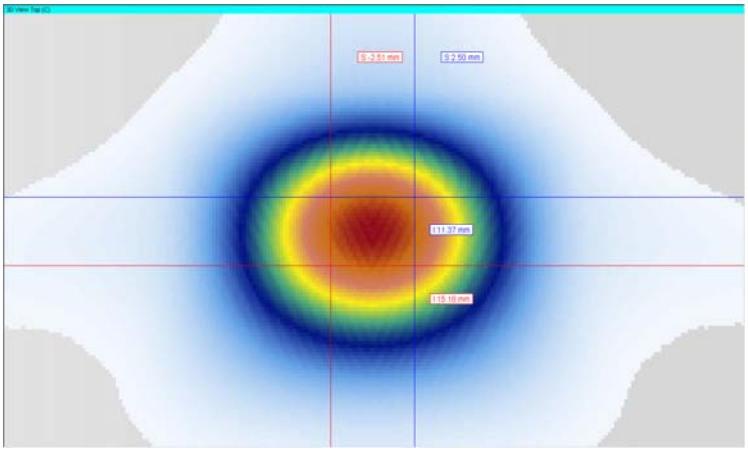

Figure 5.6 Beam Simulations for the 1.5 MHz PA Probe at 45° Incidence in the Cast PZR Surge-Line Specimen, Using a Half-Path Focus at 50 mm (1.97 in.). This is a cross-sectional view of sound field at the focal spot, where cursors mark the −3 dB points.

5.5 1.0-MHz TRL Probe

The 1.0-MHz TRL array (Figure 5.7) was originally designed for evaluating inspection effectiveness of PA methods on components with inlays, onlays, and overlays. It consists of two 5-element by 10-element matrix arrays. One array is used for transmitting, the other for receiving ultrasonic signals. This probe has a 58% BW at −6 dB and an approximately 50-mm^2 (1.97-in.^{2}) footprint with a customized wedge for data collection in tight geometrical configurations. The probe's nominal wavelength in stainless steel is 5.31 mm (0.21 in.) at its average center frequency of 1.1 MHz. Skew angles of ±20 degrees were possible with this array.

Figure 5.7 1.0 MHz, Phased-Array Probe, Originally Developed for Inlays, Onlays, and Overlays

The 1.0-MHz array was used during this study to more effectively complete the evaluation of the PA inspection over the entire frequency range between 800 kHz and 2.0 MHz, and because this is a typical frequency that is employed in field examinations. Thus, it was determined that 1.0-MHz data would provide valuable information to supplement data acquired between 800 kHz and 1.5 MHz. The 1.0-MHz probe produces a wavelength that is generally the same size as the majority of average grain diameters in all three of these PZR surge-line specimens evaluated in this study. Example simulations of the 1.0-MHz beam using one set of focal laws are shown in Figure 5.8.

The 1.0-MHz probe was found to produce a beam with a horizontal width of 6.16 mm (0.24 in.) by vertical width of 4.94 mm (0.19 in.) at 45° at the –3 dB points. This probe is able to provide an effective sound field at distances from almost directly under the probe to a distance approximately 45 mm (1.8 in.) in front of the wedge. As with the 1.5-MHz probe, the ability of the probe to accurately measure crack width and depth improves with proximity between the probe focal spot and the flaw, as this is the location of tightest focusing and highest sensitivity.

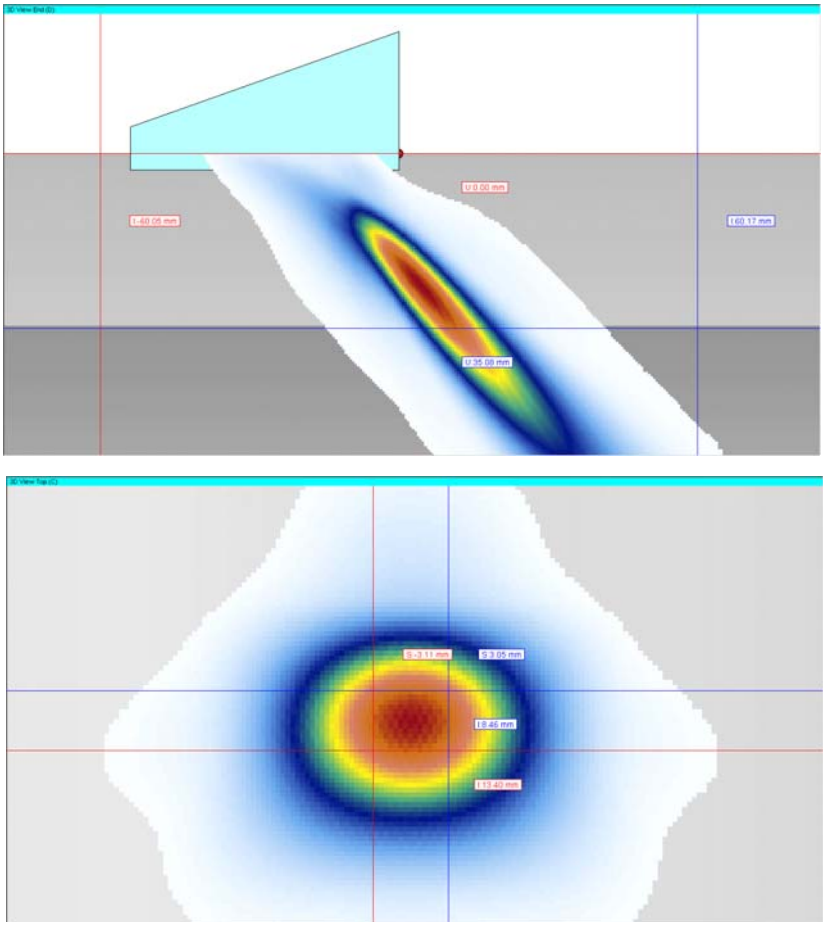

Figure 5.8 Un-normalized Beam Simulations for the 1.0-MHz PA Probe at 45° Incidence in the Cast PZR Surge-Line Specimen, Using a Half-Path Focus at 50 mm (1.97 in.). Top: side-view of focused sound field at 45° incident angle in the part. Bottom: cross-sectional view of sound field at the focal spot, where cursors mark the −3 dB points.

5.6 800-kHz TRL Probe

The 800-kHz probe was designed to provide a more optimal wavelength to allow ultrasonic penetration in the large grain structure of CASS, while maintaining suitable flaw resolution. The probes are mounted on a Rexolite wedge side-by-side to operate in a pitch-catch mode and are shown in Figure 5.9. The wedge dimensions were 63 × 63 mm (2.48 × 2.48 in.). The transmit-and-receive probes are identical in design and consisted of a 10 × 5 element array with an active area of 43.2 × 21.2 mm (1.70 × 0.84 in.) and a greater than or equal to 50% bandwidth at −6 dB. The wedges are curved to match the approximate 318-mm (12.5-in.) diameter of the surge line specimens.

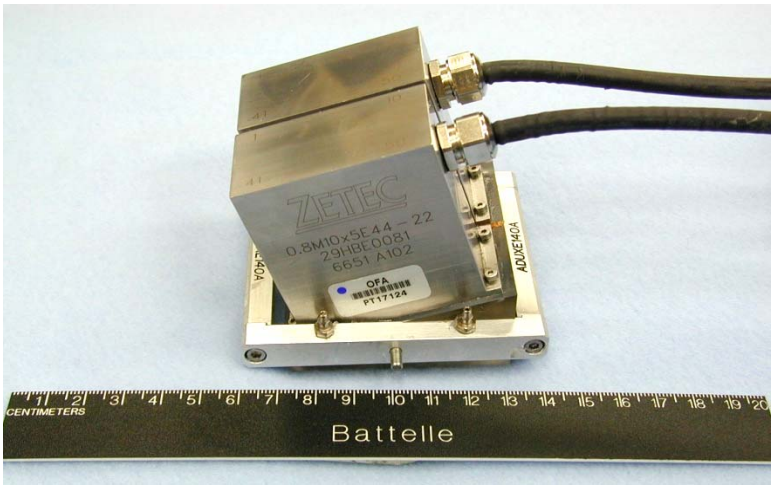

Figure 5.9 800-kHz TRL Probe

The 800-kHz probe produces a 7 mm (0.28-in.) wavelength in stainless steels, almost twice the wavelength of the 1.5-MHz probe. Example simulations of the 800-kHz beam using one set of focal laws are shown in Figure 5.10, which suggest that this probe is capable of insonifying the entire weld region and surrounding material in the CASS specimens.

The 800-kHz probe is able to provide an effective sound field at distances from directly under the probe to a distance of 36 mm (1.42 in.) in front of the wedge. Because the 800-kHz beam focal zone does not extend as far out in front of the probe as the other frequencies used in this study, it needs to be positioned axially closer to the flaw for optimal performance. The 800-kHz probe was found to produce a beam with a horizontal width of 7.19 mm (0.28 in.) by vertical width of 5.58 mm (0.22 in.) at 45° at the −3 dB points (see Figure 5.11).

Using the modeling and simulation capabilities of the UltraVision software, the focal dimensions of the sound field as a function of frequency (for the four probes used in this study) and incident angle were computed for the dimensions corresponding to the CASS PZR specimens. The focal spot size was computed at both the −3 dB and −6 dB points in both horizontal and vertical planes. Table 5.2 summarizes the focal spot size data.

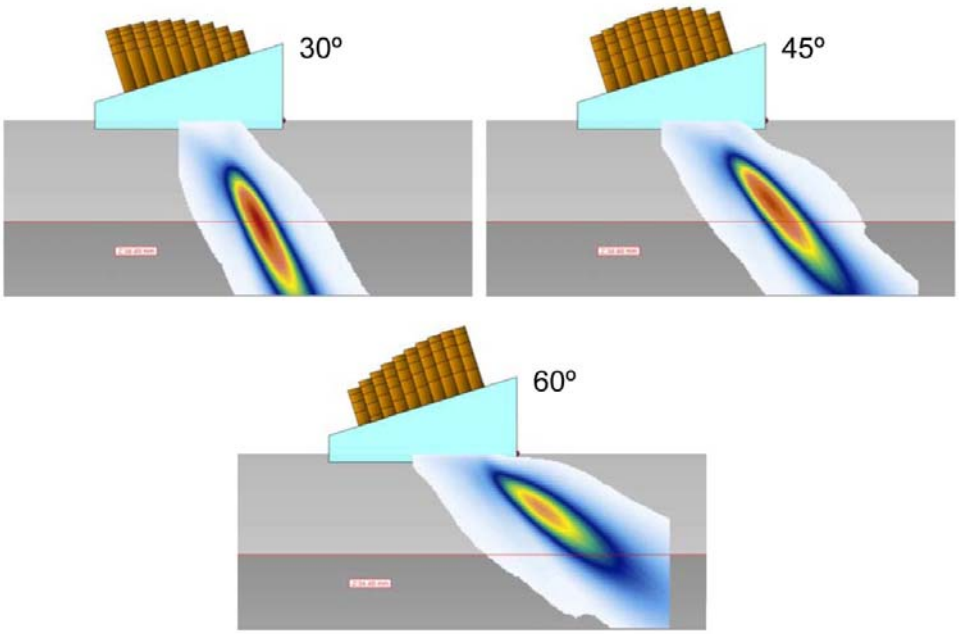

Figure 5.10 Simulations of the Beams Created by the 800-kHz TRL Arrangement for 30°, 45°, and 60°

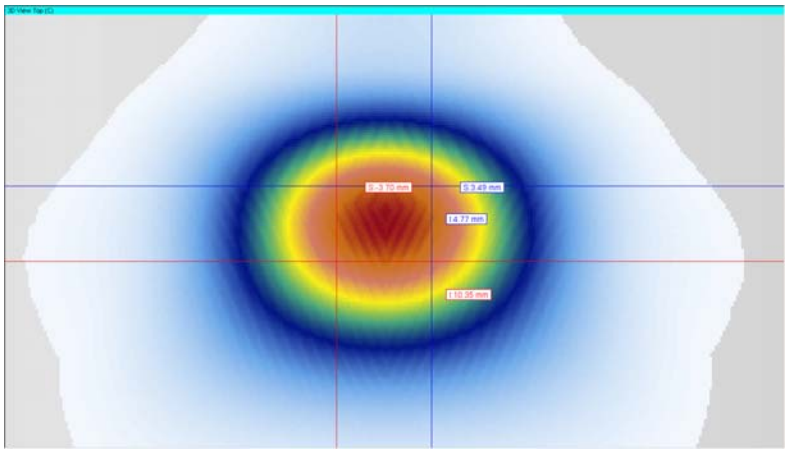

Figure 5.11 Beam Simulations for the 800 kHz PA Probe at 45° incidence in the Cast PZR Surge-Line Specimen, Using a Half-Path Focus at 50 mm (1.97 in.). This is a cross-sectional view of sound field at the focal spot, where cursors mark the −3 dB points.

The sound field dimensions at 30° were calculated at the ID surface rather than at the actual focal spot because the dimensions of the sound field extended well past the ID for the 30° sound beam. The focal spot beyond the ID surface is not of interest. As anticipated, the sound field focal dimensions decrease with increasing frequency, and the focal spots are not symmetric. Focal laws were generated for each probe to insonify the weld region at a constant

sound path from the probe (half-path focusing). The focal depth was set to 50 mm (1.97 in.). A review of Table 5.2 shows the resultant sound beam spot sizes for the 800-kHz probe at 45° as 7.2 mm by 5.6 mm (0.28 in. by 0.22 in.). The spot size for the 1.5-MHz probe at 45° was 5.0 by 3.8 mm (0.20 in. by 0.15 in.). These were measured at the approximately −3 dB points. The first dimension represents the primary axis of the probe and the second is the secondary axis of the probe; in this case, the circumferential direction. While the spot size in the circumferential direction is approximately 50% greater in the 800-kHz probe than in the 1.5-MHz probe, this represents only a 2-mm (0.08-in.) difference. A smaller spot size will give a more accurate length measurement, assuming the entire crack is detected. However, length sizing measurements should be similar for the 800-kHz, 1.0-MHz, and 1.5-MHz probes, with a slightly more substantial difference between the 800-kHz and 2.0-MHz probes.

Table 5.2 Theoretical Focal Spot Dimensions for all Probes Used in this Study

Theoretical Sound Field Spot Size for CASS PZR Specimens								
PA Probe and Incident Angle	**−3 dB point**				**−6 dB point**			
	Horizontal		**Vertical**		**Horizontal**		**Vertical**	
800 kHz TRL	**mm**	**in.**	**mm**	**in.**	**mm**	**in.**	**mm**	**in.**
30 deg @ ID	7.02	0.28	4.06	0.16	14.22	0.56	8.11	0.32
45 deg	7.19	0.28	5.58	0.22	15.14	0.60	11.38	0.45
60 deg	6.11	0.24	7.7	0.30	14.78	0.58	16.38	0.64
1 MHz TRL								
30 deg @ ID	5.89	0.23	3.46	0.14	12.49	0.49	7.95	0.31
45 deg	6.16	0.24	4.94	0.19	13.43	0.53	9.92	0.39
60 deg	5.61	0.22	7.4	0.29	12.57	0.49	15.36	0.60
1.5 MHz TRL								
30 deg @ ID	4.99	0.20	2.86	0.11	10.94	0.43	5.92	0.23
45 deg	5.01	0.20	3.81	0.15	10.72	0.42	7.86	0.31
60 deg	4.94	0.19	6.33	0.25	10.59	0.42	12.8	0.50
2 MHz TRL								
30 deg @ ID	4.2	0.17	2.62	0.10	10.11	0.40	5.79	0.23
45 deg	4.72	0.19	4.18	0.16	11.2	0.44	9.36	0.37
60 deg	4.02	0.16	2.4	0.09	9.98	0.39	6.49	0.26

6 DATA ACQUISITION SET-UP AND CONFIGURATION

Phased-array data were acquired on specimens in the 305–356 mm (12–14 in.) diameter range using a manual track scanner. The laboratory setup for handling and data acquisition of the PZR surge-line specimens is described below.

6.1 Phase Array Data Acquisition

Set-up and laboratory configuration for PA-UT data acquisition on the PZR surge lines required the use of the manual-encoded scanner mounted on an adjustable guide track or ring supported by a custom-designed floor-to-ceiling brace. The floor-to-ceiling brace was equipped with a translation slide providing additional control and degrees of freedom for movement both horizontally and vertically. This provided easy manipulation for fine-tuning of the guide-ring position, relative to the pipe specimen. The setup is shown in Figure 6.1 with the manual scanner on the guide ring section. The probe is mounted on an extension arm that is adjustable along the pipe axis. Two encoders on the manual track scanner provide positional information in either or both the axial and circumferential directions for line and raster scanning.

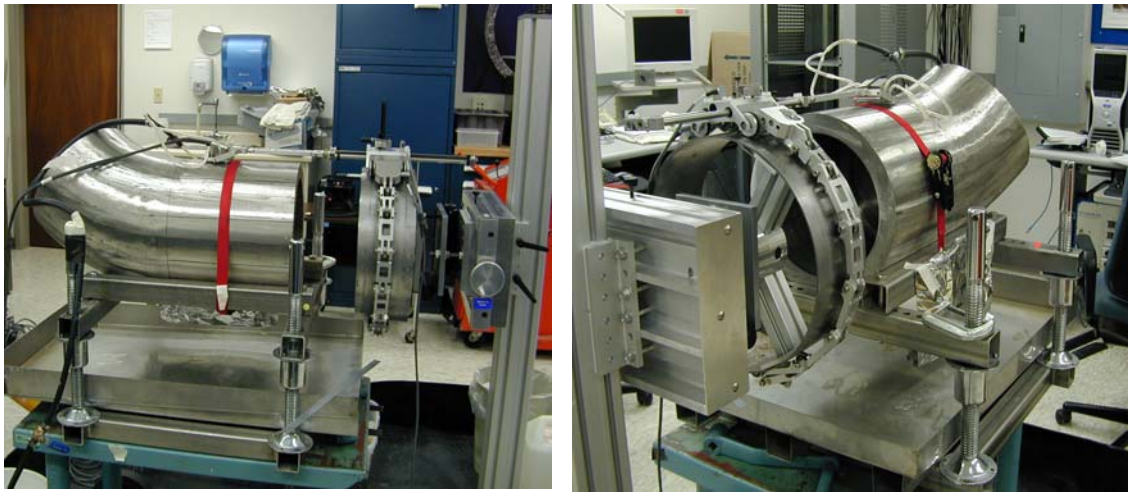

Figure 6.1 Photographs of the PZR Surge-Line Specimen 7C-059. Left: Configured for standard PA-UT with the pipe-end on the right and the elbow-end on the left side of the photograph. Right: The guide ring, translation slide, and floor-to-ceiling brace are shown to the left.

To establish adequate acoustic coupling between the probe wedge and the specimen surface, a flow loop was designed to pump water through nozzles embedded on both sides of the wedge harness that direct the flow evenly over the surface of the specimen to be scanned. As the water couplant flowed off of the top of the specimen, it was collected in a tray, channeled back to the pump, and recycled. Data acquisition was accomplished using the DYNARAY system for all PA probes evaluated in this study. This commercially available system is equipped to accommodate a maximum of 256 channels from PA probes and requires the use of UltraVision

3.1R4 software. Its frequency pulsing electronics will drive probes in the 0.2–20 MHz range. Each probe is driven with a square wave having an optimized pulse width. The pulse width is initially set to half of the probe's design period (1/2T in nsec) where the period is the inverse of the probe's center frequency. The pulse width is then adjusted slightly up or down as needed to maximize the response from a known reflector such as a notch. Phased-array data were acquired over a range of inspection angles from 30° to 70°, in 1° increments. The laboratory workstation and DYNARAY data acquisition system are shown in Figure 6.2.

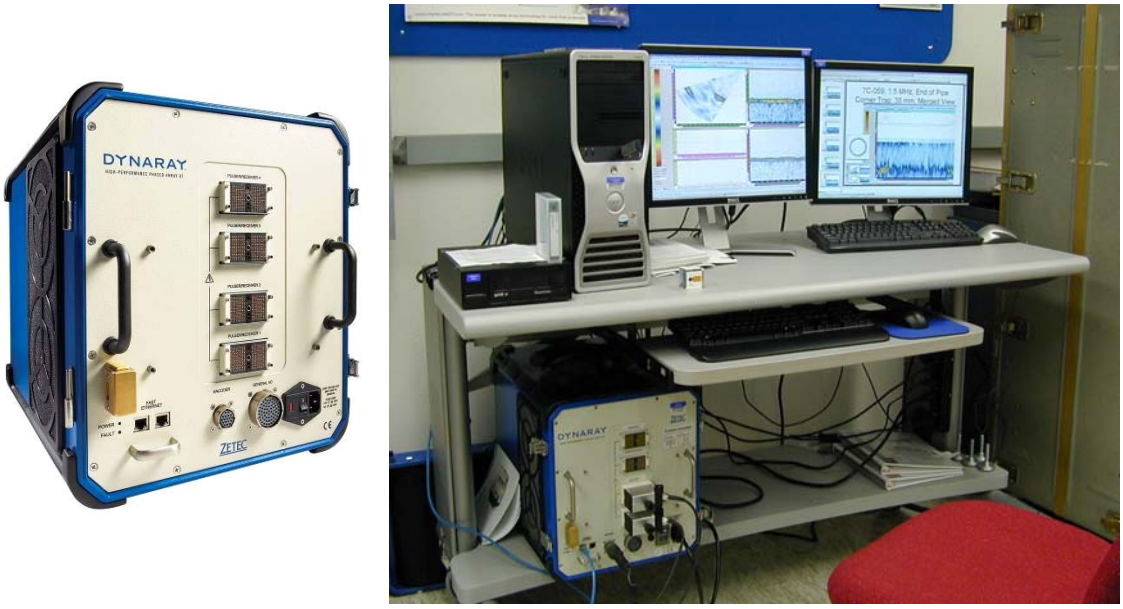

Figure 6.2 Data Acquisition System and Laboratory Workstation. Left: DYNARAY phased array data acquisition system (courtesy of ZETEC). Right: Laboratory workstation for both data acquisition and data analysis, with the DYNARAY system on the lower shelf.

7 SPECIMENS AND FLAWS EVALUATED IN THIS STUDY

7.1 Implanted Flaws in Weld Metal

The first CASS PZR specimen that was fabricated (7C-059) was comprised of moderately sized grains where the microstructure was believed to be less attenuative and thereby slightly less challenging to the PA inspection methods applied in the study. However, based on experience with CASS in large-bore piping welds (Anderson et al. 2007), it was decided to implant cracks with considerable through-wall depth, to increase the probability of detection. The four thermal fatigue cracks implanted in this specimen ranged from 30% to 50% through-wall depth in order to obtain a solid detection baseline for flaws that may pose a significant impact on structural integrity of similar field piping. Results from this initial assessment were very positive; therefore, subsequent flaw implantation in the two 9C specimens resulted in implantation of shallower cracks (ranging from 10% through-wall to 30% through-wall). This provided a more diverse set of flaws (depth-wise) in specimens with more challenging microstructures, effectively allowing the study to push the detection limits as well as the sizing limits for the PA approach. All of the flaws were specified to be implanted within the weld metal (with the exception of flaw #2 in specimen 7C-059) to minimize the potential for disturbing the parent CASS material or introducing implantation anomalies that might result in reflection of coherent sound energy.

7.1.1 CASS PZR Surge-Line Specimen 7C-059

This CASS PZR surge-line segment is 304.8-mm (NPS 12-in.) diameter Schedule 160 centrifugally cast stainless steel pipe, welded to a statically cast stainless steel elbow. This pipe segment is approximately 457.2 mm (18 in.) in length, has a 323.9-mm (12.75-in.) OD (pipe side), and is approximately 31.8-mm (1.25-in.) in wall thickness on the centrifugally cast side of the weld. This specimen was salvaged from a cancelled plant and four TFCs were implanted into the weld region. The technique includes excavation of parent/weld material in the area targeted for implantation, and then subsequent insertion of the coupon containing a thermally induced fatigue crack (see Figure 7.1). The flaw implantation vendor (FlawTech, Inc.) employs a unique proprietary process where heating/cooling under tension is used to initiate a TFC in a coupon. The number of cycles is controlled to obtain the desired crack depth and “roughness.” After taking exact physical measurements, the flaw implant is seal welded in place to establish final location and size. The remaining weld groove is then filled by standard welding procedures. The disadvantage is that the coupon is surrounded by weld metal that may potentially introduce additional UT reflectors; however, for studies on coarse-grained CASS materials, the flaws were implanted into the existing weld structures. Therefore, it was assumed that any implantation anomalies would not be detectable in the existing welds, especially in light of the coarse-grain nature of the base piping materials. Only flaw #2 was implanted outside the weld, in the CCSS parent material, to determine if this assumption was valid. All four implanted flaws were circumferentially oriented.

A schematic (side view illustration) of the four TFCs depicting flaw position relative to the weldment and flaw depth is provided as Figure 7.2. Figure 7.3 shows a full circumferential view of all flaw positions and extents on specimen 7C-059. This pipe end-view depicts the circumferential extent (length) of the implanted ID surface-connected cracks, relative to the radial position along the pipe circumference.

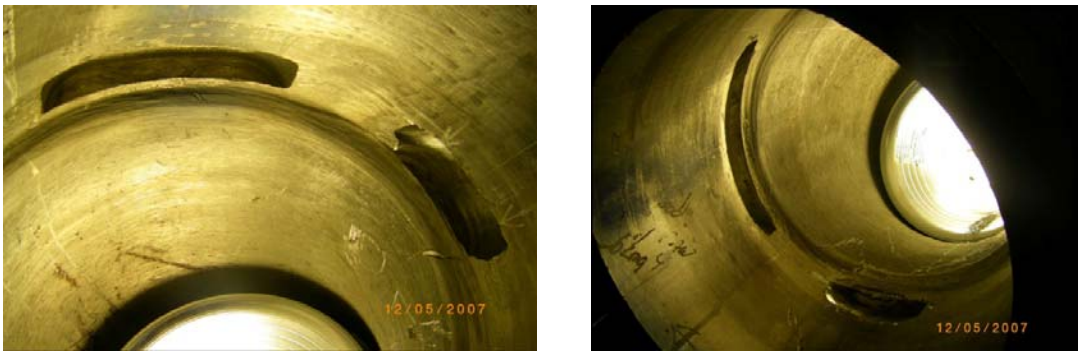

Figure 7.1 Photographs of the Inside Surface of the CASS PZR Surge-Line after Excavation and Preparation of the Areas Targeted for Flaw Implantation (courtesy of FlawTech, Inc.)

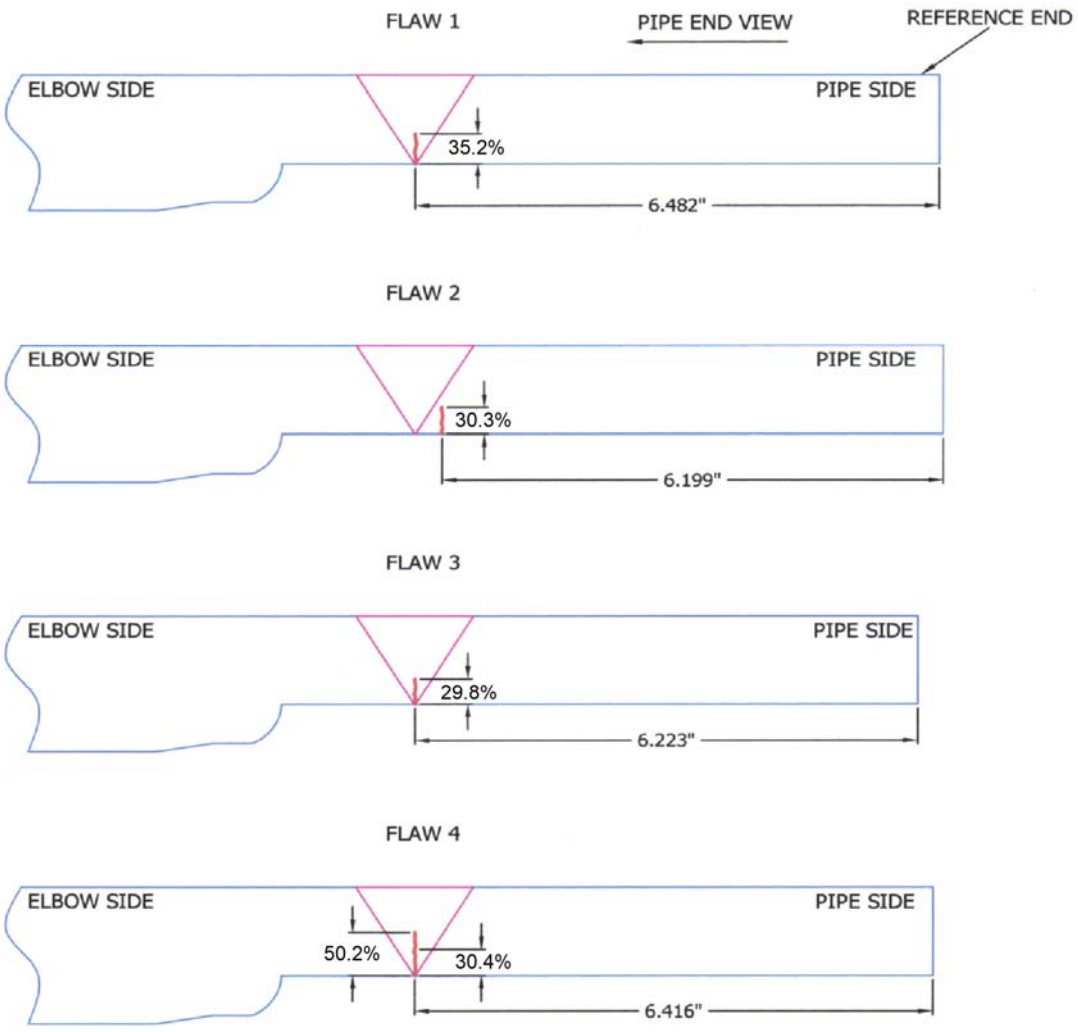

Figure 7.2 Side View Illustration of All Four Thermal Fatigue Cracks Implanted Into PZR CASS Specimen 7C-059 (courtesy of FlawTech, Inc.)

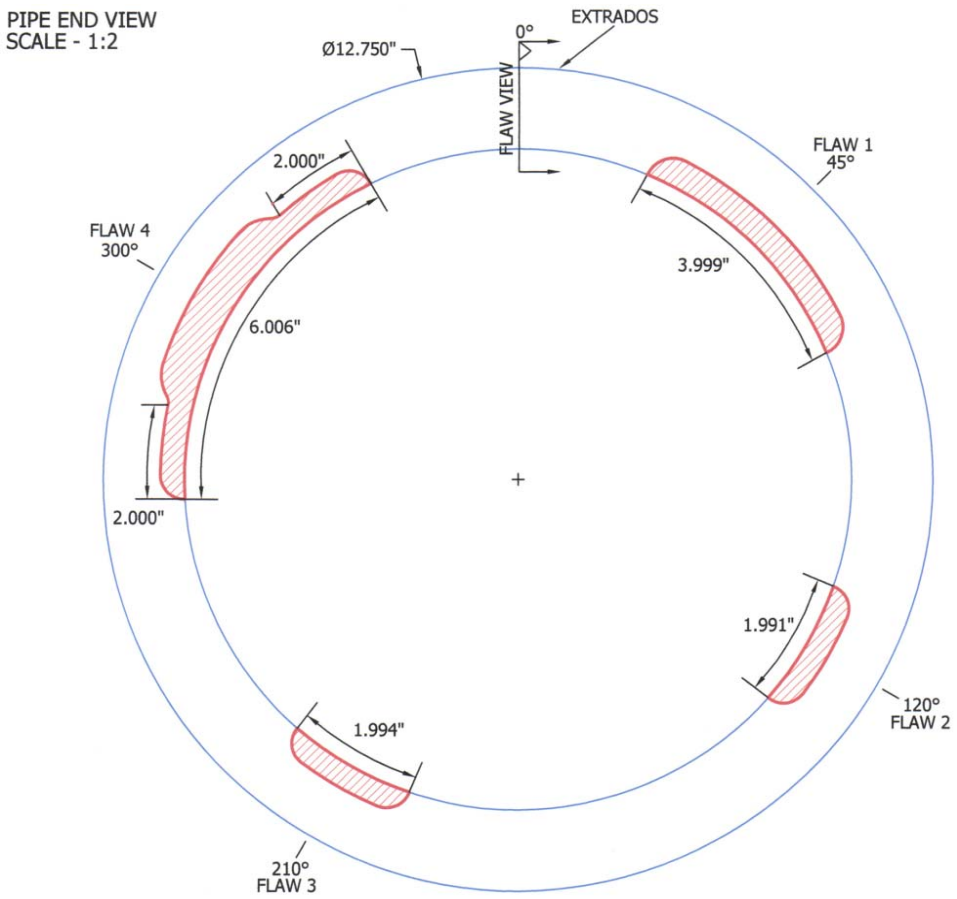

Figure 7.3 End View Illustration of All Four Thermal Fatigue Cracks Implanted into PZR CASS Specimen 7C-059 (courtesy of FlawTech, Inc.)

7.1.2 CASS PZR Surge-Line Specimen 9C-001

This CASS PZR surge-line segment is 304.8-mm (NPS 12-in.) Schedule 160 pipe, with a CCSS pipe segment welded to a SCSS elbow. This CASS PZR surge-line specimen is approximately 762 mm (30 in.) in length, 324 mm (12.75 in.) OD, and is approximately 31.8-mm (1.25-in.) in wall thickness on the centrifugally cast side of the weld (pipe side). This pipe-to-elbow specimen was cut from a longer segment of a surge line salvaged from Washington Nuclear Power, Unit 3 (WNP-3). FlawTech, Inc. performed all crack implantations in this specimen. Three implanted TFCs were introduced. These cracks were inserted via a coupon implant technique and were all circumferentially oriented flaws. Flaw number one has two distinct through-wall depths associated with it; thus, for reference purposes, each depth region will be identified individually as Flaw 1A and Flaw 1B. A side view illustration of the three flaws depicting flaw position relative to the weldment and flaw depth is provided in Figure 7.4. Figure 7.5 shows a full circumferential view of all flaw positions and extents on specimen 9C-001. This pipe end-view depicts the circumferential extent (length) of the implanted ID surface-connected cracks, relative to the radial position along the pipe circumference.

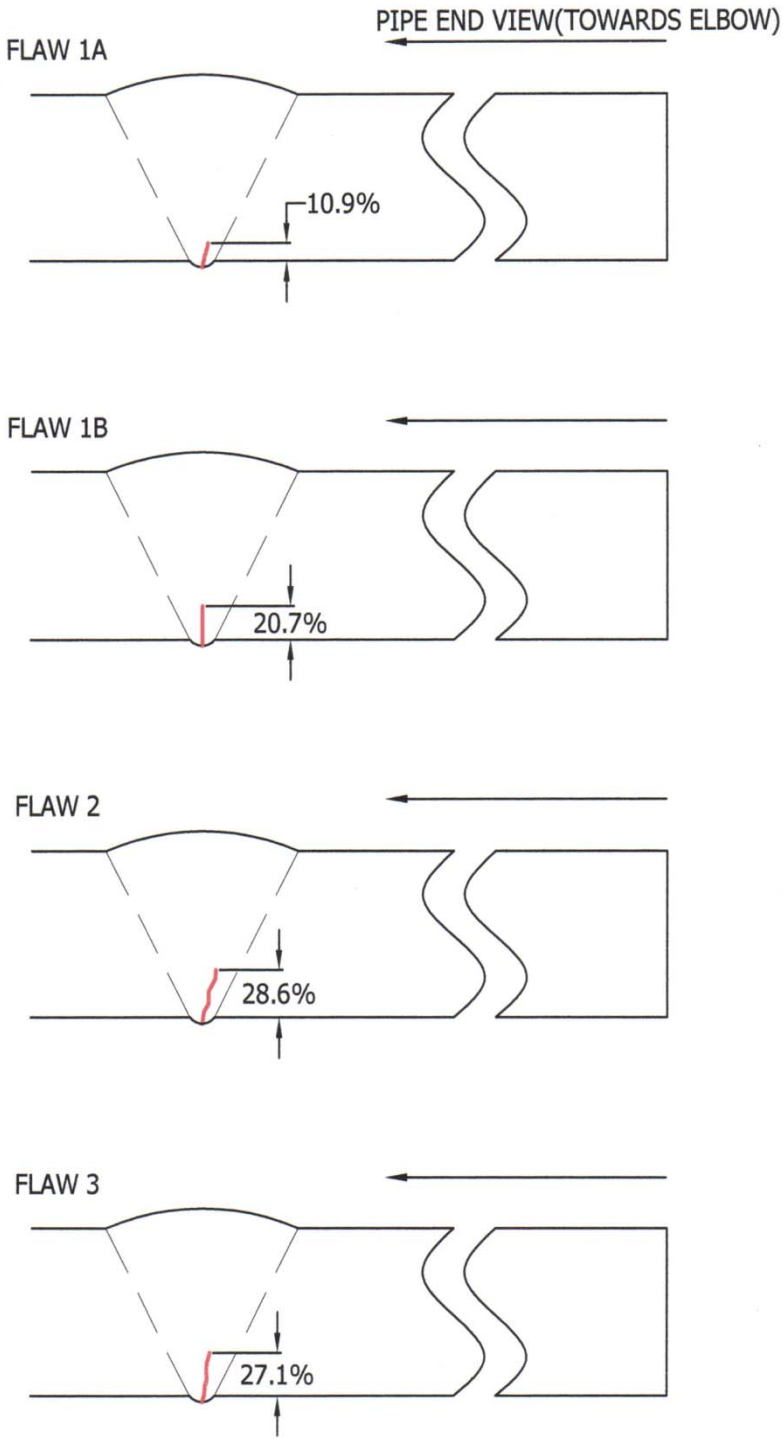

Figure 7.4 Side View Illustration of All Four Thermal Fatigue Cracks Implanted into PZR CASS Specimen 9C-001 (courtesy of FlawTech, Inc.)

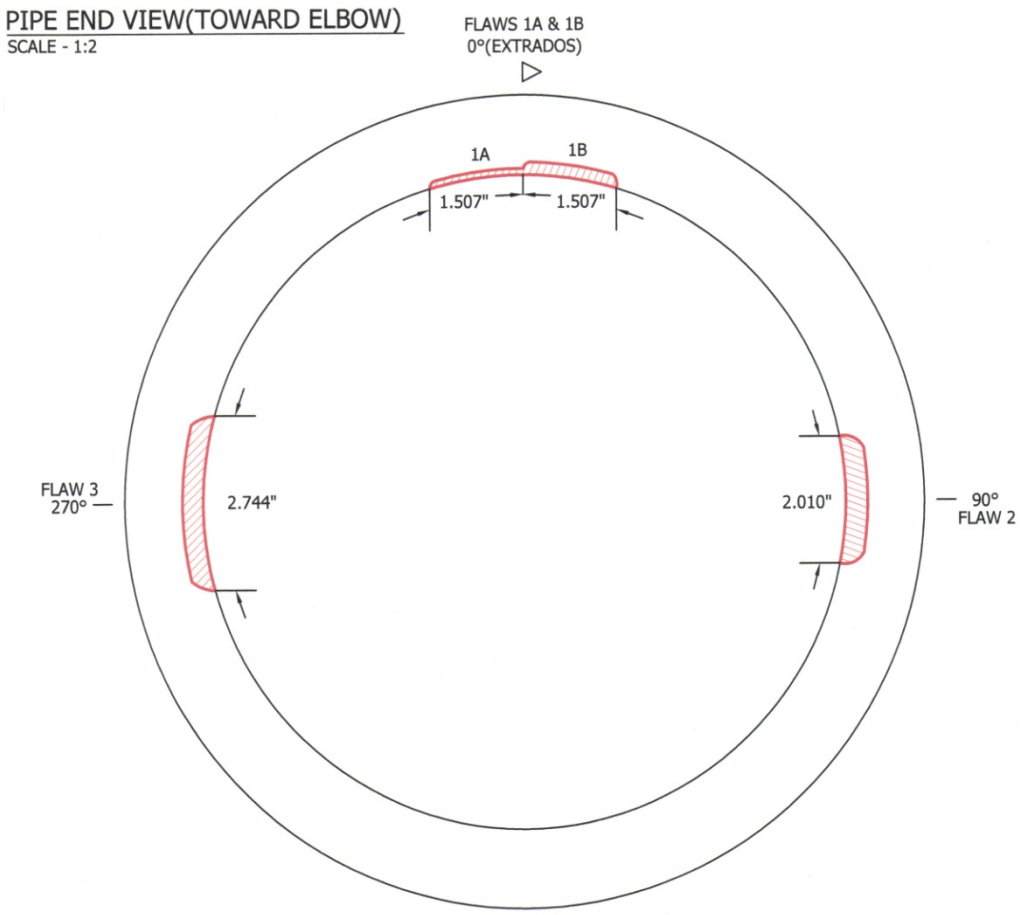

Figure 7.5 End View Illustration of All Four Thermal Fatigue Cracks Implanted into PZR CASS Specimen 9C-001 (courtesy of FlawTech, Inc.)

7.1.3 CASS PZR Surge-Line Specimen 9C-002

This CASS PZR surge-line segment is NPS 12-in. Schedule 160 pipe, with a CCSS pipe segment welded to a SCSS elbow. This CASS PZR surge-line specimen is approximately 762 mm (30 in.) in length, 324 mm (12.75 in.) OD, and is approximately 31.8-mm (1.25-in.) in wall thickness on the centrifugally cast side of the weld (pipe side). This pipe-to-elbow specimen was also cut from a longer segment of a surge line from WNP-3. As with the previous specimen described above, FlawTech, Inc. performed all crack implantations, with three implanted TFCs being introduced into this specimen. These cracks were inserted via a coupon implant technique and were all circumferentially oriented flaws. Flaw number one has two distinct through-wall depths associated with it. Therefore, in referencing this crack, each depth region will be identified individually as Flaw 1A and Flaw 1B. A side-view illustration of the three flaws depicting flaw position relative to the weldment and flaw depth is provided in Figure 7.6. Figure 7.7 shows a full circumferential view of all flaw positions and extents on specimen 9C-002. This pipe end-view depicts the circumferential extent (length) of the implanted ID surface-connected cracks, relative to the radial position along the pipe circumference.

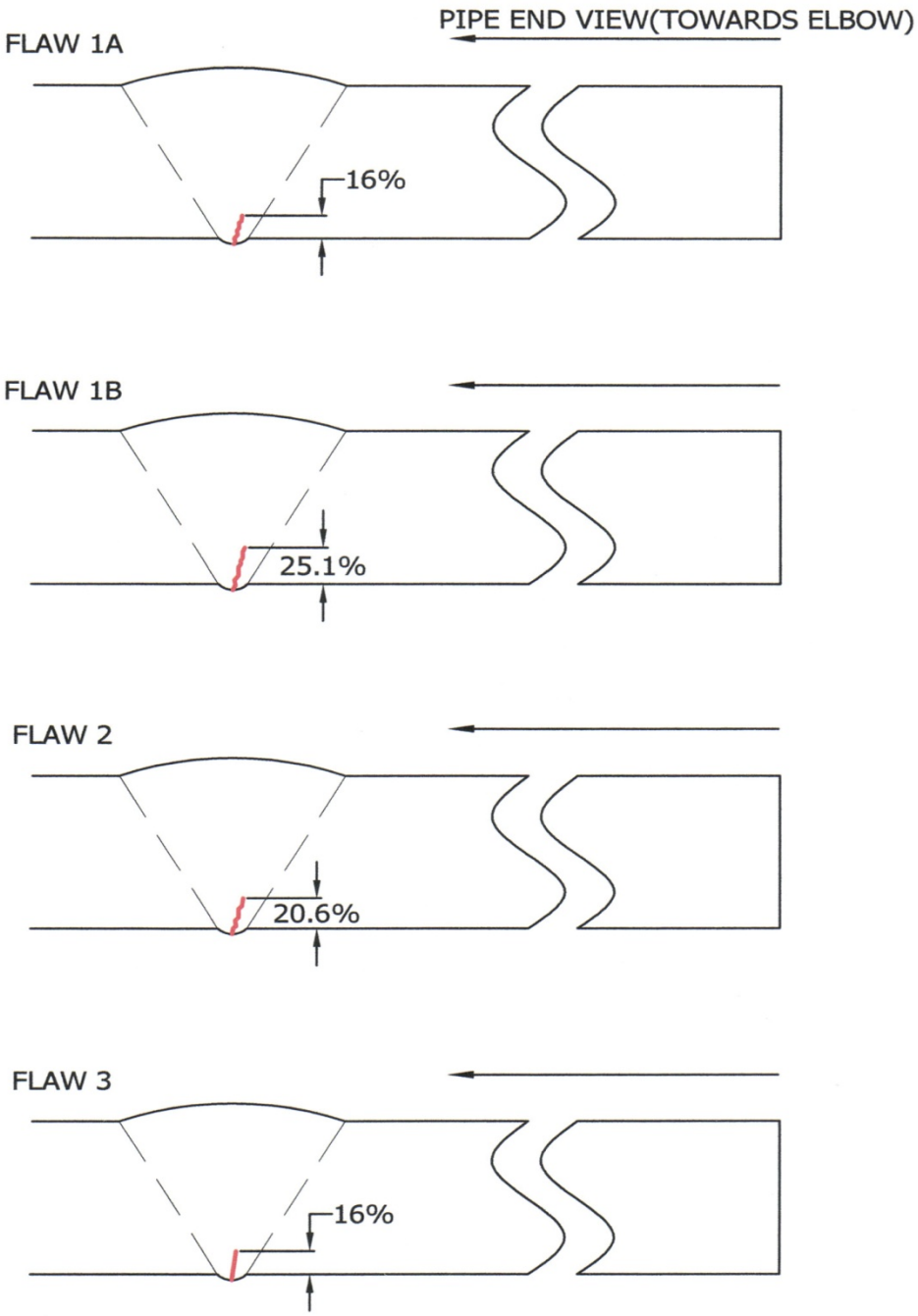

Figure 7.6 Side View Illustration of All Four Thermal Fatigue Cracks Implanted into PZR CASS Specimen 9C-002 (courtesy of FlawTech, Inc.)

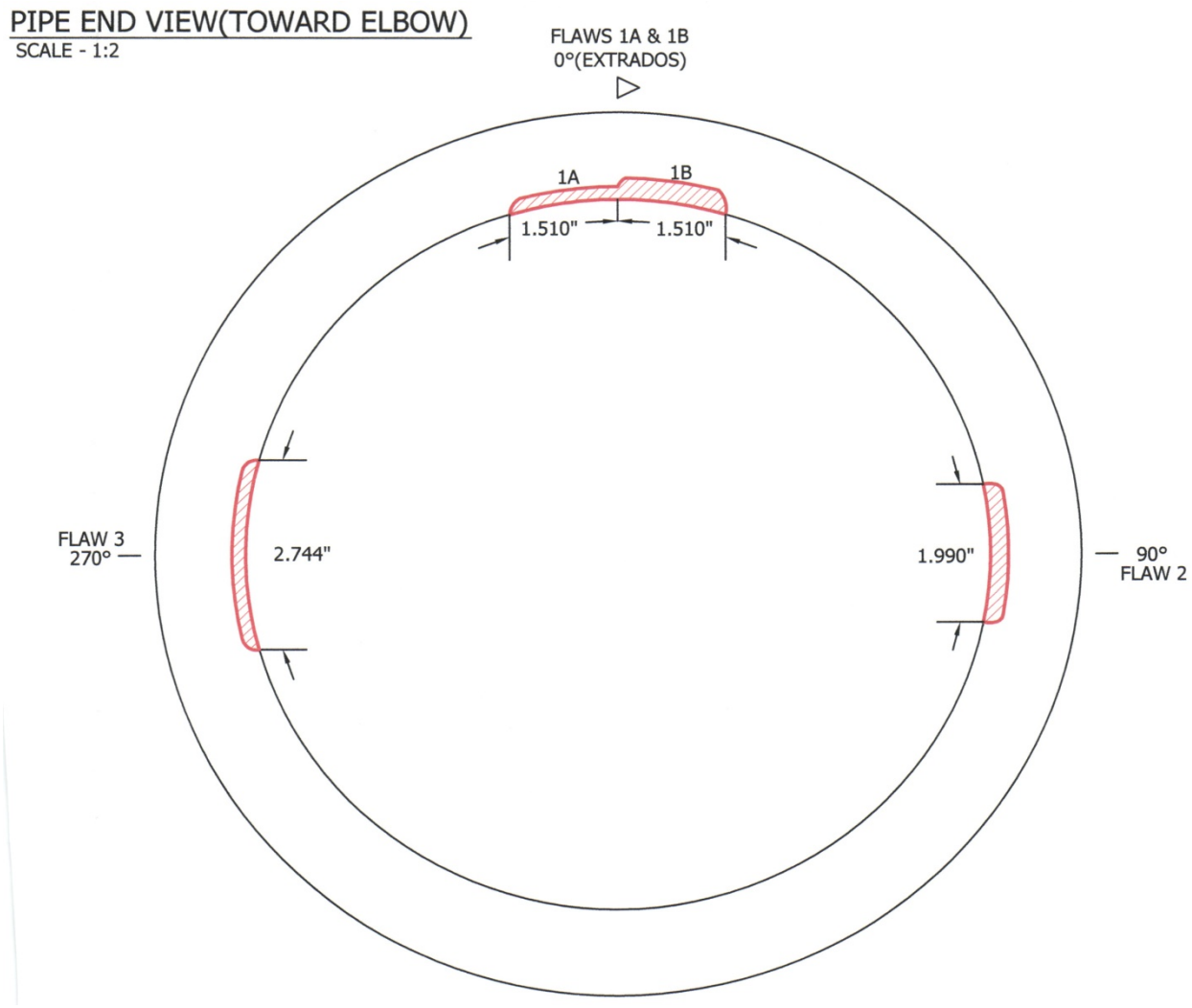

Figure 7.7 End View Illustration of All Four Thermal Fatigue Cracks Implanted into PZR CASS Specimen 9C-002 (courtesy of FlawTech, Inc.)

A summary of flaw position, location, orientation, length, and depth (flaw height) for all three PZR surge-line specimens is provided in Table 7.1. In Table 7.1, in the column depicting "Flaw," the first number represents the specific CASS PZR surge-line specimen, while the second number represents the specific flaw within that specimen. Specimen 1 is 7C-059, specimen 2 is 9C-001, and specimen 3 is 9C-002; thus Flaw #2-3 would indicate Flaw #3 on Specimen 9C-001.

Table 7.1 Summary Table Depicting True-State Dimensions and Locations of Implanted Flaws in All Three CASS PZR Surge-Line Specimens Examined

Flaw	Flaw Type	Flaw Location	Flaw Orientation	Flaw Length, cm (in.)	Flaw Depth (Height)	Degree Location
1-1	Thermal Fatigue	Weld Centerline	Circumferential	10.2 (4.0)	35.2% T	45°
1-2	Thermal Fatigue	Pipe Side Near Fusion Line	Circumferential	5.1 (2.0)	30.3% T	120°
1-3	Thermal Fatigue	Weld Centerline	Circumferential	5.1 (2.0)	29.8% T	210°
1-4	Thermal Fatigue	Weld Centerline	Circumferential	15.2 (6.0)	30.4/50.2% T	300°
2-1	Thermal Fatigue	Weld Centerline	Circumferential	7.6 (3.0)	10.9/20.7% T	0°
2-2	Thermal Fatigue	Weld Centerline	Circumferential	5.1 (2.0)	28.6% T	90°
2-3	Thermal Fatigue	Weld Centerline	Circumferential	7.0 (2.7)	27.1% T	270°
3-1	Thermal Fatigue	Weld Centerline	Circumferential	7.6 (3.0)	16/25.1% T	0°
3-2	Thermal Fatigue	Weld Centerline	Circumferential	5.1 (2.0)	20.6% T	90°
3-3	Thermal Fatigue	Weld Centerline	Circumferential	7.0 (2.7)	16% T	270°

7.2 In-Situ Grown Flaws in Base Metal

In addition to the implanted thermal fatigue cracks located in the weld region of the PZR surge-line specimens, additional ID surface-connected cracks were grown in-situ in the CASS pipe and elbow parent materials of specimen 9C-002. PNNL contracted Trueflaw Ltd. to grow two flaws in the pipe material and one flaw in the elbow material using a patented controlled thermal fatigue loading technique. This process grows thermal fatigue cracks directly in the specimen material with the use of local induction heating. Therefore, the actual cracks grown are a result of natural fatigue damage caused by the stress from thermal cycling. These cracks are directly related to the composition and microstructure of the specimen. If the specimen has inherent stresses or weakness, the cracks will tend to follow the path of least resistance, resulting in a complex crack morphology containing attributes such as branching, turns, facets, or discontinuities. It is believed that the characteristics of these flaws are representative of service-induced TF cracks.

7.2.1 Validation Flaw Specimen

Trueflaw's process to create in-situ cracks in a mock up specimen begins with testing their proprietary and patented technique on a comparable test specimen. A 203.2 mm (8 in.) long PZR surge line pipe section (Figure 7.8) was provided by PNNL with similar metallurgical characteristics as specimen 9C-002. This specimen was cut from the same PZR surge line spool-piece material as that used to fabricate the specimens evaluated in this study. Two in-situ thermal fatigue cracks were grown in this validation specimen with different lengths and depths as a means to calibrate the crack generation process. Prior to the destructive examination (DE) of the validation specimen, PNNL collected ultrasonic phased-array data on the two cracks for nondestructive crack detection and characterization. Trueflaw correlates the destructive validation results with their thermal fatigue process parameters obtained from the validation specimen and then makes necessary process adjustments to obtain the desired flaw length and depth in the actual specimen.

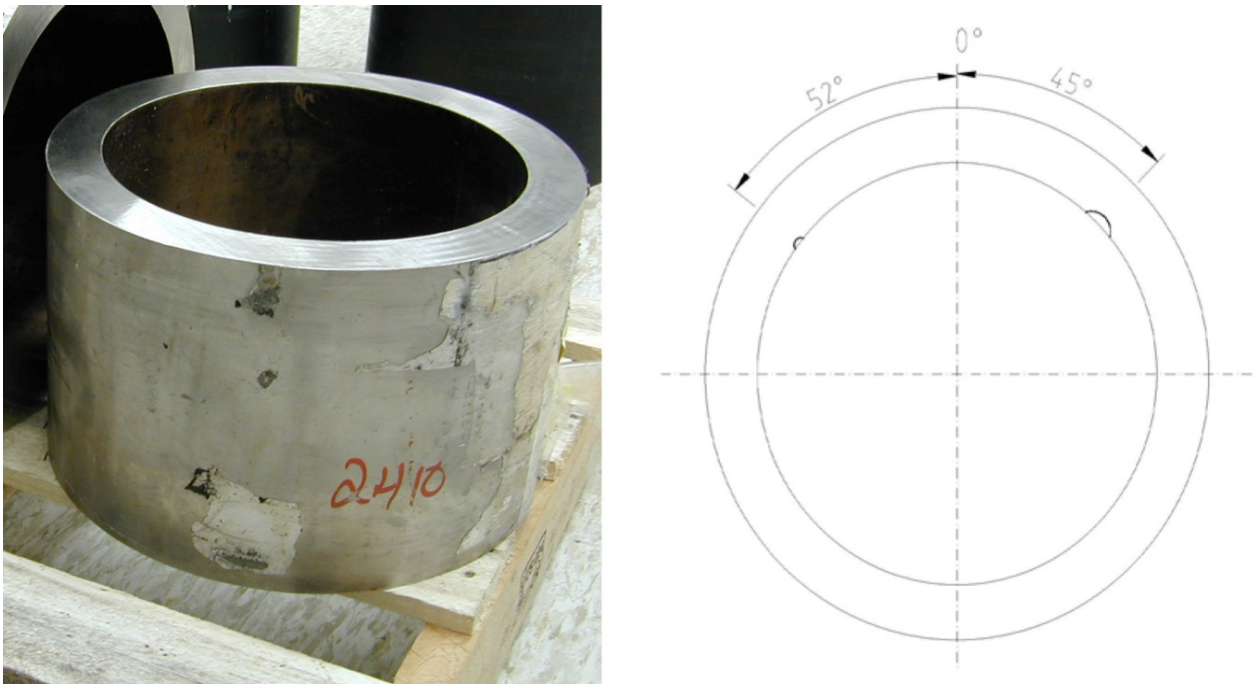

Figure 7.8 CASS Validation Specimen

Figure 7.9 shows the ID liquid penetrant test (PT) results and fracture surface image after destructive analysis of flaw 057BAB1087 (1087) in the validation test specimen. The “elbow” and “pipe” notation in the figure was arbitrarily chosen to represent an inspection side of the flaw. Side 1 or side 2 could also have been used. The circumferential axis is also noted. This shows the index direction for raster scan data and the scan direction for line scan data. This flaw has a physically measured ID length of 8.4 mm (0.33 in.) in the circumferential direction and a depth of 3.4 mm (0.13 in.) as determined from the fracture surface and PT data. Additionally, this crack exhibits an average crack opening dimension (COD) of 48.3 µm with five turns and four branches. These crack characteristics were supplied by Trueflaw personnel.

Flaw 070BAB1089 (1089) was created to have both length and depth larger than flaw 1087. Flaw 1089 has a measured length of 21.8 mm (0.86 in.) and a depth of 6.0 mm (0.24 in.) based on the ID PT and fracture surface analysis (Figure 7.10). This flaw has an average COD of 51.7 µm with six turns and five branches.

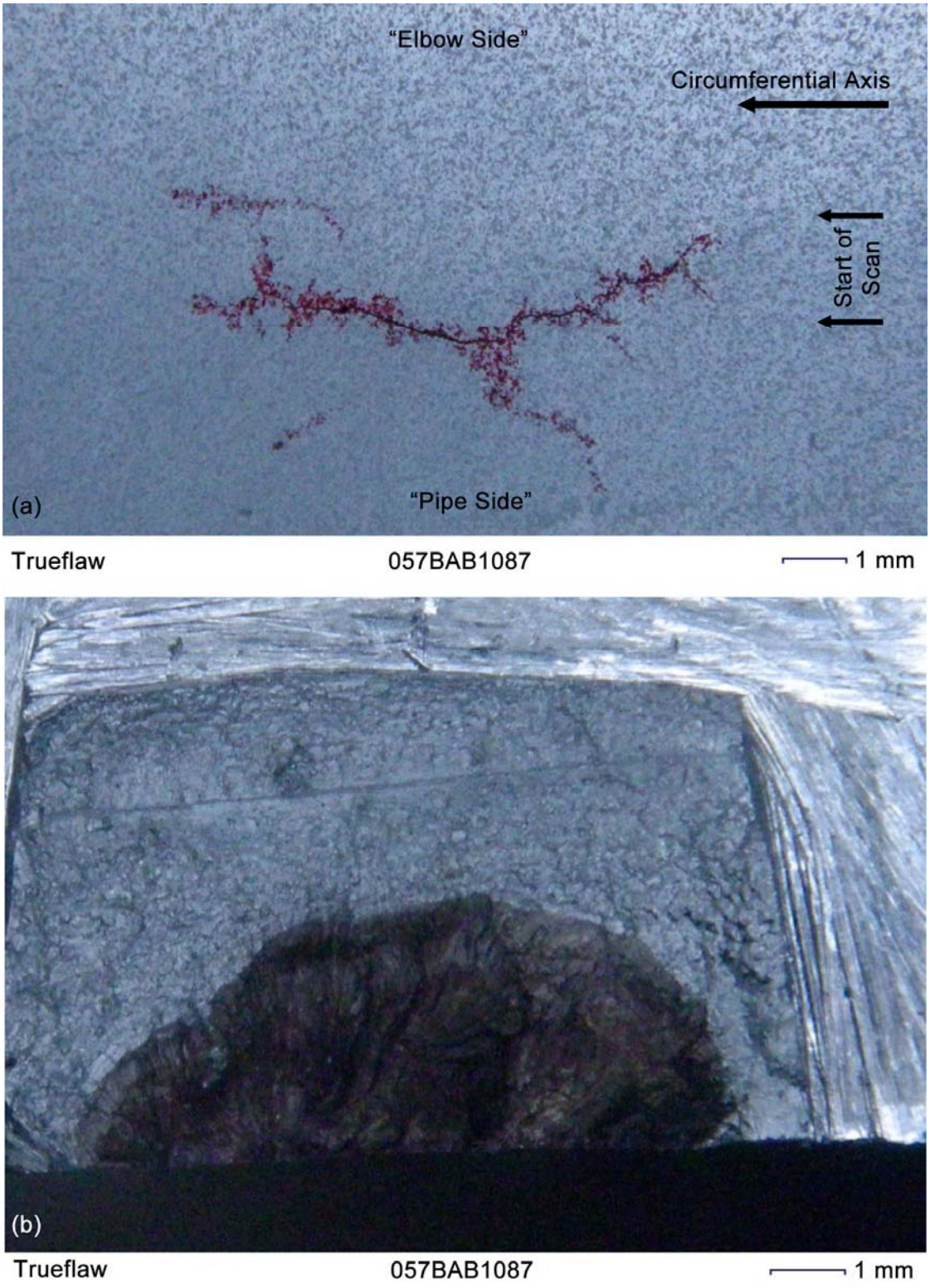

Figure 7.9 Validation Flaw 1087. (a) ID penetrant image; (b) DE fracture surface image.

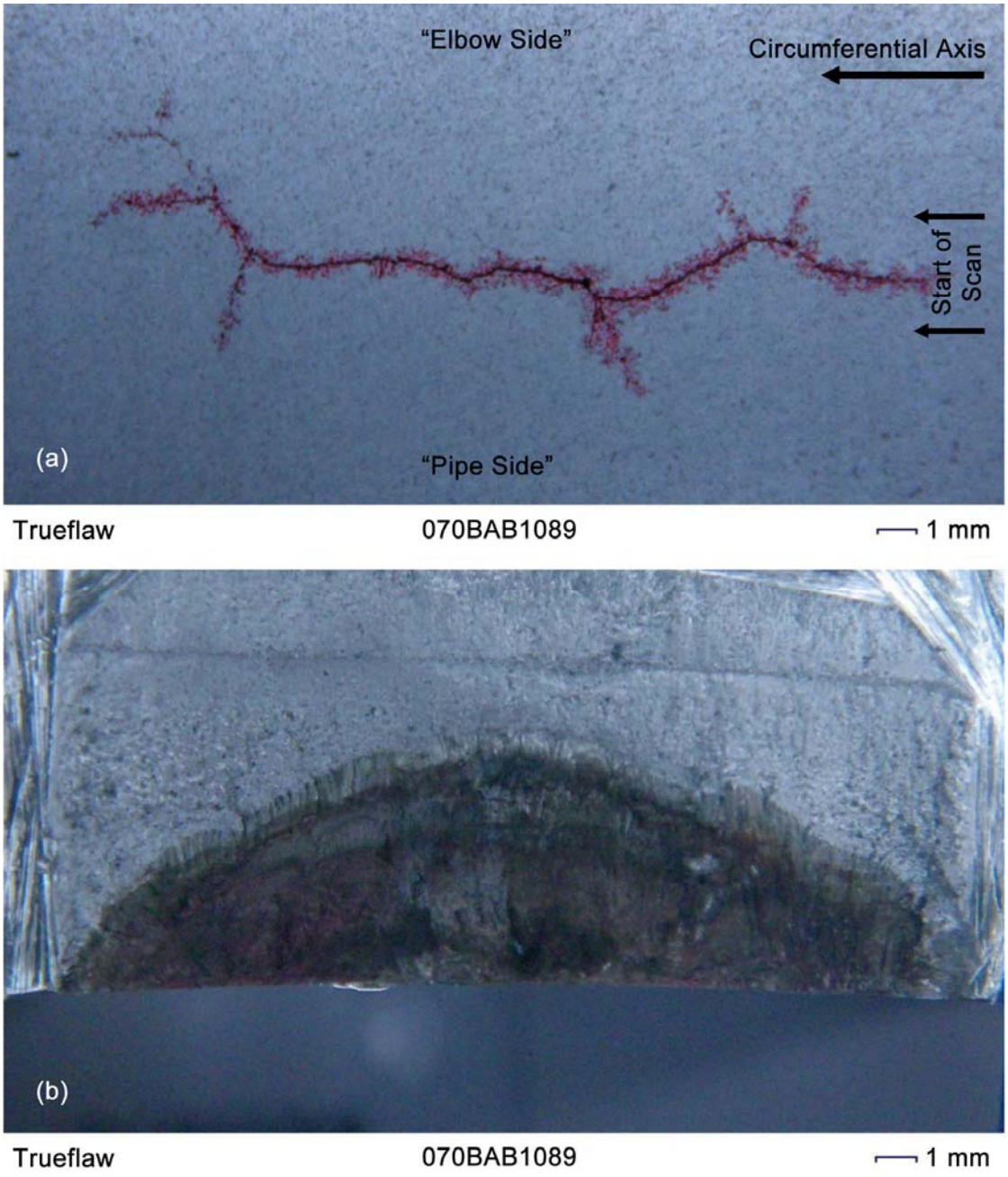

Figure 7.10 Validation Flaw 1089. (a) ID penetrant image; (b) DE fracture surface image below.

7.2.2 In-situ Flaws in Specimen 9C-002

After Trueflaw completed the destructive analysis on the validation cracks grown in the sample material, three thermal fatigue cracks were generated in the 9C-002 specimen as detailed in Figure 7.11. Crack 099BAB1102 (1102) was grown in a circumferential orientation in the centrifugally cast pipe side of 9C-002. Characteristics of this crack attained by Trueflaw using

high-resolution images after liquid penetrant testing indicate that the crack is 19.3 mm (0.76 in.) long. The depth estimate is extrapolated from the validation data and is estimated at 3.4 mm (0.13 in.) yielding an approximate 10.1% through-wall extent when using 33.5 mm (1.32 in.) as the pipe wall dimension. The crack exhibits a skew angle of 86 degrees with an average and median COD of 39.9 µm and 37.8 µm (1.6×10^{-3} and 1.4×10^{-3} in.), respectively. Further, the crack has a complex morphology including three branches, six turns, and one discontinuity above the main crack on the right. Figure 7.12 shows the ID of the pipe section after PT in the crack area.

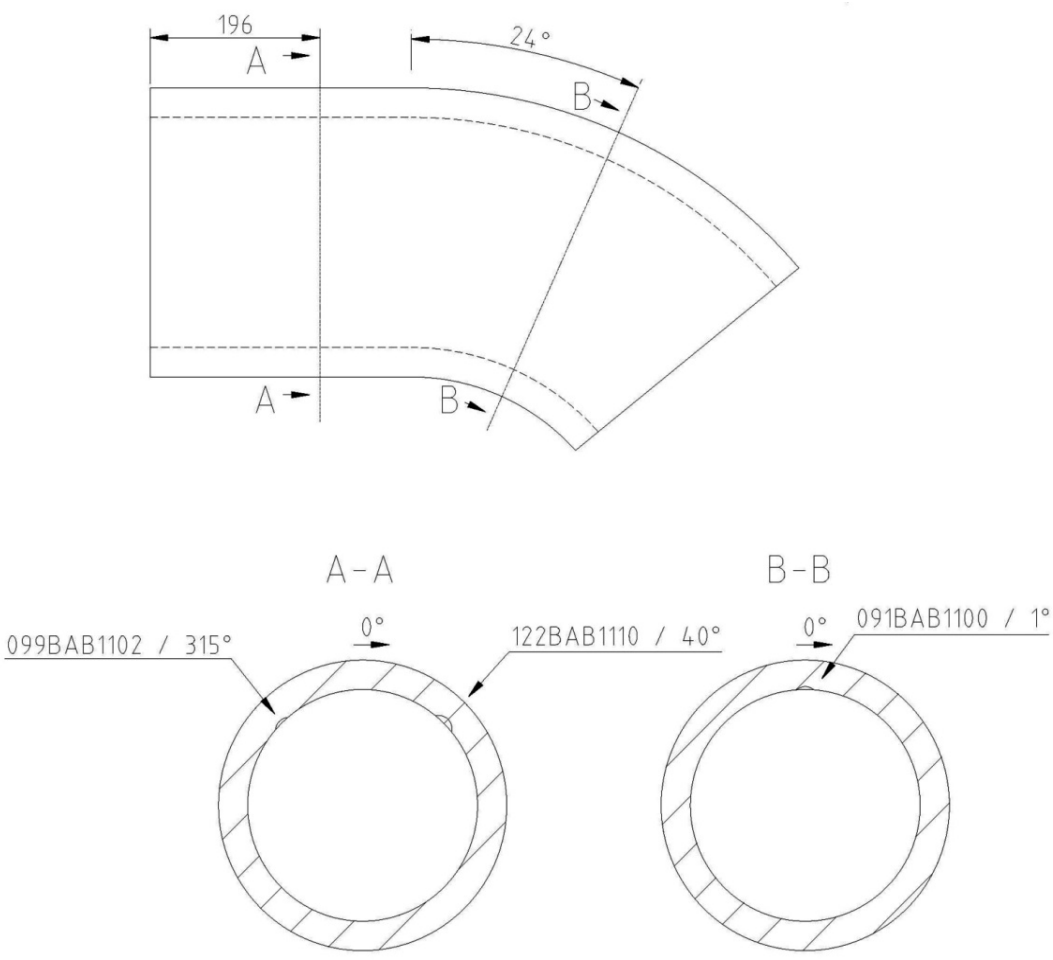

Figure 7.11 9C-002 In-situ Grown Flaw Placement Schematic

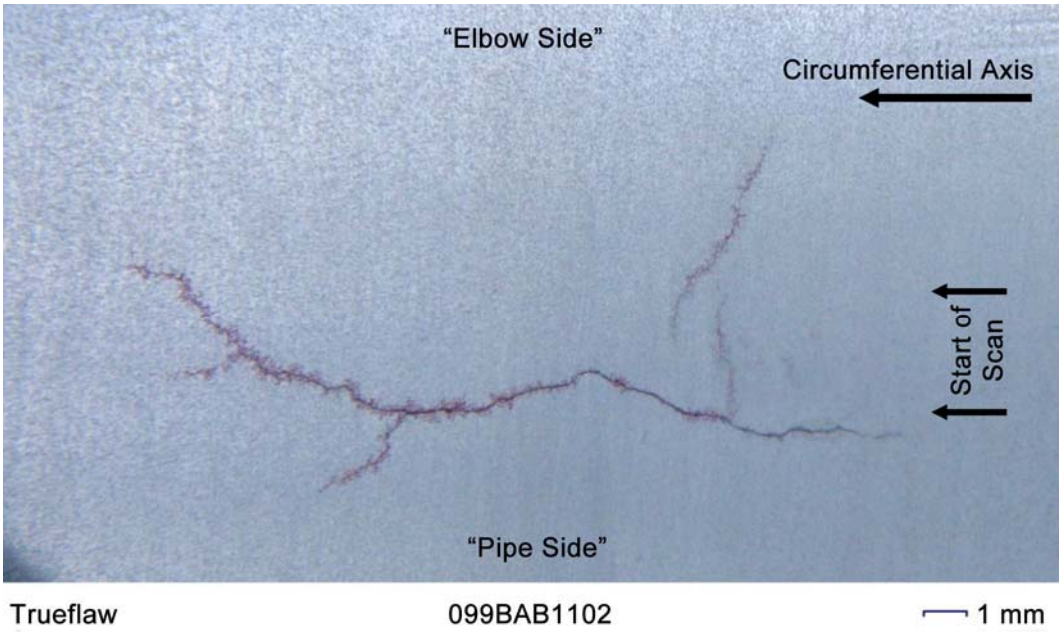

Figure 7.12 Penetrant Image of Crack 1102

Thermal fatigue crack 122BAB1110 (1110) was also grown in a circumferential orientation in the centrifugally cast pipe side of 9C-002. This crack is 25.3 mm (1.0 in.) long and estimated to be 6.0 mm (0.24 in.) deep, yielding an approximate 18.0% through-wall extent when using 33.5 mm (1.32 in.) as the pipe wall dimension. The crack exhibits a skew angle of 85 degrees and an average and median crack COD of 55.0 μm and 48.2 μm (2.2×10^{-3} and 1.9×10^{-3} in.), respectively. The crack has a winding morphology including 4 branches and 15 turns. Figure 7.13 shows the ID of the pipe section after PT in the crack area.

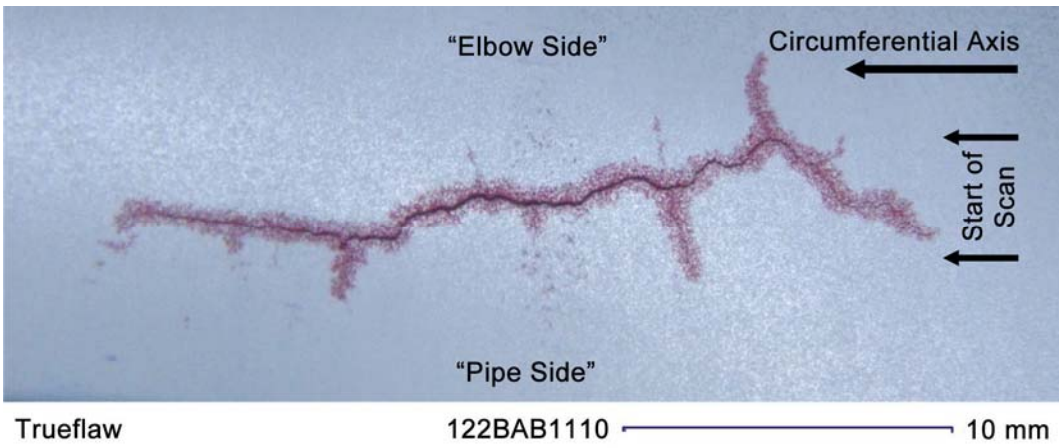

Figure 7.13 Penetrant Image of Crack 1110

The third thermal fatigue crack 091BAB1100 (1100) was grown in a circumferential orientation in the statically cast elbow side of 9C-002. This crack is 18.6 mm (0.73 in.) long and estimated at 3.4 mm (0.13 in.) deep, yielding an approximate 10.1% through-wall extent when using 33.5 mm (1.32 in.) as the wall dimension. This crack exhibits a skew angle of 90 degrees and an average and median crack COD of 39.3 µm and 32.4 µm (1.5×10^{-3} and 1.3×10^{-3} in.), respectively. The crack has 5 branches, 15 turns and no discontinuities. The PT image in the top of Figure 7.14 shows a disconnected region that appears to be part of the flaw but the enlarged photograph of the ID surface in the bottom more clearly shows that this is a region with surface anomalies not related to the flaw.

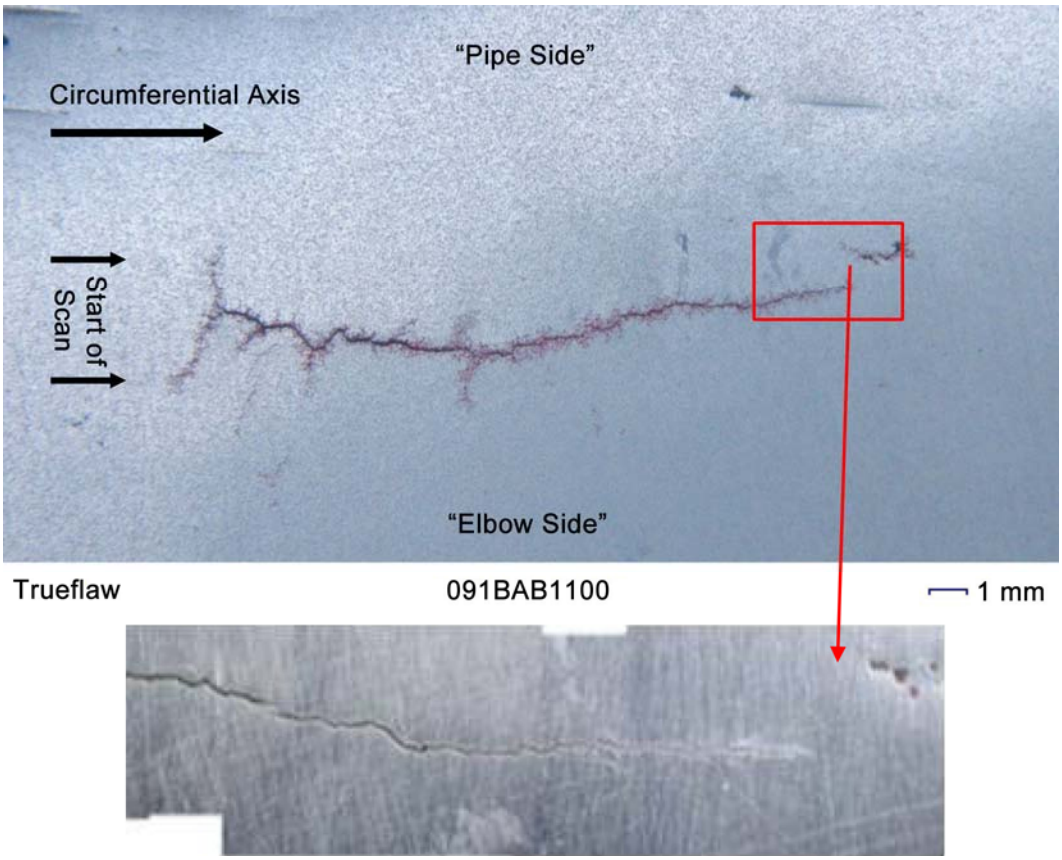

Figure 7.14 Penetrant Image of Crack 1100 in the Top and Enlarged Photograph of the Clean ID Surface in the Bottom

8 DATA ANALYSIS AND RESULTS

8.1 PNNL Phased-Array Data on Implanted Flaws

PA data were acquired and analyzed on the three CASS PZR surge-line specimens at all four inspection frequencies—800 kHz, 1.0 MHz, 1.5 MHz, and 2.0 MHz. The ZETEC DYNARAY system was used to acquire the data, with each probe being driven at its optimum frequency. Line- and raster-scan data were collected and analyzed, and are presented in this report. Multiple line scans were acquired in each flaw region at different axial offsets from the plane of the flaw. Raster scans were also used to provide more detailed characterization of the flawed regions. Both pipe-side and elbow-side data were collected. The elbow sides of the two WNP-3 9C specimens exhibited OD surface undulations, leading to less effective coupling of the probes to the specimens in several circumferential areas. Coupling of the PA probes to the pipe-sides of all three specimens was relatively consistent. Merged PA data were used for detection and length sizing only.

8.1.1 800-kHz Phased-Array Data

Line scans were performed on the PZR surge-line piece from both the CCSS pipe side and from the SCSS elbow side of the weld as the refracted angle was swept from 30° to 70° in 1° increments. Multiple line scans were acquired with different axial offsets from the weld centerline. The separation between lines varied, but typical separations ranged from 10 mm to 15 mm (0.4 in. to 0.6 in.). Data normal to the weld centerline were acquired; however, no skew was implemented during data acquisition. The data were analyzed for flaw detection, length sizing, depth sizing, and signal-to-noise information.

Each of the specified flaw areas were scanned from both sides of the weld; however, the inner radius (intrados) on specimen 7C-059 did not allow data collection on flaw #3 from the SCSS elbow side of the weld, as the surface curvature precluded effective coupling. An example of a merged data file analysis setup for flaw #1 on specimen 9C-002 (pipe-side scan) is provided in Figure 8.1. Merged files are essentially composite images that use signal response information from all angles. Merged data were used for length sizing and SNR analyses. Figure 8.2 depicts images of the same flaw as scanned from the elbow-side of the weld. The entire set of 800-kHz phased-array composite images for all flaws, are provided in Appendix A. These images depict the composite (merged data from all angles) B-scan side view in the upper left portion of the analysis window. The composite C-scan (top-view) images are provided in the upper right portion of the analysis window. The composite D-scan (end-view) images are shown in the lower right portion of the analysis window. And finally, a sectioned polar view is provided in the lower left portion of the analysis window, showing the circumferential aspects of the flaw responses. In some image representations provided, the lower left portion of the analysis window shows a representative A-scan (ultrasonic waveform – time series) at a particular point on the flaw. Additionally, in other representations of the image analysis in the appendices, the lower left portion of the analysis window will include a frequency spectrum view, resulting from the computation of the Fast Fourier Transform using mathematical functions provided by the UltraVision analysis software. The spectral views provide information associated with the frequency responses of the flaws. This can be useful to verify that a particular probe is suitably

matched to inspect the material under test. Ideally, the center frequency in the FFT of a flaw signal approximates the probe center frequency. If the flaw signal shows a downward shift in the frequency response, then the material is likely attenuating the main driving frequency and it might be better to use a probe with a lower center frequency. In the images shown here in Section 8, the corner trap signal response from the ID surface-connected crack is clearly evident in each of the three B-, C-, and D-scan views. This would indicate that flaws are detected with each of the probes over the 0.8 to 2.0 MHz frequency range. Image analysis employed various views of the detected flaws for both length and depth sizing.

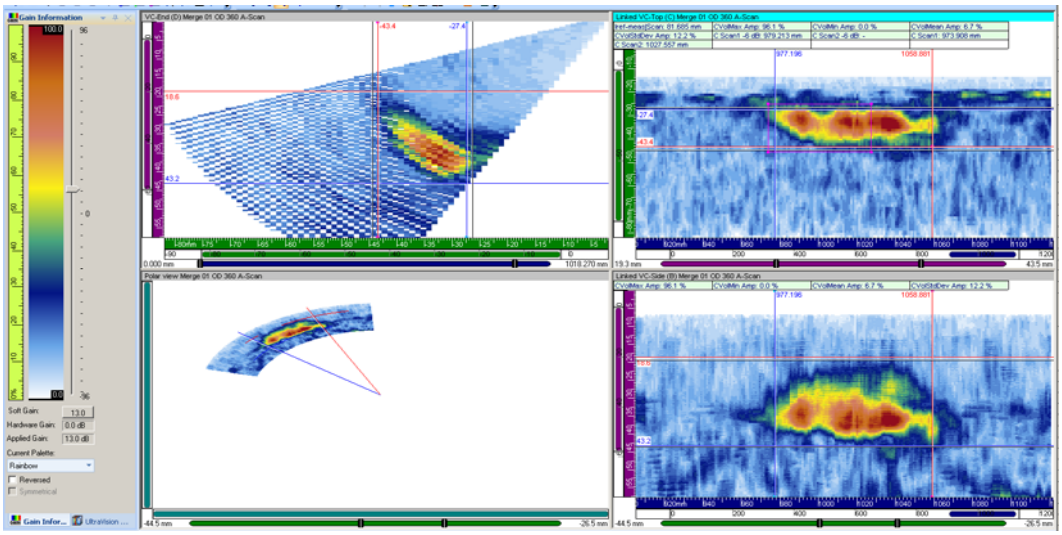

Figure 8.1 800-kHz Data on Pipe Side of 9C-002, Flaw #1, Merged Image for Length Sizing

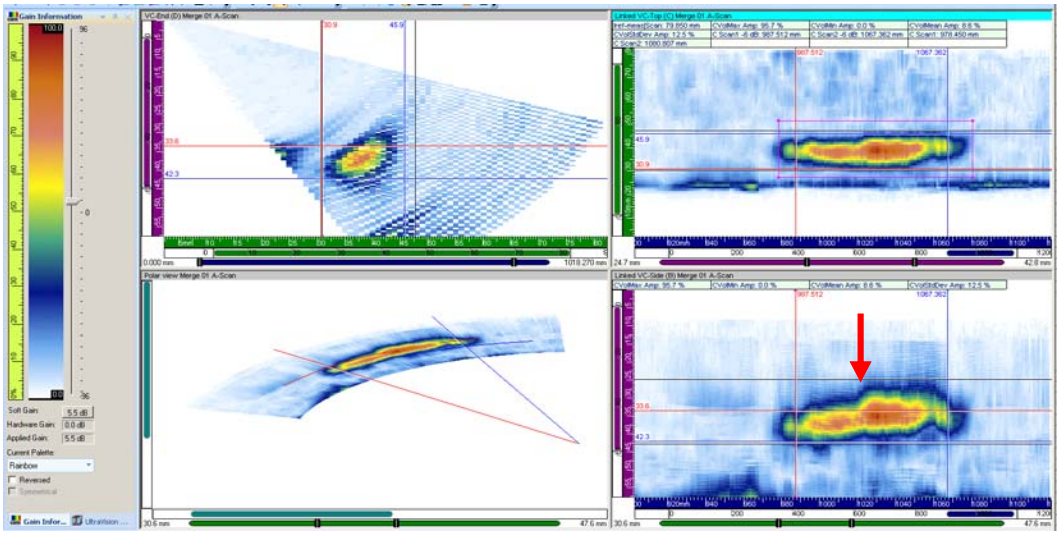

Figure 8.2 800-kHz Data on Elbow Side of 9C-002, Flaw #1, Merged Image for Length Sizing

The depth-contour of the flaw is seen in the D-scan end view and to a lesser degree in the polar view provided in Figure 8.2. This portion of the flaw signal accurately represents the transition of the depth of the flaw from one depth (approximately 15% through-wall) to the deeper portion of the flaw (approximately 25% through-wall). A red arrow indicates this feature in the lower-right portion of the analysis window in Figure 8.2. Additional views were employed for accurate depth sizing of the flaws, and examples of these views are presented in Figure 8.3 and Figure 8.4 for the same flaw in specimen 9C-002.

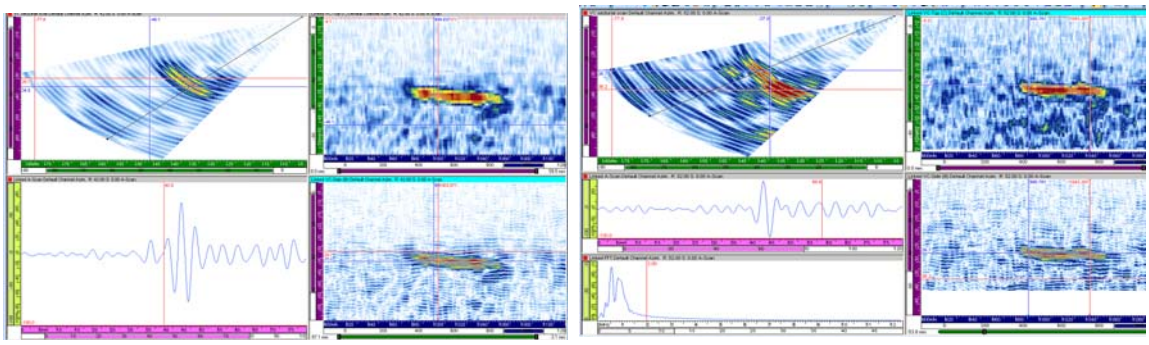

Figure 8.3 800-kHz Data on Pipe Side of 9C-002, Flaw #1A on the Left and #1B on the Right for Depth Sizing

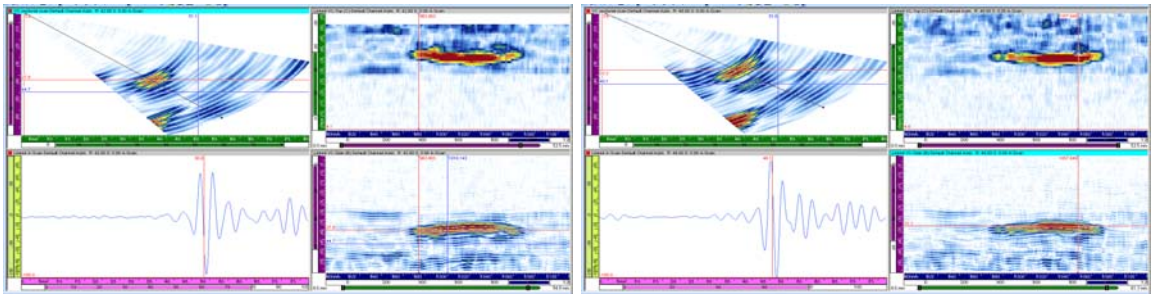

Figure 8.4 800-kHz Data on Elbow Side of 9C-002, Flaw #1A on the Left and #1B on the Right for Depth Sizing

The merged data images for each of the flaws from the CCSS and SCSS sides for 800-kHz data are shown in Appendix A. The data set with an axial offset that best positioned the flaw response in the center of the side view was analyzed and this file is shown in the appendices. As part of the data analysis, the flaw length and depth were sized and a signal-to-noise determination was made. Flaw length was measured at the half amplitude (−6 dB) points on the flaw corner signals. The results for all inspection frequencies and all specimens are listed in Tables 8.1 and 8.2 (see Section 8.1.5) summarizing length and depth measurements relative to true-state data for all flaws. Where tip signals are not detected, the depths of the flaws are based on a specular reflection from the upper portions of the flaws; therefore, the full extent of the crack depth may not be accurately measured. However, the results are still quite good and tend to oversize the crack depth, suggesting that indeed the top of the cracks were detected.

SNRs were calculated for the corner signals of the flaw responses from both the CCSS (pipe) and SCSS (elbow) sides. The SNR was determined from the peak signal response and an average noise value at the same part path. Summary SNR results for all inspection frequencies and specimens are listed in Table 8.3 (see Section 8.1.5). The lowest SNR for the 800-kHz probe across all flaws in these specimens was 10.4 dB (approximately a 3:1 ratio), while the highest SNR for the 800-kHz data was 24.6 dB (approximately a 10:1 ratio), indicating minimal sound field attenuation effects due to the microstructure.

8.1.2 1.0-MHz Phased Array Data

The 1.0-MHz data were also acquired with the DYNARAY system and, like the 800-kHz data discussed previously in Section 8.1.1, scans were performed on the PZR surge-line specimens from both the CCSS pipe side and from the SCSS elbow side of the weld as the refracted angle was swept from 30° to 70° in 1° increments. The same inspection protocols were employed, and multiple line scans were acquired with different axial offsets from the weld centerline. Each of the specified flaw areas were scanned from both sides of the weld. An example of a merged data file analysis setup for flaw #1 on specimen 7C-059 (pipe-side scan) is provided in Figure 8.5. Figure 8.6 depicts images of the same flaw as scanned from the elbow-side of the weld. The entire set of 1.0-MHz phased-array composite images for all flaws is provided in Appendix B. Again, the corner trap signal response from the ID surface-connected crack is clearly evident in each of the three B-, C-, and D-scan views, respectively. Image analysis employed various views of the detected flaws for both length and depth sizing.

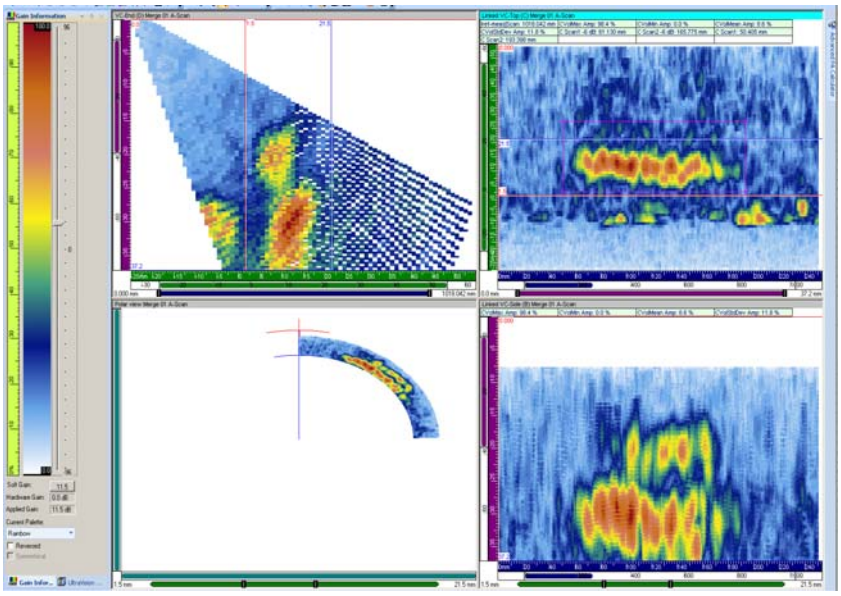

Figure 8.5 1.0-MHz Data on Pipe Side of 7C-059, Flaw #1, Merged Image for Length Sizing

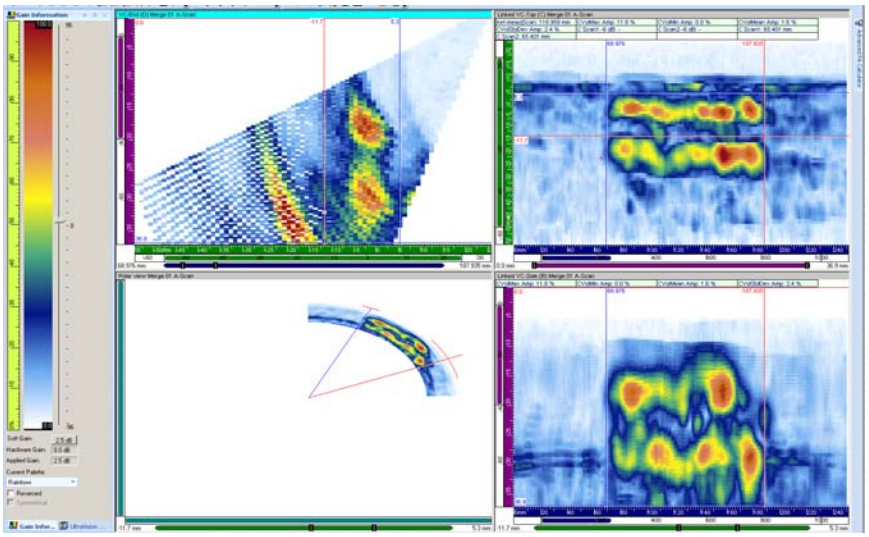

Figure 8.6 1.0-MHz Data on Elbow Side of 7C-059, Flaw #1, Merged Image for Length Sizing

An analysis of the pipe-side and elbow-side parent material from the merged data images visually illustrates the various levels of background clutter, or base material noise in the respective materials. No absolute trend regarding background clutter can be seen between the CCSS and SCSS materials.

The 1.0-MHz data provided slightly enhanced depth resolution by providing a smaller ultrasonic wavelength, while maintaining suitable penetration. In contrast to the 800-kHz probe, the 1.0-MHz data also provided a slight improvement to SNR and thus the clarity of the flaws against the parent material was very good. The lowest SNR for the 1.0-MHz probe across all flaws in these specimens was 9.5 dB (approximately a 3:1 ratio), while the highest SNR for the 1.0-MHz data was 22.6 dB (approximately a 13:1 ratio), indicating minimal sound field attenuation effects due to the microstructure.

8.1.3 1.5-MHz Phased Array Data

The 1.5-MHz data were again acquired with the DYNARAY system and like the 800-kHz and 1.0-MHz data discussed previously in Sections 8.1.1 and 8.1.2, scans were performed on the PZR surge-line specimens from both the CCSS pipe side and from the SCSS elbow side of the weld as the refracted angle was swept from 30° to 70° in 1° increments. The same inspection protocols were employed, and multiple line scans were acquired with different axial offsets from the weld centerline. Each of the specified flaw areas were scanned from both sides of the weld.

An example of a merged data file analysis setup for flaw #2 on specimen 9C-001 (pipe-side scan) is provided in Figure 8.7. Figure 8.8 depicts images of the same flaw as scanned from the elbow-side of the weld. The entire set of 1.5-MHz phased-array composite images for all flaws is provided in Appendix C. Again, the corner trap signal response from the ID surface-connected crack is clearly evident in each of the three B-, C-, and D-scan views, respectively.

Image analysis employed various views of the detected flaws for both length and depth sizing. An analysis of the pipe-side and elbow-side parent material from the merged data images visually begins to illustrate a slight trend in apparent background clutter in the respective materials. At 1.5 MHz, this slight trend can be seen between the background clutter in the CCSS and SCSS parent materials.

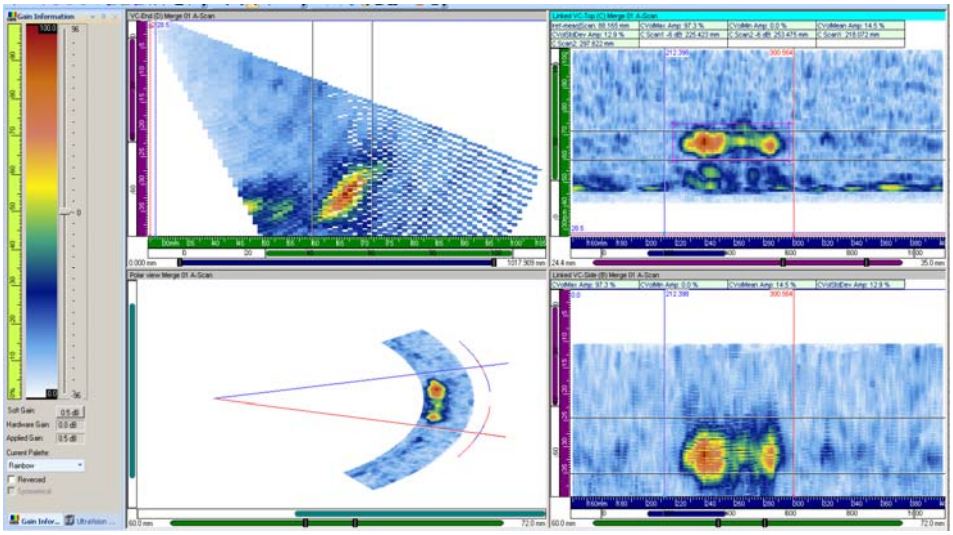

Figure 8.7 1.5 MHz Data on Pipe Side of 9C-001, Flaw #2, Merged Image for Length Sizing

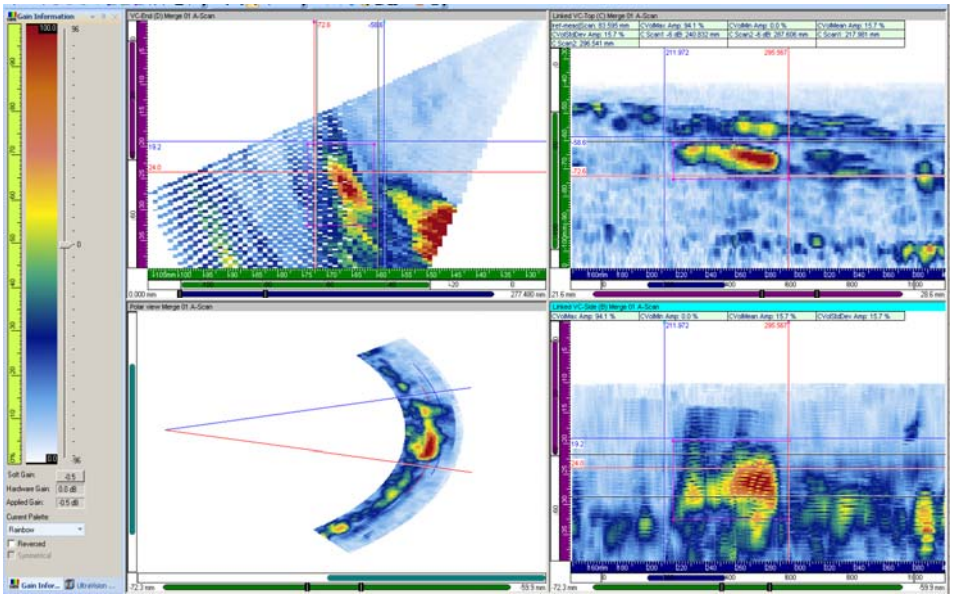

Figure 8.8 1.5-MHz Data on Elbow Side of 9C-001, Flaw #2, Merged Image for Length Sizing

Flaw length, depth, and signal-to-noise were determined from these data. Tables 8.1, 8.2, and 8.3 (see Section 8.1.5) show the summary length results, depth results, and SNR calculations for all data in this study. At 1.5 MHz, the length sizing is relatively similar to that of the other probes; however, depth sizing performance at 1.5 MHz is significantly improved over that of the lower frequency, 800-kHz and 1.0-MHz probes. Results from depth sizing at 1.5 MHz show that this probe out-performed all other probes in acquiring the most accurate depth sizing results over all flaws studied here. This may, in fact, be attributed to the smaller spot size of the zone-focused insonification area for the 1.5-MHz probe over the other arrays. For the specimens used in this study, the 1.5-MHz probe provided an optimal balance between penetration and resolution with regard to inspection of these microstructures, because this probe showed slightly better depth measurement performance over that of the 2.0-MHz probe as well.

The 1.5-MHz data provided enhanced resolution in contrast to the 800-kHz and 1.0-MHz probes, as some tip-diffracted energy was detected at this wavelength. Also, the clarity of the flaws against the parent material was very strong. The lowest SNR for the 1.5-MHz probe across all flaws in these specimens was 11.2 dB (approximately a 4:1 ratio), while the highest SNR for the 1.5-MHz data was 21.7 dB (approximately a 12:1 ratio), indicating minimal sound field attenuation effects due to the microstructure.

In order to more fully characterize the ultrasonic flaw response, raster data files were also acquired at 1.5 MHz from the CCSS side of the weld. Raster scanning acquires data over many axial locations while line scan data are acquired from a single axial position that may not best insonify the flaw. Therefore, raster data present a more complete view of the flaw from which the analyst may select optimum flaw characteristics such as length and depth. An example of raster data is provided in Figure 8.9. Images from the three flaws in each of the 9C-001 and 9C-002 specimens are displayed in Appendix C. The raster flaw sizing results will be compared to the line scan results in Section 8.1.5, Summary of Detection Results. In general, raster data more completely defines a flaw and should best represent the sound field interaction with the implanted crack. All flaws were detected with good SNR. The lowest SNR was 17.4 dB (approximately a 7:1 ratio), while the highest SNR was 22.6 dB (approximately a 13:1 ratio). This is a slight improvement over the 1.5-MHz line scan data.

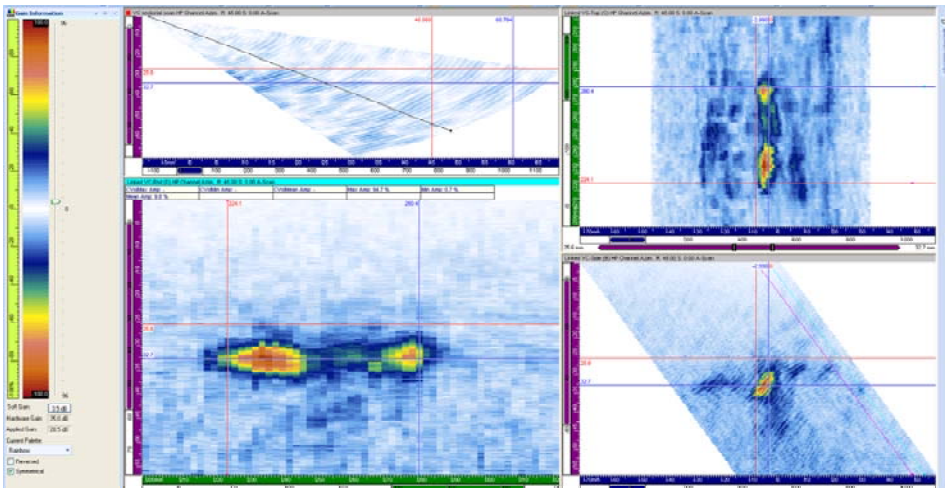

Figure 8.9 Raster Data Acquired at 1.5 MHz from the CCSS Pipe Side of the Weld on Flaw #2 in Specimen 9C-001

8.1.4 2.0-MHz Phased Array Data

The 2.0-MHz data were also acquired with the DYNARAY system and like the other data discussed previously in Sections 8.1.1, 8.1.2, and 8.1.3, scans were performed on the PZR surge-line specimens from both the CCSS pipe side and from the SCSS elbow side of the weld as the refracted angle was swept from 30° to 70° in 1° increments. The same inspection protocols were employed, and multiple line scans were acquired with different axial offsets from the weld centerline. Each of the specified flaw areas were scanned from both sides of the weld.

An example of a merged data file analysis setup for flaw #2 on specimen 9C-002 (pipe-side scan) is provided in Figure 8.10. Figure 8.11 depicts images of the same flaw as scanned from the elbow-side of the weld. The entire set of 2.0-MHz PA composite images for all flaws is provided in Appendix D. Again, the corner trap signal response from the ID surface-connected crack is clearly evident in each of the three B-, C-, and D-scan views, respectively. However, as we increase the inspection frequency, we can see that at 2.0 MHz, signal response continuity and strength begin to decrease, relative to the other probes. This is anticipated, as the effects of the anisotropic and inhomogeneous microstructures begin to have a more adverse effect on sound field propagation with increased inspection frequency. Figure 8.12 depicts the analysis window employed for depth sizing. This image shows a strong specular reflection from the upper part of the flaw as obtained from the elbow side of the weld.

Image analysis employed various views of the detected flaws for both length and depth sizing. A comparative analysis of the pipe-side and elbow-side images in these figures visually shows the differences in background clutter between the CCSS and SCSS parent material and indicates that even at a relatively higher frequency, the PA results show that an effective inspection can be conducted and relatively accurate sizing data can be computed in these coarse-grained materials.

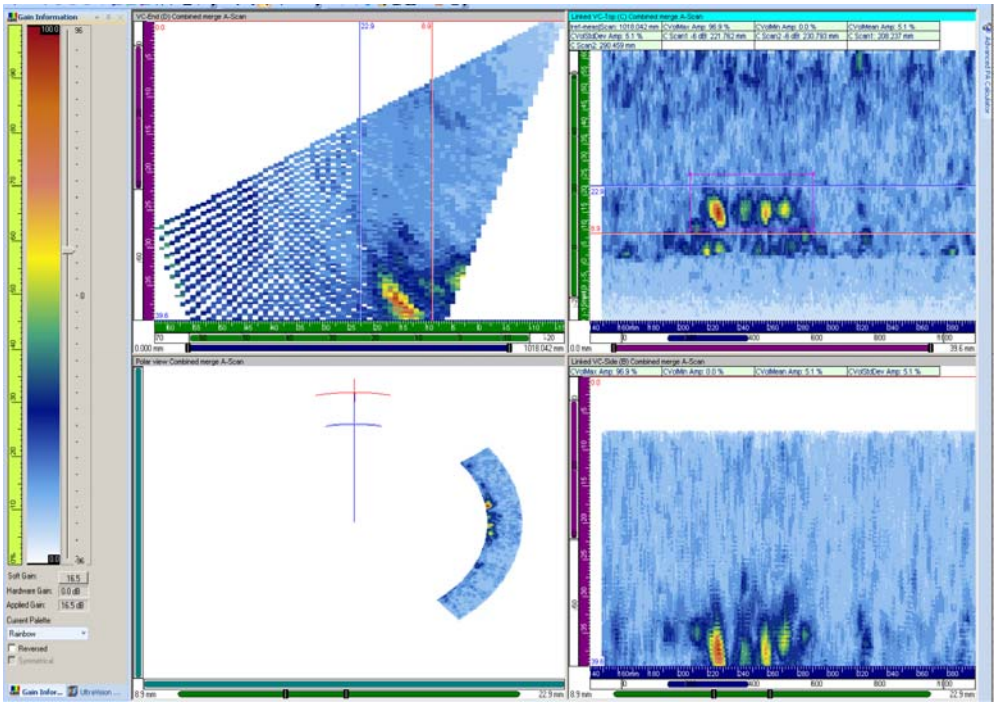

Figure 8.10 2.0-MHz Data on Pipe Side of 9C-002, Flaw #2, Merged Image for Length Sizing

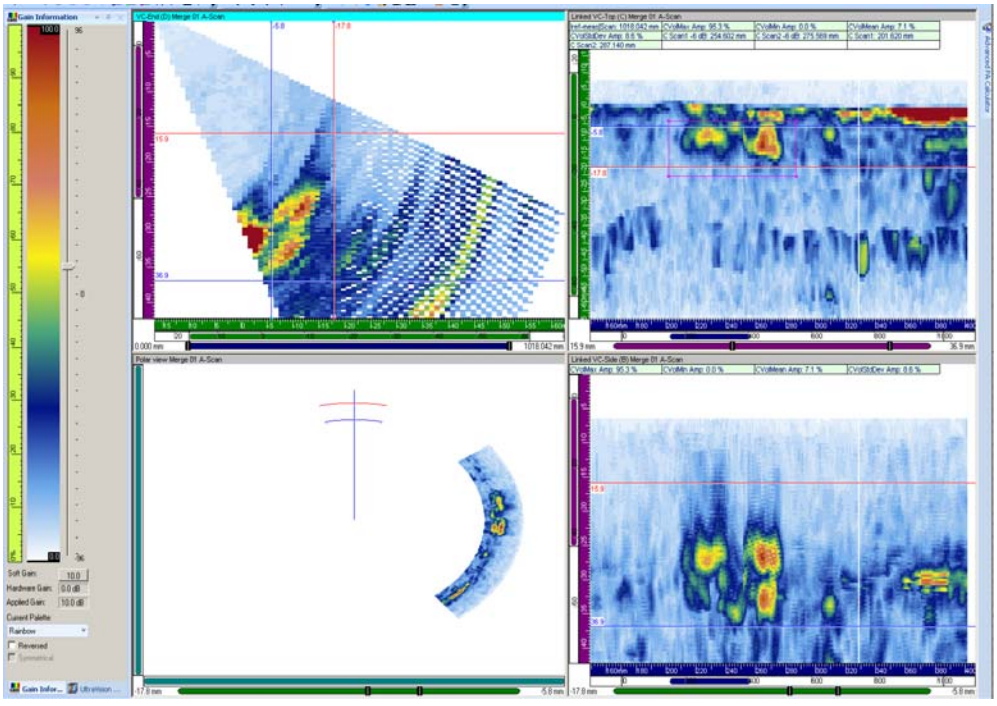

Figure 8.11 2.0-MHz Data on Elbow Side of 9C-002, Flaw #2, Merged Image for Length Sizing

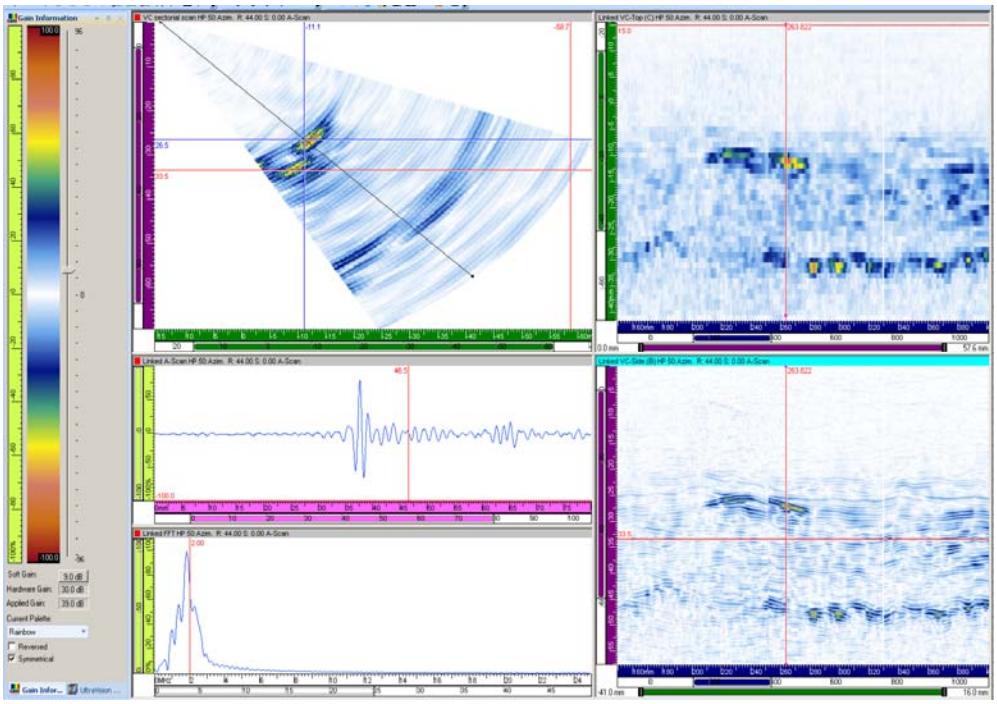

Figure 8.12 2.0-MHz Data on Elbow Side of 9C-002, Flaw #2, for Depth Sizing

Like the 1.5-MHz probe, the 2.0-MHz probe provided enhanced depth resolution in contrast to the 800-kHz and 1.0-MHz probes, as good specular reflections and/or tip-diffracted signals were detected for all flaws at this wavelength. The image clarity of the flaws against the parent material was not as good as the other frequencies, but still well above the necessary visual contrast to consistently detect the flaws in these specimens. Acoustic noise or clutter typically resulting from coherent energy scattered by the coarse-grained microstructures was much lower than anticipated at this frequency. The lowest SNR for the 2.0-MHz probe across all flaws in these specimens was 11.1 dB (approximately a 4:1 ratio), while the highest SNR for the 2.0-MHz probe was 22.4 dB (approximately a 13:1 ratio), indicating minimal sound field attenuation effects due to the microstructure.

8.1.5 Summary of Detection Results

Table 8.1 provides a summary of the length measurements for all flaws across all three specimens used in this study. This table also provides true-state flaw length data and a RMSE value for the 10 flaws as calculated from either the CCSS pipe side or the SCSS elbow side of the welds, as a function of inspection frequency (PA probe). In this same format, Table 8.2 provides a summary of the depth measurements for all flaws evaluated here. This table also provides true-state flaw depth data and RMSE calculations for the 10 flaws as inspected from either the CCSS pipe side or the SCSS elbow side of the welds, as a function of inspection frequency. Finally, Table 8.3 summarizes the SNR in dB, for each flaw as a function of the PA probe (frequency) and scan orientation to the weld (e.g., pipe side, elbow side). Also included in these tables are the 1.5-MHz raster data results.

A key benchmark used for determination of the effectiveness and utility of the inspection approach is to compare the composite length and depth sizing results from the evaluation against the ASME Code Section XI acceptance criteria for successful performance demonstration. ASME length sizing criterion calls for an RMSE less than 19.05 mm (0.75 in.), while the depth sizing is specified as an RMSE less than 3.18 mm (0.125 in.). Length sizing measurements (individual data files) were split among three different analysts, each taking specific portions of data to size. A majority of the data was straightforward and easily sized at the −6 dB and loss of signal levels, but some data required interpretation due primarily to a noncontiguous signal. This interpretation is likely to add human error into the data, either elongating or shortening the length/depth values. The least amount of length sizing error was found in the evaluation of the loss-of-signal method. These values are reported in Table 8.1.

Additionally, these data were corrected for pipe curvature because the data were acquired on the pipe OD and reported flaw lengths are from the ID.

Regarding detection capability, all of the flaws were detected with the exception of flaw #3 in specimen 7C-059 as seen from the SCSS elbow at 800 kHz. Data could not be collected on this flaw because of the large footprint of the probe and the elbow geometry on the intrados. Signal-to-noise values were very good showing that flaw detection was not an issue. The data show that flaws are detectable at frequencies up to 2.0 MHz in these surge-line specimens containing grain sizes as large as 41 mm (1.61 in.) and nominal wall thickness of 33 mm (1.30 in.).

Table 8.1 Length Sizing Summary of Results

		800 kHz		1.0 MHz		1.5 MHz			2.0 MHz	
Specimen/ Flaw	True-State Length, mm	CCSS, mm	SCSS, mm	CCSS, mm	SCSS, mm	CCSS, mm	Raster CCSS, mm	SCSS, mm	CCSS, mm	SCSS, mm
7C-059										
1	101.3	93.7	93.6	93.7	94.4	92.2	-	91.9	89.8	90.3
2	50.6	54.5	19.1	61.0	57.2	48.5	-	60.0	39.4	45.7
3	50.6	57.6	-	55.1	55.6	39.8	-	59.2	36.6	49.9
4	152.6	153.2	128.1	150.8	145.0	149.9	-	145.0	145.1	140.4
9C-001										
1	76.6	71.7	80.1	80.2	74.8	62.4	74.1	71.2	80.4	74.0
2	51.1	48.2	60.2	47.5	59.1	47.5	54.6	60.4	49.0	55.2
3	69.7	57.5	77.0	54.4	72.8	53.9	68.7	54.7	53.4	57.5
9C-002										
1	76.7	82.3	81.2	86.1	86.1	81.9	80.2	87.5	75.6	63.5
2	50.5	52.2	65.2	52.7	58.2	58.5	45.0	58.9	40.4	53.4
3	69.7	73.4	66.8	69.9	69.7	76.3	57.6	64.6	76.1	70.6
RMSE		***5.9***	***15.1***	***7.4***	***6.3***	***9.0***	***5.9***	***9.3***	***9.7***	***8.1***

Table 8.2 Depth Sizing Summary of Results

		800 kHz		1.0 MHz		1.5 MHz			2.0 MHz	
Specimen / Flaw	True-State Depth, mm	CCSS, mm	SCSS, mm	CCSS, mm	SCSS, mm	CCSS, mm	Raster CCSS, mm	SCSS, mm	CCSS, mm	SCSS, mm
7C-059										
1	10.9	12.6	11.5	10.6	11.8	10.9	-	11.5	11.4	10.6
2	9.3	11.6	9.6	11.3	9.1	9.2	-	8.3	10.9	10.5
3	9.3	9.8	--	10.4	10.0	10.6	-	10.0	11.1	10.3
4	15.6	16.3	14.5	15.0	14.7	14.5	-	14.9	15.0	15.3
9C-001										
1a	3.4	5.0	4.0	3.4	3.2	4.2	3.5	2.5	3.5	5.2
1b	6.4	7.5	7.9	5.8	6.2	5.7	5.2	7.7	6.1	6.9
2	8.9	8.6	8.0	7.7	7.1	8.1	7.1	9.2	11.5	11.2
3	8.3	11.1	7.2	9.7	9.0	8.8	7.8	7.7	10.3	9.0
9C-002										
1a	4.8	4.3	6.9	4.8	NA	4.3	4.2	4.5	4.4	5.8
1b	7.5	9.5	7.9	9.3	6.4	7.4	6.5	4.6	7.9	9.0
2	6.3	6.4	8.1	7.9	8.2	6.6	6.7	4.4	6.0	7.0
3	4.8	6.3	NA	6.5	3.6	5.3	8.3	5.1	6.0	6.9
RMSE		***1.5***	***1.8***	***1.2***	***1.7***	***0.7***	***1.5***	***1.2***	***1.3***	***1.3***

Table 8.3 Signal-to-Noise Ratio Summary of Results

	800 kHz		1.0 MHz		1.5 MHz			2.0 MHz	
Specimen/ Flaw	CCSS, dB	SCSS, dB	CCSS, dB	SCSS, dB	CCSS, dB	Raster CCSS, dB	SCSS, dB	CCSS, dB	SCSS, dB
7C-059									
1	17.0	15.7	16.6	18.3	14.7	-	18.7	18.2	22.4
2	13.7	10.4	14.2	11.4	14.3	-	11.6	16.9	11.1
3	14.5	--	16.2	9.5	17.7	-	17.5	19.9	18.1
4	15.1	17.4	16.3	15.8	17.3	-	16.6	15.7	19.0
9C-001									
1	20.0	15.2	20.7	14.2	21.1	22.6	16.3	19.4	18.1
2	19.6	15.5	18.9	14.0	17.8	21.3	15.1	20.7	15.6
3	17.4	13.7	17.2	18.1	16.4	17.4	18.9	15.5	16.7
9C-002									
1	16.6	24.6	16.8	22.6	17.6	18.4	11.2	18.3	16.5
2	13.9	20.0	14.9	21.0	15.9	19.7	21.7	17.5	19.9
3	17.2	16.7	18.0	19.7	18.1	18.9	17.3	17.1	17.9

Length sizing error was larger on specimen 7C-059 from the SCSS elbow side than on the two 9C specimens. This is in part due to surface irregularities relative to the probe footprints, differences in surface finish (both of which impact coupling efficiency), and the unanticipated detection of artifacts such as fabrication flaws. The length sizing performance is improved in the

raster data as compared to the line scan data for the CCSS pipe side data at 1.5 MHz. Raster scanning more fully captures the flaw response signals because it acquires data over many axial locations while line scan data are acquired from a single axial position that may not best insonify the flaw. It is likely that 2.0-MHz raster data, if acquired, would show an improvement in length sizing over the line scan data. A review of Table 8.2 shows that flaw depth sizing fell completely within the Code-allowable limit, even at 2.0-MHz.

The reported SNR values provided in Table 8.3 were calculated from the peak signal response and the mean noise response at the same part path in dB. These calculated values are all very good, indicating minimal attenuation effects on sound field propagation over the frequency range from 800 kHz to 2.0 MHz. Flaw detection was not in question for the TFCs implanted in these specimens as shown by the high SNRs. For the materials used in this study, adequate SNRs were achieved even at 2.0 MHz and raster data SNRs are similar to the line scan data SNRs. If CASS piping with greater attenuative properties is encountered in the field, the use of lower frequencies (800 kHz to 1.0 MHz) would be more appropriate for inspection. The elbow configuration limited elbow-side access to flaw #3 in specimen 7C-059 but all other flaws were detected from both the pipe and elbow side of the weld. The lowest SNR value for all signal responses in this study was computed to be 9.5 dB while the maximum SNR value was 24.6 dB.

8.1.6 Effects of Beam Redirection on Crack Localization and Positioning

Typically in CASS (or stainless steel welded) components, the issue of beam redirection caused by the microstructure and the potential for error in the positional registration of data (flaw responses) relative to the true position of the probe, can pose a problem. To address this issue, an analysis of the measured flaw end point positions (circumferential or lateral localization data) was conducted, as well as a study of the axial positioning or sound beam redirection.

8.1.6.1 Lateral Beam Redirection

Length sizing results are summarized in Table 8.1 with the RMSE calculated for each specimen by probe frequency and by specimen side. For the lateral beam redirection assessment, CCSS (pipe) and SCSS (elbow) data were analyzed to provide the optimal view of the flaw being evaluated, which may or may not occur at the exact same metal path length from flaw to flaw. Data for this section were analyzed with similar metal paths in order to reduce the effects of varying metal paths. Thus, exact endpoint data values may be slightly different from those obtained for the length sizing section of this report. The lateral beam redirection measurements were based on a −6 dB drop method with some analyst interpretation involved to account for signal dropout or other anomalies in the signals. The measured localization data were compared to the FlawTech reported true-state flaw positional data on the specimens, and this information was plotted and analyzed to determine the extent of lateral beam redirection. This beam redirection is assumed to be a result of the microstructural variation in the CASS base material, the weld material, or a combination of both. The lateral beam redirection occurs in the circumferential direction of the pipe. Figures 8.13 through 8.15 map the flaw end point positional data along with true state for each of the specimens. The pipe- and elbow-side data are separated as well as probe frequency. This mapping allows one to look for general trends in over or under length sizing of the flaws caused by lateral beam redirection of the data, which can be observed in cast material. Refer to Table 8.4 for the specific endpoint values illustrated in Figures 8.13–8.15.

Table 8.4 Endpoint Values for Circumferential Flaw Localization

Pipe Side										
	True-State		800 kHz		1.0 MHz		1.5 MHz		2.0 MHz	
Specimen/ Flaw	Begin (mm)	End (mm)	Begin (mm)	End (mm)	Begin (mm)	End (mm)	Begin (mm)	End (mm)	Begin (mm)	End (mm)
7C-059										
1	76.4	178.0	54.9	159.6	60.0	176.1	66.0	182.5	67.2	179.5
2	313.8	364.4	302.2	365.2	312.3	381.5	317.8	352.5	314.1	350.1
3	568.2	618.8	558.0	630.0	581.8	631.1	568.0	617.7	573.9	619.7
4	771.6	924.1	757.0	947.5	758.0	944.4	758.5	945.8	755.6	924.1
9C-001										
1	–38.3	38.3	–51.8	37.5	–37.1	53.2	–52.9	38.6	–42.7	45.9
2	228.8	279.9	227.5	283.9	227.7	286.6	225.4	289.5	227.2	265.0
3	728.2	797.9	709.6	786.7	724.3	786.6	711.1	799.5	707.3	800.5
9C-002										
1	–38.4	38.4	–38.2	30.4	–43.2	57.1	–37.1	24.9	–34.6	50.8
2	229.1	279.6	216.9	270.1	219.2	276.6	226.2	277.5	220.8	274.9
3	728.2	797.9	734.4	793.2	734.5	793.5	739.2	797.6	743.8	797.6
Elbow Side										
	True-State		800 kHz		1.0 MHz		1.5 MHz		2.0 MHz	
Specimen/ Flaw	Begin (mm)	End (mm)	Begin (mm)	End (mm)	Begin (mm)	End (mm)	Begin (mm)	End (mm)	Begin (mm)	End (mm)
7C-059										
1	76.4	178.0	66.0	180.9	73.0	185.9	82.0	184.4	87.8	184.4
2	313.8	364.4	308.0	327.1	313.0	361.3	317.8	352.5	306.8	368.2
3	568.2	618.8	——	——	584.3	623.6	559.9	633.9	565.8	632.0
4	771.6	924.1	778.5	938.7	755.4	936.6	756.3	937.6	777.8	921.1
9C-001										
1	–38.3	38.3	–23.8	47.8	–41.2	40.1	–41.6	47.6	–43.6	39.7
2	228.8	279.9	243.4	294.1	221.3	289.1	238.3	289.2	228.3	286.2
3	728.2	797.9	711.4	790.9	738.7	802.8	718.1	798.5	719.8	791.9
9C-002										
1	–38.4	38.4	–29.5	52.4	–26.2	63.3	–34.1	44.9	–25.8	64.7
2	229.1	279.6	217.6	278.6	215.7	279.6	221.4	289.8	209.7	276.6
3	728.2	797.9	746.0	816.2	750.2	813.5	737.2	792.5	744.9	816.8

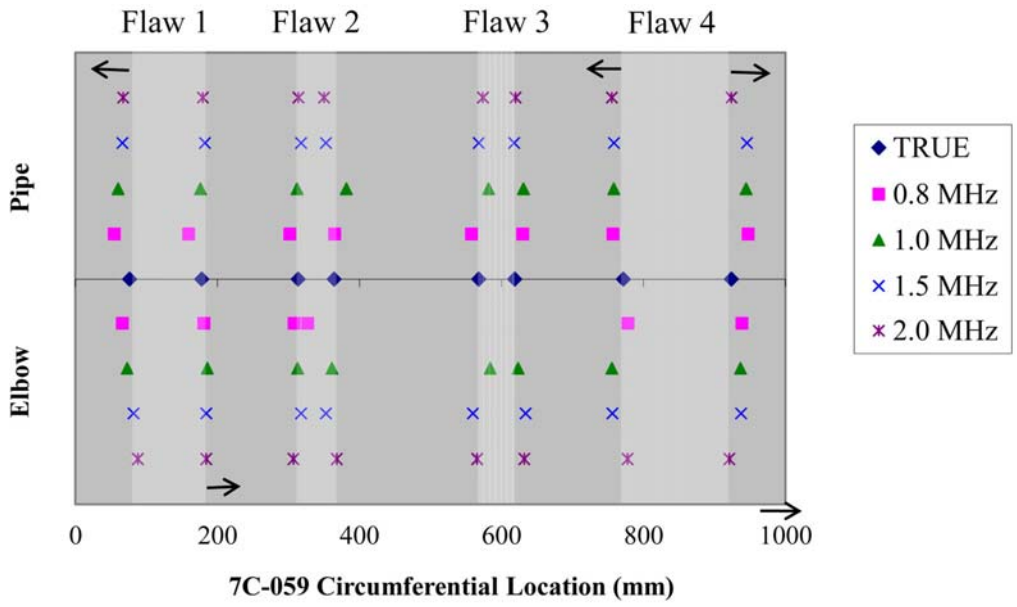

Figure 8.13 Map of True-State and Measured, Circumferential Flaw Localization Data for CASS PZR Surge-Line Specimen 7C-059. The arrows indicate a noticeable shift on average in flaw end points.

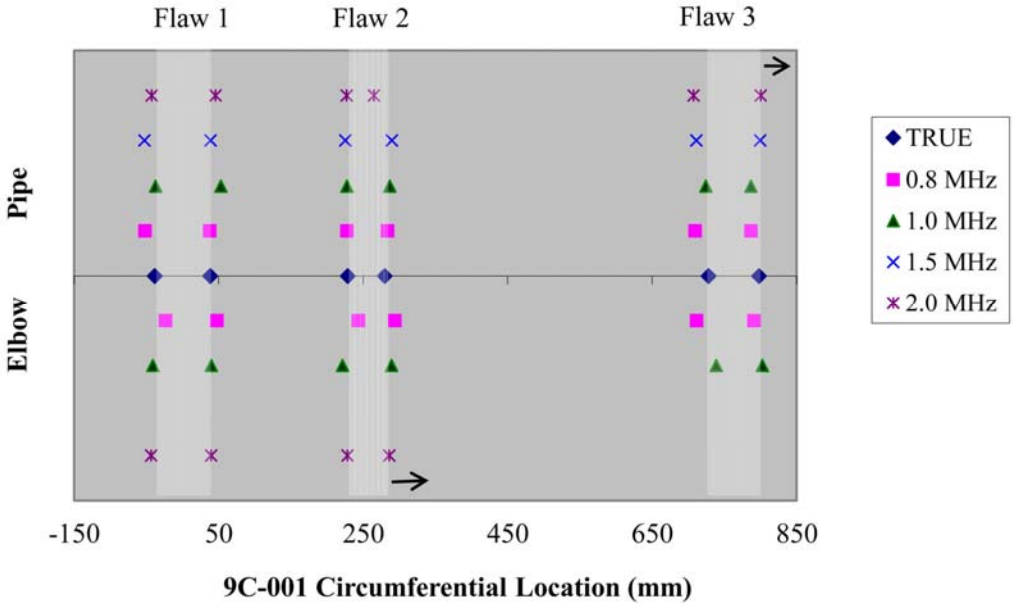

Figure 8.14 Map of True-State and Measured, Circumferential Flaw Localization Data for CASS PZR Surge-Line Specimen 9C-001. The arrows indicate a noticeable shift on average in flaw end points.

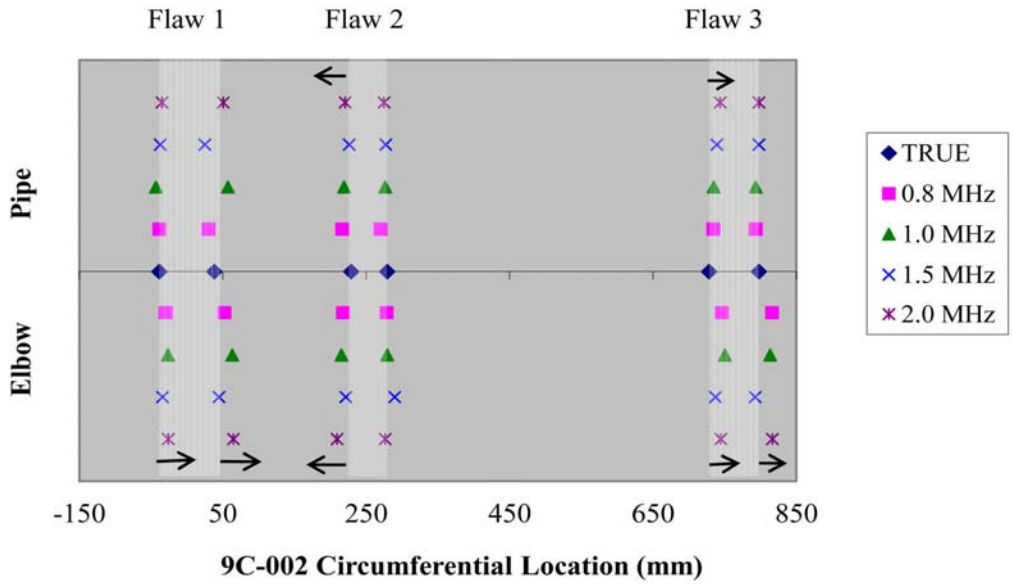

Figure 8.15 Map of True-State and Measured, Circumferential Flaw Localization Data for CASS PZR Surge-Line Specimen 9C-002. The arrows indicate a noticeable shift on average in flaw end points.

For specimen 7C-059, the 0° reference point lies at the far left of the plot at 0 mm. For the 9C specimens, a flaw was centered at the 0° reference point so the horizontal axis was shifted to start at −150 mm. The horizontal line (X-axis) on the plots represents linear distance (corresponding to the circumferential position of the flaws) around the circumference of the pipe specimens in millimeters. Points that are plotted above the X-axis are measured flaw end positions from each of the four PA probes acquired from data taken from the CCSS pipe side of the specimens. Points that are plotted below the X-axis are measured flaw end positions from each of the four PA probes as obtained from the SCSS elbow side of the specimens. Points that lay directly on the X-axis horizontal line in the middle of the graph represent reported true-state end positions in the circumferential direction in the specimen. The true-state flaw length regions are additionally marked as lighter shaded regions in the plots for easier data comparisons. Flaws are plotted in ascending order from left to right on each of the plots.

A trend toward over sizing of the flaw lengths can be expected as the probe spot size will inherently be added to the ultrasonic measurement values. Section 5 gave the lateral spot sizes for each of the probes and these values were nominally in the 5–7 mm range. This accounts for small changes in the end point positions, in the order of 2–4 mm to the outside. End point shifts exceeding these values, either inward or outward, will be considered as possible lateral beam redirection. Therefore, lateral beam redirection was considered in this report as end point shifts in the same direction over all four frequencies, with an average result greater than 5 mm. These conditions are marked with arrows in Figures 8.13–8.15 and show the direction of shift as well. These measurements were made from line scan data with nearly the same part path for a particular specimen. For example, the left end point in flaw #1 pipe side in specimen 7C-059 is redirected left on average by 14 mm. The end points for flaw #4 in specimen 7C-059 from the pipe side are redirected left by 14 mm and right by 16 mm on average over the four inspection

frequencies. Elbow-side data also showed a redirection in flaws #1 and #4 of the right end points to the right by 6 and 11 mm, respectively. Specimen 9C-001 shows some redirection in flaw #2 from the elbow side (by 10 mm) and flaw #3 from the pipe sides (by 15 mm). Specimen 9C-002 shows some redirection in flaw #1 from the elbow side by 10 and 18 mm in the left and right end points; in flaw #2 from the pipe side by 8 mm in the left end point, in flaw #2 from the elbow side by 13 mm in the left end point; in flaw #3 pipe side by 10 mm in the left end point; and by flaw #3 elbow side by 16 mm in the left and right end points. These noted areas of potential lateral beam redirection account for 35% of the total observations.

In summary, potential lateral beam redirection was considered as measured flaw end points over the four inspection frequencies that varied in the same direction from true state by more than 5 mm on average. These averaged redirections of the flaw endpoint responses can be attributed to beam redirection caused by the coarse grained cast base metal and austenitic weld material. The redirection was observed in as much as 35% of the end point data and is as great as 18 mm in this material. Note that this is a preliminary screening test. Because the specimens have not been destructively analyzed, the microstructure at the flaw and the exact flaw true state are unknown.

8.1.6.2 Axial Beam Redirection

The purpose of this study was to examine the effects of the columnar CASS and dendritic weld microstructures on the ultrasonic wave propagation as observed in data acquired from the pipe sides of 9C-001 and 9C-002 PZR surge-line specimens. Previous studies (Anderson et al. 2007) conducted on cast stainless steels have revealed that the columnar, equiaxed, or mixed microstructures found in this material have significant effects on the propagation of ultrasonic waves. It has been reported (Kupperman et al. 1987) for a columnar microstructure, which can be considered as anisotropic, that both the speed and direction of sound waves are affected. A normal beam inspection on a columnar microstructure specimen yielded a consistently slower longitudinal velocity than that of equiaxed specimen (Kupperman et al. 1987). Moreover, a directed 45° longitudinal wave can be redirected to a wave normal direction of 49° longitudinal, based on the variations of velocity in cast stainless steel. The resulting direction of ultrasonic energy is not necessarily along the calculated wave normal, but rather it follows the path of least resistance. The wave propagation angle is a result of the material velocity properties and the beam interactions at various grain boundaries.

This study focused on an experimental approach using phased-array ultrasonics. The effect of beam redirection along the pipe axis in CASS materials was studied at the angles of 30, 45, and 60 degrees using a transmit-receive-longitudinal (TRL) configuration containing two, 1.5-MHz, 10×3 element arrays. End-of-pipe (corner) responses, as well as flaw base corner responses, were analyzed from the centrifugally cast stainless steel pipe sides of both 9C-001 and 9C-002 specimens. A wrought stainless steel (WSS) pipe segment of approximately the same thickness was used as a calibration specimen. These CCSS specimens have a known coarse-grained columnar microstructure (Figure 8.16) that likely affects the ultrasonic wave propagation. Meanwhile, the wrought pipe section with its homogeneous composition will support wave propagation at a constant wave speed and with minimal redirection from the primary insonification angle.

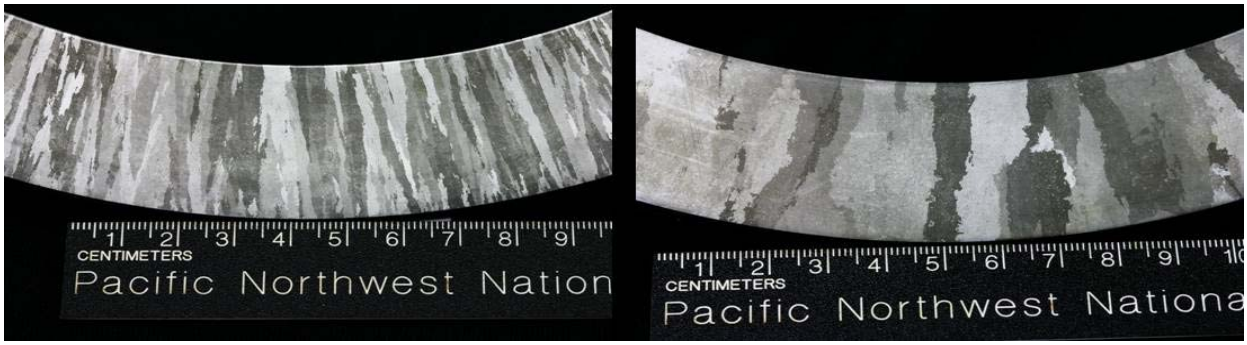

Figure 8.16 Columnar Grain Structure of Cast Specimens Examined. From left to right are the microstructures of specimens 9C-001 and 9C-002, respectively.

8.1.6.3 Setup and Procedure

The experimental procedure used ZETEC's UltraVision 3.1R9 software package to control the DYNARAY phased-array ultrasonic system. Acoustic velocities were held constant in the software and were set at 2230 m/sec for the Rexolite wedge and at 5770 m/sec for the specimens. Typically, in flaw detection and sizing studies at PNNL, a set of focal laws are constructed for a range of angles such as 30 to 70 degrees, applied at one degree increments for a particular focusing style and a single wedge delay is applied to all angles. The wedge delay is an adjustable parameter that allows the user to account for the overall system delay and can include delays caused by cables, the wedge, etc. The delay is set based on the ultrasonic response from a known reflector such that the flaw response is placed at the correct depth and axial position. This is accomplished by measuring the response in the volume-corrected sector view (basically a side-view) image of the beam with an example shown in Figure 8.17. This axial redirection study examined responses at three angles, 30, 45, and 60 degrees. To be more precise in the measurements, PNNL took advantage of the software's ability to allow a user to establish multiple channels of focal laws to allow for customization of the wedge delay for each channel. Thus, with three target angles, three separate channels each with an optimized half-path focus targeted at the fiducial response location was constructed for data acquisition. Each channel acquired data at ±5° from the primary angle in 1° increments. Specifically, the combined three channels provided data ranges of 25 to 35, 40 to 50, and 55 to 65 degrees.

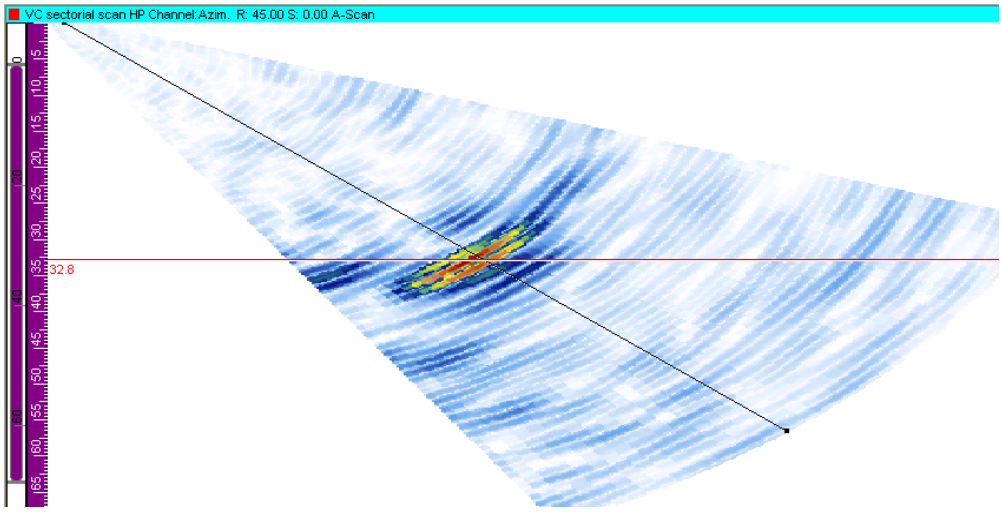

Figure 8.17 Side View or Volume-Corrected Sectorial View Showing Visual Depth Measurement at 45 Degrees

Calibration of each focal law channel was conducted at the '0' circumferential reference mark on the end of the WSS pipe. True-state thickness measurements were first collected using a dial caliper to accurately determine the wall thickness of the specimen at the end of pipe area. Five independent measurements yielded an average thickness to be 32.4 mm (1.28 in.). Based on this true-state thickness, calculations were then made to determine the proper A-scan length (metal path) from the approximate exit point on the wedge to the corner for each angle of interest. Additional calculations were made to determine the axial distance from the wedge exit point to the corner of the pipe shown as 'X' in Figure 8.18. From these measurements and calculations the three true-state sides of the right triangle were established for each center beam angle.

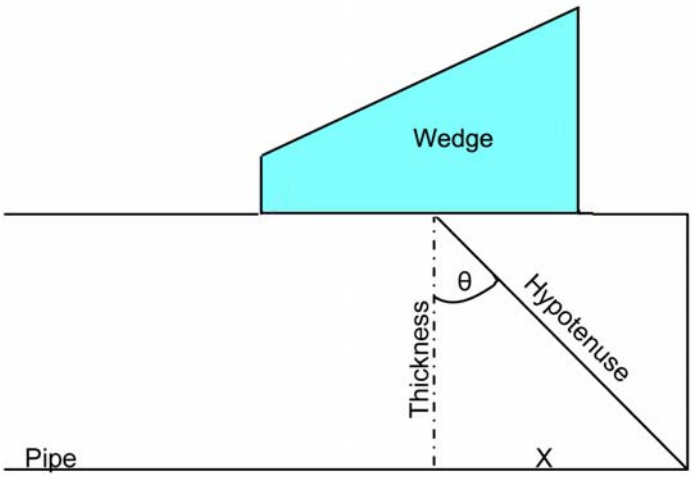

Figure 8.18 Schematic of Trigonometric Calculations

The ultrasonic system was then calibrated on the WSS pipe by ultrasonically measuring the pipe thickness and adjusting the wedge delay until the ultrasonic measurement matched the true-state value. A-scan length and axial distance were also measured. A-scan length was measured to the leading edge of the response in the actual A-scan signal as opposed to the peak response in the side-view image. During typical examinations of most specimens, PNNL normally sets a single wedge delay using the ultrasonically measured depth from a known fiducial point, such as a corner response, at 45 degrees. The peak response of the phased-array image displayed in the volume-corrected sector, or side, view is matched to the physically measured thickness by adjusting the wedge delay. This one wedge delay is then applied to all laws contained in the set channel, typically 30 to 70 degrees with 1-degree increments. However, the axial beam redirection study required a greater degree of optimization; thus, the measurements were refined in two ways. First, the wedge delay was optimized for each of the three primary angles (30, 45, and 60 degrees). Second, the corner response depth was measured at the leading edge in the A-scan signal. As mentioned before, each angle of interest was set up in its own channel, which allowed for custom optimization of focusing location and wedge delay. The proper calibration for angles 30°, 45°, and 60° required half path focusing at 37.41 mm (1.47 in.), 45.82 mm (1.80 in.), and 64.80 mm (2.55 in.) with accompanying wedge delays of 1.25 μs, 1.30 μs, and 1.40 μs, respectively, based on the WSS pipe. With these set values, additional end-of-pipe areas at ±100 mm (3.94 in.) circumferentially from the ‘0’ reference mark were evaluated to ensure the wedge delays held true in more than one location on the calibration specimen. Once confirmed, these wedge delays were fixed for the inspection of CASS specimens 9C-001 and 9C-002.

Data were collected in the form of raster scans on the machined ends, then on the weld centerline, in both specimens, similar to the procedures described in Section 8. The only difference was that only a few lines of data were acquired in the circumferential direction, whereas the full raster scan acquired data over the entire length of the flaw and beyond. Before collecting data, the axial encoder was zeroed with the front of the wedge at either the end of pipe or weld center line (Figure 8.19). The scans were set up so that data were collected across both sides of the established zero axial position, whether it was the end of pipe or the weld center line. An axial scan range of −60 mm to 20 mm (−2.36 in. to 0.79 in.) with a resolution of 0.5 mm (0.02 in.) was implemented into the raster setup. Because the complete wedge dimension information is a required input to focal law development, the software establishes the front of the wedge as the zero axial position.

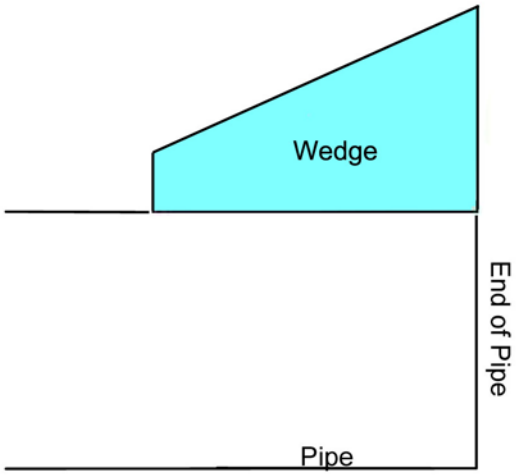

Figure 8.19 Example of Wedge Position When Zeroing the Axial Encoder on the End of Pipe

In addition to data collected via a varying wedge delay for each of the three primary angles on the end-of-pipe (corner) and flaw-base (corner) responses, previously collected full raster data on the flaws of 9C-001 and 9C-002 were also analyzed for a measure of axial beam redirection. These previously acquired raster data were not calibrated on the end of a wrought pipe specimen, but rather on the machined end of the CCSS pipe; that is, specimen 9C-001 or 9C-002, at 45 degrees. The required wedge delay was 2.5 µsec and was used for all angles. Typically when visually analyzing data for flaw detection and sizing, the peak of the response is used as the primary marker because it is clearly distinguishable by the color red when soft gain is properly adjusted in the analysis view. Both the leading edge and the peak response techniques were used in analyzing the full raster data set. A comparison of the data acquired specifically for the axial beam redirection study and the full raster, constant wedge delay data will be discussed later in this section.

8.1.6.4 Benchmarking Data on the Wrought Specimen

Data from the wrought sample were collected on the end of pipe at circumferential locations where the wedge delays were originally determined, the ‘0’ location, and at ±100 mm (3.93 in.) (Table 8.5) to confirm the wedge delays were properly set and held true at multiple locations on the calibration specimen. The true-state thickness is the value taken from the dial caliper while the measured thickness value comes from the A-scan analysis. The length, or metal path, as depicted by the A-scan was recorded and compared to the calculated A-scan length based on the true-state thickness and the incidence angle. Additionally, the axial position cursor value, as displayed in the volume corrected (VC) sectorial view, was recorded to show how the leading edge of the response signal varied from the nominal value of zero. This axial offset is a measure of axial beam redirection.

Table 8.5 Calibration True-State and Measured Values

Angle Of Incidence, Degree	Wedge Delay	Circumferential Location on Pipe, mm	True State Thickness, mm (in.)	Measured Thickness, mm (in.)	Calculated A-Scan Length, mm	A-Scan Length, mm	Axial Offset from Zero*, mm	FFT Peak Amplitude, MHz
30	1.25	0	32.4 (1.28)	32.4 (1.28)	37.4	37.4	0.07	1.33
		100	32.4 (1.28)	32.4 (1.28)	37.4	37.4	−0.24	1.35
		−100	32.6 (1.29)	32.6 (1.29)	37.7	37.7	0.27	1.38
45	1.30	0	32.4 (1.28)	32.4 (1.28)	45.8	45.9	0.04	1.42
		100	32.4 (1.28)	32.4 (1.27)	45.8	45.8	−0.09	1.46
		−100	32.6 (1.29)	32.6 (1.28)	46.2	46.2	0.03	1.46
60	1.40	0	32.4 (1.28)	32.4 (1.28)	64.8	64.8	−0.87	1.53
		100	32.4 (1.28)	32.4 (1.28)	64.8	64.8	−1.12	1.53
		−100	32.6 (1.29)	32.6 (1.29)	65.2	65.2	-0.96	1.55

*Taken from cursor in VC-sectorial view.

The corner response from the end of pipe should display at the axial position of zero. Any variation from zero, either positive or negative, could be indicative of the UT beam being slightly redirected either upwards or downwards from the ideal metal path in the insonified region of the specimen. Consistency on the end of the wrought pipe was confirmed when values of the measured thickness and A-scan (metal path) length were within 0.1 mm (0.004 in.) of their respective nominal values and the axial position cursor displayed the fiducial response to within ±1.2 mm (0.05 in.) of zero for all angles evaluated. These acceptable values were found at all three tested locations on the machined end of the pipe, showing that the adjusted wedge delays held true on a homogeneous isotropic material such as wrought stainless steel. The calibration specimen shows very little error in axial position, demonstrating, as expected, that there is insignificant axial beam redirection occurring in the wrought material for the 1.5-MHz longitudinal wave applied.

8.1.6.5 CCSS Analysis

Beam redirection caused by the anisotropy of the CCSS material was measured by the axial positional error (X in Figure 8.18); however, this value is also linked to the error in depth and A-scan length (triangle vertical side and hypotenuse). The axial positional error is plotted in Figure 8.20 for the WSS calibration pipe and for CCSS specimen 9C-001 as observed on the end of pipe and flaw corner signals at the three primary angles of 30, 45, and 60 degrees. These data sets were acquired with the same variable wedge delays. There are three points plotted at each angle, which represent three positions on the WSS end of pipe, the CCSS end of pipe, and three flaws in the 9C-001 specimen. The 9C-001 pipe-end measurements were taken at similar circumferential locations as the flaws in an effort to insonify material with similar microstructural features. Note that the axial error (beam redirection) changes from a negative to a positive value as the angle increases from 30 to 60 degrees, with a zero crossing (based on a linear regression equation) occurring at 61.7 degrees for the pipe-end and 56.1 degrees for flaw locations in the CCSS 9C-001 specimen. A negative axial position error implies that the beam is being directed toward the pipe ID before the central sound beam can reach the pipe end or true flaw location. This also is accompanied by a positive projected depth error indicating a flaw position that is deeper (relative to the sound entry point on the outside surface) in the material than true state. In comparison, a positive axial position error implies that the beam is being directed beyond the intended axial position, and the data (Figure 8.20) show that this is accompanied by a negative projected depth error or shallower placement of the indication. The depth and axial position errors have an inverse relationship.

For CCSS 9C-002 specimen data, the zero crossing was calculated to be 57.5 and 63.4 degrees for the end of pipe and flaw data, respectively.

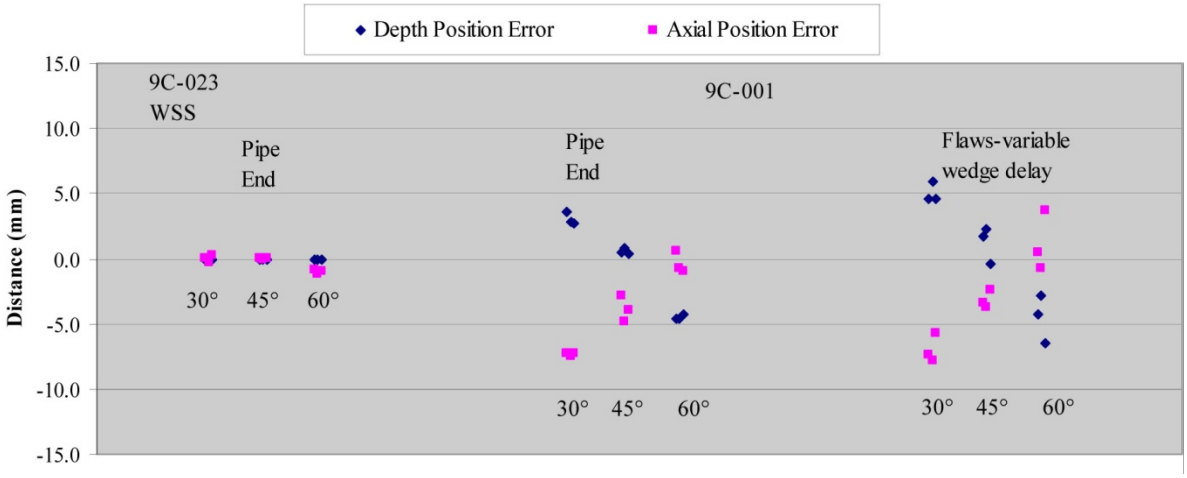

Figure 8.20 Comparison of Axial Position (and Projected Depth) Errors from the WSS Calibration Specimen and CCSS Specimen 9C-001 for Three Primary Angles. The CCSS specimen 9C-001 data includes the measurement errors from the end of pipe and flaw corner signals.

Literature (Kupperman et al. 1981) shows that beam redirection due to velocity variations are taking place in material with a columnar grain structure. Both theoretical and empirical changes in longitudinal velocity for a columnar material were reported and varied from 6400 m/sec to 5100 m/sec. Beam redirection was noted to be as much as 22 degrees. Furthermore, this deviation changes from a positive to a negative value at an approximately 50 degree insonification angle, whereas, the PNNL data crosses over at nearly 60 degrees. The crossover angle difference is likely attributed to different grain sizes between the Kupperman material and the PNNL material. The present PNNL study is primarily measuring the changes in axial position (while also recording depth changes) and attributing these changes to beam redirection due to existing CCSS microstructure. PNNL acknowledges that the sound velocity can change from grain to grain, but this phenomenon is not specifically being measured in the study, only the cumulative effect over the sound beam metal path in terms of depth and axial position is considered.

The flaw responses discussed above were analyzed with the variable wedge delay, where the wedge delay was optimized for each beam-forming angle, 30, 45, and 60 degrees on the WSS calibration specimen. All data collected previously to this beam redirection study were acquired with a constant wedge delay, where the wedge delay was determined from the end-of-pipe signal in the CASS material at only 45 degrees and applied to all other insonification angles. To determine the validity of the earlier constant wedge delay data in regard to measuring beam redirection, the results are compared to the variable wedge delay data. The data from the flaws in specimen 9C-001 are depicted in Figure 8.21 for both a variable and constant wedge delay. End-of-pipe data is also shown on the left for reference and was acquired with a variable wedge delay. The two data sets (pipe-end and flaw) acquired with the variable wedge delay are in general agreement. Axial position errors at 30, 45, and 60 degrees are approximately 7, 3.5, and 1 mm, respectively. The flaws acquired with a constant wedge delay produce an 11, 8, and 4 mm axial position error for 30, 45, and 60 degrees, respectively. These values are greater by

3–5 mm. It therefore appears that the less accurate constant wedge delay setup produces an artificially larger axial beam redirection by 3–5 mm. It is reasonable to conclude that the PA system should be calibrated on a known homogeneous material of similar wall thickness as the CASS pipe being evaluated. The wedge delays should be individually set for each of the insonification angles, or small groupings of angles. This is necessary when absolute mapping of flaw position is required. The constant wedge delay data is, however, still valid for flaw detection and sizing.

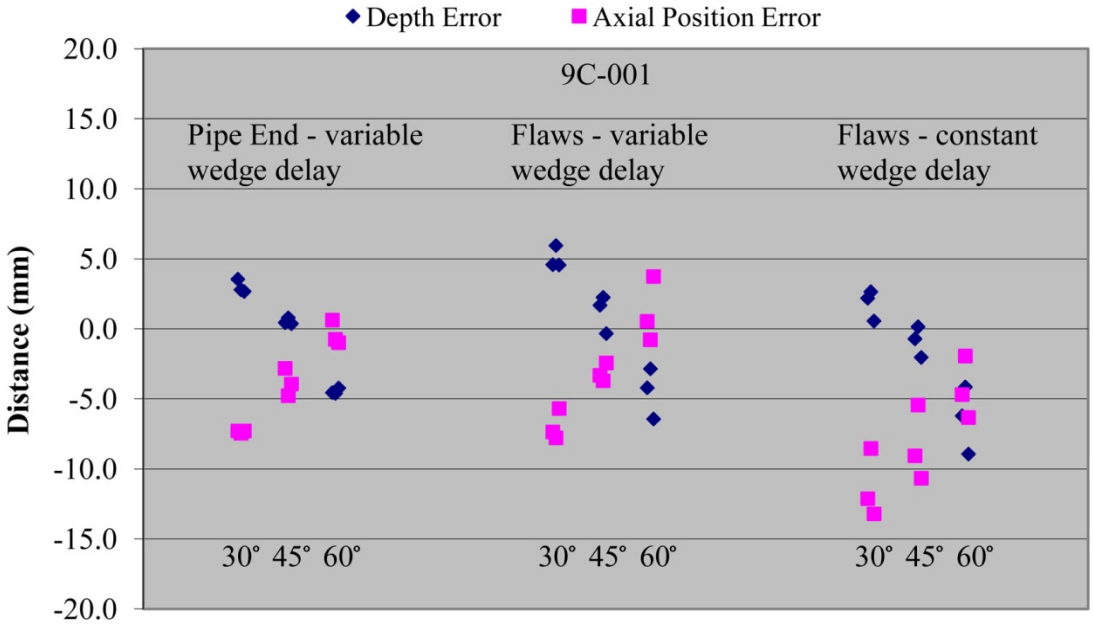

Figure 8.21 Comparison of Axial Position (and Projected Depth) Errors from Implanted Flaws in CCSS Specimen 9C-001 with a Variable Wedge Delay and a Constant Wedge Delay for the Three Primary Angles. The pipe end response from Specimen 9C-001 is also shown and was acquired with a variable wedge delay.

From the above discussions, one concludes that the variable wedge delay setup produces a more true representation of the beam redirection occurring in the material. A summary table of beam redirection based on an A-scan measurement for data acquired with the variable wedge delay is presented in Table 8.6, for WSS and both 9C-001 and 9C-002 specimens. Clearly the WSS material shows minimal or no beam redirection (less than 1.2 mm) in the pipe axial direction. Both CCSS pipes 9C-001 and 9C-002 show decreasing beam redirection with increasing angle. The minimal redirection has been shown to occur at approximately 61.7 and 56.1 degrees for the 9C-001 data and at 57.5 to 63.4 degrees for the 9C-002 data. Flaw detection was accomplished at approximately 45 degrees as this angle produced the best flaw response in the data. Theoretically, it is also the optimal angle to receive a strong corner response from the base of the flaw. At this angle, the Table 8.6 redirection measurements suggest an axial redirection or error in flaw placement of 3 mm on average is likely. While this axial beam redirection study did not include the 0.8, 1.0, and 2.0 MHz probes one would

anticipate the redirection to be less pronounced at lower frequencies and more significant at higher frequencies as the large grains have a greater impact on the sound field with increasing frequency.

Table 8.6 Axial Beam Redirection Measurements

	WSS End, mm	9C-001 End, mm	9C-001 Flaw, mm	9C-002 End, mm	9C-002 Flaw, mm
30 Degree					
1	0.07	−7.28	−7.37	−5.37	−1.29
2	−0.24	−7.45	−7.78	−3.70	−3.76
3	0.27	−7.29	−5.685	−6.28	−4.72
45 Degree					
1	0.04	−2.82	−3.32	−2.88	−1.04
2	−0.09	−4.77	−3.71	−1.38	−3.15
3	0.03	−3.94	−2.43	−1.54	−3.17
60 Degree					
1	−0.87	0.63	0.55	−0.58	0.58
2	−1.12	−0.75	−0.77	1.13	−0.82
3	−0.96	−0.98	3.74	0.35	0.02

As part of the beam redirection study, the peak frequency of the measured signals was also recorded. The limited data does not conclusively show a correlation between frequency content and insonification angle. The only real conclusion that can be drawn is that the CCSS material is filtering out the higher frequencies. The data show that the 1.5-MHz probe is only receiving data in the 0.95–1.2-MHz range in the cast material whereas the WSS material is sustaining frequencies in the 1.3–1.5-MHz range in general. On average, the WSS material supports 1.45 MHz whereas the CCSS supports 1.17 MHz, a 19 percent offset to center frequency. This does not singularly suggest that a 1-MHz probe should be used for inspections as there are other factors to consider. For the lower frequency probe, the footprint is larger, which can limit access to a flaw; the probe spot size is larger, which adds to the length sizing error; and the probe resolution is lower making it, for example, more difficult to separate a flaw tip signal from a corner response. Additionally, these probes are broadband, which enables transmission and reception of energy over a range of frequencies and not just at a single frequency. With all of these considerations, the probe that best detects and characterizes the flaws should be used; therefore, it was deemed not reasonable to use more than one probe for the best evaluation results.

8.1.7 Baseline CASS Material Noise Analyses

Full circumferential PA line scans were conducted at 800 kHz and 1.5 MHz on the CCSS pipe ends of the three surge-line specimens to assess baseline material noise and attenuation. The corner responses from the end of the pipe sections were recorded as the probe was scanned circumferentially in a full 360° path. From a geometrical perspective, the end of the pipe represents a full 100% through-wall flaw. The corner response from the ID was recorded with

the axial probe offset selected to give the strongest response at approximately 45 degrees. Ideally, the maximum signal reflection occurs at this position. In a homogeneous material, the corner signal response would be very similar over the entire 360° of the pipe. Variations in the corner response data from this cast material are seen in the following six figures. These variations can be attributed to the mixture of columnar and equiaxed fine- and coarse-grain structures (essentially causing the material's acoustic anisotropy and inhomogeneity). However, to a lesser extent, component surface irregularities, undulations, and surface finish, all affect coupling for this contact UT technique. We have not explored the random nature of these surface-induced coupling phenomena, but they are considered to be minor, with respect to the loss of signals due to microstructure of the CASS materials.

Figures 8.23 through 8.28 show the corner signal responses from the pipe ends of specimens 9C-001, 9C-002, and 7C-059 at both 800 kHz and 1.5 MHz. The images are of merged data (composite data using responses from all angles) and thus represent the full sweep of collected data from 30° to 70° with 1° increments. Circumferential data were acquired at a 1-mm resolution over the approximately 1017-mm (40.0-in.) circumference. The D-scan end-view image is shown on the left and a polar plot on the right. A loss of corner signal or signal dropout was measured from a contour line drawn through the end view data. The contour line is displayed at the top of the D-scan end-view image. Data regions that fell below a 10 dB level (31%) from the peak response were recorded as a loss, or diminishing, of the signal. The data from 9C-001 at 800 kHz show the most consistent response and have a diminished signal on only 0.2% of the circumference. Because the wavelength is longest at 800 kHz, sound field propagation should be inherently less sensitive to the effects of the grain boundaries within the microstructure of the CASS material. Therefore, this result was fully anticipated.

These data show that the corner response is detected at essentially 100% of the circumference at the 800-kHz inspection frequency. This drops to about 94.8% detection at 1.5 MHz, which is still very good. The worst response is in specimen 7C-059 at 1.5 MHz, which has a 60.9% diminished signal or conversely a 39.1% detection of the corner signal response (see Figure 8.28) over the pipe circumference. This poor result is primarily due to a large amplitude response in a limited circumferential region. The high amplitude region is at approximately −60 to 110 mm (−2.36 to 4.33 in.) and represents nominally 17% of the circumferential length. The inner corner (edge) of the pipe in this region is gouged (see Figure 8.22), and is likely the cause of these higher amplitude responses. Outside of this region, the end view shows that there are corner signal responses over much of the circumference. To account for this anomaly, the threshold for diminished signal determination was lowered to −12 dB (0.25 level) and the signal dropout recalculated at 31.4% (see Figure 8.29). This is perhaps a better representation of this data set. Results from the measurements are listed in Table 8.7. Regardless of the degree of correlation between the data in Table 8.7 and general detection capability, the results from the evaluation of PA ultrasonic inspection of smaller bore, CASS PZR surge-line components available for this study show that the welds are inspectable over a wide range of frequencies.

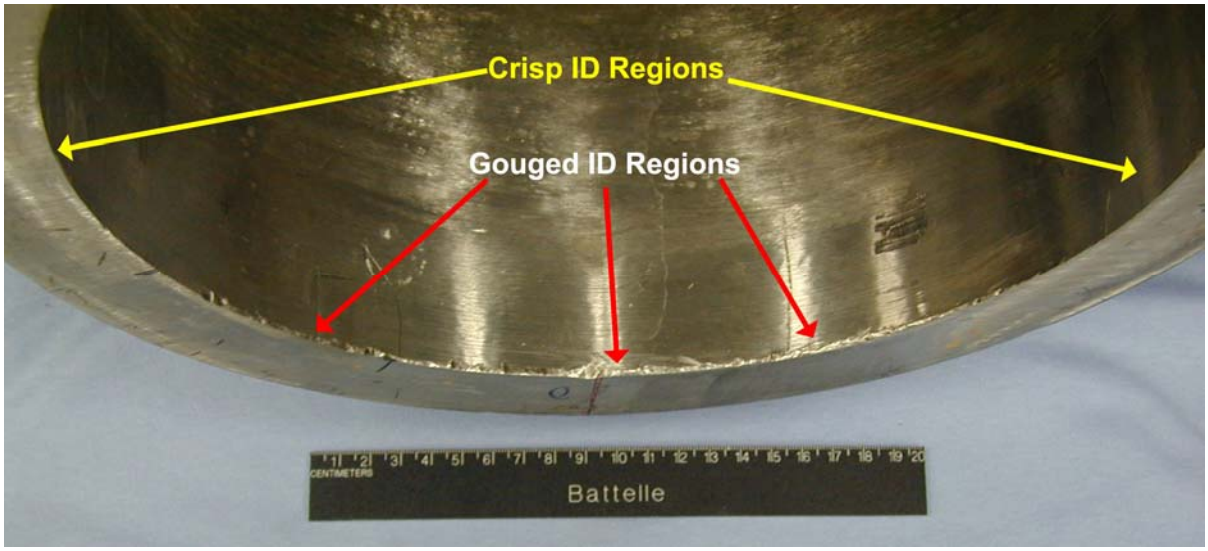

Figure 8.22 Pipe End of Specimen 7C-059 Showing the Gouged Regions of the ID Corner that Likely Lead to a Heightened Ultrasonic Response

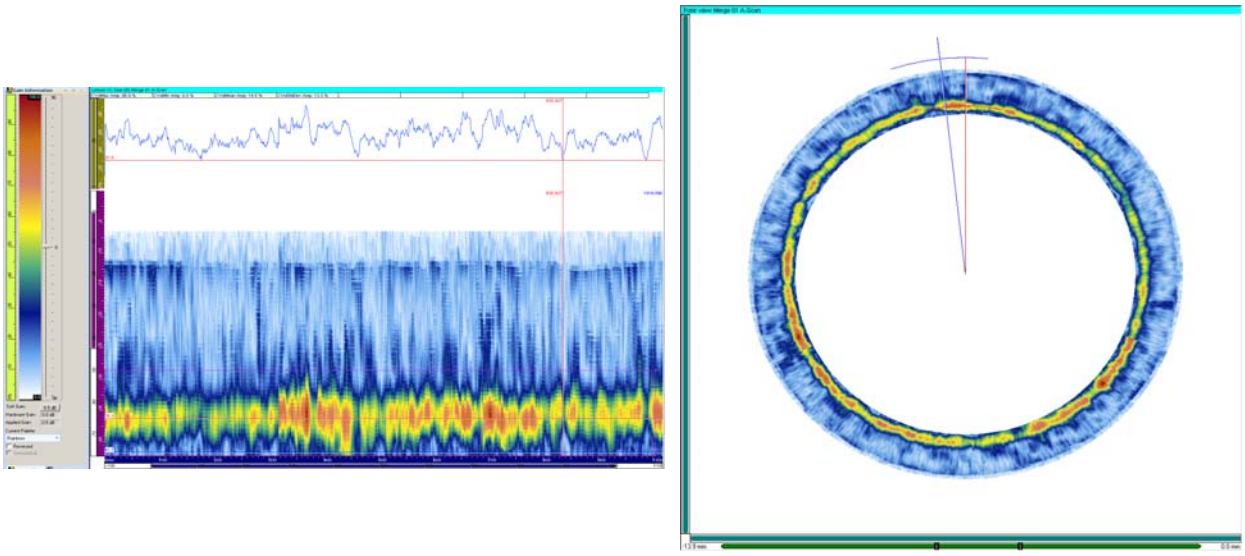

Figure 8.23 Pipe End Corner Response on 9C-001 at 800 kHz. The end view is on the left and the polar view on the right. A signal dropout of 0.2% is measured from the contour line in the end view.

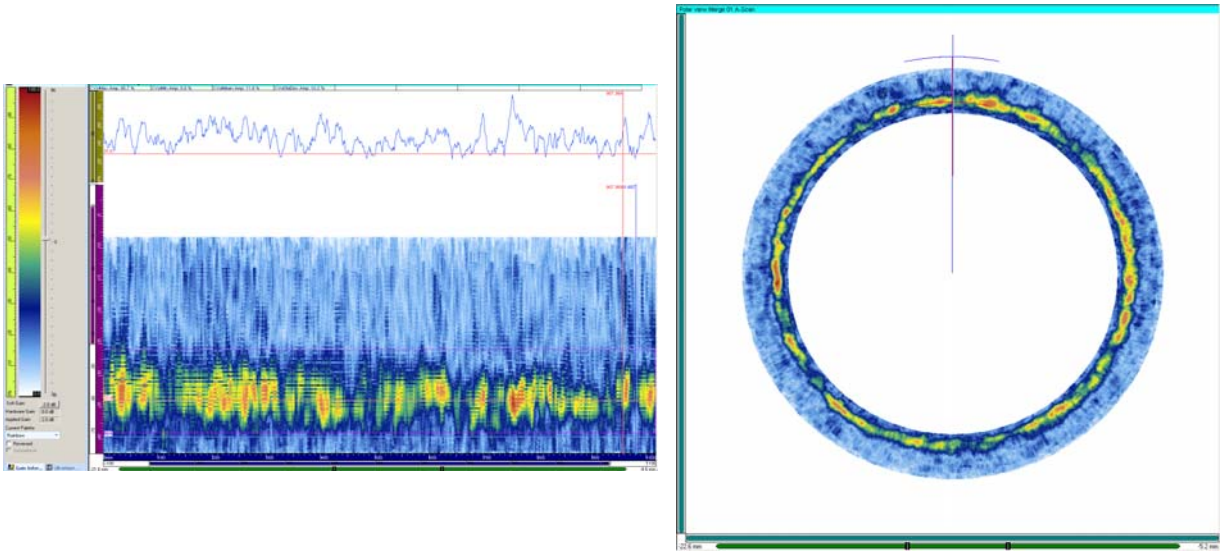

Figure 8.24 Pipe End Corner Response on 9C-001 at 1.5 MHz. The end view is on the left and the polar view on the right. A signal dropout of 5.2% is measured from the contour line in the end view.

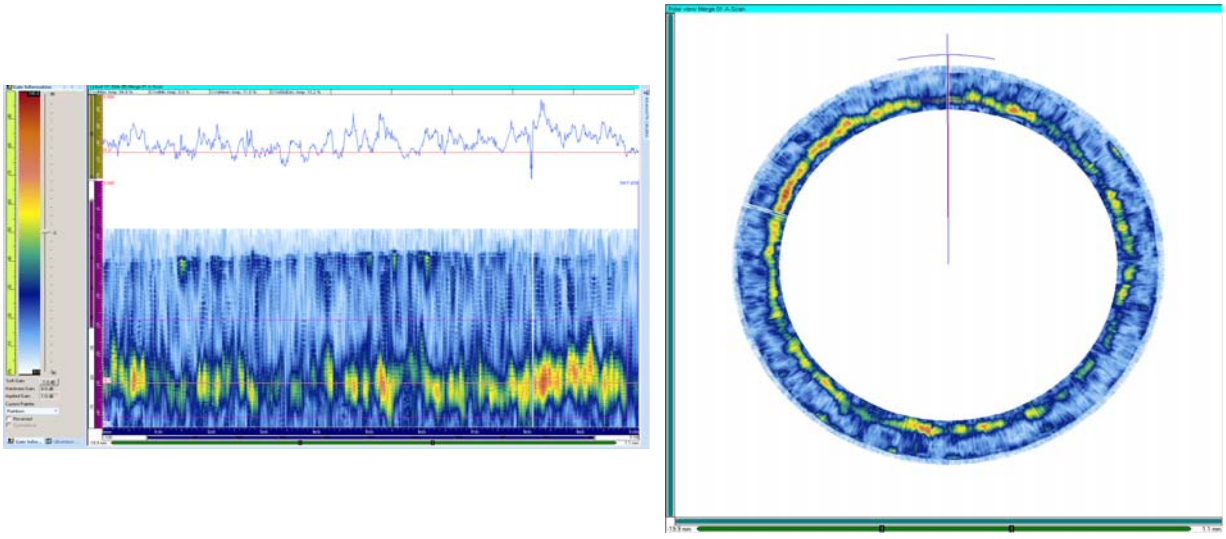

Figure 8.25 Pipe End Corner Response on 9C-002 at 800 kHz. The end view is on the left and the polar view on the right. A signal dropout of 14.4% is measured from the contour line in the end view.

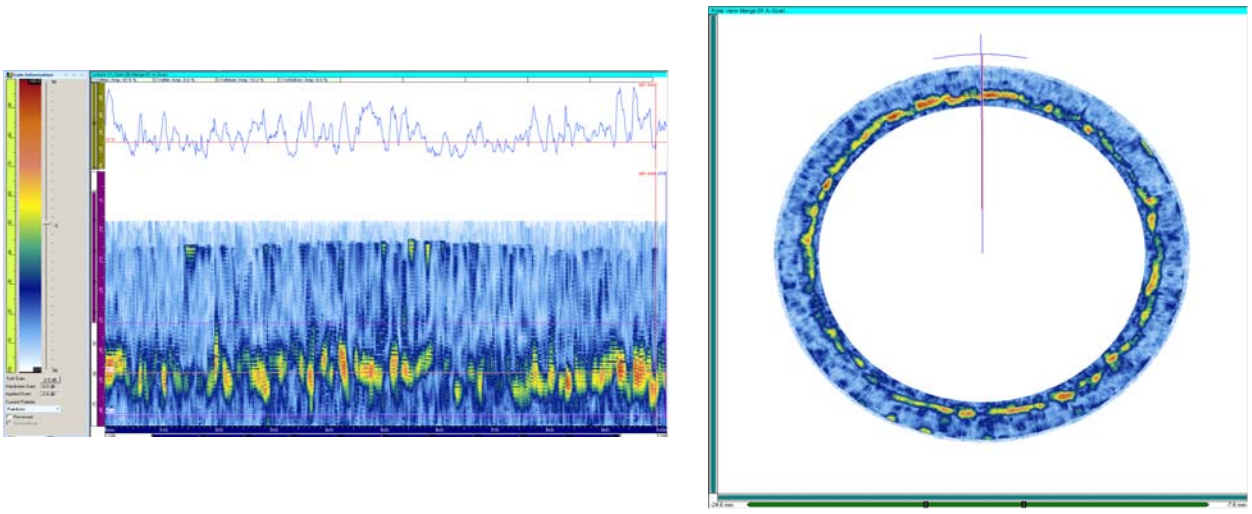

Figure 8.26 Pipe End Corner Response on 9C-002 at 1.5 MHz. The end view is on the left and the polar view on the right. A signal dropout of 27.9% is measured from the contour line in the end view.

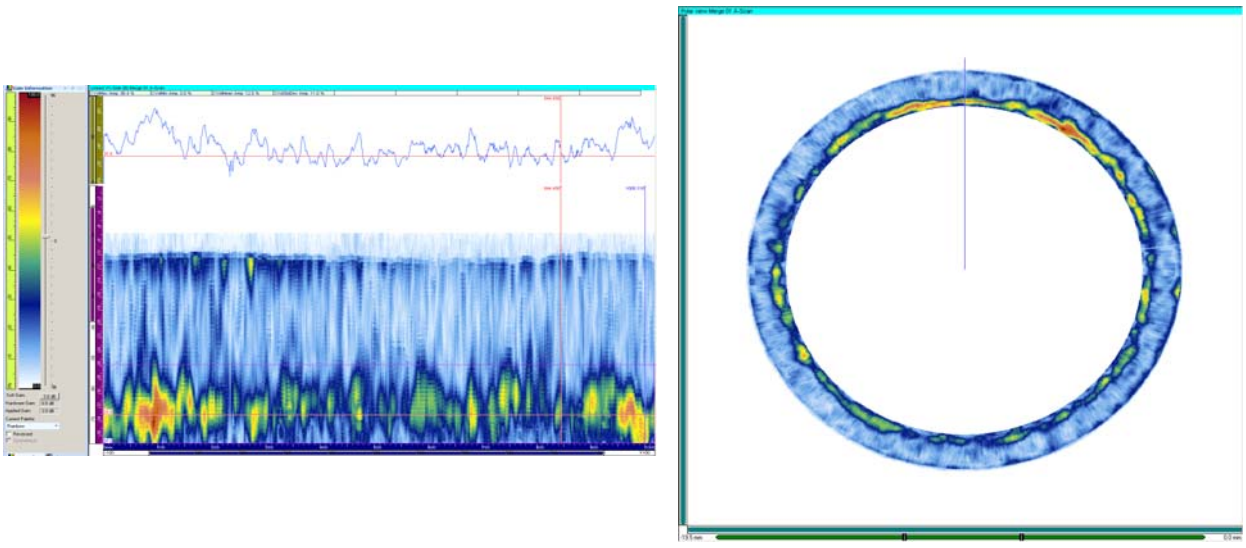

Figure 8.27 Pipe End Corner Response on 7C-059 at 800 kHz. The end view is on the left and the polar view on the right. A signal dropout of 22.5% is measured from the contour line in the end view.

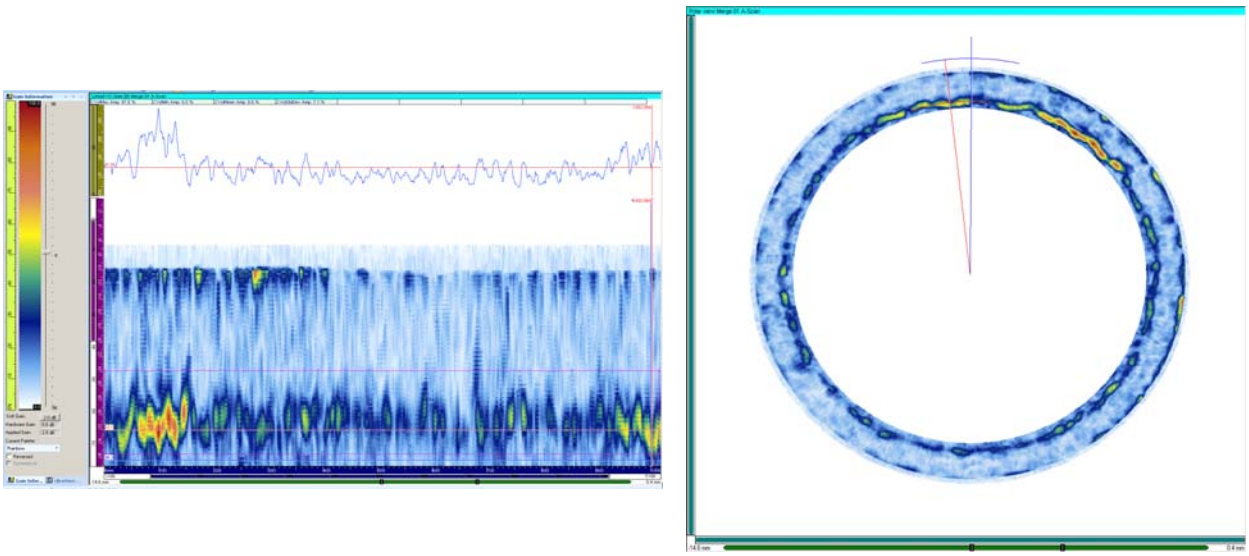

Figure 8.28 Pipe End Corner Response on 7C-059 at 1.5 MHz. The end view is on the left and the polar view on the right. A signal dropout of 60.9% is measured from the contour line in the end view at a −10 dB level (0.31).

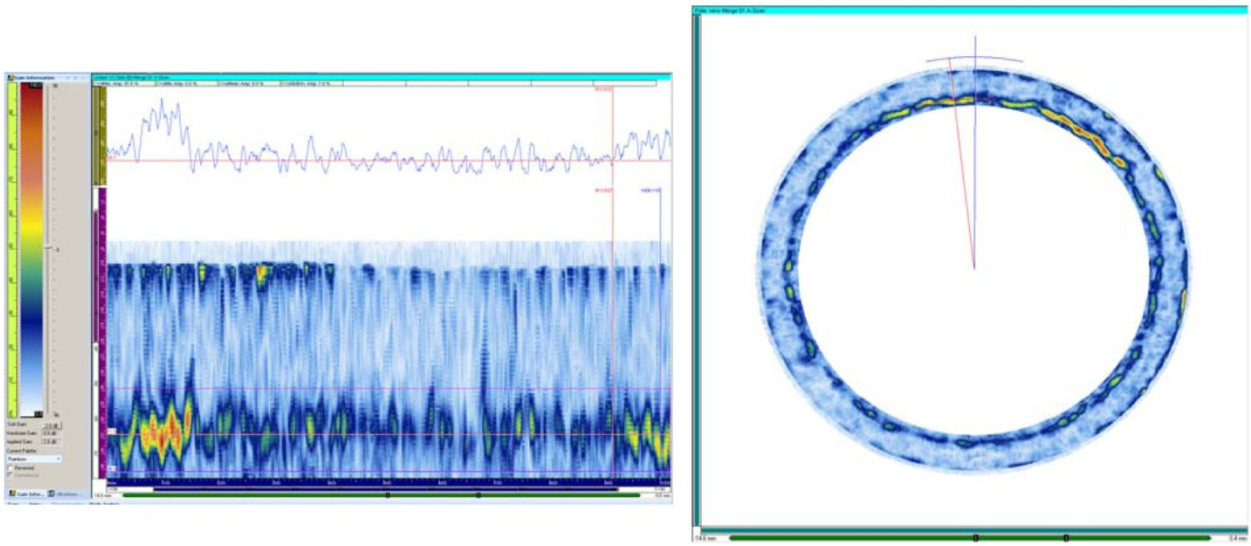

Figure 8.29 Pipe End Corner Response on 7C-059 at 1.5 MHz. The end view is the same as in Figure 8.30 but the threshold for the signal dropout measurements has been lowered to −12 db (0.25 level). A signal dropout of 31.4% is measured at the −12 dB level.

Table 8.7 Regions of Diminished Signal as Observed from the Corner Response off the Pipe End of the Surge-Line Specimens at a −10 dB Level

Specimen	Freq., MHz	No. of Regions Observed	Measured Length of Diminished Signal Regions, mm (in.)				Percent Dropout
			Minimum	Maximum	Average	Median	
9C-001	0.8	2	1.0 (0.04)	1.0 (0.04)	1.0 (0.04)	1.0 (0.04)	0.2
	1.5	18	1.0 (0.04)	7.0 (0.28)	3.0 (0.12)	3.0 (0.12)	5.2
9C-002	0.8	41	1.0 (0.04)	17.2 (0.68)	3.6 (0.14)	2.0 (0.08)	14.4
	1.5	36	1.0 (0.04)	33.4 (1.31)	7.9 (0.31)	6.6 (0.26)	27.9
7C-059	0.8	27	1.0 (0.04)	28.2 (1.1)	8.5 (0.33)	6.8 (0.27)	22.5
	1.5	27	1.0 (0.04)	171.2 (6.7)	23.0 (0.90)	14.6 (0.57)	60.9
			Measured at a −12 dB level				
7C-059	1.5	34	1.0 (0.04)	29.1 (1.15)	9.41 (0.37)	7.3 (0.29)	31.4

The overall results show that higher frequencies cause more regions of diminished signal response, which one would expect. The higher frequency (1.5 MHz) is more sensitive to attenuation and beam redirection, as the wavelength-to-average grain diameter ratio found in these specimens is much less than unity. In previous work (Anderson et al. 2007), the median length of the diminished signal was suggested as an indication of flaw length that could go undetected due to a loss-of-signal effect from the coarse-material microstructure. With this assumption, the data show that a flaw less than 14.6 mm (0.57 in.) could go undetected in this material as a worst-case scenario. This is only 1.4% of the circumference and exhibits acceptable detection.

8.2 ISI Supplier Phased-Array Data on Implanted Flaws

An inservice inspection (ISI) supplier was contacted to conduct an ASME Code-qualified evaluation of the implanted flaws in the surge line specimens. Personnel from LMT, Inc. visited PNNL in July 2010 to conduct an encoded PA examination of cracks in the two CASS PZR surge line specimens, specifically 9C-001 and 9C-002. LMT Inc. provided their own equipment and inspection methods based on an ASME Section XI, Appendix VIII qualified procedure. The procedure is ZETEC OmniScanPA_03rev E, “Procedure for Encoded, Manually Driven, Phased Array Ultrasonic Examination of Dissimilar Metal Piping Welds.” It was used as guidance for the CASS examination because the specimen size and thickness fell within the limits of the procedure and the procedure was developed for highly attenuative materials.

8.2.1 Equipment

A ZETEC OmniScan 32/128PR portable phased-array ultrasonic instrument was used for the examinations. This option allows the inspector to employ separate matrices of individual channels (32 separate pulser and 32 separate receiver channels) as well as 256 focal laws. UltraVision software version 1.2R4 was used to control the OmniScan phased-array instrument during the data acquisition process and for focal law development and data analyses. The UltraVision software allows the operator to remotely control the OmniScan unit via an Ethernet connection with a remote computer.

A dual TRL probe was used with a nominal center frequency of 1.5 MHz. The probe characteristics are listed in Table 8.8. This probe was operated with a splitter cable to pair the secondary axis elements thereby creating a 32 × 1, 1D-linear array with a secondary axis pitch of 15 mm (0.59 in.). The wedge footprint was 85.0 × 50.0 mm (3.35 × 1.97 in.) with a wedge angle of 22.3 degrees and a roof angle of 7.0 degrees.

Table 8.8 ISI Supplier LMT PA Probe Characteristics

Array Type	Contact longitudinal
Reference	1.5M32X2E64-15
Manufacturer	Imasonic
Frequency	1.5 MHz
Total Aperture	64.0 × 15.0 mm (2.5 × 0.59 in.)
# elements primary axis	32
# elements secondary axis	2
Element size primary axis	1.80 mm (0.071 in.)
Element size secondary axis	7.30 mm (0.29 in.)
Primary axis pitch	2.00 mm (0.79 in.)
Secondary axis pitch	7.50 mm (0.30 in.)

8.2.2 Data Acquisition

Line scan data with electronic rastering were acquired. An aperture size of 15.0 mm × 32.0 mm (0.59 in. × 1.26 in.) was used for examinations with two paired elements in the secondary axis (2 × 7.5 mm (0.30 in.)) and 16 elements in the primary axis (16 × 2.0 mm (0.08 in.)). The first focal law consisted of elements 1 through 16 and the last focal law consisted of elements 17 through 32. The total length of electronic scanning was approximately 35 mm (1.38 in.) for each static probe position. Seventeen individual focal laws were created for each individual beam angle. Individual linear scan beam angles selected for examination were 40°, 45°, 50°, 55°, 60°, and 65°. The focus type was selected as half path but the emission focus varied as a function of the beam angle. Focus positions were selected at 43, 46.5, 51, 57.5, 66, and 78 mm (1.69, 1.83, 2.01, 2.26, 2.60, and 3.07 in.) for beam angles 40 to 65, respectively.

8.2.3 Data Analysis

Length sizing measurements were based on the 12-dB amplitude drop method. This method is consistent with dissimilar metal weld length sizing techniques for flaws located near the centerline of the weld. This length sizing technique provides an outside diameter length dimension that is longer than the actual inside diameter length dimension due to curvature of the piping material. To calculate the actual flaw length at the inside surface, the following formula was used:

$$(ID/OD) \times OD \text{ flaw length} = \text{Reported ID flaw length.}$$

The data acquired on specimen 9C-001 from flaw 1, as observed from the pipe side of the weld, 270 degree skew, is displayed in Figure 8.30. The flaw is noted in the lower left D-scan end view and is clearly visible. All other data images are displayed in Appendix F. A flaw length summary is listed in Table 8.9. The RMSE for the flaws as observed from the pipe side is well within the 19 mm (0.75 in.) ASME-required limit. Due to the long probe footprint, the probe was unable to couple properly to the elbow extrados. As a result, data were not acquired from the elbow side on specimen 9C-001 and only one flaw was examined in specimen 9C-002 on the elbow side.

Flaw depth measurements to the flaw tip were taken using the Absolute Arrival Time Technique (Davis 1998). This gives the remaining ligament dimension which is then subtracted from the thickness of the component at the flaw location to determine actual flaw height. Depth sizing measurements were taken at the deepest portion of the flaw only. A flaw depth summary is listed in Table 8.10.

Signal-to-noise ratios were determined from the volumetrically merged data in a manner similar to that used by PNNL. The summary values for the implanted flaws are listed in Table 8.11. The flaws all have good signal-to-noise ratios. This indicates that the flaw signals are well above the background noise levels.

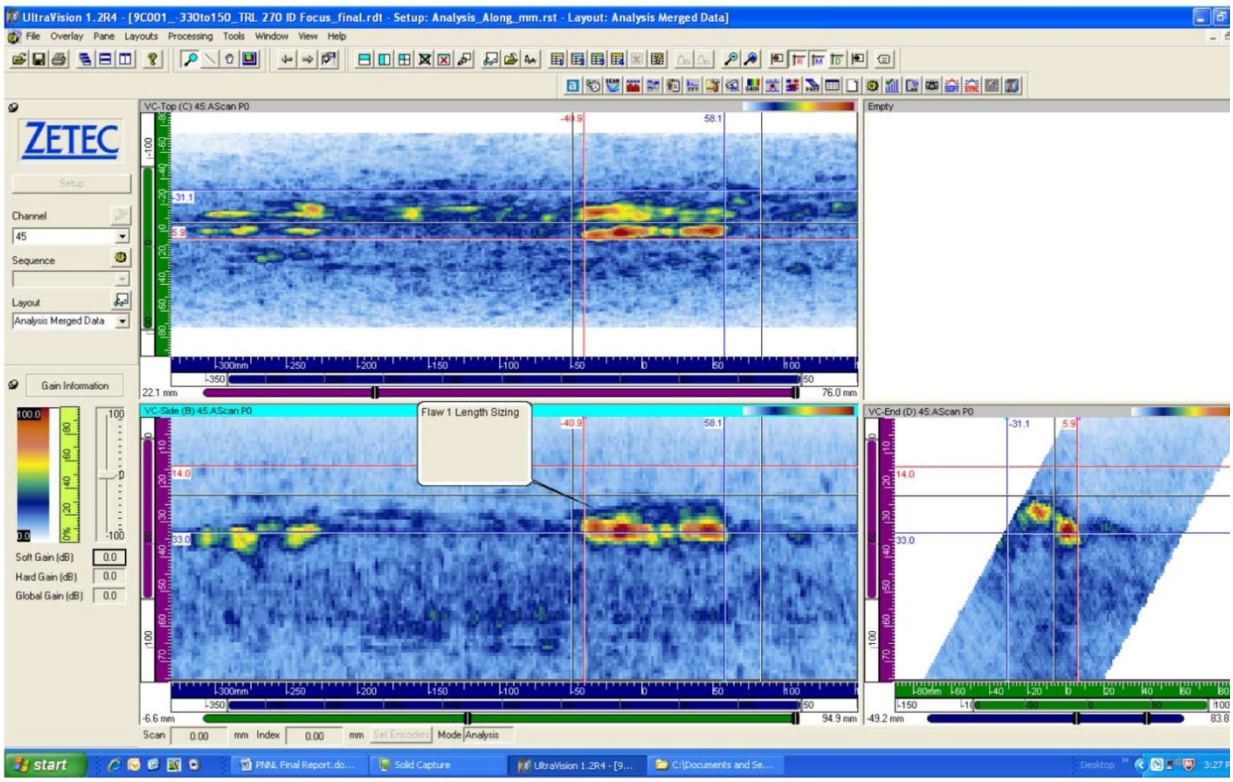

Figure 8.30 ISI Supplier, LMT, Data from Flaw 1 in Specimen 9C-001 at 270 Degree Skew, Pipe Side

Table 8.9 Flaw Lengths as Reported by ISI Supplier LMT

Specimen/Flaw	Reported Flaw Length 270°Skew CCSS (Pipe Side) (mm / inch)	Reported Flaw Length 90°Skew SCSS (Elbow Side) (mm / inch)	Actual Flaw Length
9C-001/Flaw 1	80.7 / 3.18	Note 1	76.6 / 3.02
9C-001/Flaw 2	52.7 / 2.07	Note 1	51.1 / 2.01
9C-001/Flaw 3	79.0 / 3.11	Note 1	69.7 / 2.74
9C-002/Flaw 1	69.8 / 2.75	76.4	76.7 / 3.02
9C-002/Flaw 2	50.4 / 1.98	Note 2	50.5 / 1.99
9C-002/Flaw 3	63.4 / 2.50	Note 2	69.7 / 2.74
RMSE	**5.7 / 0.22**		

Note 1: No 90° skew exams performed on 9C-001.
Note 2: Limited 90° skew exams performed on 9C-002 due to configuration/probe footprint conflicts.

Table 8.10 Flaw Depths as Reported by ISI Supplier LMT

Specimen/Flaw	Reported Flaw Depth 270°Skew CCSS (Pipe Side) (mm / inch)	Reported Flaw Depth 90°Skew SCSS (Elbow Side) (mm / inch)	Actual Flaw Depth
9C-001/Flaw 1	6.1 / 0.24	Note 1	6.4 / 0.25
9C-001/Flaw 2	6.4 / 0.25	Note 1	8.9 / 0.35
9C-001/Flaw 3	5.8 / 0.23	Note 1	8.3 / 0.33
9C-002/Flaw 1	6.5 / 0.26	3.8 / 0.15	7.5 / 0.30
9C-002/Flaw 2	6.9 / 0.27	Note 2	6.3 / 0.25
9C-002/Flaw 3	4.8 / 0.19	Note 2	4.8 / 0.19
RMSE	**1.52 / 0.06**		

Note 1: No 90° skew exams performed on 9C-001.
Note 2: Limited 90° skew exams performed on 9C-002 due to configuration/probe footprint conflicts. Only Flaw 1 was imaged.

Table 8.11 Flaw Signal-to-Noise Ratios as Reported by ISI Supplier LMT

Specimen/Flaw	Signal-to-Noise Ratio CCSS (Pipe Side)	Signal-to-Noise Ratio SCSS (Elbow Side)
9C-001/Flaw 1	12.3 dB	Note 1
9C-001/Flaw 2	13.2 dB	Note 1
9C-001/Flaw 3	10.2 dB	Note 1
9C-002/Flaw 1	13.2 dB	15.8 dB
9C-002/Flaw 2	12.0 dB	Note 2
9C-002/Flaw 3	13.0 dB	Note 2

Note1: No 90° skew exams performed on 9C-001.
Note 2: Limited 90° skew exams performed on 9C-002 due to configuration/ probe footprint conflicts. Only Flaw 1 was imaged.

8.3 Comparison of Implanted Flaws

As previously discussed, the ISI supplier, LMT Inc, evaluated the three implanted flaws from the CCSS pipe side in both 9C-001 and 9C-002 specimens. Flaw 1 in specimen 9C-002 was the only flaw examined from the elbow side, and none of the flaws were evaluated from the elbow side in specimen 9C-001. For simplicity, the comparison of data results between PNNL and LMT will only discuss the pipe-side data. Additionally, the PNNL summary will be limited to line scan data. A flaw by flaw comparison can be made by sorting through Appendix C for PNNL line scan data at 1.5 MHz and through Appendix F for the ISI supplier data. An example is given in Figures 8.31 and 8.32 for a pipe side examination of flaw 3 in specimen 9C-001. These images show similar responses in the D-scan end views.

The flaws were detected and sized with good signal-to-noise values evident in the data. PNNL reported SNR values in the 13.7 to 21.2 dB range and LMT reported a 10.2 to 13.2 dB range. Flaw detection was not in question. The length sizing of these implanted flaws at 1.5 MHz by LMT had a 5.7 mm (0.22 in.) RMSE and the PNNL data had RMSE values of 5.9, 7.4, 9.0, and 9.7 mm (0.23, 0.29, 0.35, and 0.38 in.) for probe frequencies of 0.8, 1.0, 1.5, and 2.0 MHz, respectively. All error values are within the 19.05 mm (0.75 in.) ASME Code-allowable limit for length. The depth sizing of these flaws by LMT had a 1.5 mm (0.06 in.) RMSE and the PNNL data had a 1.5, 1.2, 0.7, and 1.3 mm (0.06, 0.05, 0.03, and 0.05 in.) RMSE values for the same four probe frequencies above. These error values all fall within the ASME Code allowable limit of 3.18 mm (0.125 in.) for depth. Overall the data comparison is very good. PNNL results and the ISI supplier results on flaws implanted in the piping weld indicate that the flaws are detected and sized within ASME Code accepted guidelines.

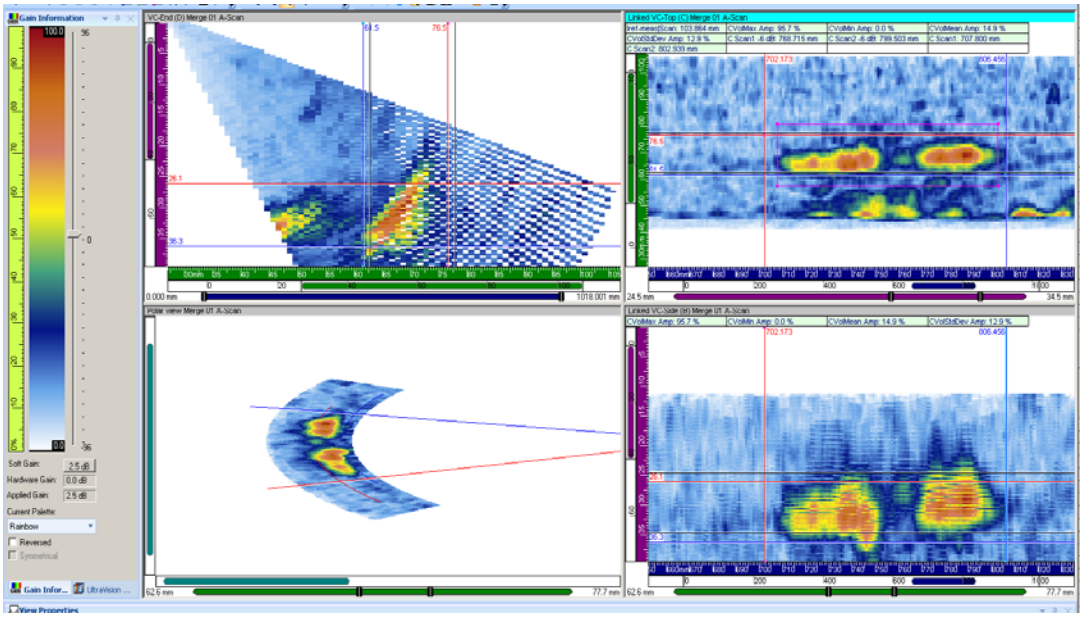

Figure 8.31 PNNL 1.5 MHz Data on Pipe Side of 9C-001, Flaw 3, Merged Image for Length Sizing. The D-scan end view is in the lower right.

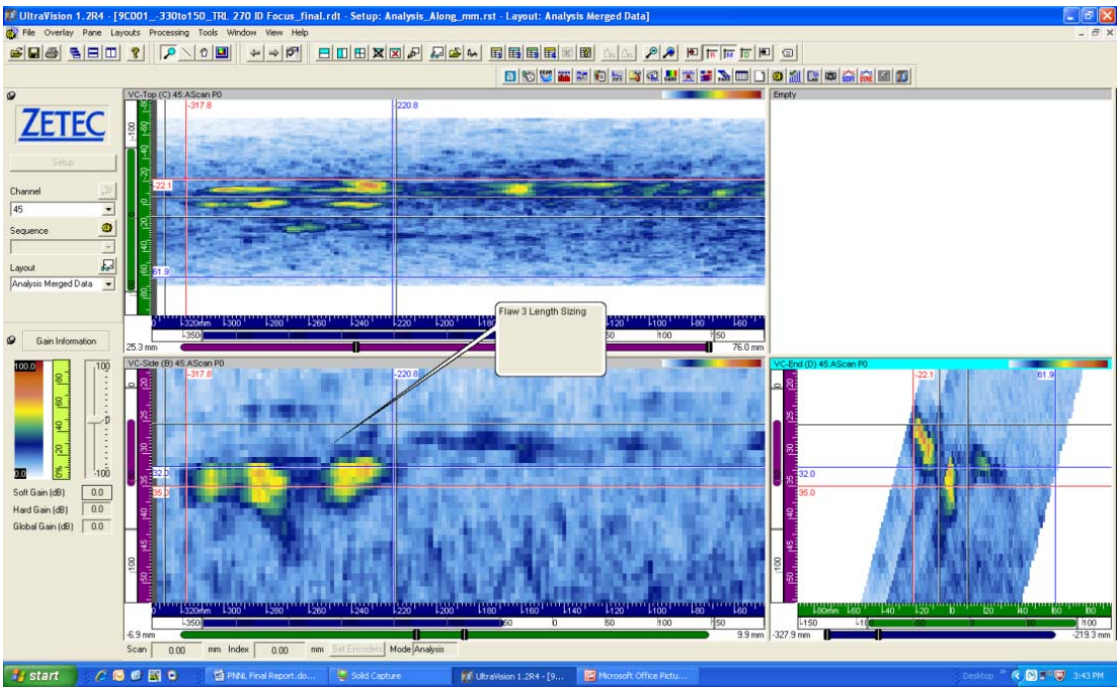

Figure 8.32 ISI Supplier data on Specimen 9C-001 Implanted Flaw 3 from the CCSS Pipe Side for Length Sizing. The D-scan end view is in the lower left.

8.4 PNNL Phased-Array Data on In-Situ Grown Flaws

8.4.1 Ultrasonic Examination

The phased-array ultrasonic inspections of the two validation flaws contained in the practice specimen and the three in-situ flaws contained in the parent pipe and elbow material of specimen 9C-002 were conducted at several frequencies. Using the phased-array probes previously described in Section 5, data were acquired at 800 kHz, 1.5 MHz, and 2.0 MHz using the DYNARAY electronics and automated scanner system. The automated scanner system consists of an ATCO dual-axis magnetic wheel scanner driven by a ZETEC Motor Control Drive Unit (MCDU-02). The scanning system links directly to the Dynaray unit via Ethernet and encoder cabling to allow control of the scanning system using the UltraVision software package. Spatially encoded data are acquired in both axes using this system (Figures 8.33 and 8.34).

Prior to scanning the flaw regions of the specimens, calibrations were conducted by peaking the 45-degree corner response from the geometric end-of-pipe locations. Adjustments were made to the wedge delay correction so that the corner response at each frequency aligned at the proper through-wall extent for each specimen. Data acquisition on the flaw regions was conducted as similarly described in Section 6 using water as a couplant and the ring scan track outfitted to accommodate the automatic scanner. Data were acquired with both line and raster scans using the skewing capabilities of the matrixed (2D) phased-array probes. Focal laws were generated using a half-path focusing technique with the focus at 40 mm (1.57 in.). Data

were collected over three separate channels that invoked beam skews of −10, 0, and +10 degrees, one skew per channel. Azimuthally, the insonification angles were swept from 30 to 70 degrees with 1-degree resolution for the line scan configurations. Data were acquired at multiple axial distances from the flaw location and from both sides of the flaw. Similarly, raster scan data were acquired using the same skewing parameters and incrementing the azimuthal sweep from 30 to 69 degrees at a resolution of 3 degrees. With respect to scanning resolution, line scans were collected at 0.5 mm (0.02 in.) in the scan direction while incrementing 5 mm (0.2 in) in the index. Raster scans were collected at 0.5 mm (0.02 in.) in the scan and 1.0 mm (0.04 in.) in the index axis for all frequencies.

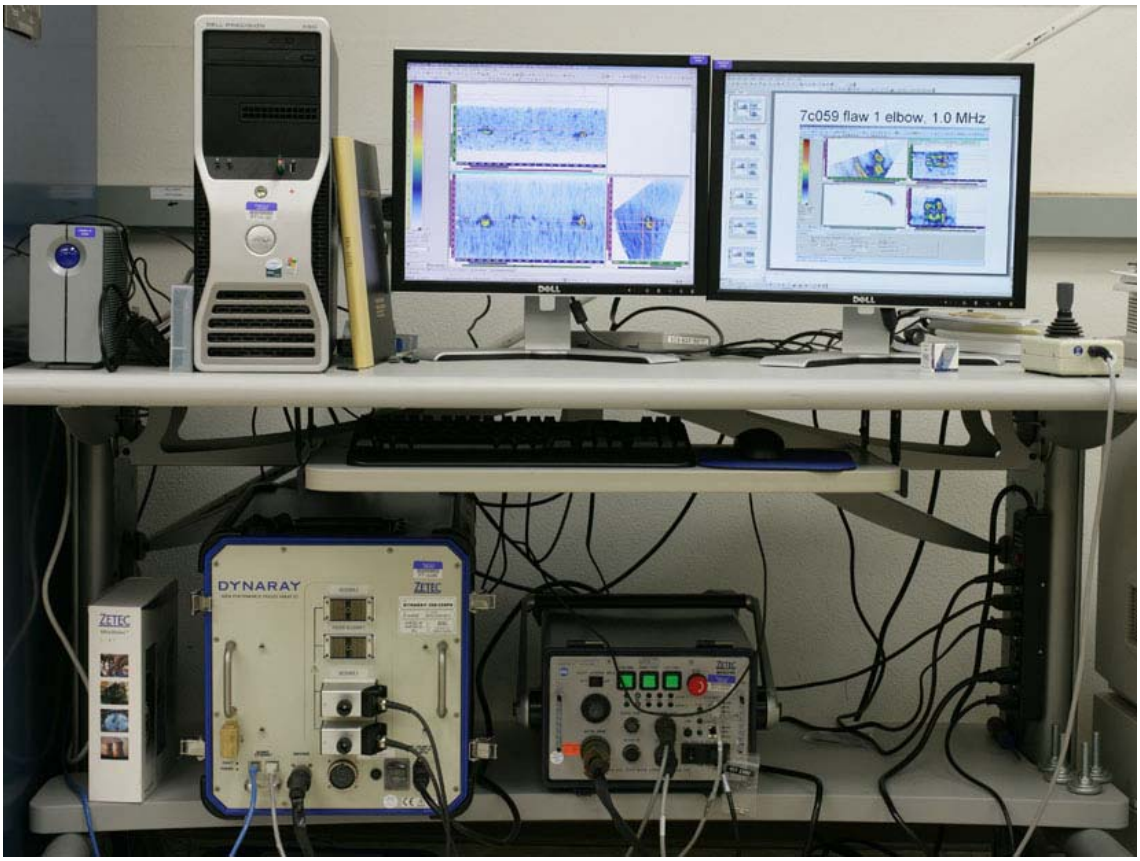

Figure 8.33 DYNARAY and Motor Control Drive Unit

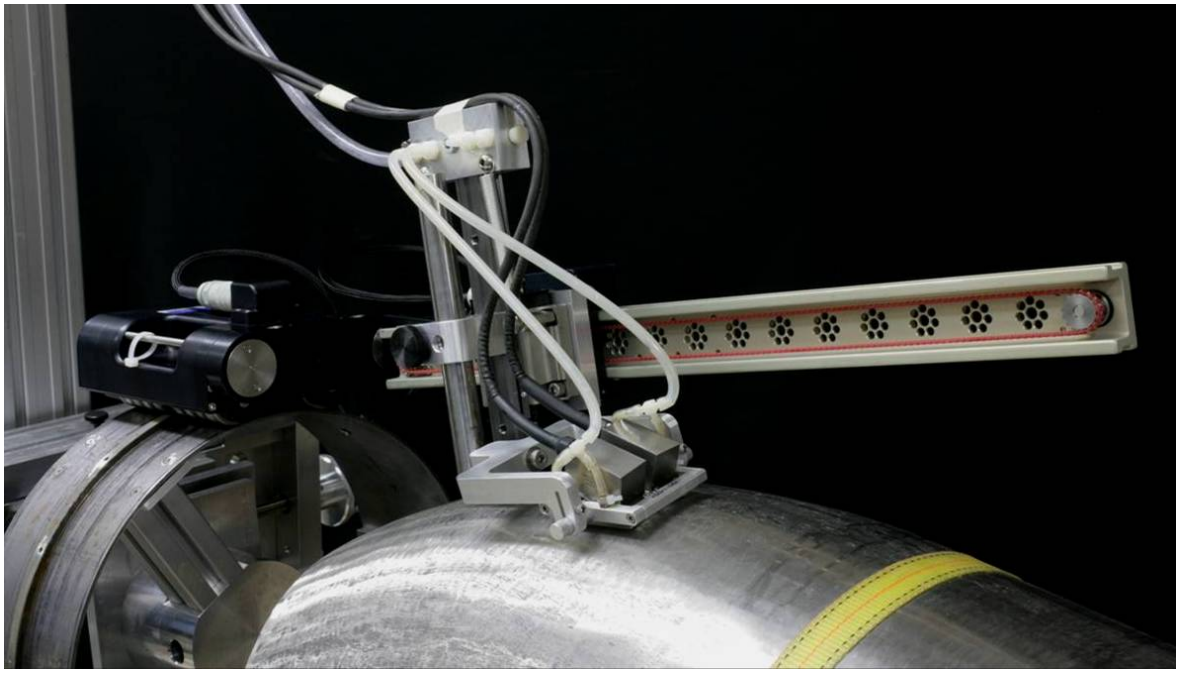

Figure 8.34 Automated Scanner and Probe System on Specimen

8.4.2 Data Analysis

Line and raster scans were acquired at multiple frequencies, various beam skews, and from both sides of the five in-situ grown, circumferentially oriented cracks contained in the validation and 9C-002 specimens. Again, flaws 1087 and 1089 were located in the centrifugally cast validation specimen, flaws 1110 and 1102 in the centrifugally cast pipe side, and flaw 1100 in the statically cast elbow side of 9C-002. The data were analyzed for flaw detection, length sizing, depth sizing, and signal-to-noise values.

The in-situ crack morphology has a significant impact on the ultrasonic response as illustrated in the side-by-side comparison in Figure 8.35. The image on the left is 2.0 MHz raster data collected on flaw 1110 acquired in the 'looking positive' direction, while the right figure is the complementary 2.0 MHz data 'looking negative'. Comparing the datasets at equal gain settings reveals that the flaw response is more intense when 'looking negative' (98.2%) than 'looking positive' (35.1%). Qualitatively, there is no more or less material noise in either dataset—verified by evaluating the region above the flaw in the D-scan end view. The ultrasonic flaw response is simply lower in amplitude when inspecting from the 'looking positive' side. This reduction in response in the left image requires the addition of more gain to maximize the flaw response to 100% screen height thereby amplifying the material noise as well. Typically, data comparisons and analyses are performed on datasets that have been normalized to set the flaw response at nearly 100% of the screen height amplitude. In doing so, signal responses are all nearly 100% and noise values vary as are seen in later figures such as in Figure 8.36. In this figure the left images from 'looking positive' clearly have more background noise than the 'looking negative' data on the right.

Ultrasonic inspection frequency also played a role in detection and characterization of the in-situ thermal fatigue cracks. Figure 8.36 shows a comprehensive display of raster data collected with a 0 degree beam skew on crack 1110 from both sides of the flaw at three ultrasonic frequencies, 0.8 MHz, 1.5 MHz, and 2.0 MHz (top to bottom). All D-scan end views show the flaw response maximized slightly below saturation (100% screen height) in the image. As is shown in these screen images, the left side data, 'looking positive', required elevated gain settings to maximize the flaw responses. Signal-to-noise ratios for data on flaw 1110 slightly increase with higher frequencies. As an example, for flaw 1110 'looking positive' (left side of figure), the 0.8 MHz data resulted in a SNR of 8.9 dB while the 2.0 MHz data had a SNR of 11.8 dB. The flaw response, however, is less cohesive with increasing frequency. Responses from flaws 1102 in the centrifugally cast pipe and 1100 in the statically cast elbow material, Figures 8.37 and 8.38 respectively, are more variable than flaw 1110.

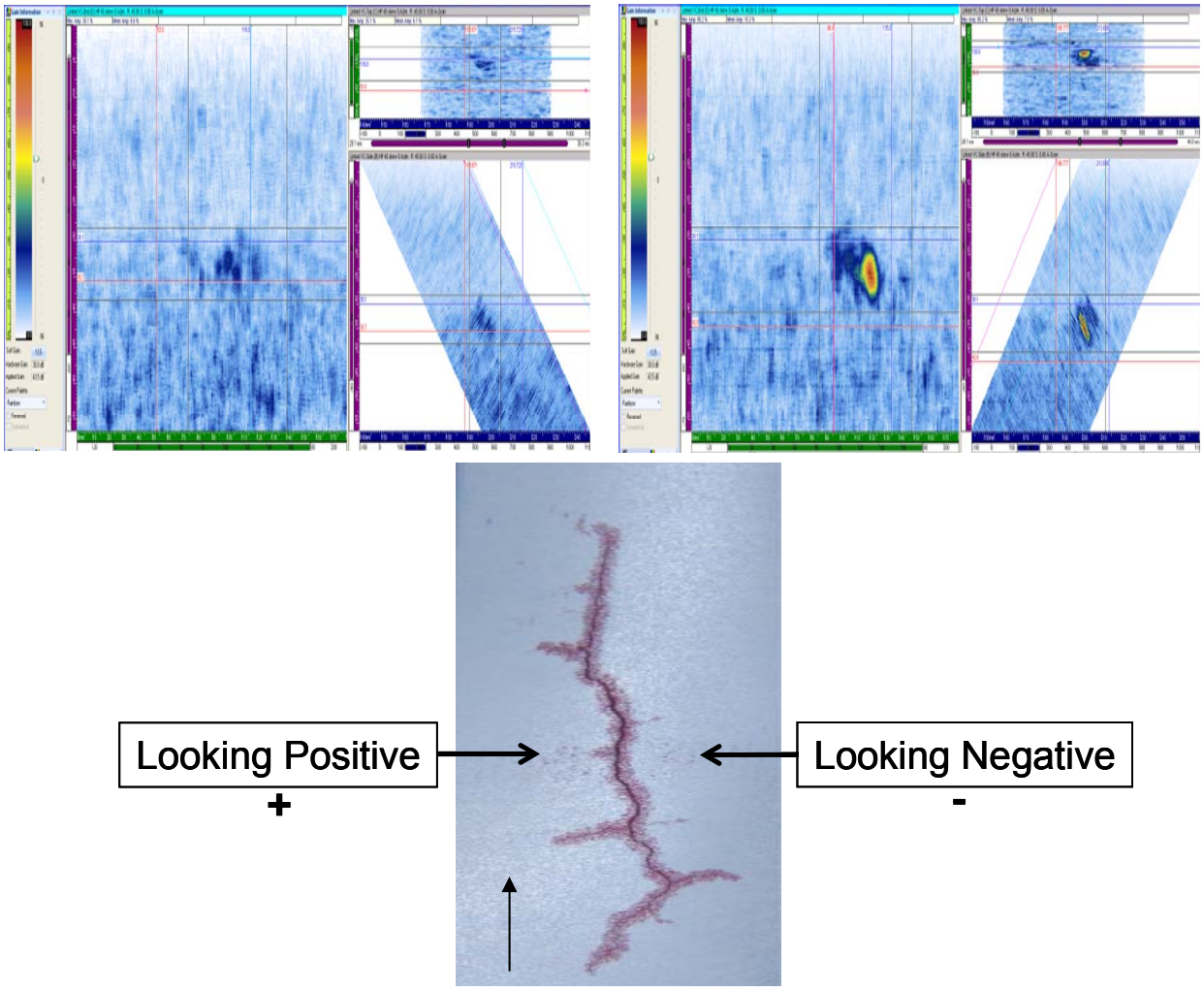

Figure 8.35 2.0 MHz Raster Data Collected from Both Sides of Flaw 1110. Left data were acquired looking positive; right data were acquired looking negative. Below is the ID liquid penetrant image of the crack with the vertical arrow showing the direction of the circumferential axis.

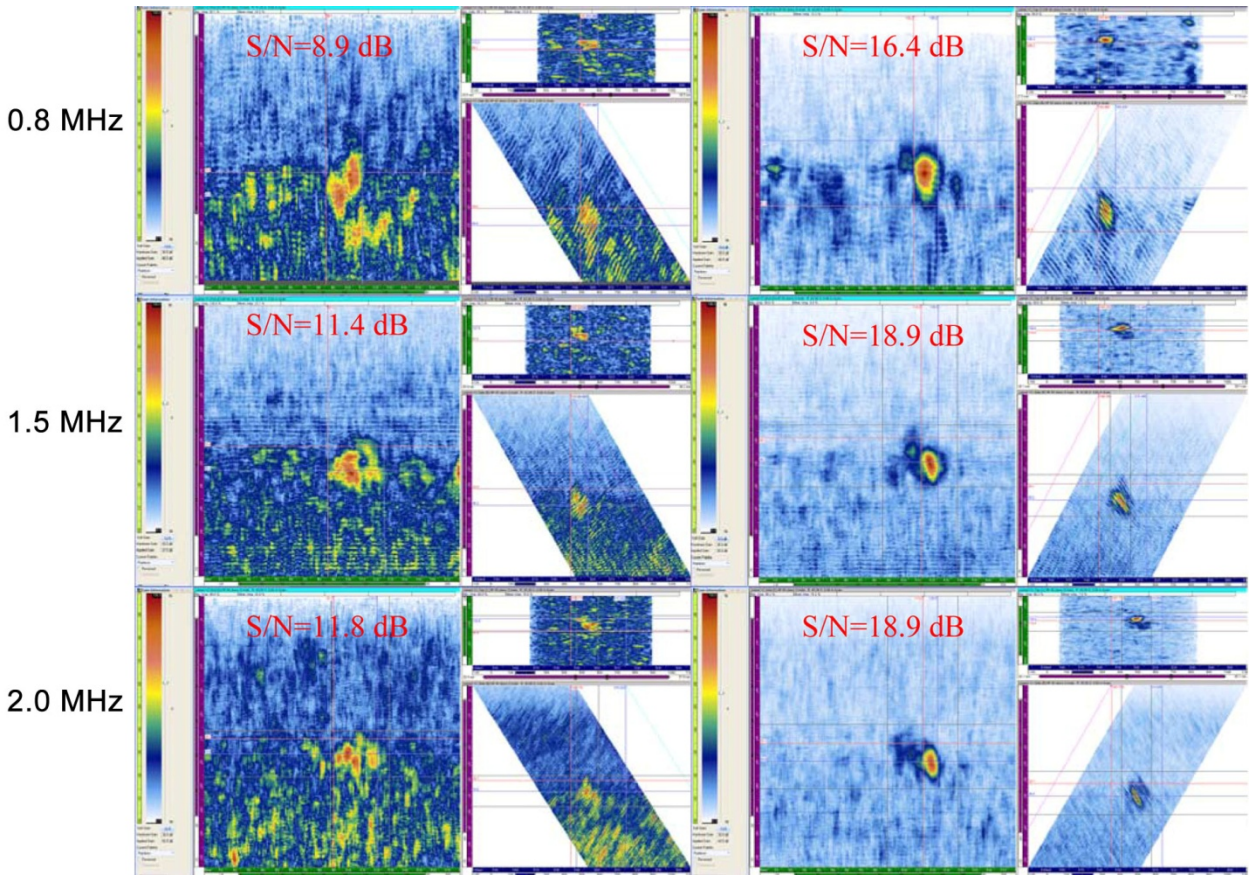

Figure 8.36 Raster Data on Flaw 1110. Left side looking positive; right side looking negative.

Raster data tend to show less error in length sizing from the elbow side over all frequencies as compared to the pipe side. As in the line data, the small 1087 flaw is greatly oversized in the raster scans. The best length sizing on this flaw is seen in the 2.0 MHz data with no skew from the elbow side. Depth sizing attempts were more common on the shallower flaws than in the line data but tended to oversize the flaw leading to a greater depth RMSE. Signal-to-noise ratios were as low as 10.9 dB and as high as 18.9 dB showing generally stronger flaw responses than from the line scan data. This is reasonable as the flaw is more completely insonified by the nature of raster scanning and therefore better captures the optimum flaw response.

In summary, raster and line data over three probe frequencies, with and without probe skew and obtained from both sides of a flaw, show that these in-situ grown flaws were readily detected and accurately sized within ASME Code sizing criteria/guidelines. One inspection scenario does not prove to be the best for all flaws. Some of the flaws show a much stronger response from one side over the other while others do not. Skewing helps occasionally. The lowest frequency is not always the best. The multifaceted nature of the flaws complicates the flaw response. All of these observations indicate that flaws, as represented by in-situ grown thermal fatigue cracks, can be effectively detected and accurately sized in this material with the given phased array ultrasonic technology. These observations also show that by obtaining multiple views of a flaw, the ability to characterize is enhanced.

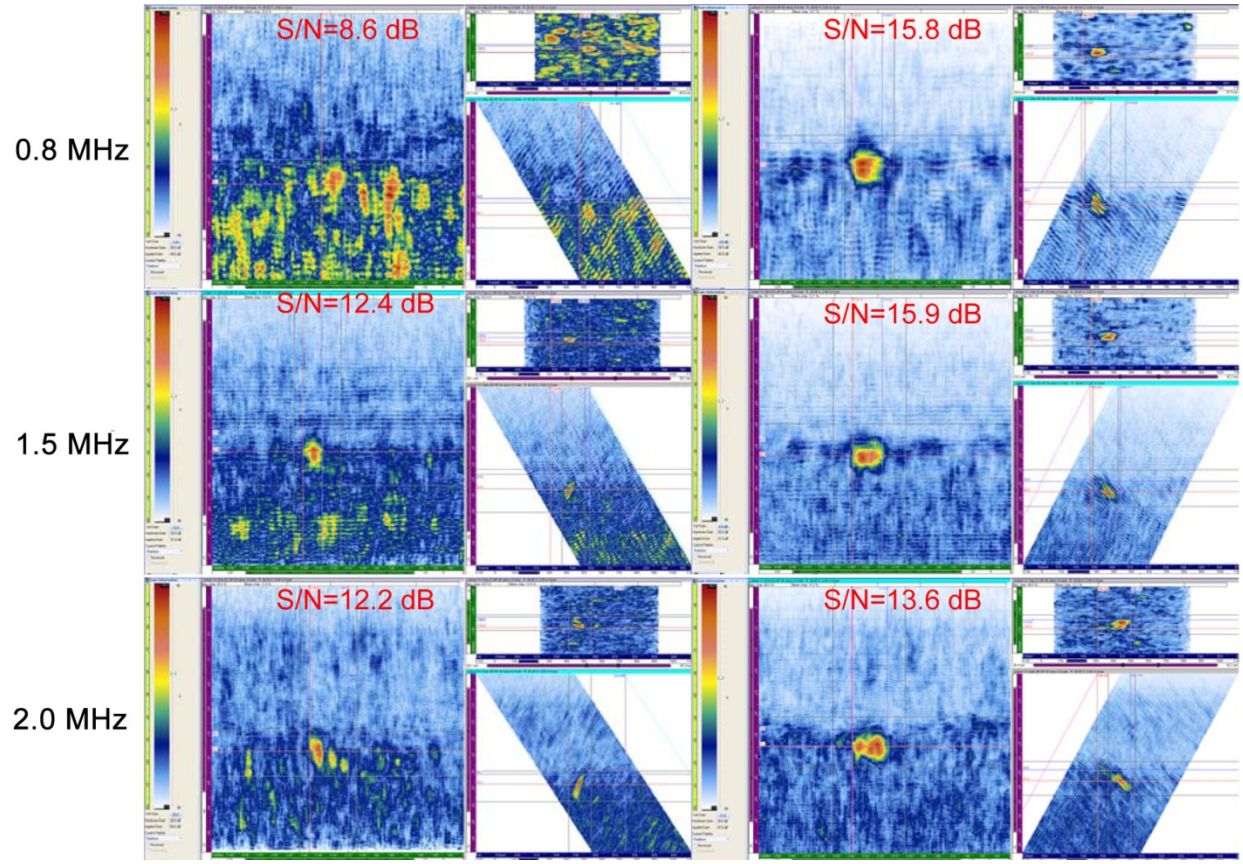

Figure 8.37 Raster Data on Flaw 1102. Left side looking positive; right side looking negative.

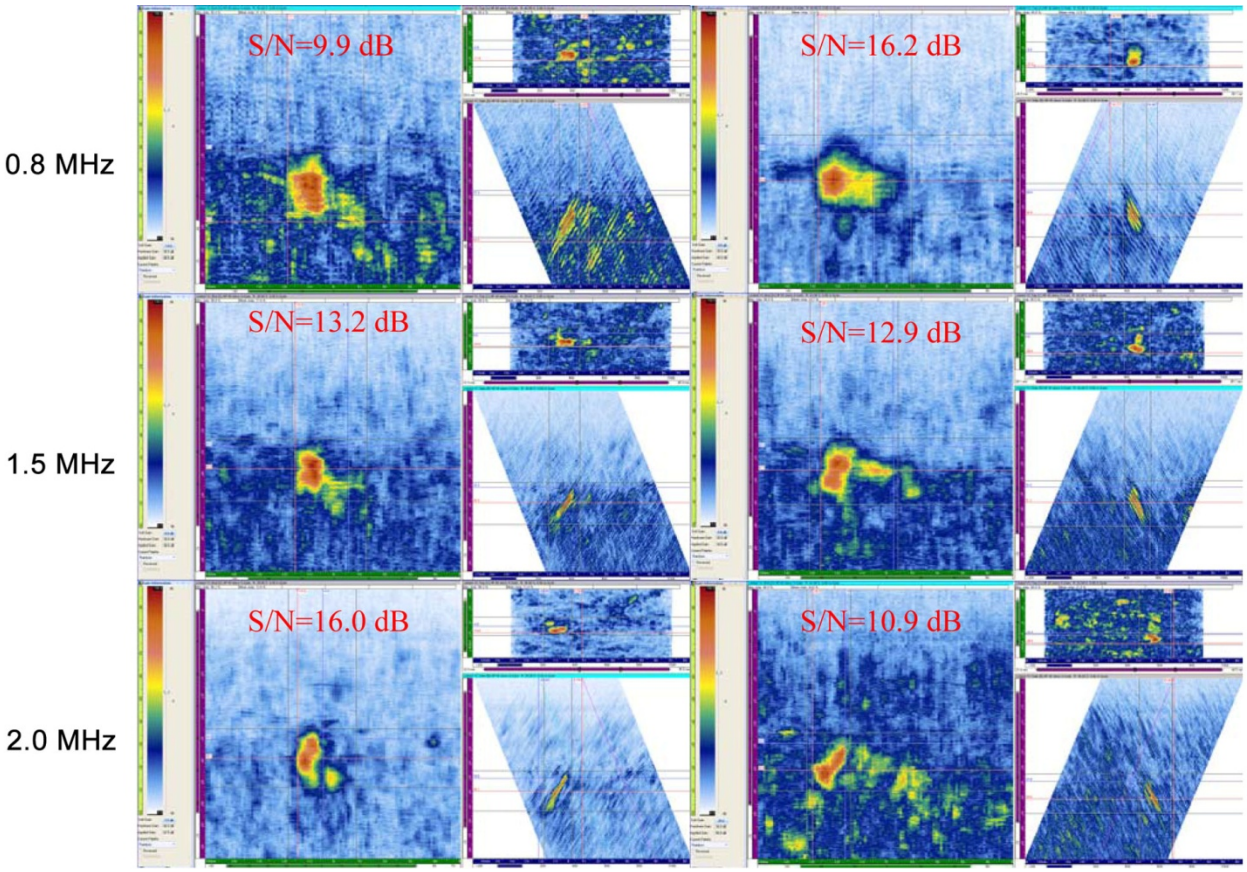

Figure 8.38 Raster Data on Flaw 1100. Left side looking positive; right side looking negative.

In addition to the 0-degree beam skew (axial or perpendicular to flaw) line and raster data collected from both sides of each flaw, +10 and −10 degree skewed beam data were also acquired at each frequency. Figure 8.39 shows the ID liquid penetrant image for flaw 1110 with arrows indicating the beam skew directions. Figure 8.40 shows 1.5 MHz raster data acquired on flaw 1110 at 0 and ±10 degrees. It is observed that with a slight beam skew in either direction, left side 'looking positive' and right side 'looking negative', the resultant signal response can be affected. Thus, detection and characterization of the flaws may be influenced by the beam skew. In the data below, it is observed that the +10 degree skew decreased the SNR by approximately 3 dB from the 0 and −10 degree skew scans when inspecting in the 'looking positive' direction. However, from the looking negative side, the −10 degree skew decreases the SNR by 2 dB. In general the in-situ grown crack responses may be improved with skew but are not consistently improved with skew.

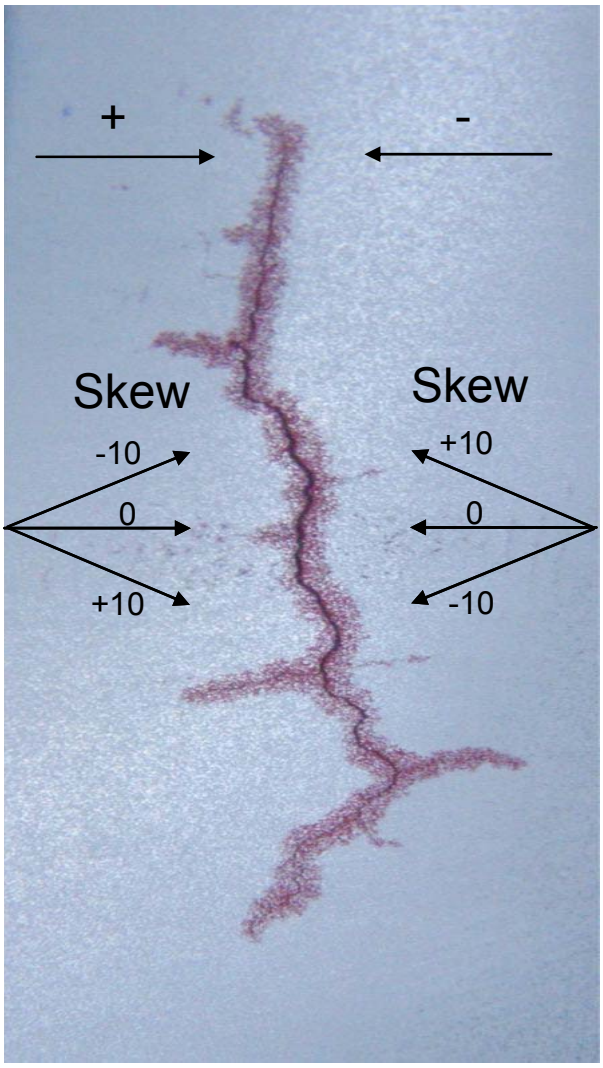

Figure 8.39 ID Penetrant Image of Flaw 1110 Using Arrows to Show the Beam Skew Directions (angles are not drawn to scale)

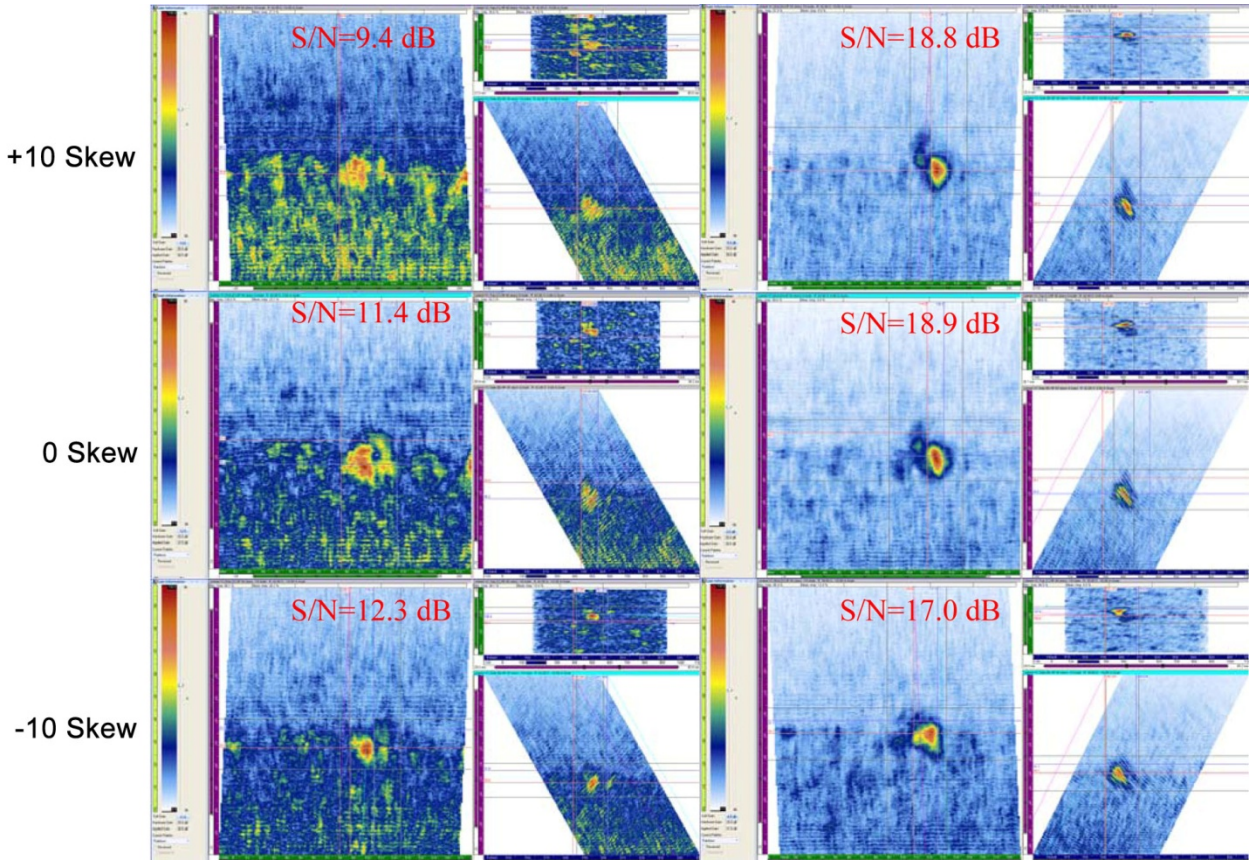

Figure 8.40 1.5 MHz Raster Data on Flaw 1110. Left side looking positive; right side looking negative.

All images for both line and raster data are displayed in Appendix E. A summary of the length and depth sizing results as well as calculated signal-to-noise ratios are presented in Table 8.12 for the line scan data and in Table 8.13 for the raster data. The table groups the data acquired from the pipe side of the flaw (looking positive) on the left, as a function of frequency, while on the right side the data from the elbow side of the flaw (looking negative) are presented. A dash entry in the table corresponds to a no detection condition. In general, line scan data were volumetrically merged for length sizing and not for depth sizing. The RMSE for length and depth are displayed at the bottom of each table. For all data (all sides, frequencies, and skews), the RMSEs for both length and depth fall within the ASME Code allowable limits of 19.1 mm (0.75 in.) for length and 3.18 mm (0.125 in.) for depth.

In the line scan data, length values tend to show less error from the pipe side and depth values are more comparable from either side. All data greatly over size the small, 8.4 mm (0.33 in.) long flaw, 1087. Depth sizing of the shallow 3.4 mm (0.13 in.) deep flaws 1100, 1102, and 1087 are challenging as no upper portion of the flaw or tip signal was discernable or separable from the corner response in the majority of the data. Finally, signal-to-noise ratios ranged as low as 6.5 dB and as high as 17.4 dB.

Table 8.12 PNNL Line Data Characterization Summary on In-situ Grown Cracks

	Flaw	True State	Pipe Side (looking positive)									Elbow Side (looking negative)								
			800 kHz			1.5 MHz			2.0 MHz			800 kHz			1.5 MHz			2.0 MHz		
			skew +10	skew 0	skew −10	skew +10	skew 0	skew −10	skew +10	skew 0	skew −10	skew +10	skew 0	skew −10	skew +10	skew 0	skew −10	skew +10	skew 0	skew −10
1100	Length (mm)	18.6	16.1	14.5	16.5	24.9	16.9	15.3	20.1	18.1	18.5	39.4	26.1	13.3	16.1	16.5	17.3	40.2	19.3	18.5
	Depth (mm)	3.4	-	-	-	-	-	-	-	-	-	-	-	-	-	4.6	2.9	3.8	-	3.5
	SNR		12.8	13.0	13.9	13.8	15.5	17.4	12.9	13.0	14.8	11.1	11.6	12.2	12.3	11.5	11.5	12.2	11.7	11.2
1102	Length (mm)	19.3	13.7	12.9	22.5	18.1	17.7	10.9	15.7	33.0	37.0	22.5	20.5	20.5	26.9	24.1	30.6	22.9	21.3	23.3
	Depth (mm)	3.4	-	7.0	-	-	-	-	-	3.5	-	-	-	-	-	3.8	-	3.6	2.5	3.0
	SNR		6.5	8.3	7.4	8.8	9.4	8.2	8.6	10.7	10.2	13.4	14.7	15.6	15.0	17.2	17.7	16.3	15.9	16.1
1110	Length (mm)	25.3	30.6	33.8	28.5	31.8	30.6	17.3	27.7	14.1	22.5	39.8	40.6	39.0	25.3	16.1	20.5	16.1	15.3	28.9
	Depth (mm)	6.0	6.7	6.1	7.7	4.6	7.5	4.7	5.4	5.1	7.8	5.7	3.4	3.8	7.7	5.9	2.9	4.0	5.7	5.3
	SNR		7.3	7.8	8.3	7.7	8.8	10.3	9.7	9.4	9.3	14.3	14.2	12.9	16.0	15.2	15.7	16.5	15.6	12.7
1087	Length (mm)	8.4	19.3	22.5	25.7	27.7	21.3	22.5	16.9	18.5	13.3	23.3	20.5	24.9	26.5	22.5	20.9	20.9	13.1	13.3
	Depth (mm)	3.4	3.9	4.0	-	2.5	4.2	3.4	2.4	2.3	3.3	3.7	-	-	3.3	3.2	2.6	3.6	2.2	-
	SNR		10.5	11.6	11.5	11.9	12.8	14.4	11.1	9.9	10.6	11.9	13.6	12.0	12.4	12.0	16.0	12.6	11.5	10.6
1089	Length (mm)	21.8	28.5	28.9	29.3	21.7	26.9	16.9	21.3	16.9	13.7	21.3	19.3	18.9	24.9	24.1	21.3	23.7	22.5	20.1
	Depth (mm)	6.0	6.4	5.7	-	5.0	-	-	4.5	6.2	5.4	6.4	-	-	6.3	6.5	-	5.0	5.2	5.1
	SNR		12.4	13.8	15.5	11.8	13.6	10.6	13.5	12.1	8.1	12.7	14.7	14.6	10.6	12.7	15.0	10.3	11.6	13.1
RMSE (Length)			**6.8**	**8.7**	**8.7**	**9.6**	**6.7**	**8.6**	**4.3**	**9.4**	**9.1**	**13.2**	**9.4**	**10.0**	**9.0**	**8.0**	**7.8**	**12.0**	**5.1**	**3.3**
RMSE (Depth)			**0.5**	**1.8**	**1.7**	**1.1**	**1.2**	**0.9**	**1.1**	**0.7**	**1.1**	**0.3**	**2.6**	**2.2**	**1.0**	**0.6**	**1.9**	**1.0**	**0.9**	**0.6**

Table 8.13 PNNL Raster Data Characterization Summary on In-situ Grown Cracks

	Flaw	True State	Pipe Side (looking positive)									Elbow Side (looking negative)								
			800 kHz			1.5 MHz			2.0 MHz			800 kHz			1.5 MHz			2.0 MHz		
			skew +10	skew 0	skew −10	skew +10	skew 0	skew −10	skew +10	skew 0	skew −10	skew +10	skew 0	skew −10	skew +10	skew 0	skew −10	skew +10	skew 0	skew −10
1100	Length (mm)	18.6	15.3	16.9	20.9	21.7	23.3	24.9	10.5	11.3	-	29.7	26.6	29.0	28.9	25.7	19.3	24.1	28.1	16.1
	Depth (mm)	3.4	5.1	5.8	4.9	4.6	-	4.8	7.4	-	-	6.7	6.7	7.5	6.0	4.5	7.1	-	-	2.5
	SNR		12.3	9.9	13.0	13.7	13.2	11.9	15.6	16.0	-	15.5	16.2	13.6	12.4	12.9	12.2	13.2	10.9	12.8
1102	Length (mm)	19.3	-	17.8	24.9	20.1	15.3	18.5	15.3	25.7	24.9	29.0	24.2	20.9	24.9	20.1	15.3	23.3	24.1	28.9
	Depth (mm)	3.4	-	4.9	4.6	-	-	-	-	-	-	-	-	4.7	-	3.4	5.3	-	-	-
	SNR		-	8.6	9.3	10.6	12.4	11.4	11.7	12.2	13.7	15.8	15.8	15.4	15.7	15.9	16.1	15.4	13.6	14.1
1110	Length (mm)	25.3	29.8	24.2	23.4	25.7	36.2	16.9	28.1	30.6	25.7	26.5	26.5	17.7	23.3	23.3	20.9	20.9	27.3	16.9
	Depth (mm)	6.0	6.7	4.6	6.8	5.5	5.3	4.0	5.7	3.3	5.2	3.9	-	-	4.9	5.1	5.5	-	-	-
	SNR		10.2	8.9	9.1	9.4	11.4	12.3	11.2	11.8	12.4	15.8	16.4	13.2	18.8	18.9	17.0	19.9	18.9	16.2
1087	Length (mm)	8.4	28.9	24.1	21.7	33.0	19.3	15.3	15.3	23.3	20.9	20.2	24.9	23.3	22.5	20.9	16.9	20.1	12.1	20.1
	Depth (mm)	3.4	3.9	3.5	4.4	6.0	3.8	4.1	3.7	-	3.6	3.8	3.3	4.4	4.8	3.4	4.4	-	-	4.3
	SNR		9.4	13.4	11.7	8.7	11.7	13.2	10.1	11.2	10.1	12.0	12.6	13.4	11.3	12.5	11.6	13.7	13.0	10.5
1089	Length (mm)	21.8	28.9	30.6	32.0	16.9	24.9	19.3	20.8	21.7	18.5	21.7	19.3	17.7	25.7	20.1	18.5	21.7	18.5	16.1
	Depth (mm)	6.0	6.1	5.9	6.2	-	6.5	3.9	4.1	-	-	6.2	4.7	4.8	6.0	6.3	4.5	3.6	-	4.0
	SNR		16.5	14.1	13.4	11.5	14.1	13.3	14.0	13.5	9.3	12.9	15.1	14.8	13.9	13.9	14.7	12.8	12.1	13.1
RMSE (Length)			**11.2**	**8.1**	**8.0**	**11.3**	**7.6**	**5.7**	**5.3**	**8.3**	**7.1**	**8.5**	**8.6**	**9.0**	**8.5**	**6.6**	**4.9**	**6.4**	**5.3**	**8.2**
RMSE (Depth)			**1.0**	**1.4**	**1.0**	**1.7**	**0.5**	**1.6**	**2.2**	**2.7**	**0.6**	**2.0**	**2.0**	**2.3**	**1.6**	**0.6**	**2.0**	**2.4**	**-**	**1.4**

8.5 ISI Supplier Phased-Array Data on In-situ Grown Flaws

The ISI supplier, LMT, Inc., additionally evaluated the two Trueflaw in-situ grown cracks in the centrifugally cast pipe side base material of specimen 9C-002. They did not examine the statically cast elbow flaw as the specimen curvature precluded good probe contact, in large part due to the length dimension of their PA probe. The two flaws were evaluated with the same procedure as was used for the implanted flaws. Resultant length, depth, and signal-to-noise ratio values are listed in Table 8.14. For reference, true state length values are estimated at 19.3 and 25.3 mm (0.76 and 1.0 in.) and depth values are 3.4 and 6.0 mm (0.13 and 0.24 in.), respectively. The flaws were inspected from both sides but were only detected from one side, the side closest to the weld/elbow. The D-scan end view of the 1110 flaw is displayed in Figure 8.41. All other data images from the in-situ grown flaws are displayed in Appendix F.

Table 8.14 ISI Supplier LMT Sizing Results on In-situ Grown Flaws

Base Metal Flaw	Length (mm/in.)	Depth (mm/in.)	SNR (dB)
1102	21.2 / 0.84	4.0 / 0.16	13.2
1110	34.2 / 1.35	7.9 / 0.31	11.0

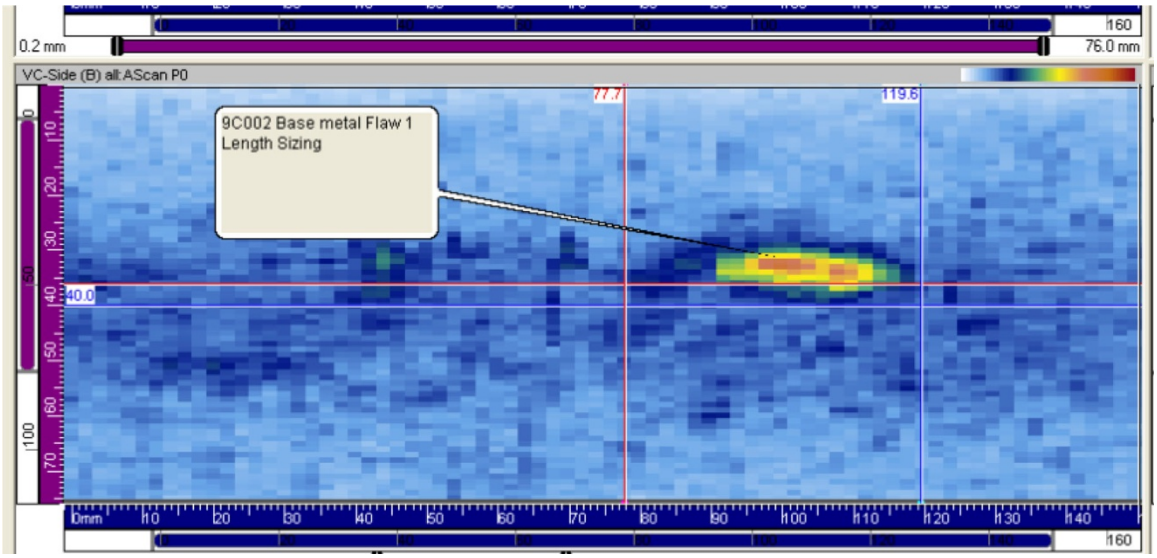

Figure 8.41 ISI Supplier LMT D-scan End View Image of Flaw 1110

8.6 Comparison of In-situ Grown Flaw Data

As previously reported, PNNL detected all five of the in-situ grown flaws from both sides of the flaw. The ISI supplier, LMT Inc., evaluated only two of these flaws and was able to detect the flaws from only one side. Figure 8.42 displays a comparison of the 1102 flaw data at 1.5 MHz.

The reported flaw length is 19.3 mm (0.76 in.); PNNL sized the flaw at 20.0 mm (0.79 in.) and LMT sized it at 21.2 mm (0.84 in.) from the elbow side evaluation. The reported depth is 3.4 mm (0.13 in.) and PNNL and LMT sized it at 3.4 mm (0.13 in.) and 4.0 mm (0.16 in.), respectively. Signal-to-noise ratios were 15.9 dB and 13.2 dB for PNNL and LMT, respectively. These data are quite comparable.

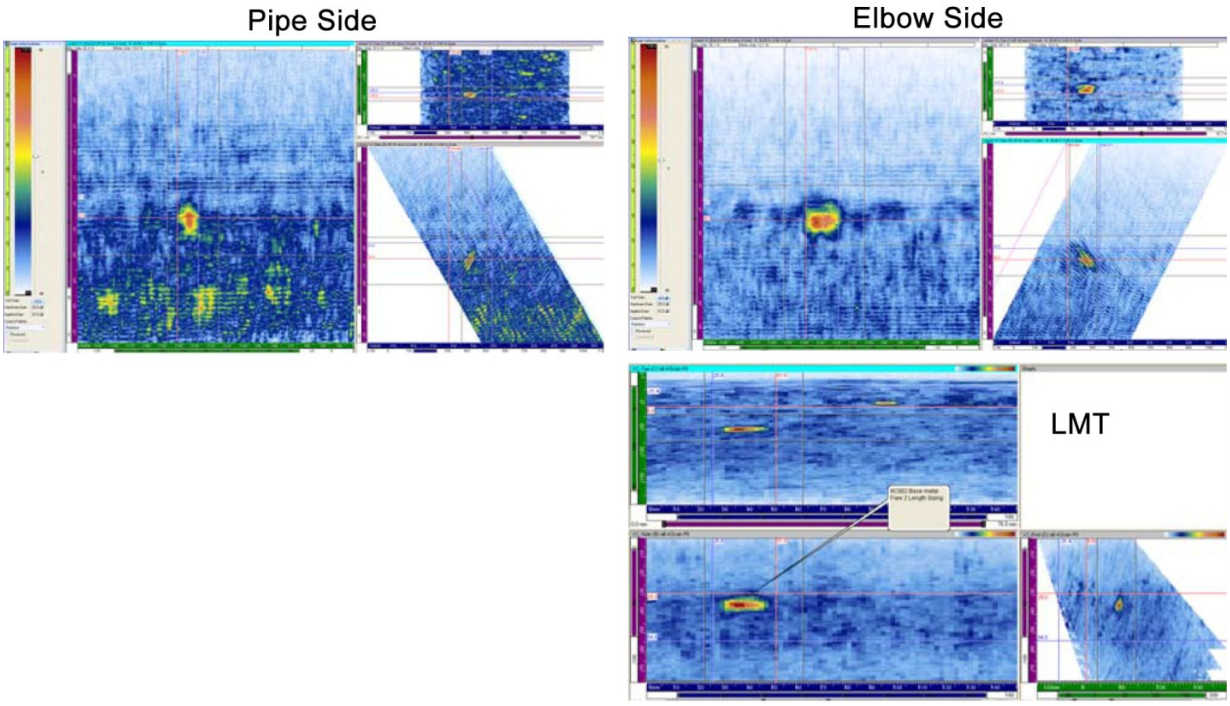

Figure 8.42 Flaw 1102 as Observed by PNNL (top two images) and LMT (bottom)

The data images for flaw 1110 are displayed in Figure 8.43. This flaw has a reported length of 25.3 mm (1.00 in.) and was sized at 23.3 mm (0.92 in.) and 34.2 mm (1.35 in.) by PNNL and LMT, respectively. A true state depth of 6.0 mm (0.24 in.) was reported with measurements of 5.1 mm (0.20 in.) and 7.9 mm (0.31 in.), and signal-to-noise values of 18.9 and 11 dB from PNNL and LMT, respectively. While flaw sizing was slightly different, the flaw is clearly detected and SNR values are good for both data sets. Additionally, true state depth values provided here are estimated based on the in-situ growth method.

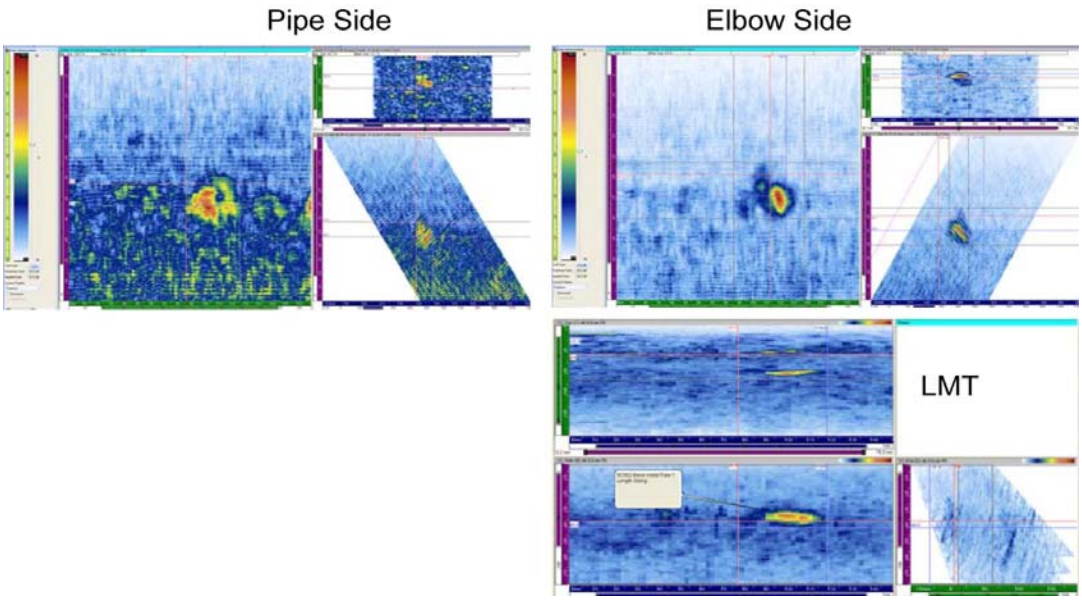

Figure 8.43 Flaw 1110 as Observed by PNNL (top two images) and LMT (bottom)

8.7 PNNL Comparison of Implanted and In-situ Grown Flaw Responses

An initial comparison was made based on the SNR values of the implanted and in-situ grown flaws, as a function of the inspection side of each flaw. Other considerations were additionally taken into account such as probe frequency and flaw size.

The implanted TFCs were placed in the center of the weld for all flaws except flaw 2 in specimen 7C059. This flaw was implanted in the HAZ on the pipe side of the weld. Approximately half of the flaws were tilted towards the pipe side, providing the potential for a favorable reflection plane to the elbow side evaluation. Flaw "tilt" was not a requested specification for any implanted flaws in these specimens. Any tilting of the flaws was a result of the fabrication/implantation process. On the other hand, the micrographs show larger grains in the elbow material and coupling is decreased from the elbow side due to the curved OD surface. These two effects could lead to decreased flaw response as compared to the responses observed from the pipe side of the weld. However, as depicted in Figure 8.44, signal-to-noise ratio values for all probe frequencies employed show no observable trend in flaw responses obtained from the CCSS pipe side as compared to the SCSS elbow side. The SNR range (upper and lower values) for the CCSS side examinations is 13.7 to 21.1 dB and for the SCSS side, 9.5 to 24.6 dB. Only SCSS side data are found below 13 dB. Most of the data fall into the 13 to 22 dB range, where it can be easily seen that CCSS responses are coincidental with SCSS responses. Further, the average CCSS SNR of 17.2 dB is quite similar to the SCSS SNR of 16.7 dB. These data show that implanted TFCs in the welds do not present a preferential inspection side in these CASS specimens regardless of base material grain size and flaw tilt variations.

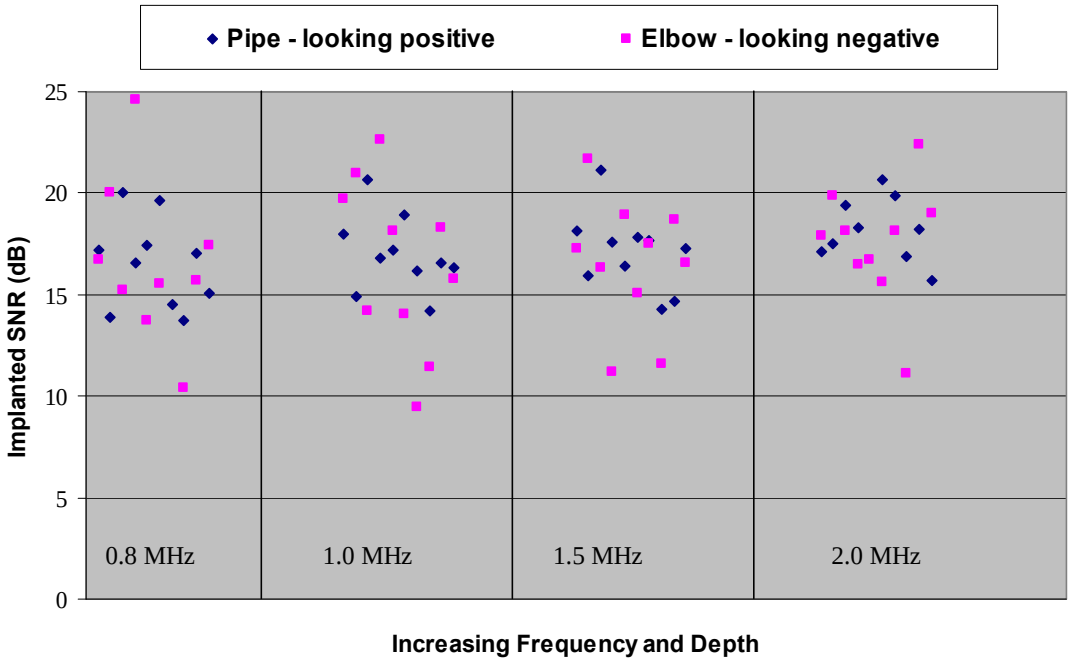

Figure 8.44 SNR Values for All Implanted TFCs at Four Frequencies

SNR values from raster data for the in-situ grown TFCs are displayed in Figure 8.45 for the three probe frequencies. This data was presented earlier as Table 8.13 (where two flaws were not detected at skewed angles). Within a frequency band the data are arranged by increasing depth, which also corresponds to increasing length for these flaws. The validation flaws 1087 and 1089 as well as flaws 1102 and 1110 were grown in CCSS pipe material while flaw 1100 was grown in SCSS elbow material. The SNR values for flaw 1100 do not appear to be significantly different than the values for the pipe material flaws. Thus, these data show no difference in SNR values as they relate to the base material.

Data from flaws 1102 and 1110 show greater SNR values when observed from the negative side for all three frequencies. This was also previously seen in Figures 8.36 and 8.37. Side-to-side SNR values for flaws 1087 and 1089 overlap at each frequency and flaw 1100 shows variable results. Since the side-to-side flaw response differences for flaws 1102 and 1110 are unlikely due to base material grain size differences, it is reasonable to assume that the significant flaw response variations are due to crack morphology. The morphological flaw variations are shown in a summary of in-situ grown flaw parameters in Table 8.15.

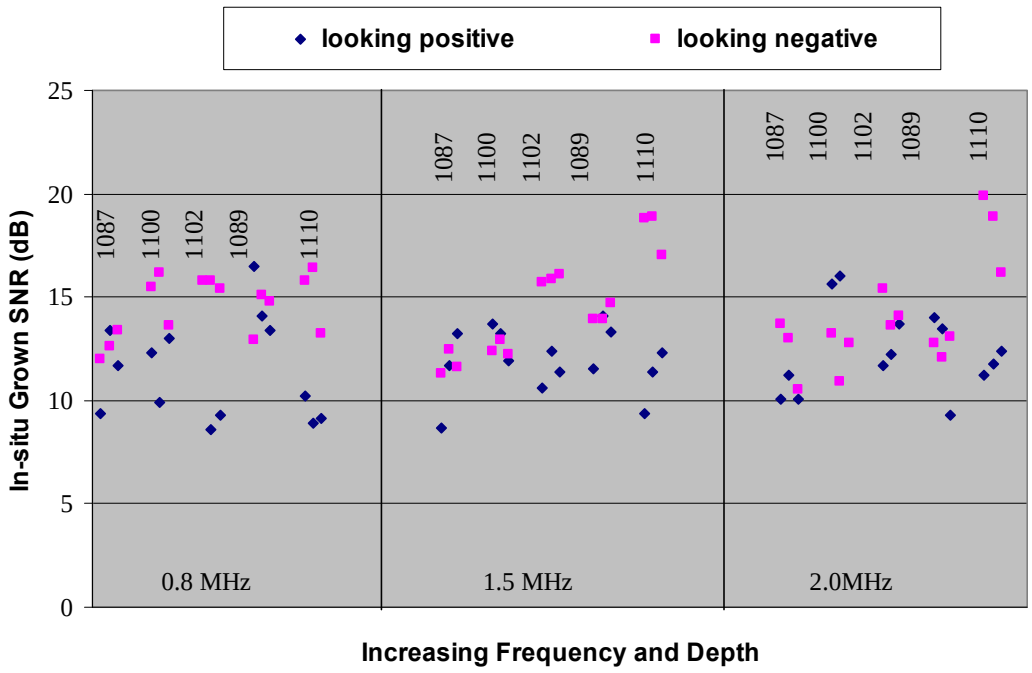

Figure 8.45 SNR Values for All In-situ Grown TFCs at Three Frequencies and Three Skews

Table 8.15 In-situ Grown Crack Parameters[a]

Flaw	Length (mm)	Depth (mm)	Avg. COD[b] (μm)	Median COD[b] (μm)	Skew (deg.)	Turns	Branching	Discontinuities
1087	8.4	3.4	48.3	36.8	90	5	4	0
1089	21.8	6.0	51.7	49.7	85	6	5	0
1100	18.6	3.4	39.3	32.4	90	15	5	0
1102	19.3	3.4	39.9	37.8	86	6	3	1
1110	25.3	6.0	55.0	48.2	85	15	4	0

(a) COD – crack opening dimension
(b) For comparison implanted flaw maximum COD is approximately 51 μm (0.002 in.)

The in-situ grown flaws 1102 and 1110 in the CCSS pipe material of specimen 9C-002 follow the same trends in that the looking negative side SNR is greater than the looking positive side SNR over all three frequencies. These two flaws are skewed by 4 and 5 degrees, respectively, relative to the circumferential axis orientation. In contrast, the flaw grown in the elbow material, flaw 1100, is not skewed. The two pipe material flaws (1102 and 1110) also have the strongest flaw response when viewed from the more concave side of the flaw (refer back to Figures 7.12 and 7.13).

In-situ grown flaw number 1100 was placed in the elbow material, and does not have a consistently stronger response from one side or the other over all three frequencies employed. At 0.8 MHz, the looking-negative side is stronger than the looking-positive side. At 2.0 MHz, the looking-positive side response is equal or stronger than the looking-negative side, and at 1.5 MHz, the response is approximately equal from either side. This flaw is similar in length and depth to pipe flaw 1102, which does have a preferential inspection side over all three probe frequencies. Both flaws, 1100 and 1102, are similar in that they exhibit a number of turns and branching. Two possible significant differences between the elbow 1100 flaw and the pipe 1102 and 1110 flaws are in skew and the amount of curvature. The 1100 elbow flaw, which again does not have a preferential inspection side, has a 90 degree skew that places it parallel to the pipe circumference. Additionally, it is more planar than the two pipe flaws (1102 and 1110) that show inspection side preference. One would expect a more equal response from either side of a non-skewed flaw that is more planar in morphology.

As discussed, ultrasonic responses from the implanted TFCs differ with those of the in-situ grown TFCs. Some of the in-situ grown flaws show a favorable inspection side while implanted flaws display similar responses from either side. Another difference between implanted and in-situ grown flaws was noted in overall SNR levels, with an average SNR of 17.0 dB for the implanted and 12.9 dB for in-situ grown flaws. This implies that implanted TFCs are nominally 4 dB brighter than the in-situ grown flaws. However, the flaw sizes must also be taken into account. The in-situ grown flaws were much smaller in comparison to the implanted flaws. Flaw lengths for the in-situ grown cracks ranged from 8.4 to 25.3 mm (0.33 to 1.00 in.) and for the implanted cracks 50.5 to 101.3 mm (1.99 to 3.99 in.). Depths of the flaws ranged from 3.4 to 6 mm (0.13 to 0.24 in.) for the in-situ grown and from 4.8 to 15.6 mm (0.19 to 0.61 in.) for the implanted flaws. Therefore, the theoretical reflecting surface, which should account for an overall specular response, is much smaller in the in-situ grown flaws. Furthermore, a rough estimate on the reflective surface areas from the three smallest in-situ grown flaws is less than the probe focal area size (at the −6 dB level for all three probe frequencies). This would lead to a smaller flaw response and hence a lower SNR value for these small flaw.

In summary, the implanted flaws are larger, not skewed, and possibly more planar than the in-situ grown flaws. As such, these flaws exhibit a similar response based on SNR values from either inspection side and have SNR values greater than the values for the small in-situ grown flaws. The smaller in-situ grown flaws have reflective areas less than the probe spot size (for all three probes) and produce smaller SNRs but ones that increase with increasing flaw size. Some of the in-situ grown flaws exhibit a preferential inspection side, which is attributed to crack morphology. Because the flaw size regimes effectively do not overlap between the implanted and in-situ grown flaws, a direct comparison cannot be made of the flaw responses. However, it is likely that the differences in flaw morphology are producing the noted effects in SNR values.

9 DISCUSSION AND CONCLUSIONS

A technical evaluation of the phased-array ultrasonic inspection method was conducted to evaluate detection and sizing performance for inspection of small bore, CASS piping components. A set of ten thermal fatigue cracks was implanted into three CASS PZR surge-line specimens that were salvaged from cancelled plants, thus representing weld fabrication methods on vintage CASS materials. Additionally, three in-situ grown cracks were placed in the base material of pipe specimen 9C-002, and two, in-situ grown validation flaws were developed in a representative test pipe specimen. PA-UT flaw responses from these cracks were used to evaluate detection and characterization performance. This effort included technical assessments and confirmatory research that addressed:

- The use of microstructure knowledge (dimensional analysis, grain orientation, and grain type) and sound-field modeling to more effectively modify inspection parameters and enhance the inspection outcomes;
- The use of PA-UT methods and advanced probe design/modeling to enhance detection and characterization of circumferentially oriented flaws in CASS PZR surge line piping specimens;
- An analysis of flaw localization capability and performance for all probes on all flaws characterized in this study;
- An analysis of flaw detection, length sizing, depth sizing, and signal-to-noise ratio for all flaws in all specimens, as a function of various inspection parameters;
- A confirmatory examination using an ASME Code, Appendix VIII-qualified ISI supplier; and
- An analysis of the baseline CASS material noise/attenuation and the potential impact on flaw detection as correlated to the specimens studied here.

The CASS PZR surge-line specimens used in this study were polished and chemically etched to bring out the microstructures of both pipe and elbow segments. This work included an evaluation of the grain structures to better understand the microstructural variability and range of grain sizes that were prevalent in the PZR surge-line components being evaluated. Because the analysis was conducted on CCSS parent material approximately 305 mm (12 in.) from the welds, some level of microstructural variability is expected; these data were used for acquiring a general understanding of grain orientation, type, and size, and it was assumed that overall microstructural differences were minimal between the areas mapped and those adjacent to the weld. Dimensional analyses were conducted, and results provided insights into the inspection wavelength-to-grain diameter ratios. Grain diameters ranged from very small 0.5 mm (0.02 in.) to very large 41.0 mm (1.61 in.). From the initial analysis, it was anticipated that the average grain diameters and overall microstructural variability of these segments would provide a more challenging inspection scenario; however, this was not the case.

The anticipated inspection challenges (based upon work conducted on thicker CASS reactor coolant loop piping) drove the efforts to develop more effective PA probes for application to smaller bore, relatively thin-walled, coarse-grained component inspections. Effective probe matrix design evolved as previous work shed light on inspection issues and critical aspects of probe performance in CASS materials. This evolution was important to the efforts reported here. Key elements included fabricating probes with minimal footprints, higher bandwidths, and improved beam steering and lateral skewing capabilities. The 800-kHz probe was designed to provide a more optimal wavelength to allow the ultrasound to penetrate the large grain structure of CASS and yet maintain suitable resolution allowing the probe to resolve smaller flaws. The 1.5-MHz probe employed in this study was originally designed for far-side examinations of austenitic welds in WSS piping, but performed quite well on these coarse-grained specimens. Finally, both the 1.0-MHz and 2.0-MHz PA probes were originally designed for evaluating inspection effectiveness of PA methods on components with inlays, onlays, and overlays; however, these probes also performed quite well with regard to detection and flaw characterization in these materials.

A baseline CASS material noise analysis was also conducted. Full circumferential PA scans were acquired at 800 kHz and 1.5 MHz on the CCSS pipe ends of the three surge-line specimens to assess baseline material noise and attenuative signal loss. In all specimens, the higher frequency resulted in more signal dropout, as anticipated. The higher frequency (1.5 MHz) is more sensitive to attenuation and beam redirection as the wavelength, relative to the average grain diameters found in these specimens, is much smaller. The median length of the diminished signal was suggested as an indication of flaw length that could go undetected due to a loss of signal effect from the coarse-material microstructure. With this assumption, the data show that a flaw less than 14.6 mm (0.57 in.) could go undetected in this material as a worst-case scenario. This represents only 1.4% of the circumference and suggests that a flaw with any significant length would be readily detected. The results showed that the lower frequency (800 kHz) was much more effective and consistent at detecting the corner response in all three specimens.

The detection and sizing data showed that all implanted ID surface-breaking thermal fatigue cracks in these specimens were easily detected from both the CCSS (pipe) and the SCSS (elbow) sides of the welds at 800 kHz, 1.0 MHz, 1.5 MHz, and 2.0 MHz. Data at 800 kHz were not collected on one of the cracks from the SCSS elbow side because of geometrical constraints that precluded effective coupling of the PA probe. The results reported here show that longitudinal mode, transmit-receive matrix arrays over the frequency range investigated, can provide effective sound fields for detection and characterization of implanted TFCs in CASS PZR surge-line components. While the flaw depths of the TFCs employed in this study ranged from approximately 10% to 50% through-wall depth, the majority of the cracks reported here were in the range of 20% to 30%, or approximately 6.4 mm (0.25 in.) to 10.2 mm (0.4 in.) deep for the implanted flaws. These flaws were from approximately 50 mm (2.0 in.) to 150 mm (6.0 in.) in length, with the majority of the flaws in the 50 mm (2.0 in.) to 75 mm (3.0 in.) range. All but one flaw were positioned in the weld. PA-UT results were compared against true-state data for all flaws, and RMSE was computed as a metric for both length-sizing and depth-sizing capabilities. Also, signal-to-noise measurements were made and SNR values were computed and documented for all flaws and scanning scenarios.

Additionally, the detection and sizing data showed that all Trueflaw in-situ grown ID surface-connected thermal fatigue cracks in the base material were detected from both sides of the crack at 800 kHz, 1.5 MHz, and 2.0 MHz. These cracks tend to exhibit more complex crack morphology, similar to service-induced cracks, which can influence detection and characterization. They were also generally smaller in overall dimensions, with through-wall depths in the approximate 10–24% range (3.4 to 6 mm or 0.13 to 0.24 in.) and lengths of 8 to 25 mm (0.31 to 0.98 in.), and generally produced lower SNRs when compared to the implanted flaws. It was observed that some of the in-situ grown flaws had a preferential inspection side. This finding is likely based on crack morphology, not material microstructure. Two parameters, flaw skew and curvature, were observed and could also suggest a reason for the enhanced flaw response from a particular side. Again, the results reported here show that longitudinal mode, transmit-receive matrix arrays over the frequency range investigated, can provide effective sound fields for detection and accurate characterization of in-situ grown TFCs in CASS PZR surge-line components.

A primary metric used for determination of the effectiveness and use of the inspection approach is to compare the composite length- and depth-sizing results from the evaluation against ASME Code, Section XI, Appendix VIII acceptance criteria for performance demonstration. The length sizing criterion calls for an RMSE less than 19.05 mm (0.75 in.), while depth sizing requires an RMSE less than 3.18 mm (0.125 in.). The data show that the length-sizing and depth-sizing RMSE values fell within the ASME Code, Section XI, Appendix VIII sizing limits.

Flaw length-sizing measurements were made by three different analysts, each analyzing different portions of the data. While much of the data were straightforward and easily sized at the loss of signal −12 dB level, some data required interpretation due primarily to the noncontiguous nature of TFC signals (slight variations in judgment/interpretation and application of sizing criteria). Thus, sizing error due to variability in individual analyst interpretations of signal response is a factor that has not been quantified in this study. Human factors issues are considered outside the scope of this work; nevertheless, it is noted here. Regarding detection capability, all flaws were detected with the exception of flaw #3 in specimen 7C-059 at 800 kHz, because data could not be collected on this flaw due to the large footprint of the probe and the tight OD surface geometry on the elbow intrados.

Signal-to-noise values for the flaws were high, providing further evidence that detection was not a significant issue in the materials studied. The lowest SNR value for all signal responses (for the flaws located in the weld region), was computed to be 9.5 dB while the maximum SNR value was 22.6 dB. The data show that flaws are detectable at frequencies up to 2.0 MHz in these surge-line specimens containing grain sizes as large as 41 mm (1.61 in.) and nominal wall thickness of 33 mm (1.3 in.). The detection performance is only slightly degraded by using a higher frequency (2.0-MHz), while sizing is not affected at this frequency. The higher frequencies (especially the 2.0-MHz probe) were surprisingly capable of detecting tip-diffracted energy and specular reflections. Results show that aggregate flaw depth-sizing and length-sizing fell completely within the ASME Code-allowable limit.

The issue of microstructure-induced beam redirection, and the potential for error in the positional registration of flaw responses relative to their true position, was also evaluated. To address this issue, an analysis of the measured flaw lengths and positions (localization data) was conducted. The measured localization data were compared to the true-state flaw position data in the specimens, and this information was plotted and analyzed to determine if errors in localization of the cracks caused by beam redirection were induced by the microstructures. A limited flaw mapping exercise was conducted and the data showed that potential lateral (circumferential) beam redirection was measured in 35% of the flaw end points and was as great as 18 mm (0.71 in.). Beam redirection in the axial direction was also addressed and found to be dependent on insonification angle. At a nominal 45 degrees, the average amount of axial beam skew was determined to be approximately 3 mm (0.12 in.) in the CCSS 9C-001 and 9C-002 specimens.

PNNL employed an ISI supplier to examine the implanted and in-situ grown flaws from the pipe side of specimens 9C-001 and 9C-002 with a procedure qualified to ASME Code Appendix VIII, Supplement 10. The supplier used a 1.5-MHz PA probe operating in an electronic raster mode that acquired a portion of the data without probe motion in the axial direction of the specimen. The supplier results compared favorably to the PNNL line scan and full raster data (scanning in the axial direction and incrementing in the circumferential direction). As with the PNNL results, the supplier length- and depth-sizing RMSE values were within ASME Code allowable limits and SNR values were very good.

As with the inspection of all CASS components, a question remains regarding critical flaw size in these smaller-bore piping components. A rigorous flaw tolerance evaluation needs to be performed to address the question of critical flaw size, as this information can then be combined with microstructure knowledge, advanced probe design, and other state-of-the-art processes to build the foundation for a genuinely effective and reliable inspection technique that can pass a performance demonstration test and provide meaningful inspection results on these coarse-grained materials.

With respect to the evaluations conducted on the CASS PZR surge lines, the primary issues that would benefit from further research include gaining a better understanding of the role of different microstructures in CASS components and the various casting processes, and how variations in these processes and microstructures affect crack initiation, crack growth, and inspection performance. Also, having some level of knowledge of the microstructure in the part being inspected is valuable, and can lead to improved examinations through enhanced array development. Therefore, development and evaluation of in-situ methods for characterizing and/or classifying microstructures as applied from the OD of a component would provide a great deal of valuable information for optimal tailoring of inspection parameters. While advances in phased-array inspection systems continue to improve general capabilities for crack detection and relatively accurate lateral resolution, overcoming the main inspection challenges posed by coarse-grained microstructures requires finding the optimal balance between three key factors: achieving suitable signal-to-noise ratio, obtaining effective penetration of the sound field from the OD, and acquiring optimal resolution for flaw localization and sizing. These are all critical toward improving flaw detection and sizing capabilities in CASS.

Currently, this work has focused primarily on flaw detection and characterization of TFCs in the weld material. However, additional work is needed to address important inspection issues associated with the morphology of other cracking mechanisms (intergranular stress corrosion cracking, mechanical fatigue, primary water stress corrosion cracking, etc.) as well as crack growth/location in the parent material near the weld, and the impact on detection and characterization performance. Also, as PA-UT detection and sizing approaches evolve for smaller-bore components, and mitigation activities are being implemented on existing plant systems, further work could include evaluation of longer-wavelength techniques to address similar CASS components with full structural overlays.

Finally, because this technical evaluation employed only three sample specimens (four including the pipe section containing the two in-situ grown validation flaws), with a limited flaw set, there may be a need to evaluate additional specimens with diverse CASS microstructures, which would provide the basis for a more rigorous and statistically relevant set of recommendations. Based on preliminary data reported to ASME Code, the Electric Power Research Institute (EPRI) NDE Center agreed to conduct an evaluation on the CASS PZR surge-line specimens used in this study. Their data will include assessments of UT methods that have been successfully qualified through the industry's Performance Demonstration Initiative. It is expected that the EPRI results will be made available to the NRC and PNNL so that joint conclusions can be made addressing smaller-bore CASS component inspections, and ASME Code rules can be developed for future examinations.

In conclusion, based upon the results of this work, state-of-the-art phased-array inspection approaches are rapidly evolving and the capability to detect cracks in CASS components where the wall thickness is generally less than 50 mm (2.0 in.) has been demonstrated here. While additional questions remain to be answered, long-wavelength ultrasonic approaches coupled with advanced signal processing technologies are beginning to show signs of success toward addressing this challenging inspection issue.

10 REFERENCES

Anderson MT, SL Crawford, SE Cumblidge, KM Denslow, AA Diaz and SR Doctor. 2007. *Assessment of Crack Detection in Heavy-Walled Cast Stainless Steel Piping Welds Using Advanced Low-Frequency Ultrasonic Methods*. NUREG/CR-6933, PNNL-16292, U.S. Nuclear Regulatory Commission, Washington, D.C.

Anderson MT, SE Cumblidge and SR Doctor. 2003. "Applying Ultrasonic Phased Array Technology to Examine Austenitic Coarse-Grained Structures for Light Water Reactor Piping." In *Third EPRI Phased Array Inspection Seminar*. June 9–11, 2003, Seattle, Washington.

Chopra OK. 1992. *Long-Term Embrittlement of Cast Duplex Stainless Steels in LWR Systems, Semiannual Report, October 1990 – March 1991*. NUREG/CR-4744, Vol. 6, No. 1, ANL-91/22, U.S. Nuclear Regulatory Commission, Washington, D.C.

Davis JM. 1998. "Advanced Ultrasonic Flaw Sizing Handbook." *NDT.net* 3(11). http://www.ndt.net/article/1198/davis/davis.htm.

Diaz AA, AD Cinson, SL Crawford, SE Cumblidge, KM Denslow, M Morra, MS Prowant and MT Anderson. 2008. *Technical Letter Report: Assessment of Ultrasonic Phased Array Testing for Cast Austenitic Stainless Steel Pressurizer Surge Line Piping Welds and Thick Section Primary System Cast Piping Welds*. PNNL-17698, Pacific Northwest National Laboratory, Richland, Washington.

Diaz AA, SR Doctor, BP Hildebrand, FA Simonen, GJ Schuster, ES Andersen, GP McDonald and RD Hasse. 1998. *Evaluation of Ultrasonic Inspection Techniques for Coarse-Grained Materials*. NUREG/CR-6594, PNNL-11171, U.S. Nuclear Regulatory Commission, Washington, D.C.

Jeong YH. 1987. *An Ultrasonic Material State Classifier for Elastically Anisotropic Materials*. Ph.D. Thesis, Drexel University, Philadelphia, Pennsylvania.

Kupperman DS, KJ Reimann and J Abrego-Lopez. 1987. "Ultrasonic NDE of Cast Stainless Steel." *NDT International* 20(3):145–152.

Kupperman DS, KJ Reimann and DI Kim. 1981. "Ultrasonic Characterization and Microstructure of Stainless Steel Weld Metal." In *Proceedings of Nondestructive Evaluation: Microstructural Characterization and Reliability Strategies*, pp. 199–216. October 5–9, 1980, Pittsburg, Pennsylvania. The Metallurgical Society of AIME, Warrendale, Pennsylvania.

Taylor TT. 1984. *An Evaluation of Manual Ultrasonic Inspection of Cast Stainless Steel Piping*. NUREG/CR-3753, PNL-5070, U.S. Nuclear Regulatory Commission, Washington, D.C.

APPENDIX A

800-KHZ PHASED-ARRAY DATA ON FLAWS IN THE PRESSURIZER SURGE LINE SPECIMEN

APPENDIX A

800-KHZ PHASED-ARRAY DATA ON FLAWS IN THE PRESSURIZER SURGE LINE SPECIMEN

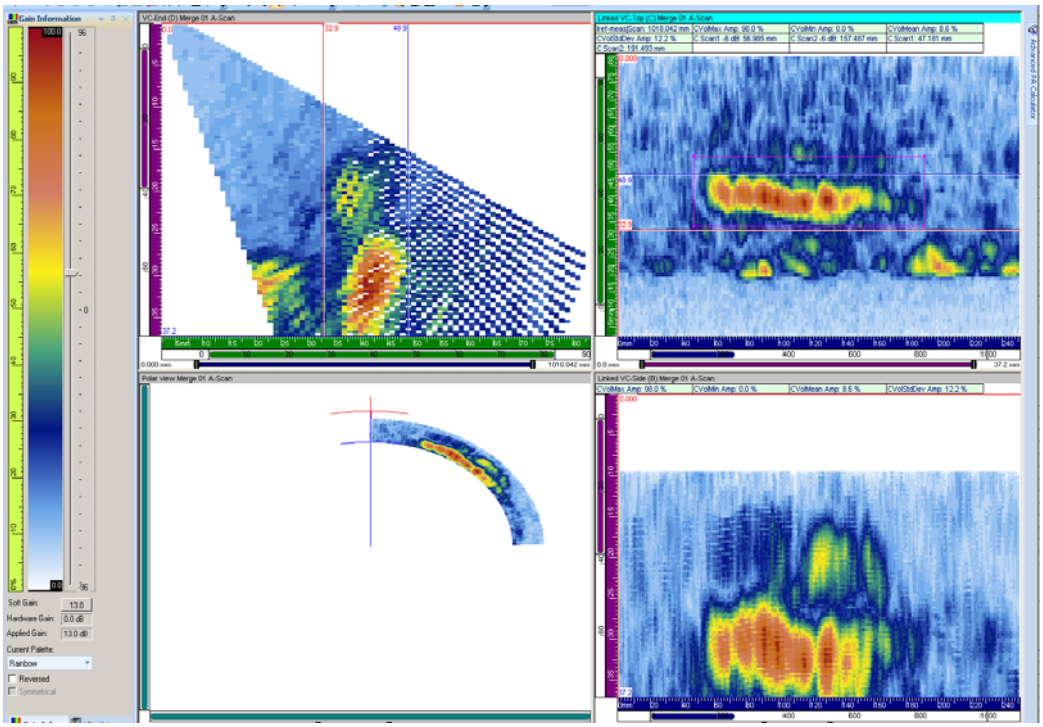

Figure A.1 800-kHz Data on Pipe Side of 7C-059, Flaw 1, Merged Image for Length Sizing

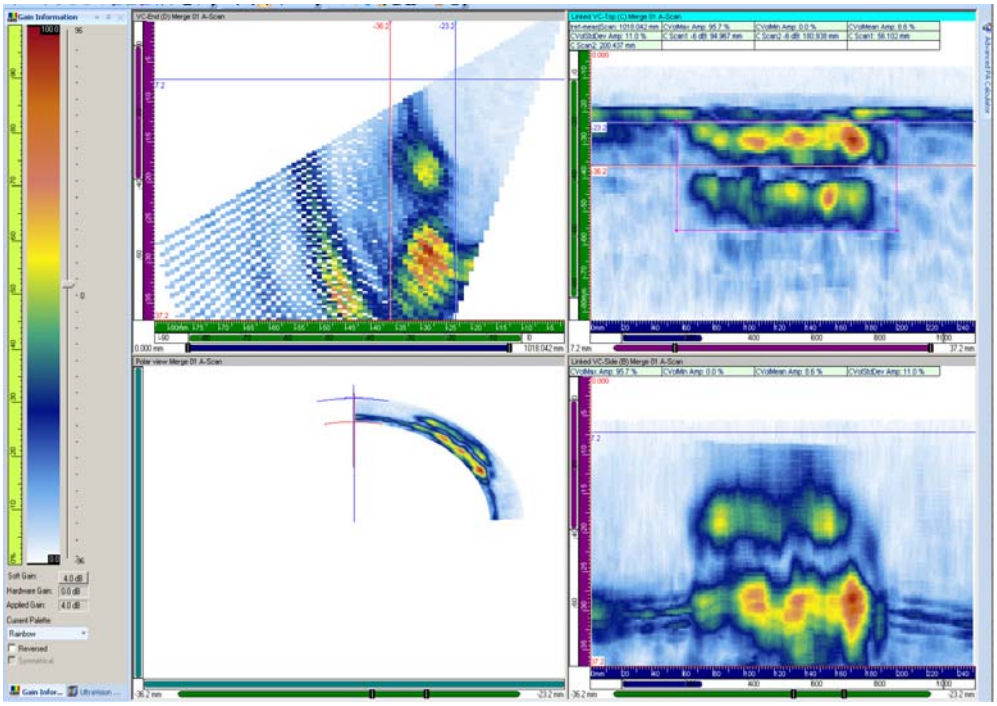

Figure A.2 800-kHz Data on Elbow Side of 7C-059, Flaw 1, Merged Image for Length Sizing

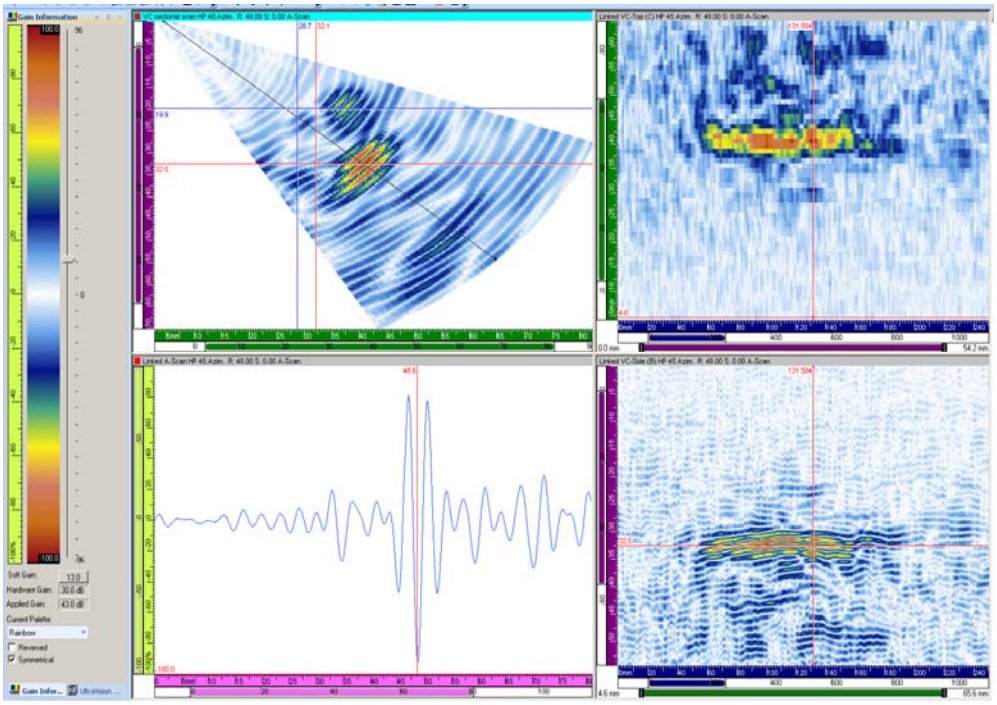

Figure A.3 800-kHz Data on Pipe Side of 7C-059, Flaw 1, for Depth Sizing

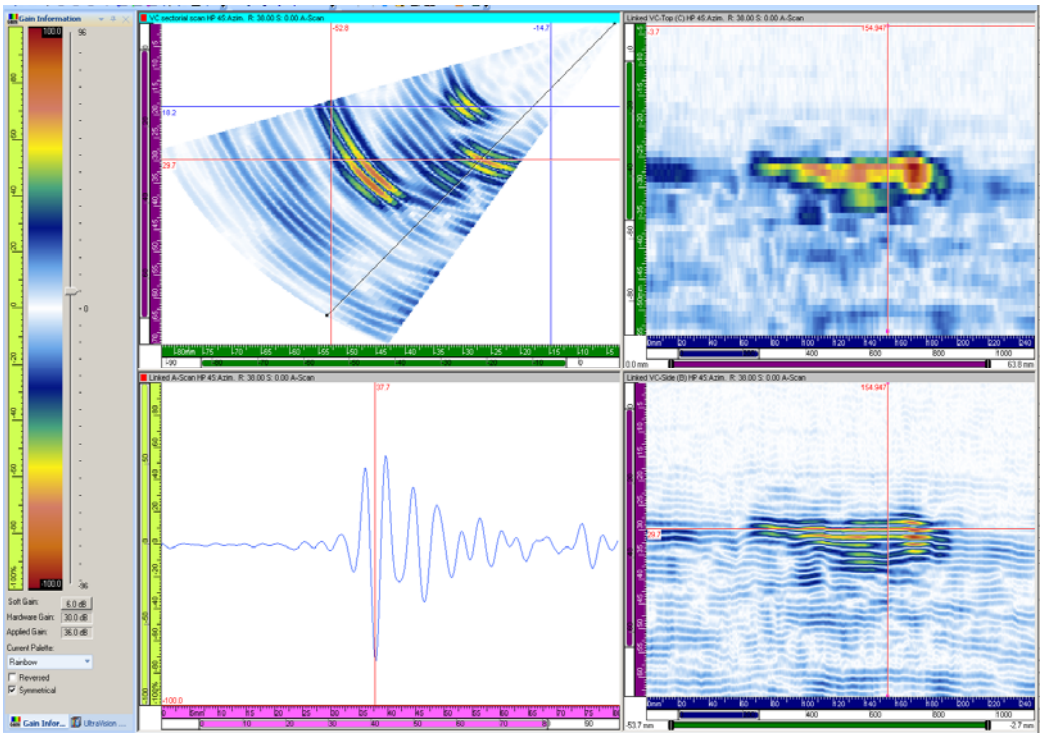

Figure A.4 800-kHz Data on Elbow Side of 7C-059, Flaw 1, for Depth Sizing

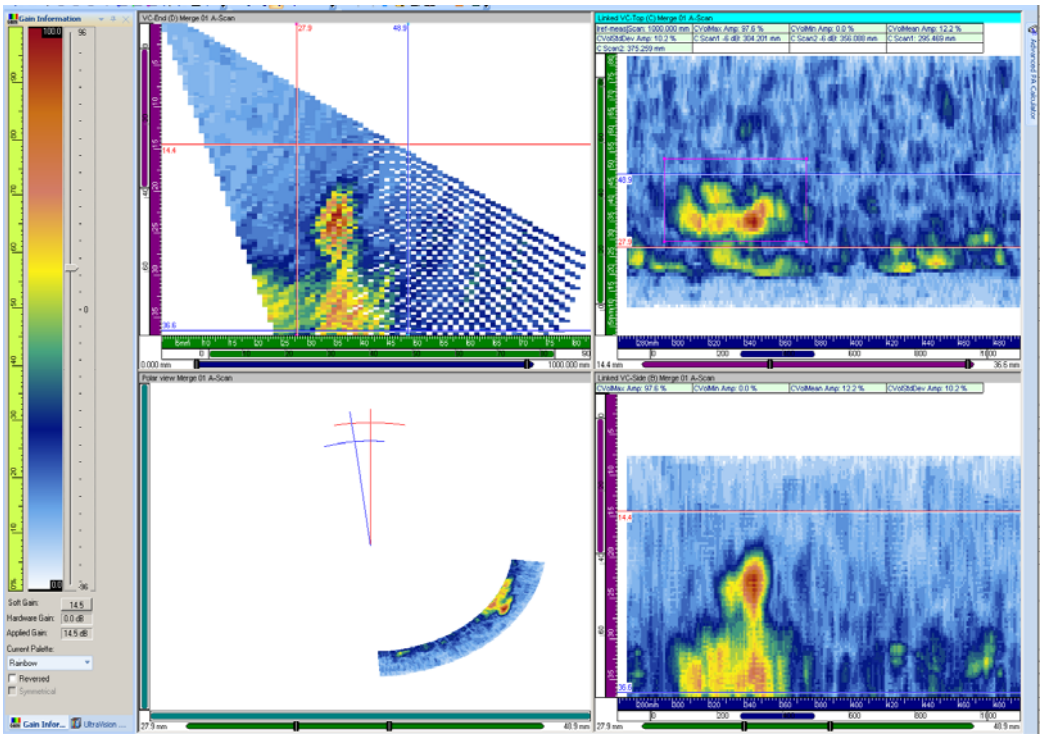

Figure A.5 800-kHz Data on Pipe Side of 7C-059, Flaw 2, Merged Image for Length Sizing

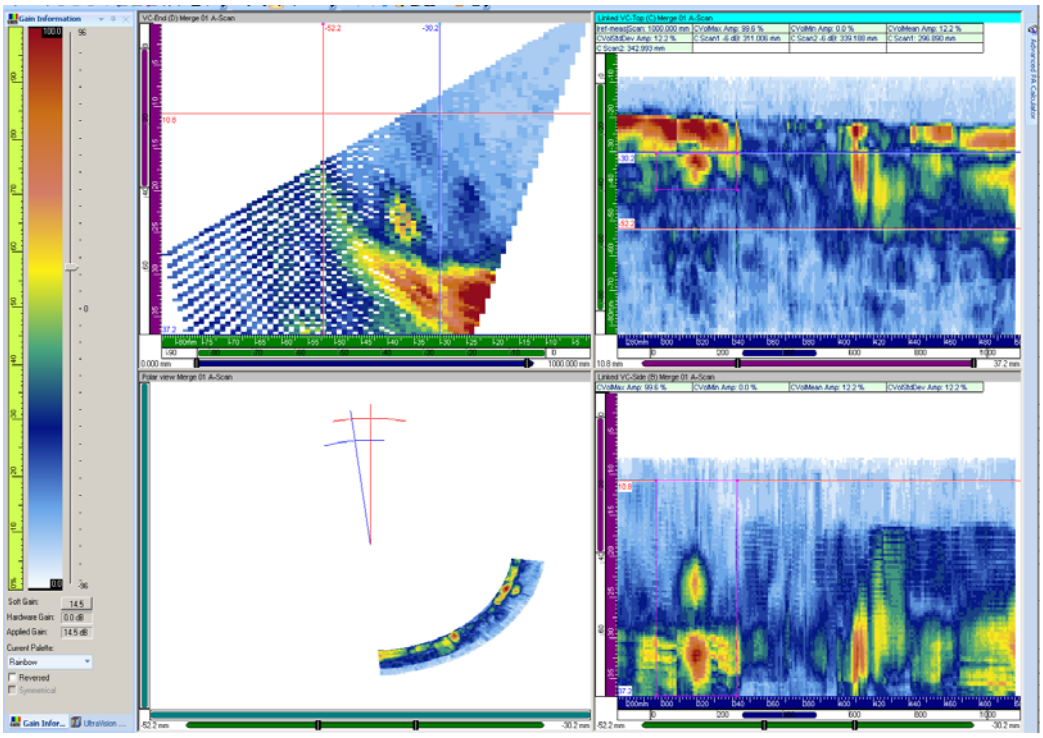

Figure A.6 800-kHz Data on Elbow Side of 7C-059, Flaw 2, Merged Image for Length Sizing

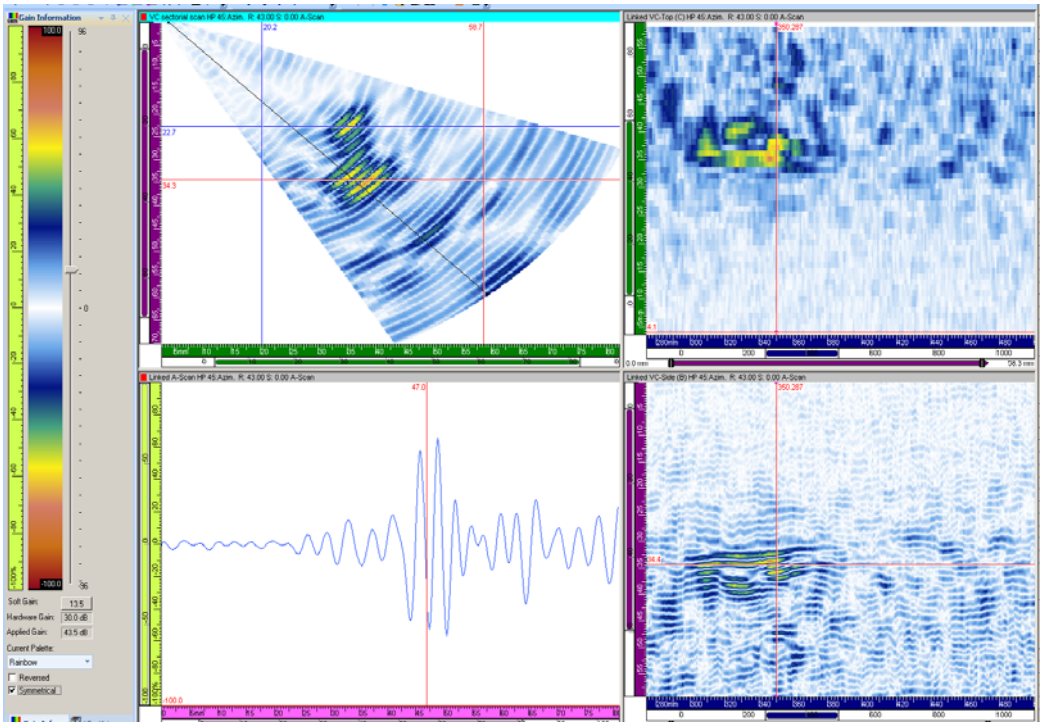

Figure A.7 800-kHz Data on Pipe Side of 7C-059, Flaw 2, for Depth Sizing

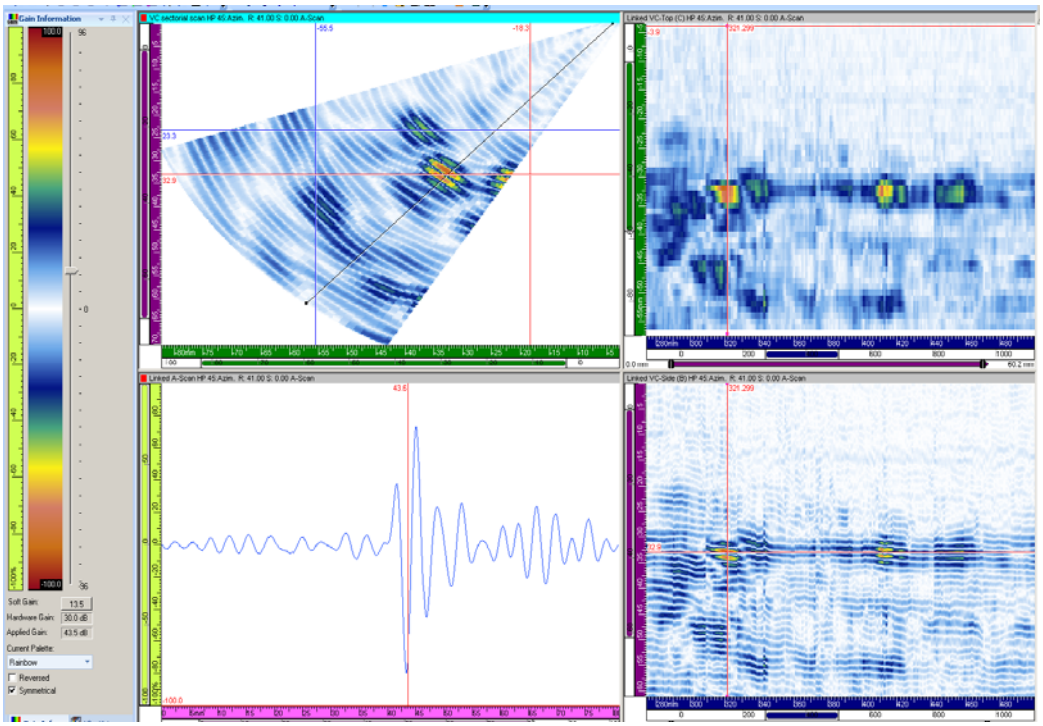

Figure A.8 800-kHz Data on Elbow Side of 7C-059, Flaw 2, for Depth Sizing

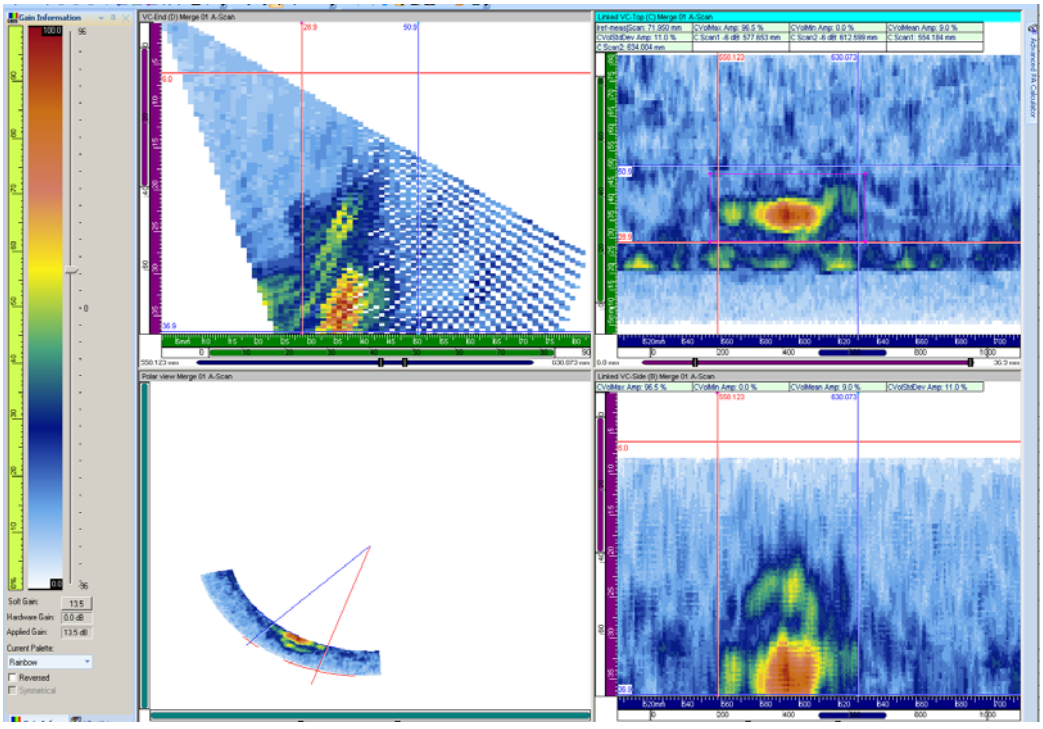

Figure A.9 800-kHz Data on Pipe Side of 7C-059, Flaw 3, Merged Image for Length Sizing

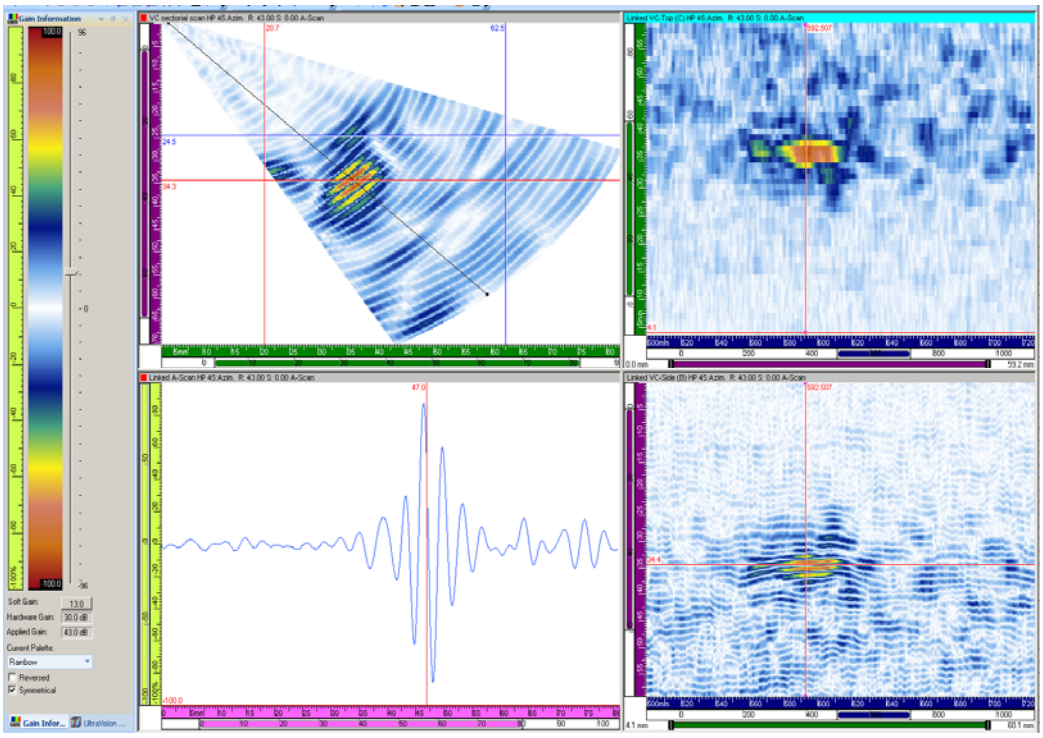

Figure A.10 800-kHz Data on Pipe Side of 7C-059, Flaw 3, for Depth Sizing

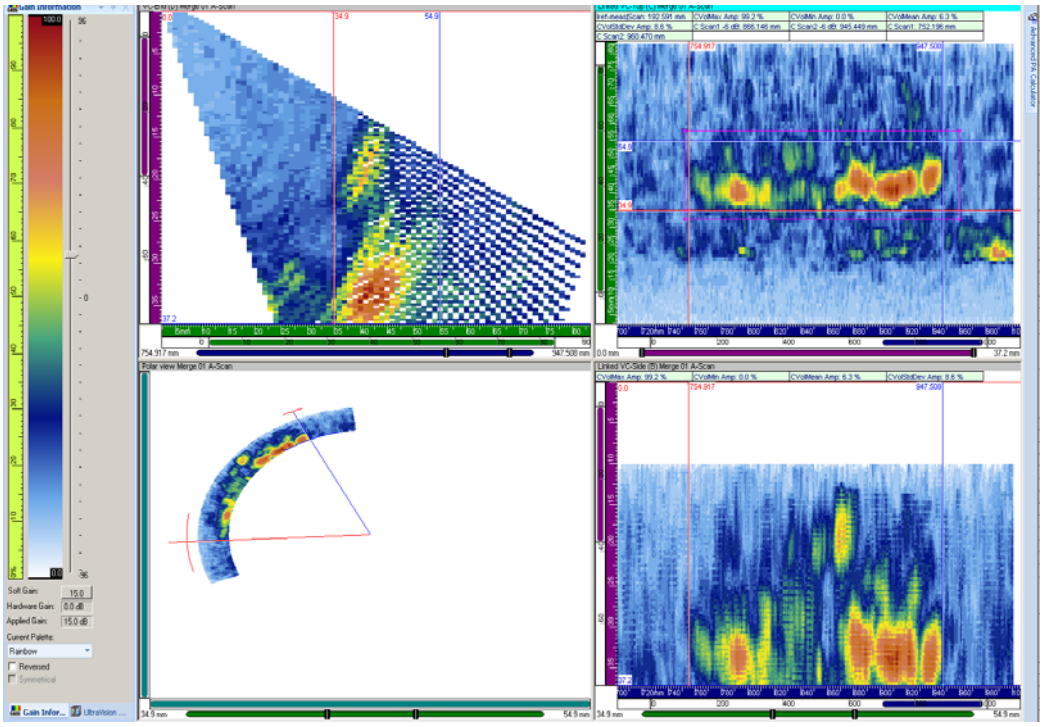

Figure A.11 800-kHz Data on Pipe Side of 7C-059, Flaw 4, Merged Image for Length Sizing

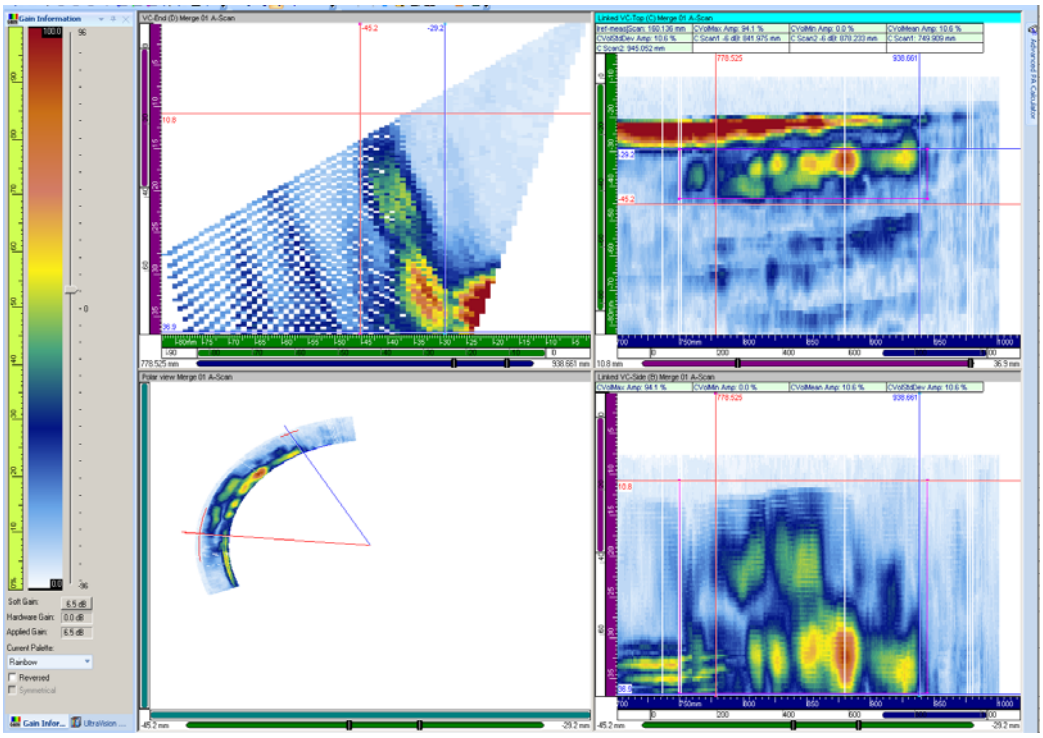

Figure A.12 800-kHz Data on Elbow Side of 7C-059, Flaw 4, Merged Image for Length Sizing

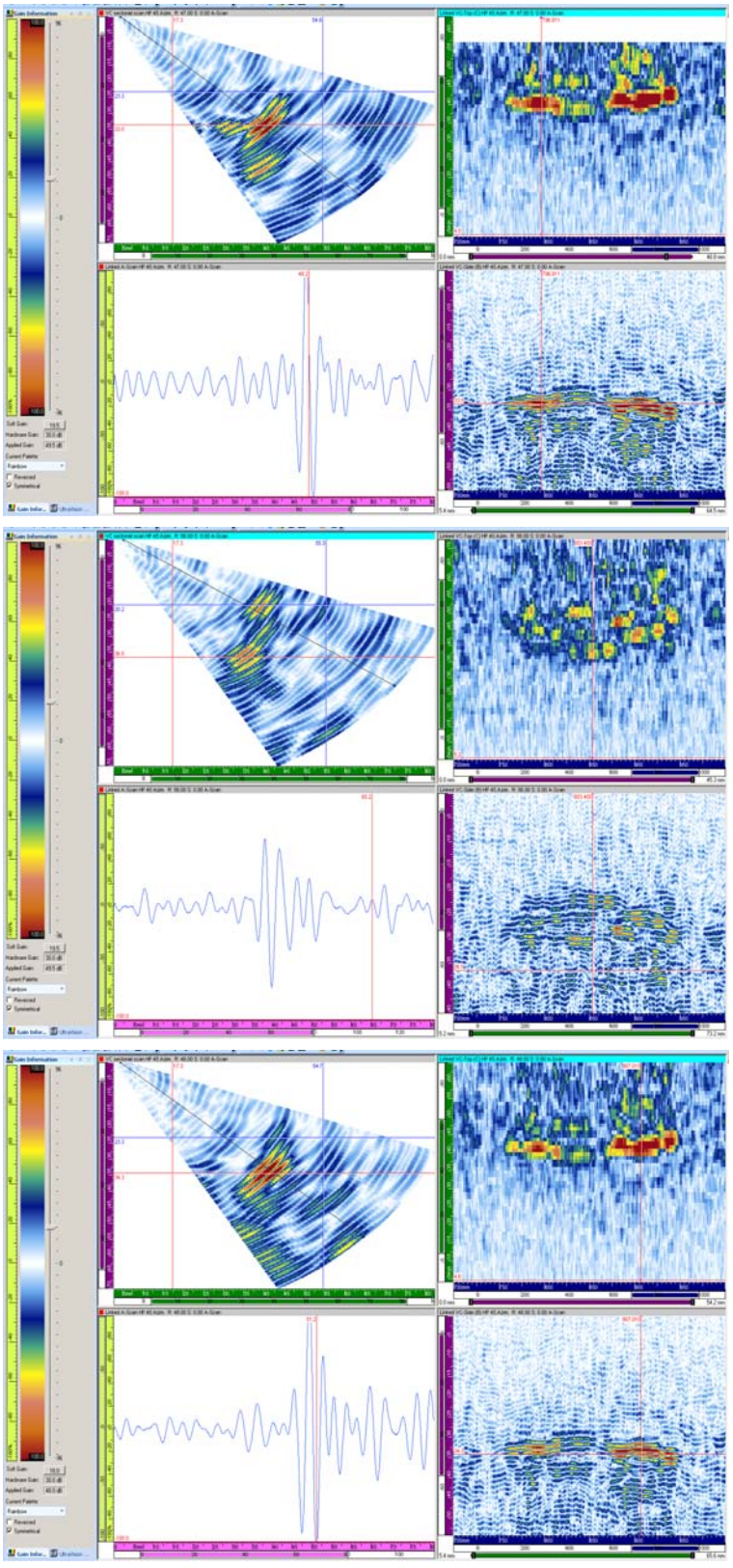

Figure A.13 800-kHz Data on Pipe Side of 7C-059, Flaw 4a, 4b, and 4c Top to Bottom for Depth Sizing

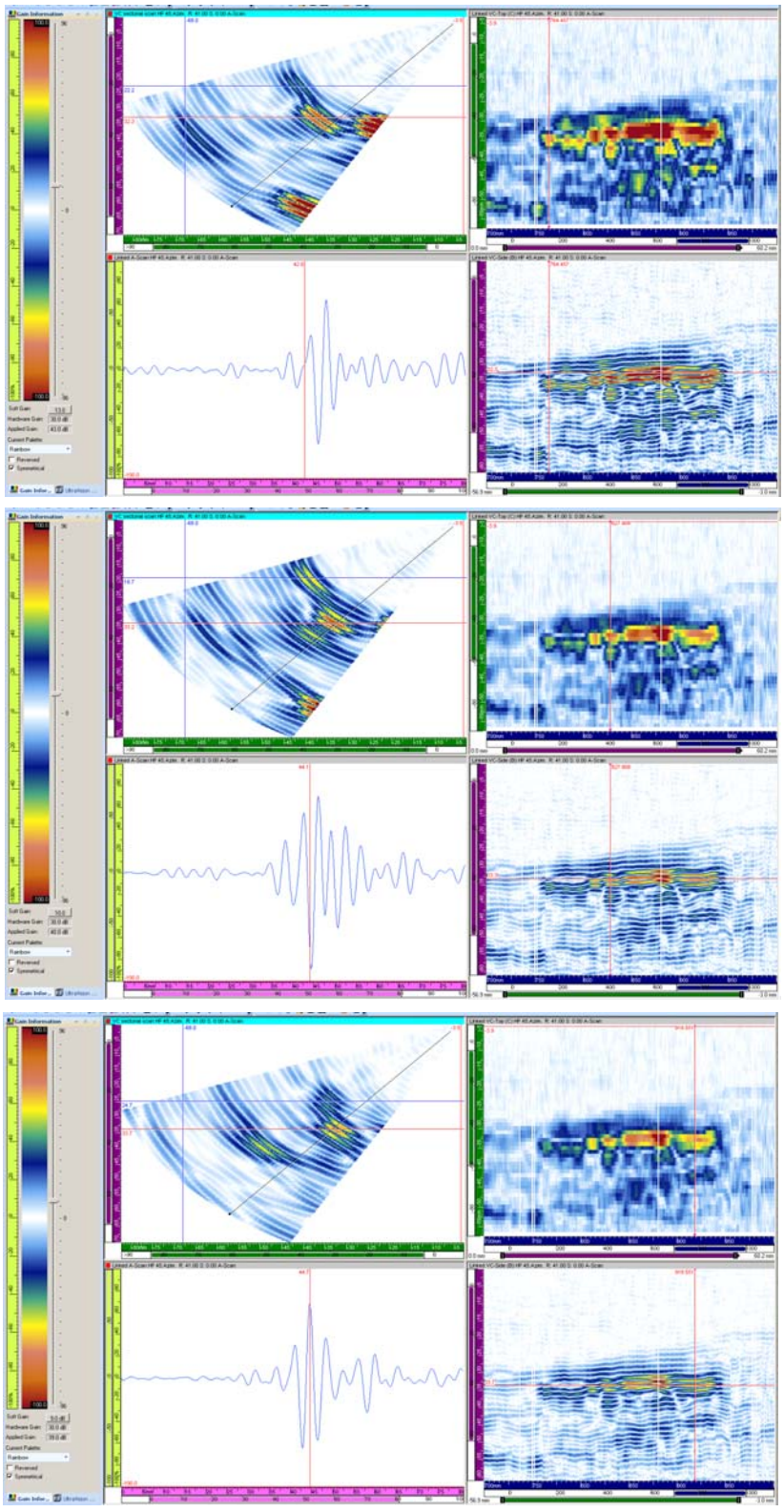

Figure A.14 800-kHz Data on Elbow Side of 7C-059, Flaw 4a, 4b, and 4c Top to Bottom for Depth Sizing

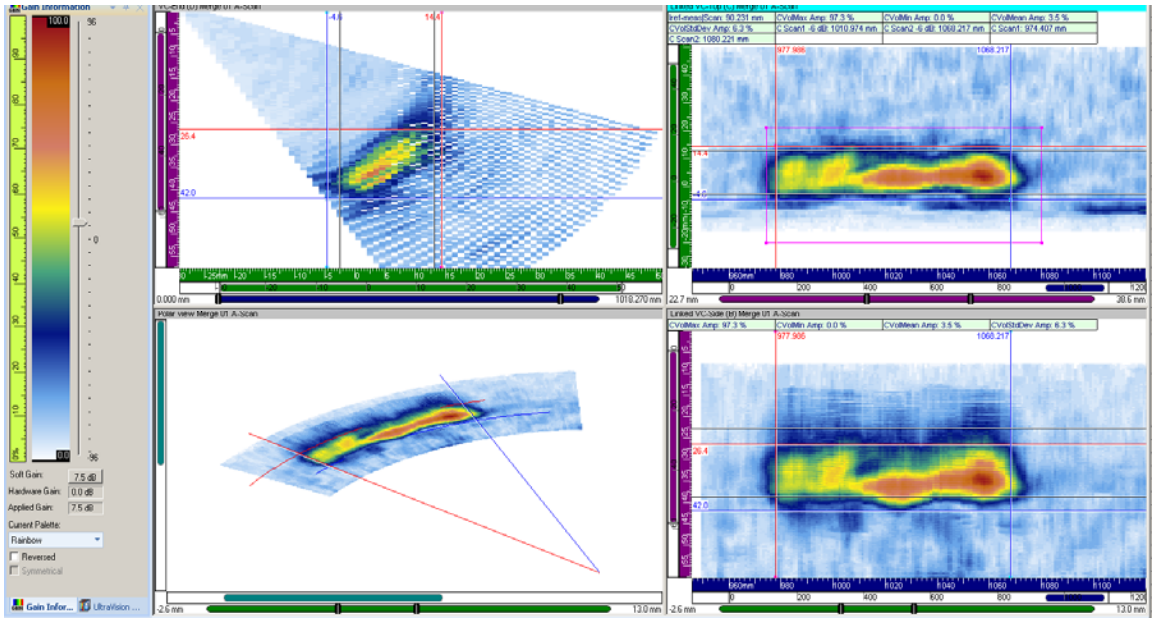

Figure A.15 800-kHz Data on Pipe Side of 9C-001, Flaw 1, Merged Image for Length Sizing

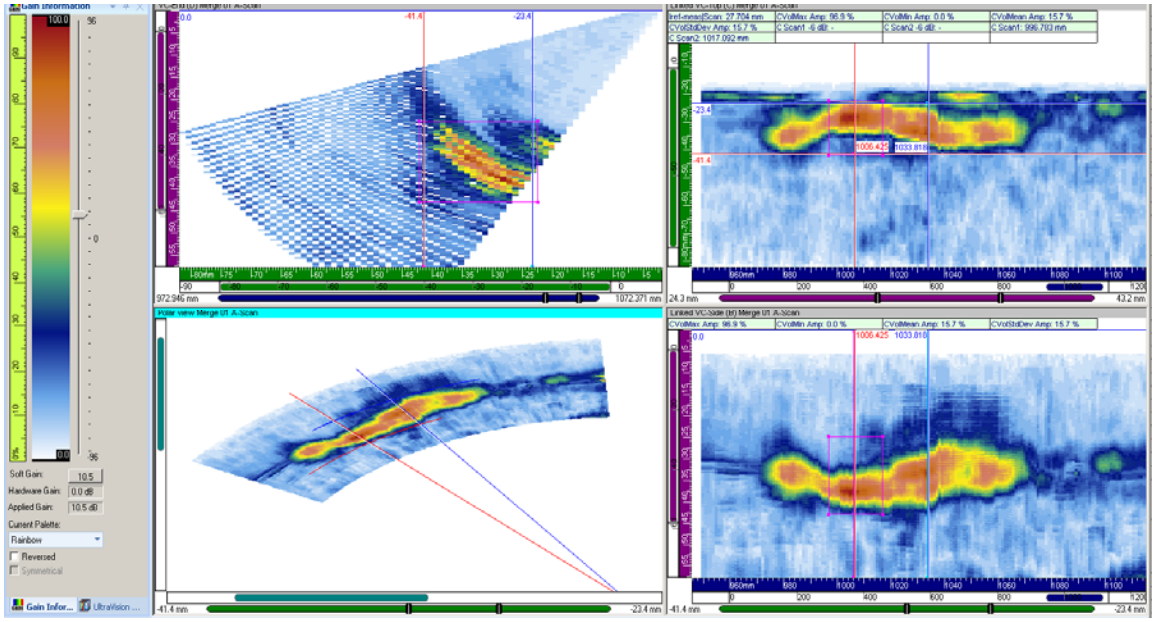

Figure A.16 800-kHz Data on Elbow Side of 9C-001, Flaw 1, Merged Image for Length Sizing

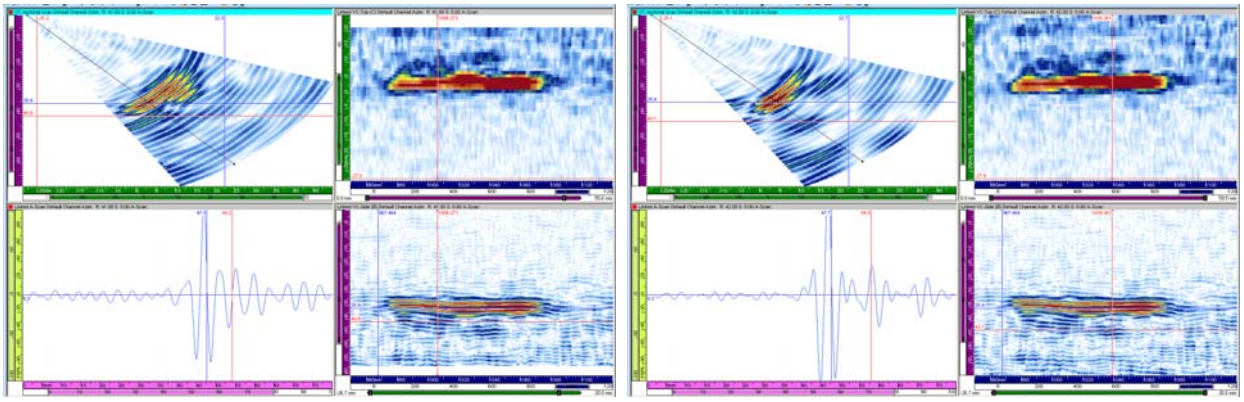

Figure A.17 800-kHz Data on Pipe Side of 9C-001, Flaw 1a on the Left and 1b on the Right for Depth Sizing

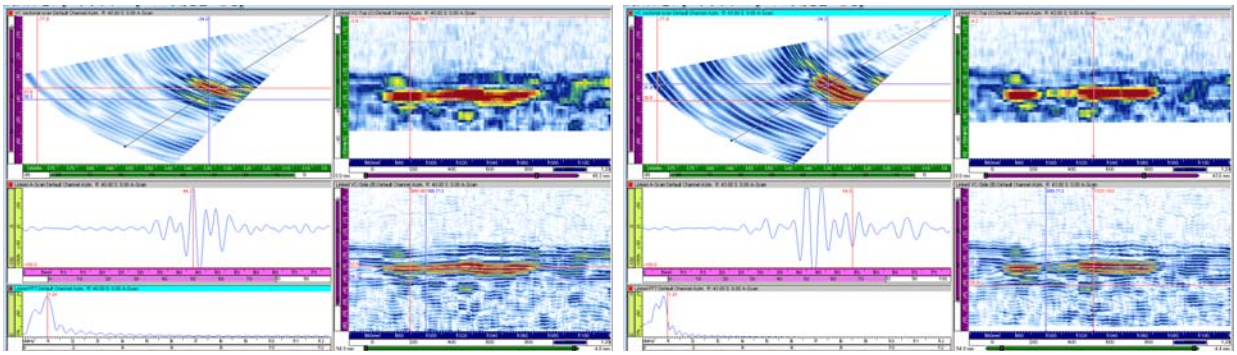

Figure A.18 800-kHz Data on Elbow Side of 9C-001, Flaw 1a on the Left and 1b on the Right for Depth Sizing

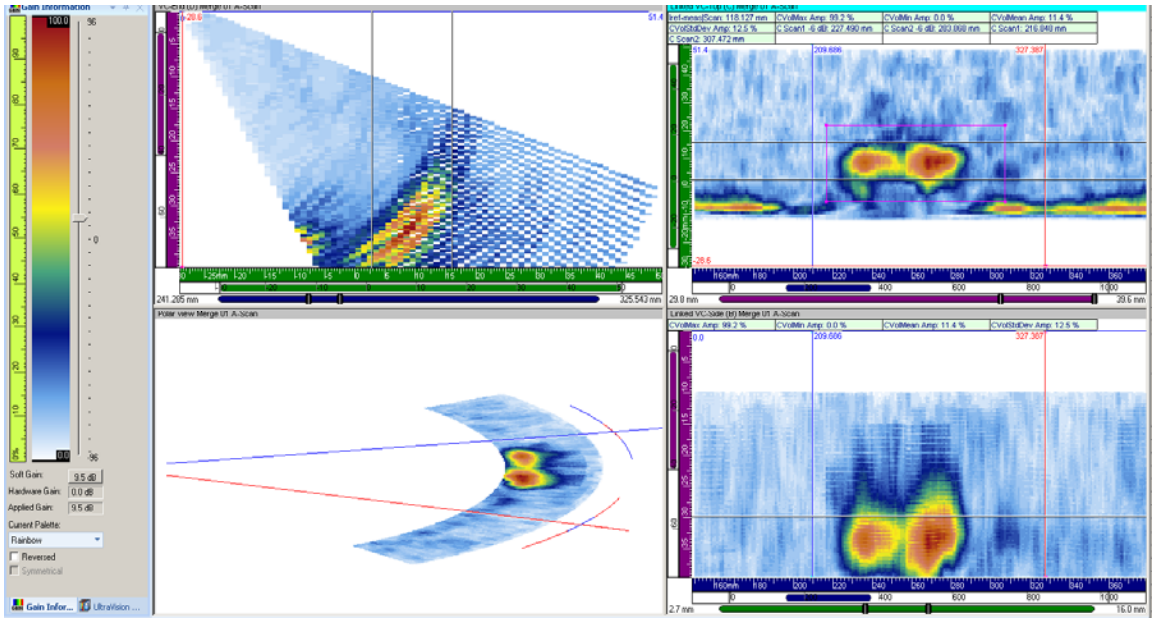

Figure A.19 800-kHz Data on Pipe Side of 9C-001, Flaw 2, Merged Image for Length Sizing

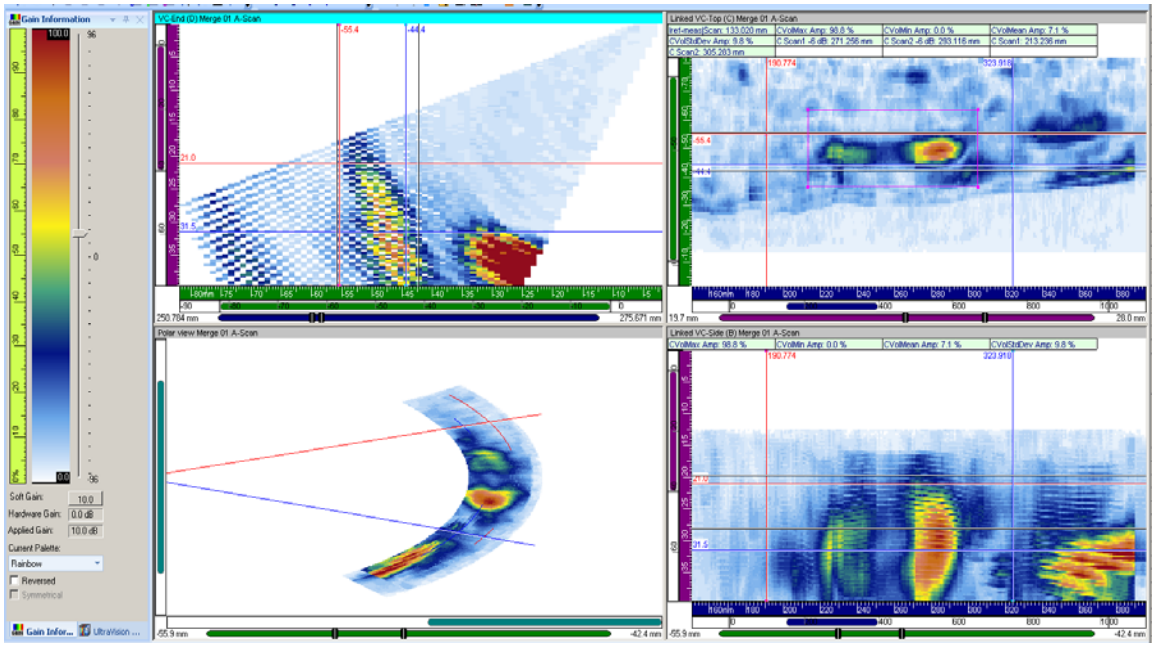

Figure A.20 800-kHz Data on Elbow Side of 9C-001, Flaw 2, Merged Image for Length Sizing

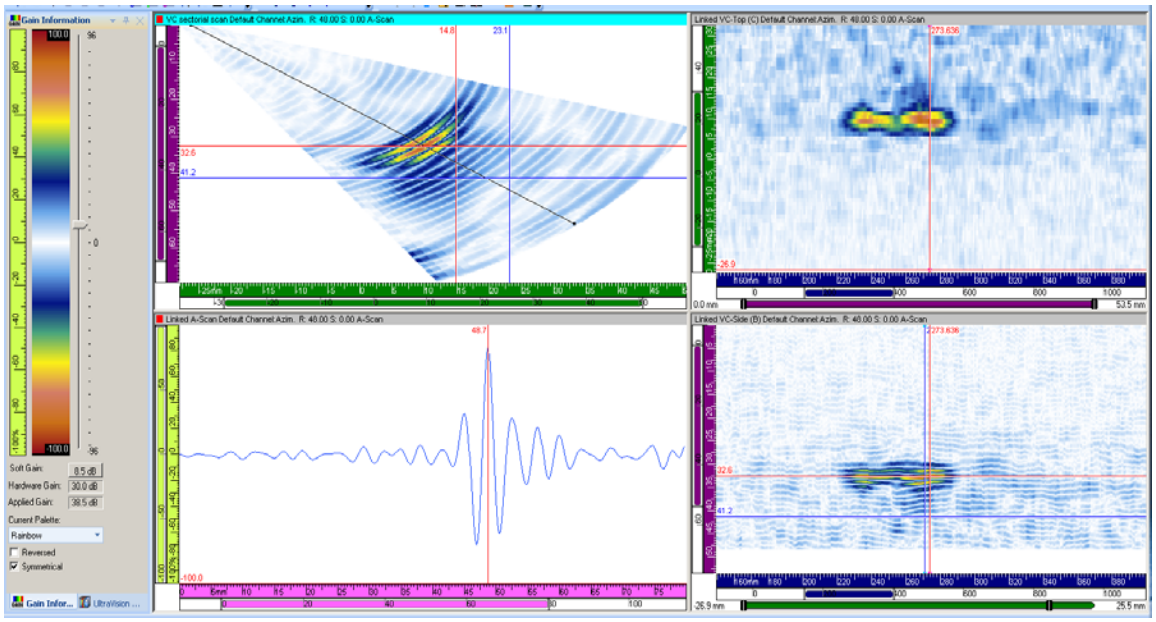

Figure A.21 800-kHz Data on Pipe Side of 9C-001, Flaw 2, for Depth Sizing

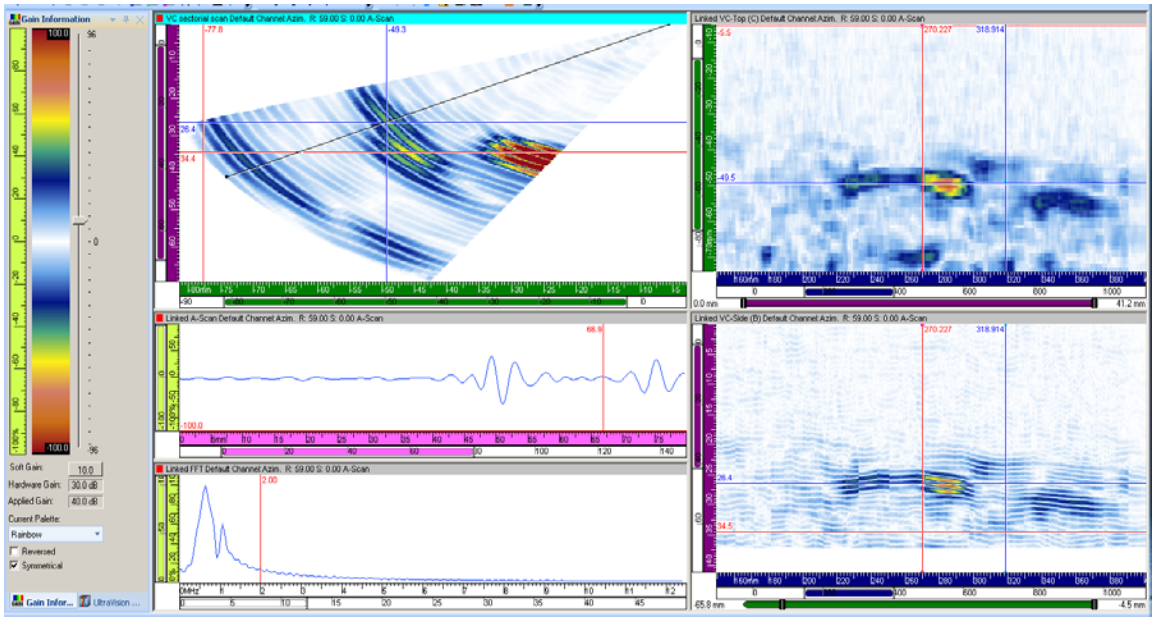

Figure A.22 800-kHz Data on Elbow Side of 9C-001, Flaw 2, for Depth Sizing

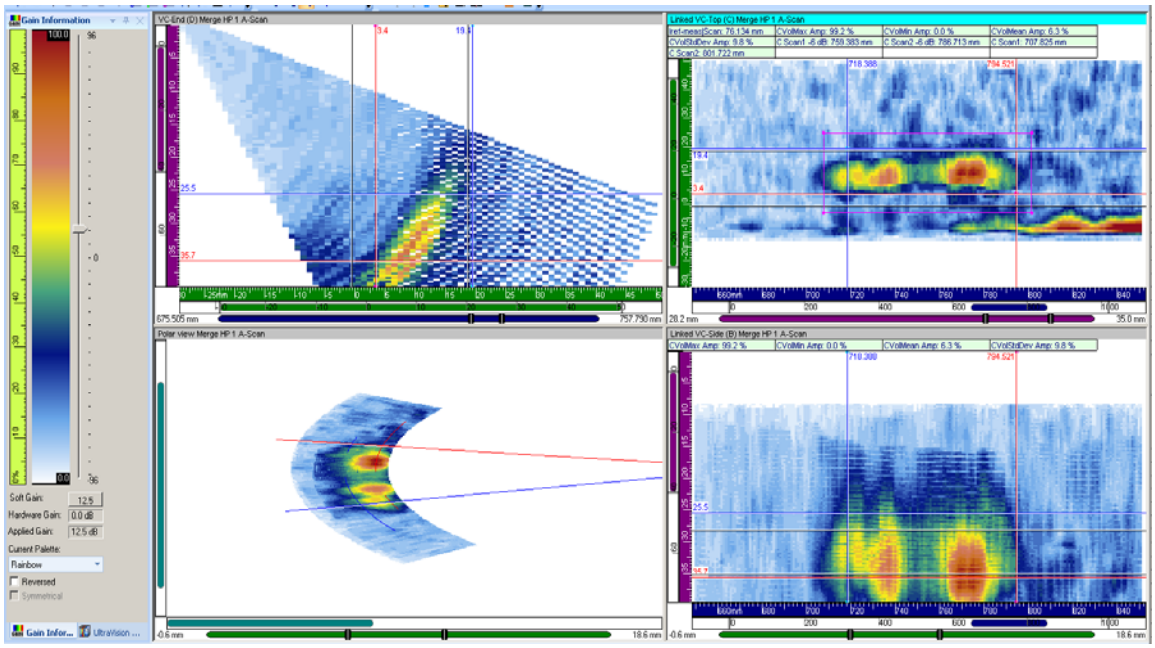

Figure A.23 800-kHz Data on Pipe Side of 9C-001, Flaw 3, Merged Image for Length Sizing

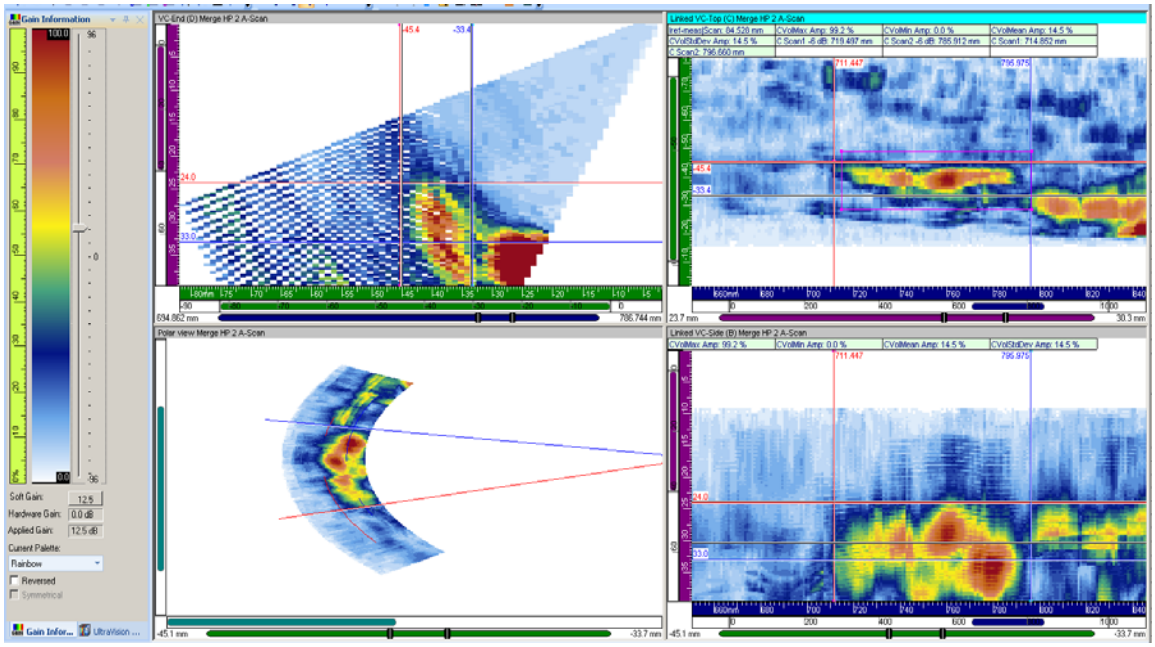

Figure A.24 800-kHz Data on Elbow Side of 9C-001, Flaw 3, Merged Image for Length Sizing

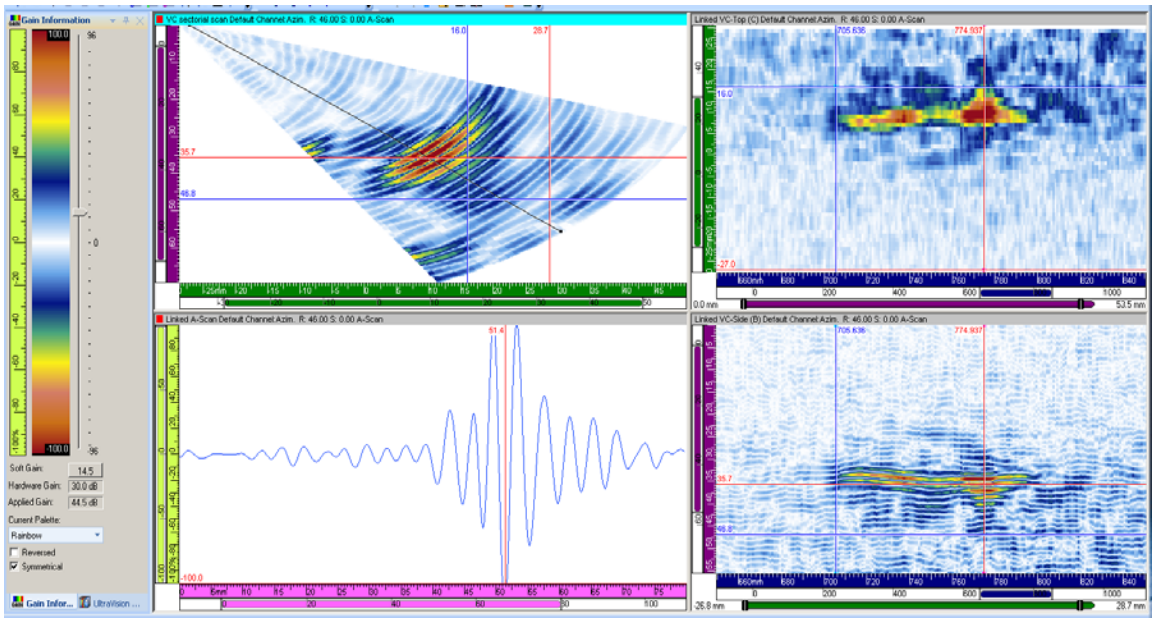

Figure A.25 800-kHz Data on Pipe Side of 9C-001, Flaw 3, for Depth Sizing

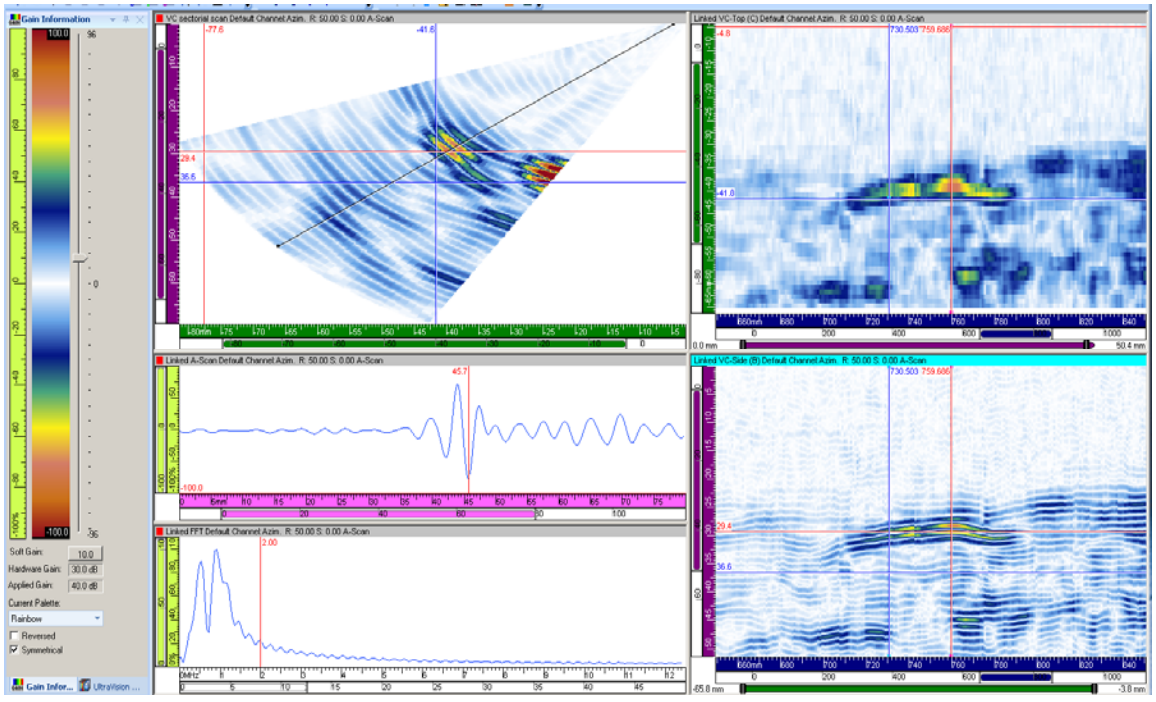

Figure A.26 800-kHz Data on Elbow Side of 9C-001, Flaw 3, for Depth Sizing

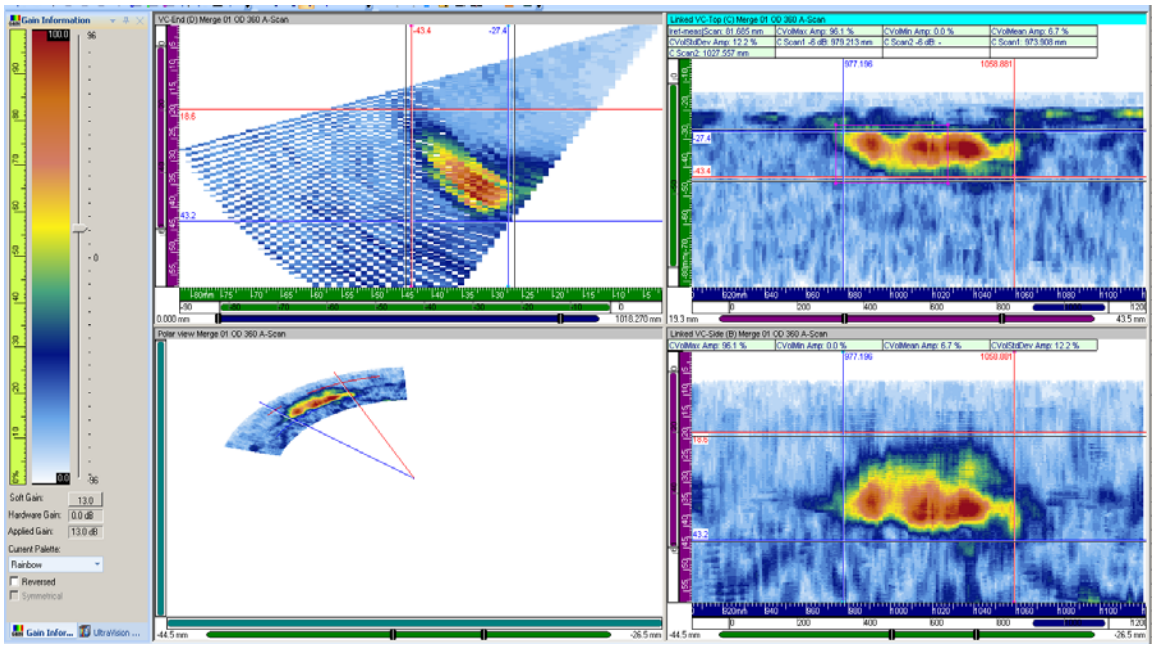

Figure A.27 800-kHz Data on Pipe Side of 9C-002, Flaw 1, Merged Image for Length Sizing

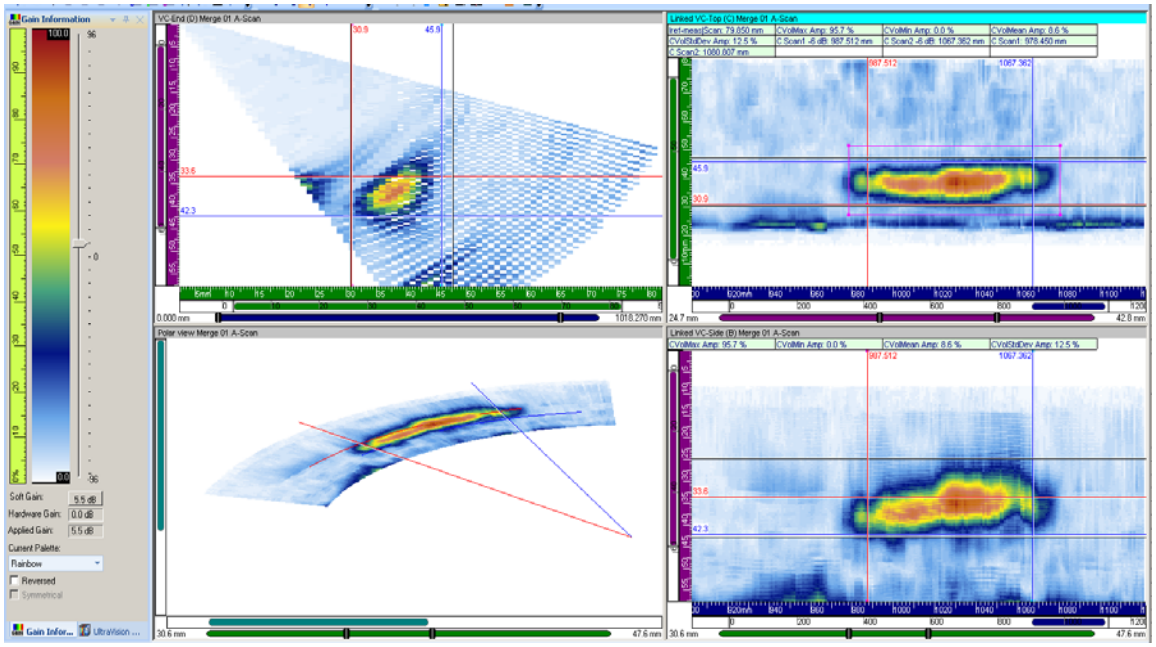

Figure A.28 800-kHz Data on Elbow Side of 9C-002, Flaw 1, Merged Image for Length Sizing

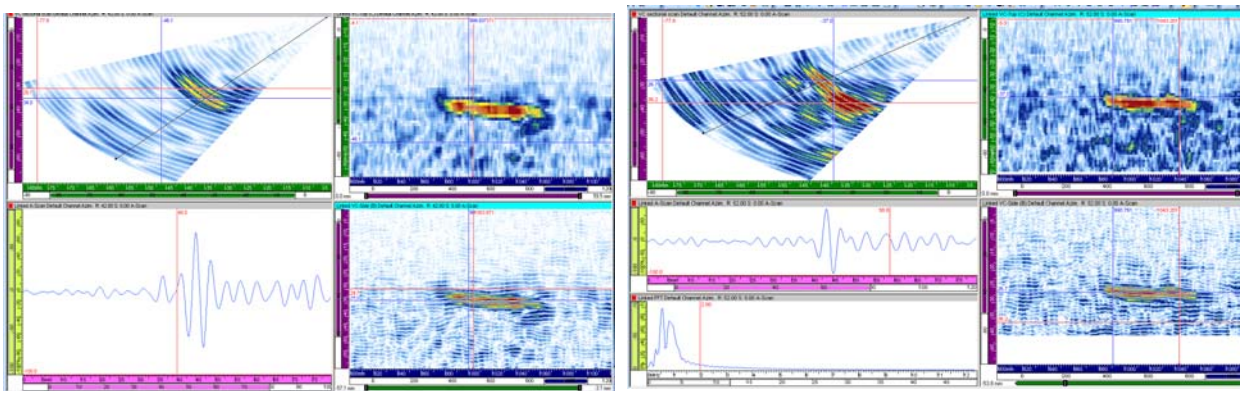

Figure A.29 800-kHz Data on Pipe Side of 9C-002, Flaw 1a on the Left and 1b on the Right for Depth Sizing

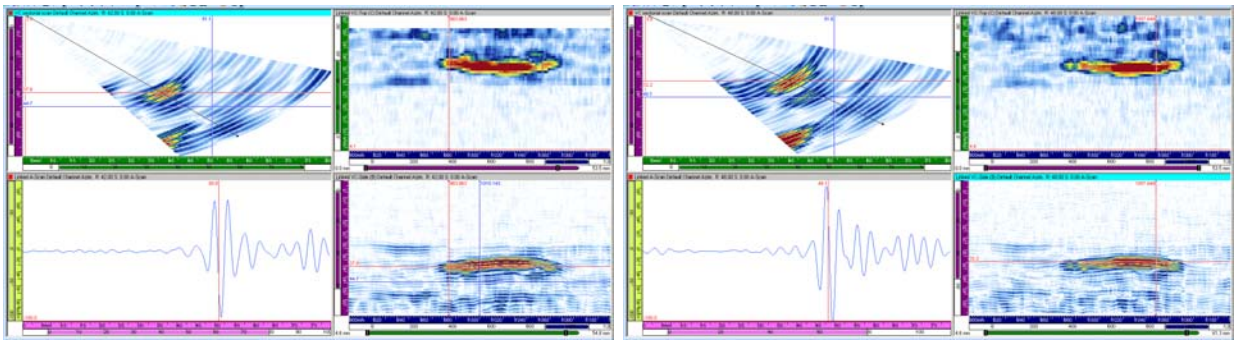

Figure A.30 800-kHz Data on Elbow Side of 9C-002, Flaw 1a on the Left and 1b on the Right for Depth Sizing

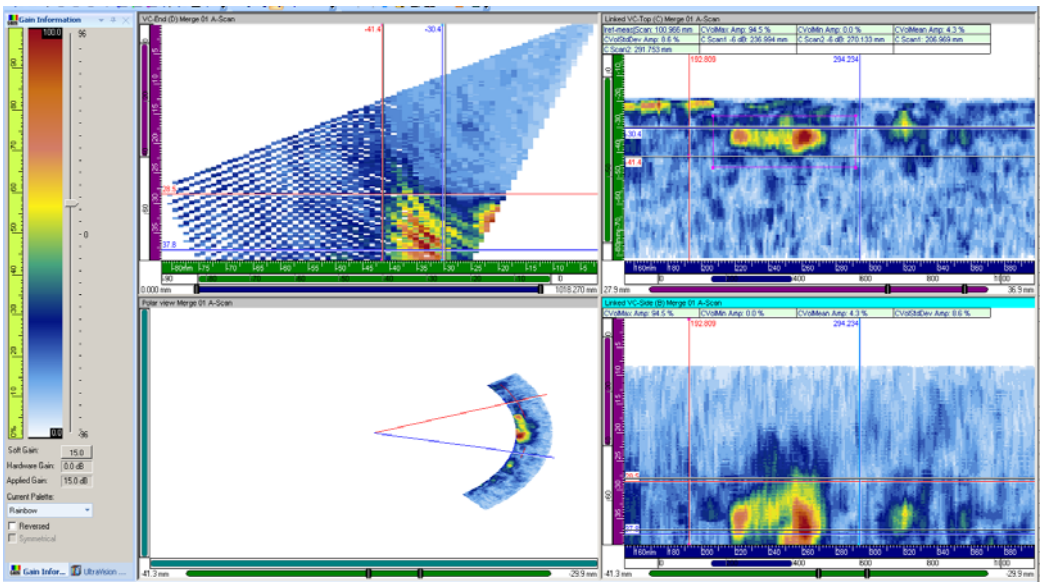

Figure A.31 800-kHz Data on Pipe Side of 9C-002, Flaw 2, Merged Image for Length Sizing

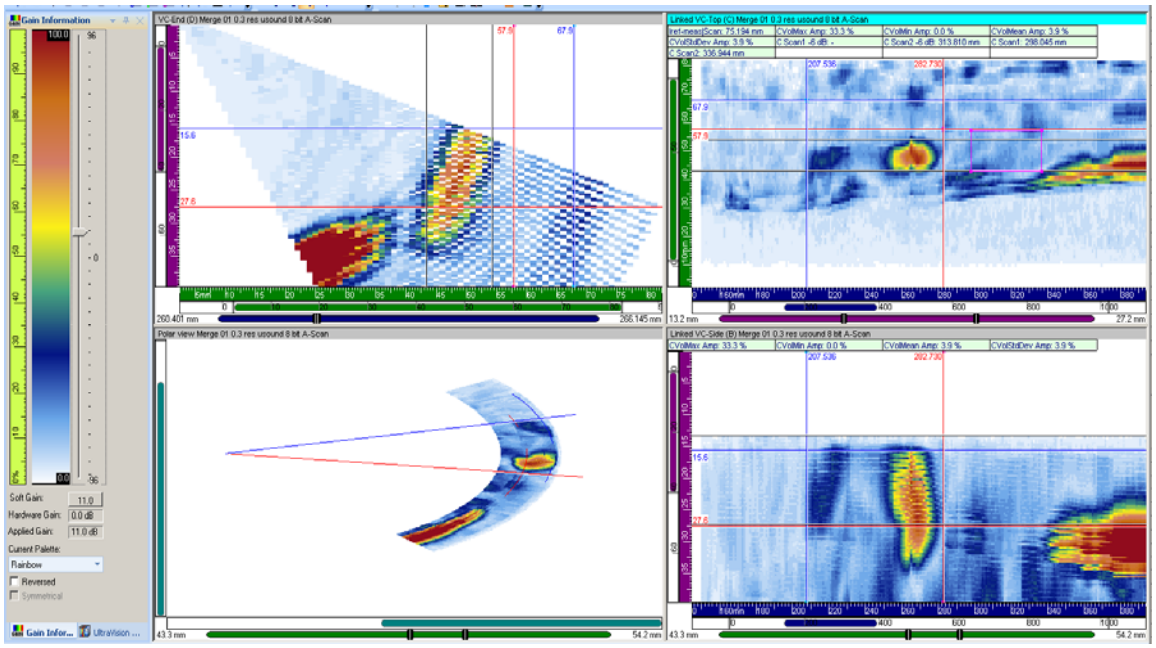

Figure A.32 800-kHz Data on Elbow Side of 9C-002, Flaw 2, Merged Image for Length Sizing

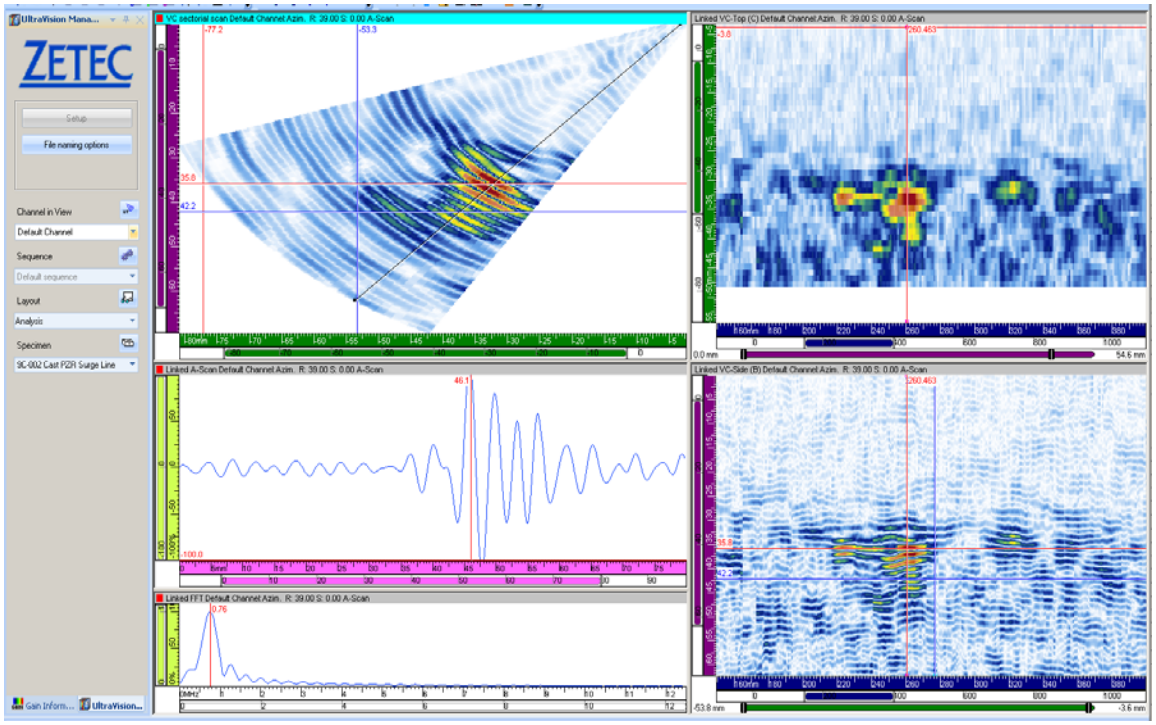

Figure A.33 800-kHz Data on Pipe Side of 9C-002, Flaw 2, for Depth Sizing

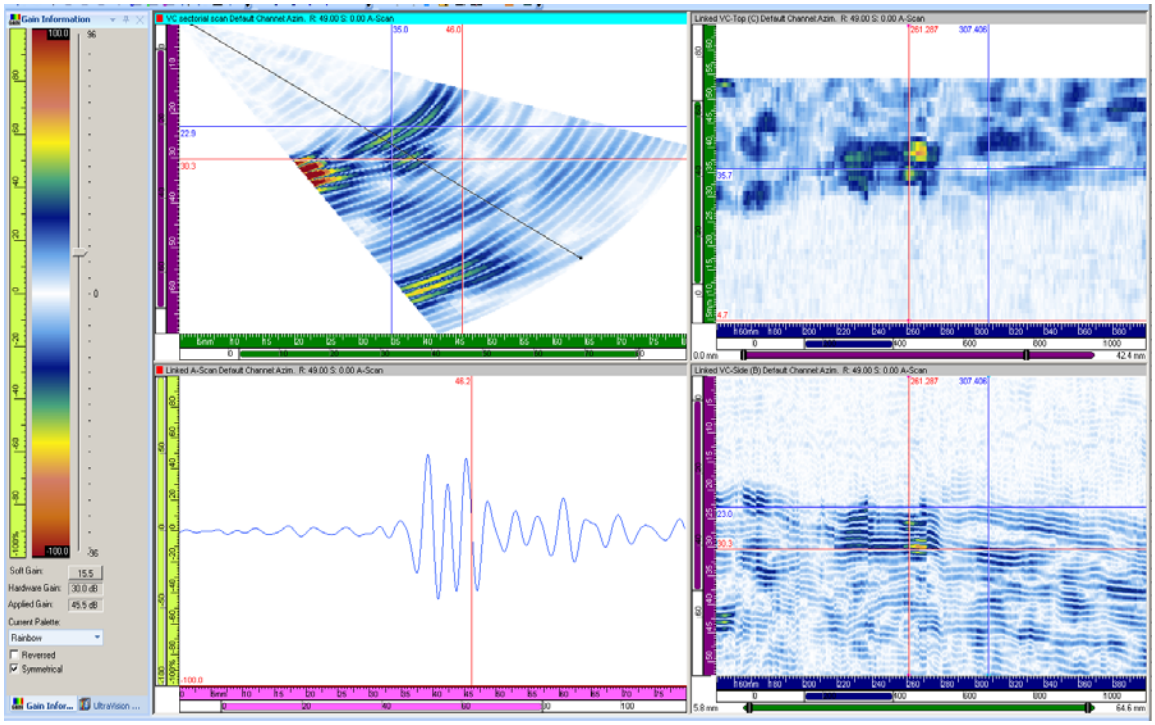

Figure A.34 800-kHz Data on Elbow Side of 9C-002, Flaw 2, for Depth Sizing

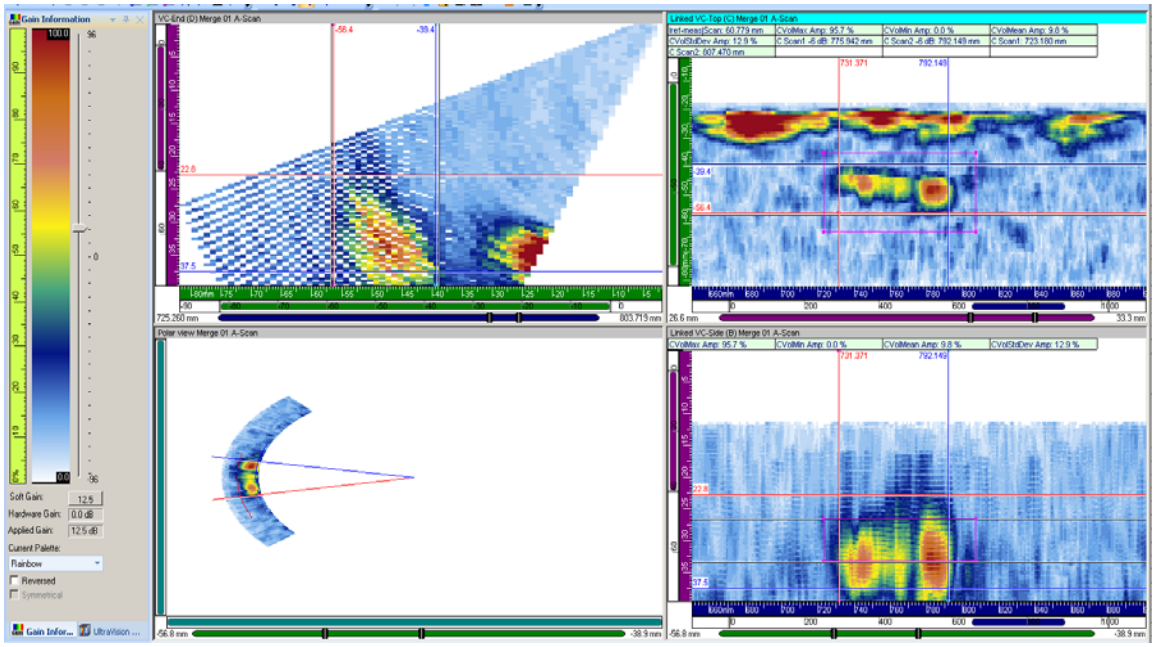

Figure A.35 800-kHz Data on Pipe Side of 9C-002, Flaw 3, Merged Image for Length Sizing

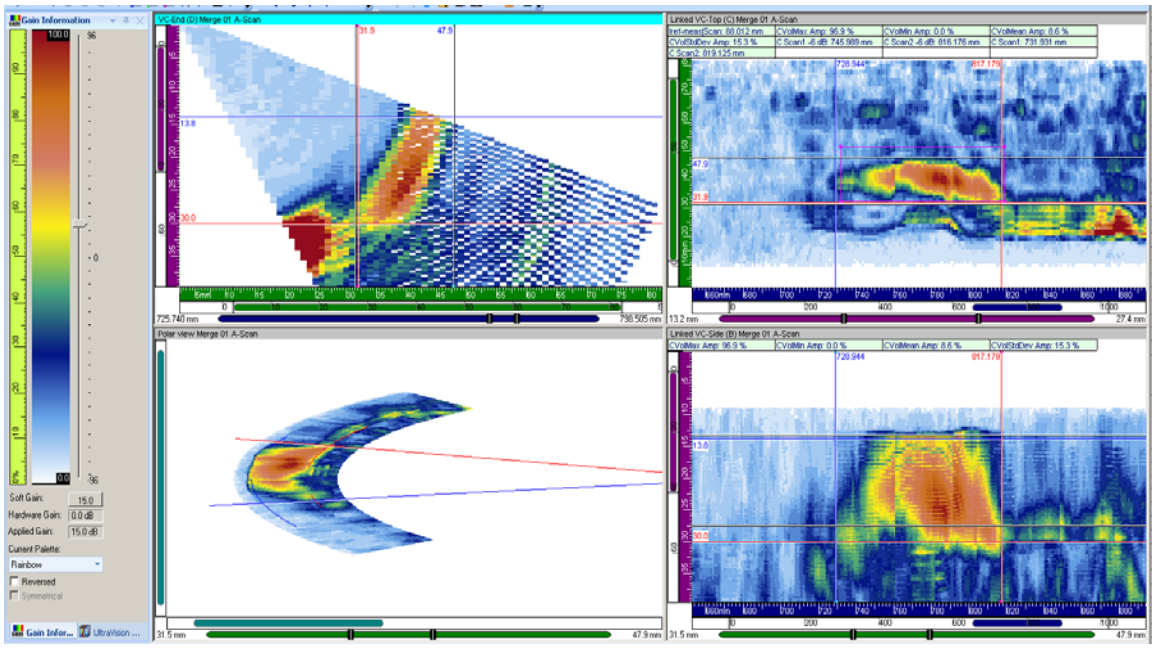

Figure A.36 800-kHz Data on Elbow Side of 9C-002, Flaw 3, Merged Image for Length Sizing

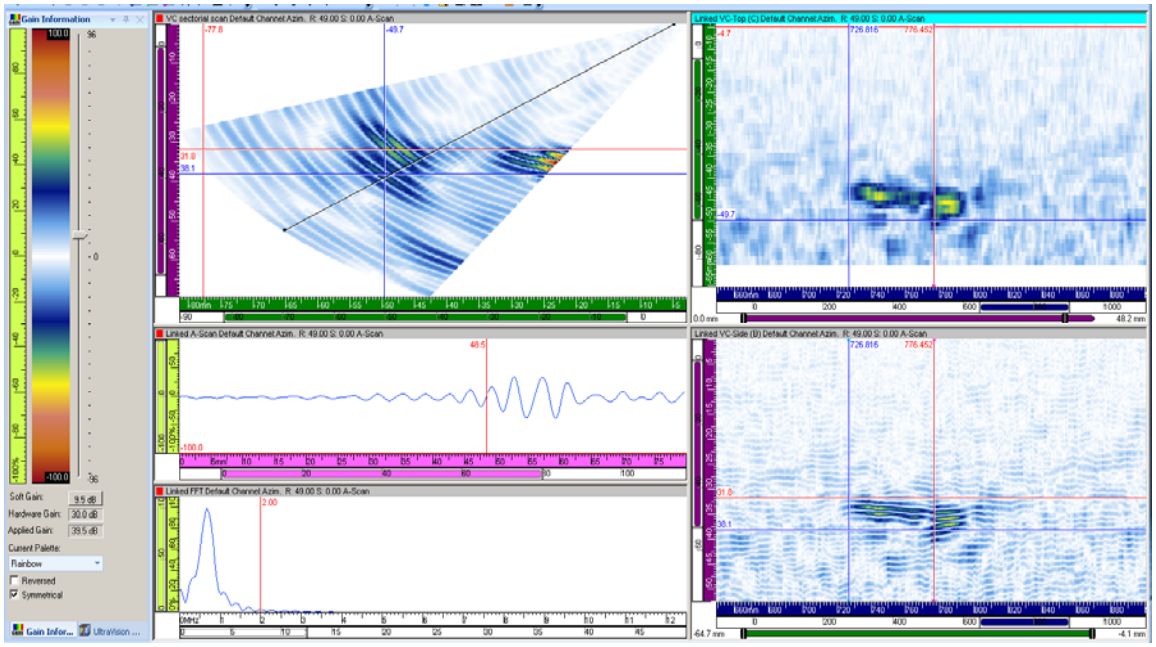

Figure A.37 800-kHz Data on Pipe Side of 9C-002, Flaw 3, for Depth Sizing

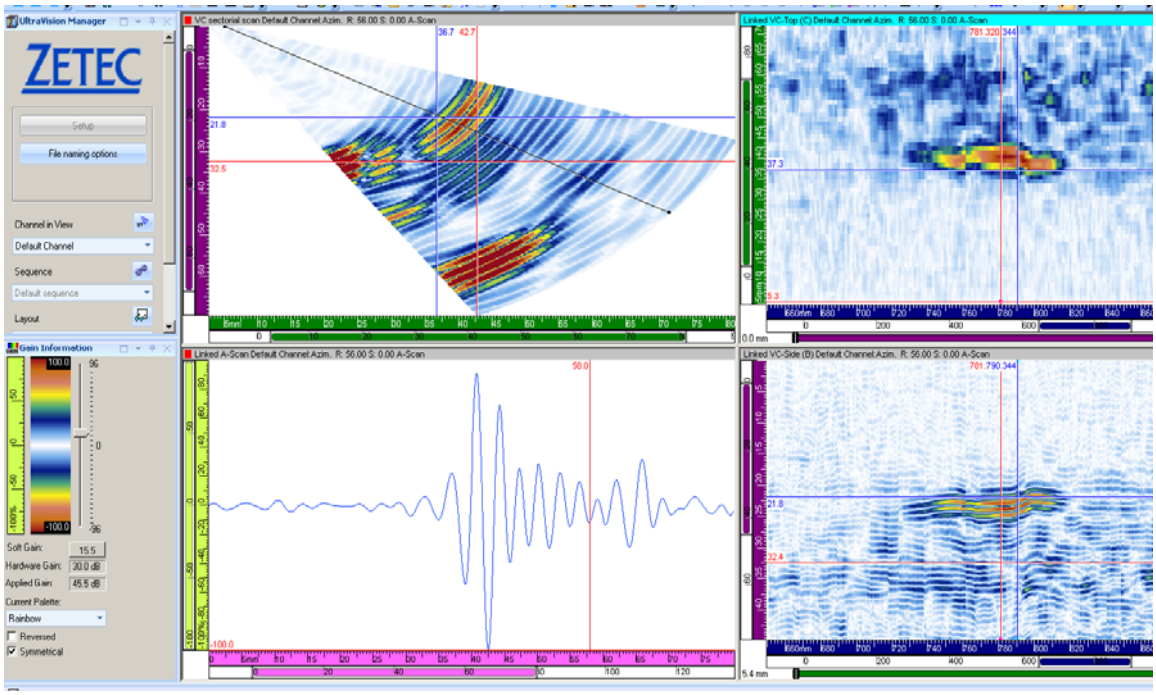

Figure A.38 800-kHz Data on Elbow Side of 9C-002, Flaw 3, for Depth Sizing

APPENDIX B

1.0-MHZ PHASED-ARRAY DATA ON FLAWS IN THE PRESSURIZER SURGE LINE SPECIMEN

APPENDIX B

1.0-MHZ PHASED-ARRAY DATA ON FLAWS IN THE PRESSURIZER SURGE LINE SPECIMEN

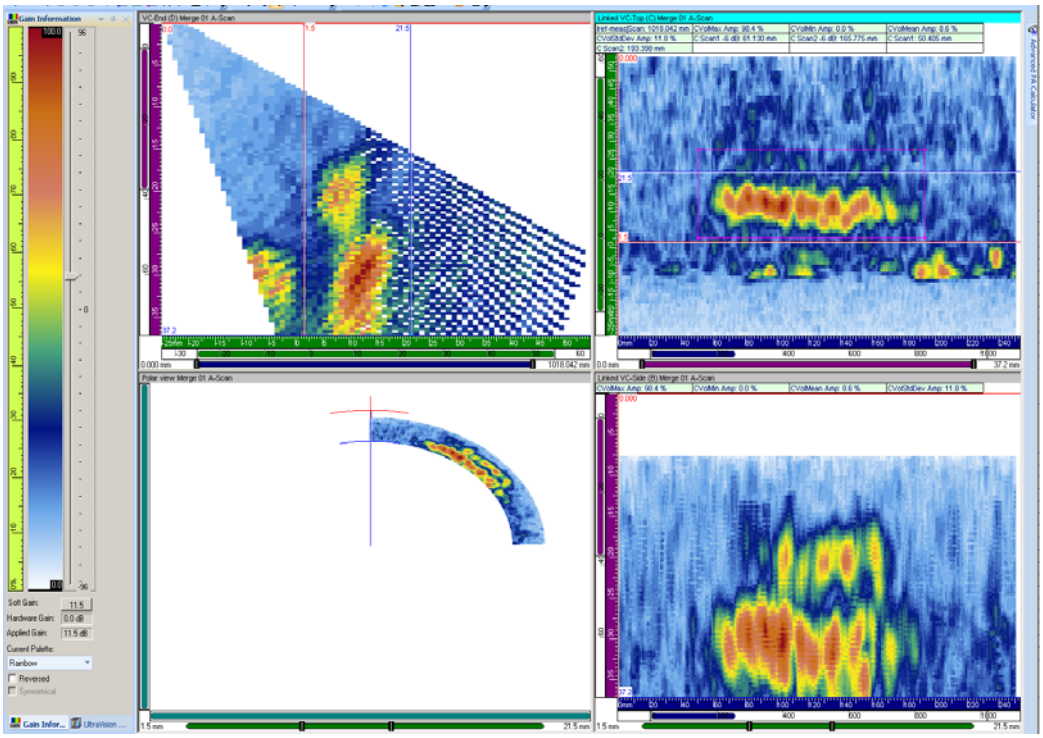

Figure B.1 1.0 MHz Data on Pipe Side of 7C-059, Flaw 1, Merged Image for Length Sizing

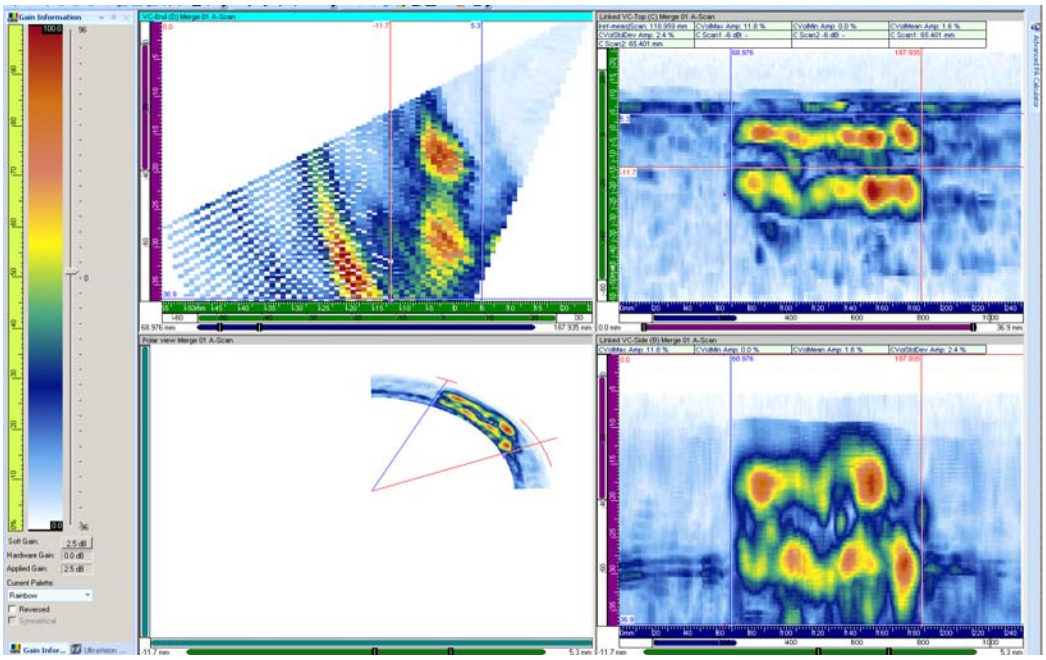

Figure B.2 1.0 MHz Data on Elbow Side of 7C-059, Flaw 1, Merged Image for Length Sizing

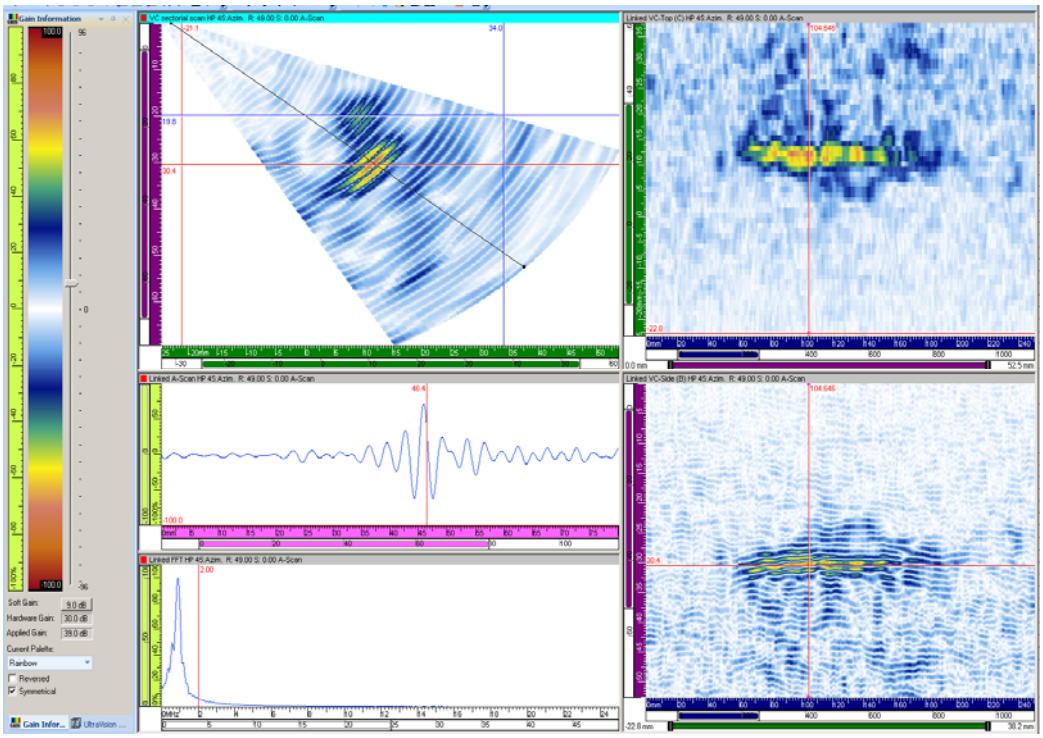

Figure B.3 1.0 MHz Data on Pipe Side of 7C-059, Flaw 1, for Depth Sizing

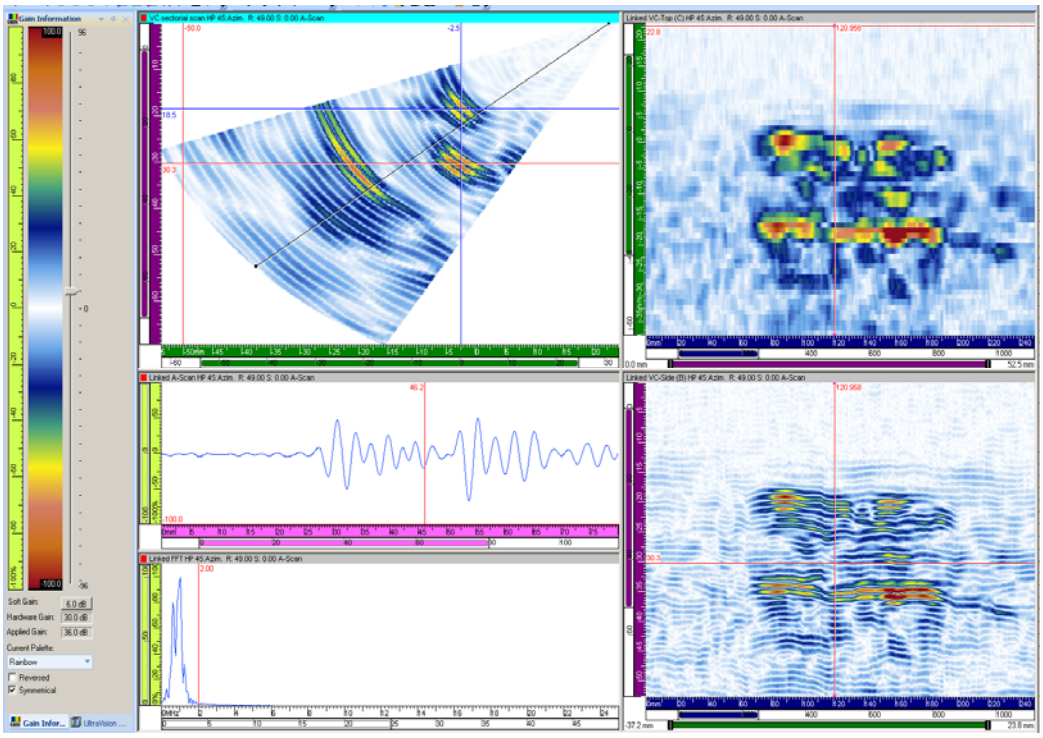

Figure B.4 1.0 MHz Data on Elbow Side of 7C-059, Flaw 1, for Depth Sizing

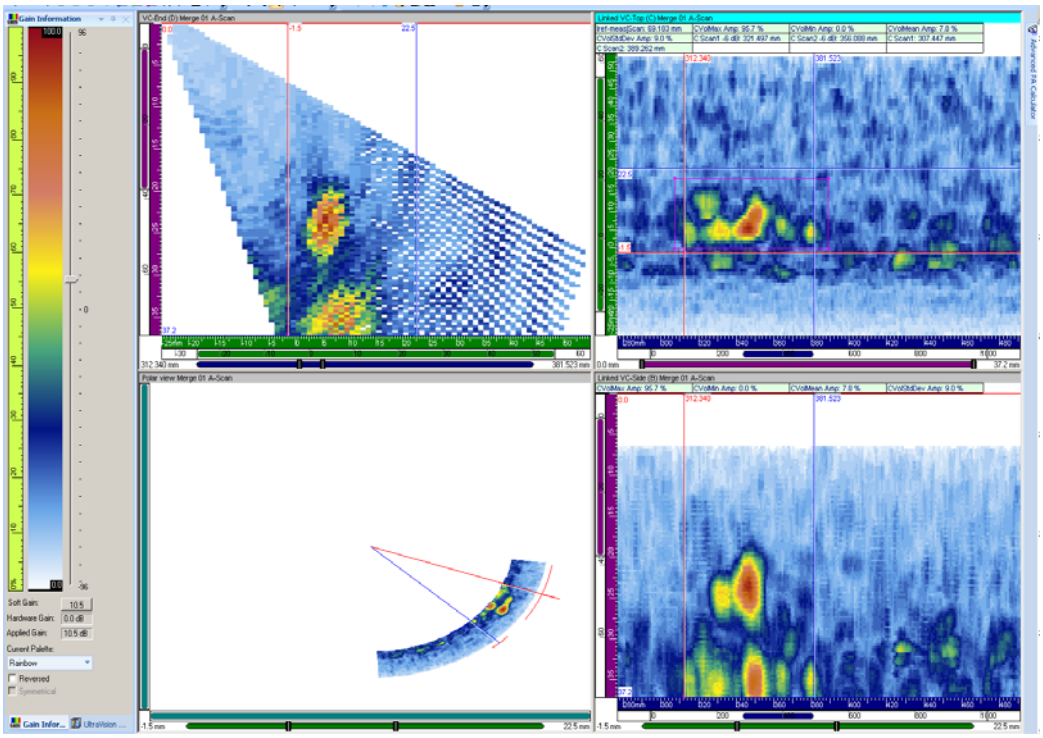

Figure B.5 1.0 MHz Data on Pipe Side of 7C-059, Flaw 2, Merged Image for Length Sizing

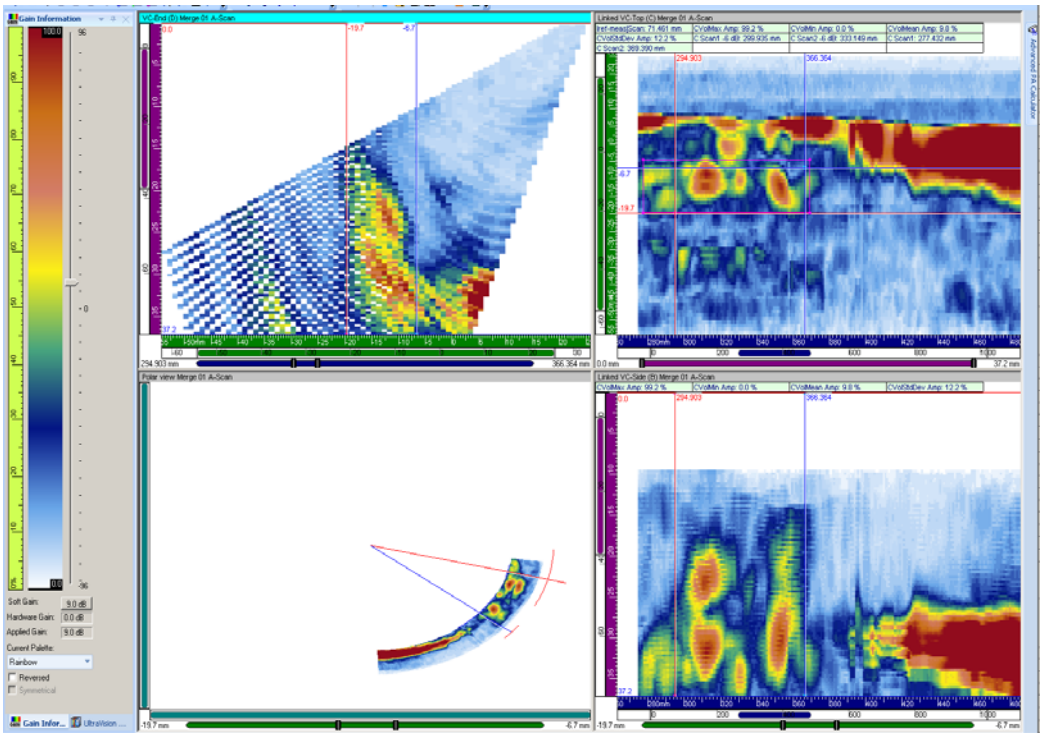

Figure B.6 1.0 MHz Data on Elbow Side of 7C-059, Flaw 2, Merged Image for Length Sizing

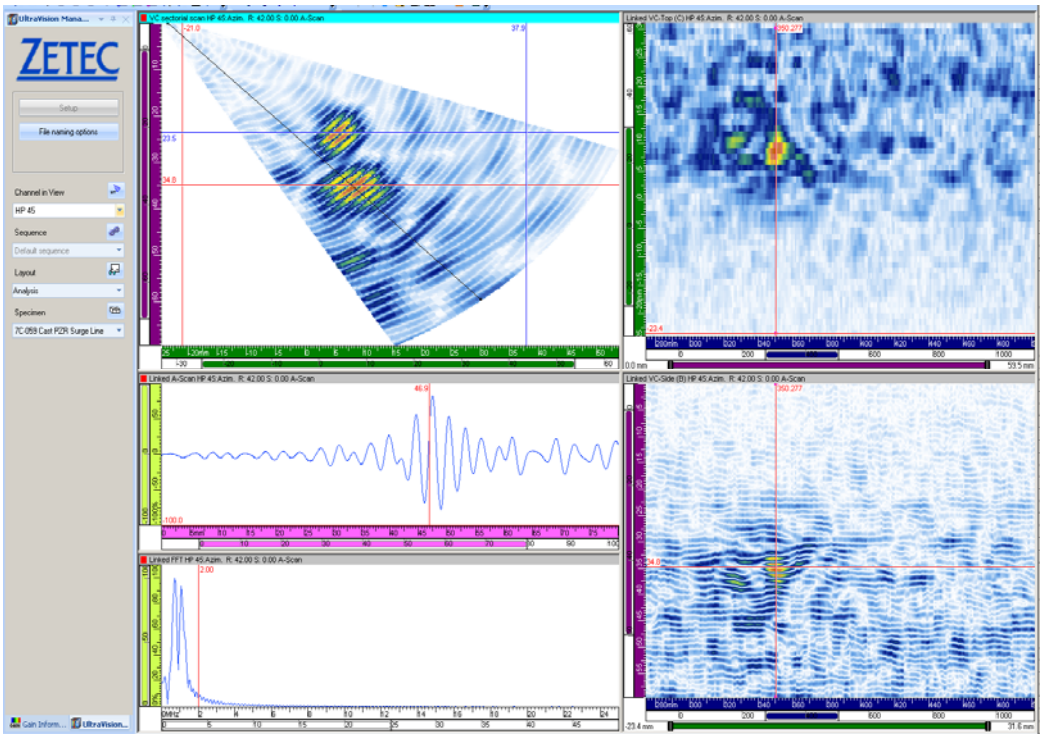

Figure B.7 1.0 MHz Data on Pipe Side of 7C-059, Flaw 2, for Depth Sizing

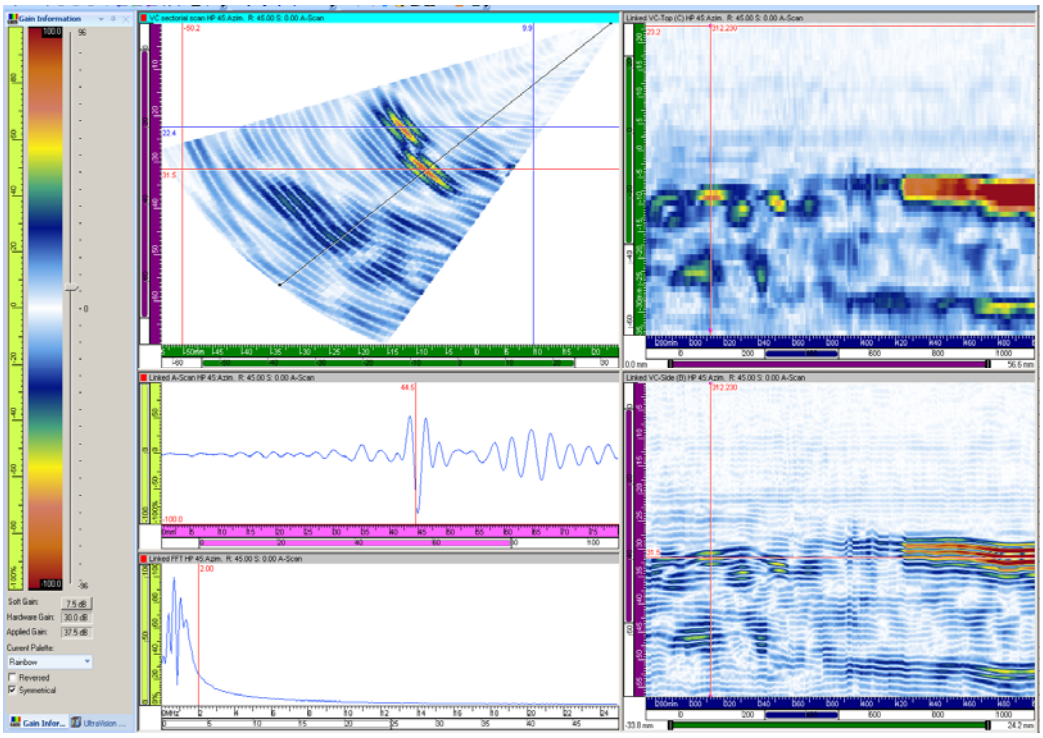

Figure B.8 1.0 MHz Data on Elbow Side of 7C-059, Flaw 2, for Depth Sizing

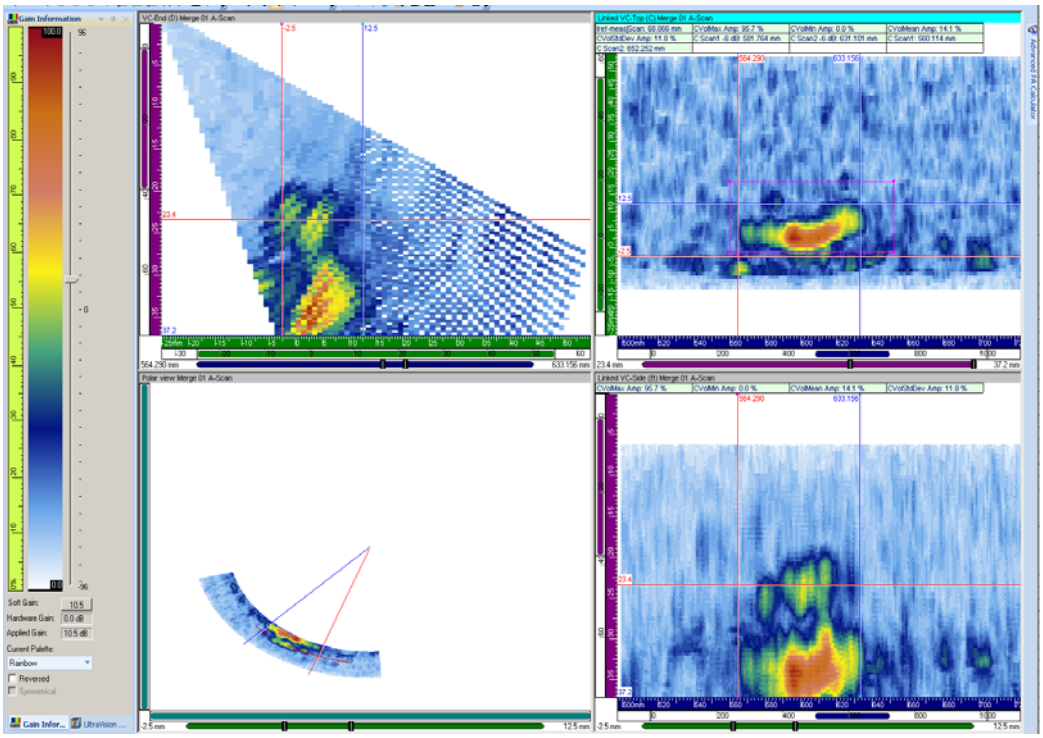

Figure B.9 1.0 MHz Data on Pipe Side of 7C-059, Flaw 3, Merged Image for Length Sizing

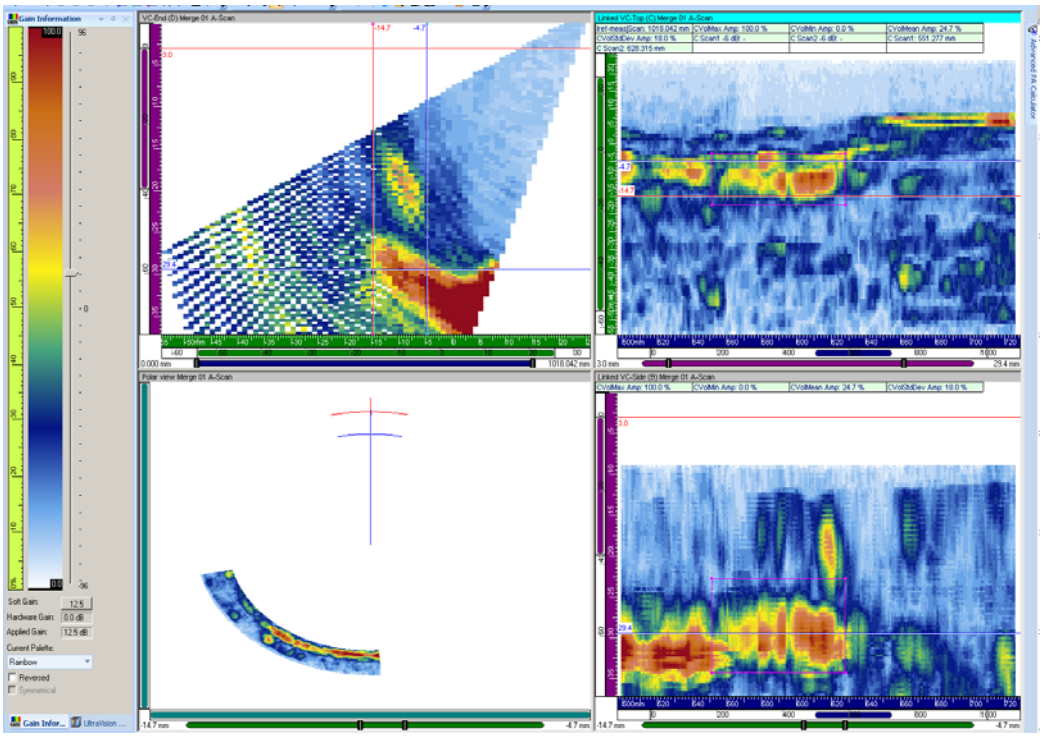

Figure B.10 1.0 MHz Data on Elbow Side of 7C-059, Flaw 3, Merged for Length Sizing

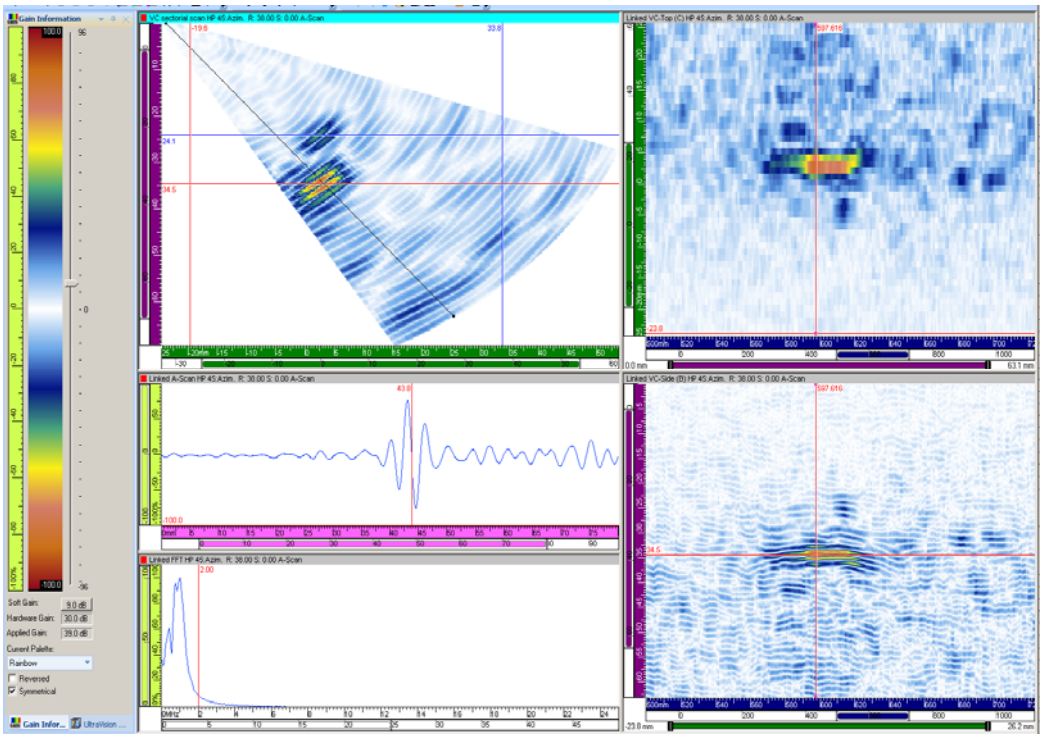

Figure B.11 1.0 MHz Data on Pipe Side of 7C-059, Flaw 3, for Depth Sizing

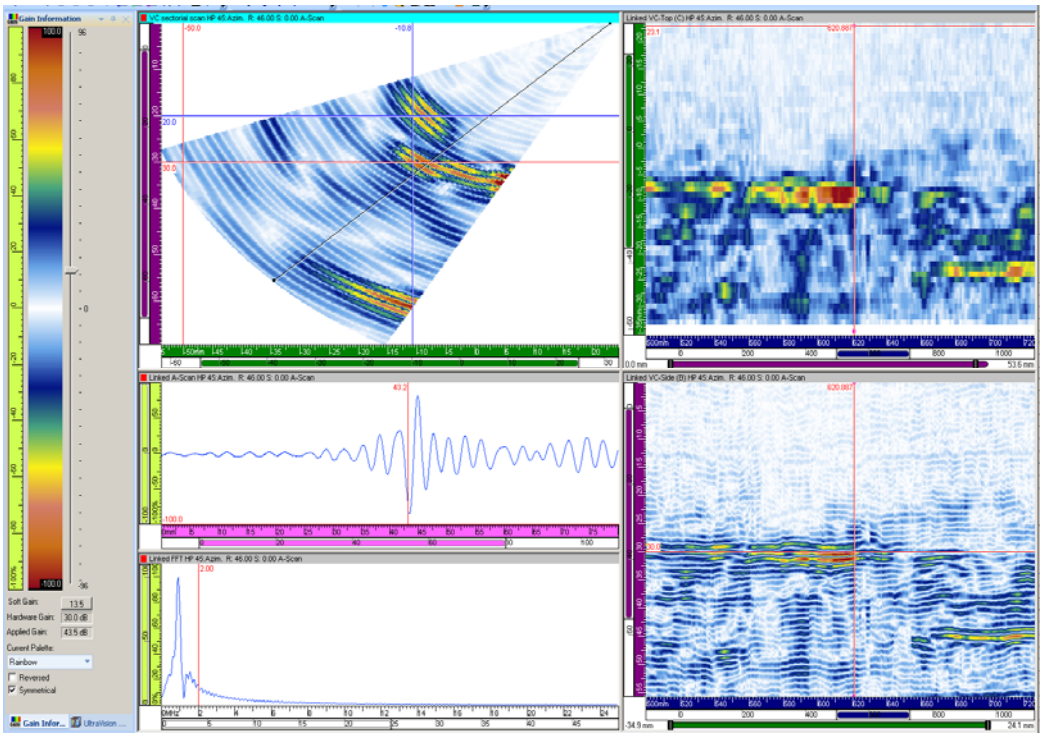

Figure B.12 1.0 MHz Data on Elbow Side of 7C-059, Flaw 3, for Depth Sizing

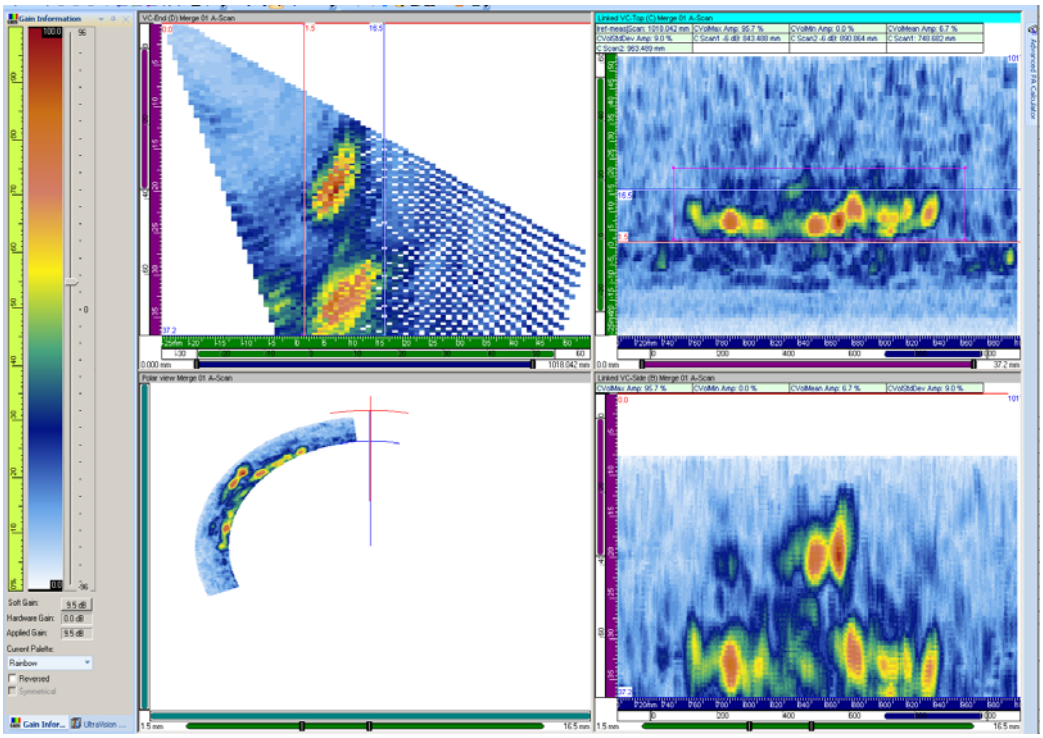

Figure B.13 1.0 MHz Data on Pipe Side of 7C-059, Flaw 4, Merged Image for Length Sizing

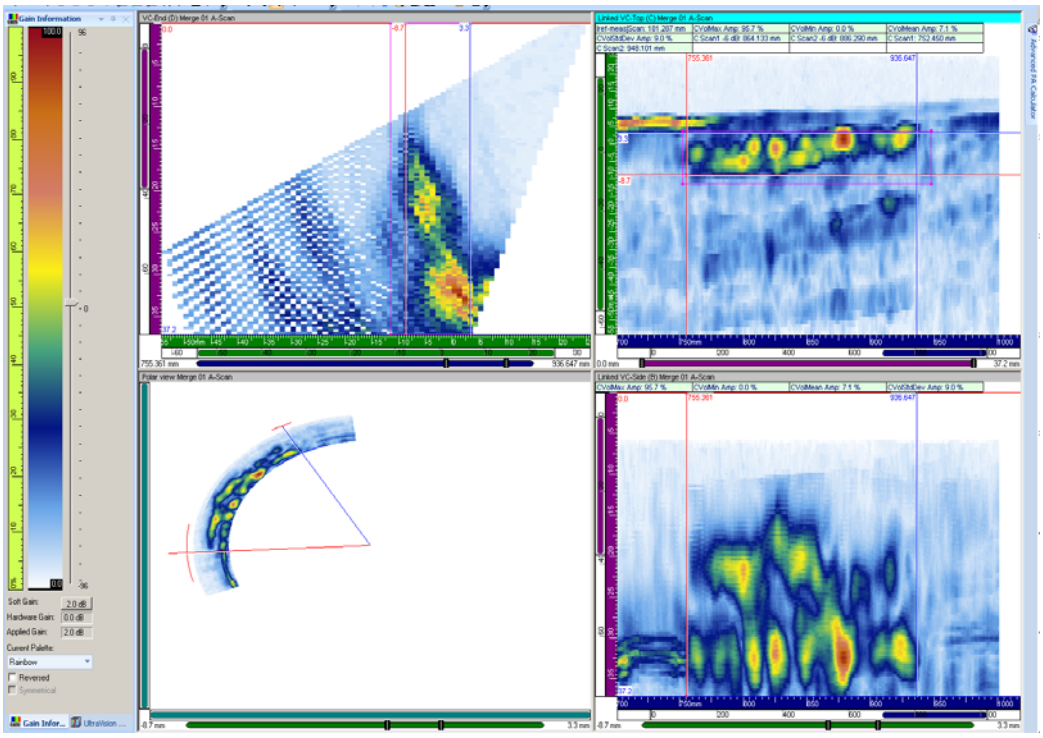

Figure B.14 1.0 MHz Data on Elbow Side of 7C-059, Flaw 4, Merged Image for Length Sizing

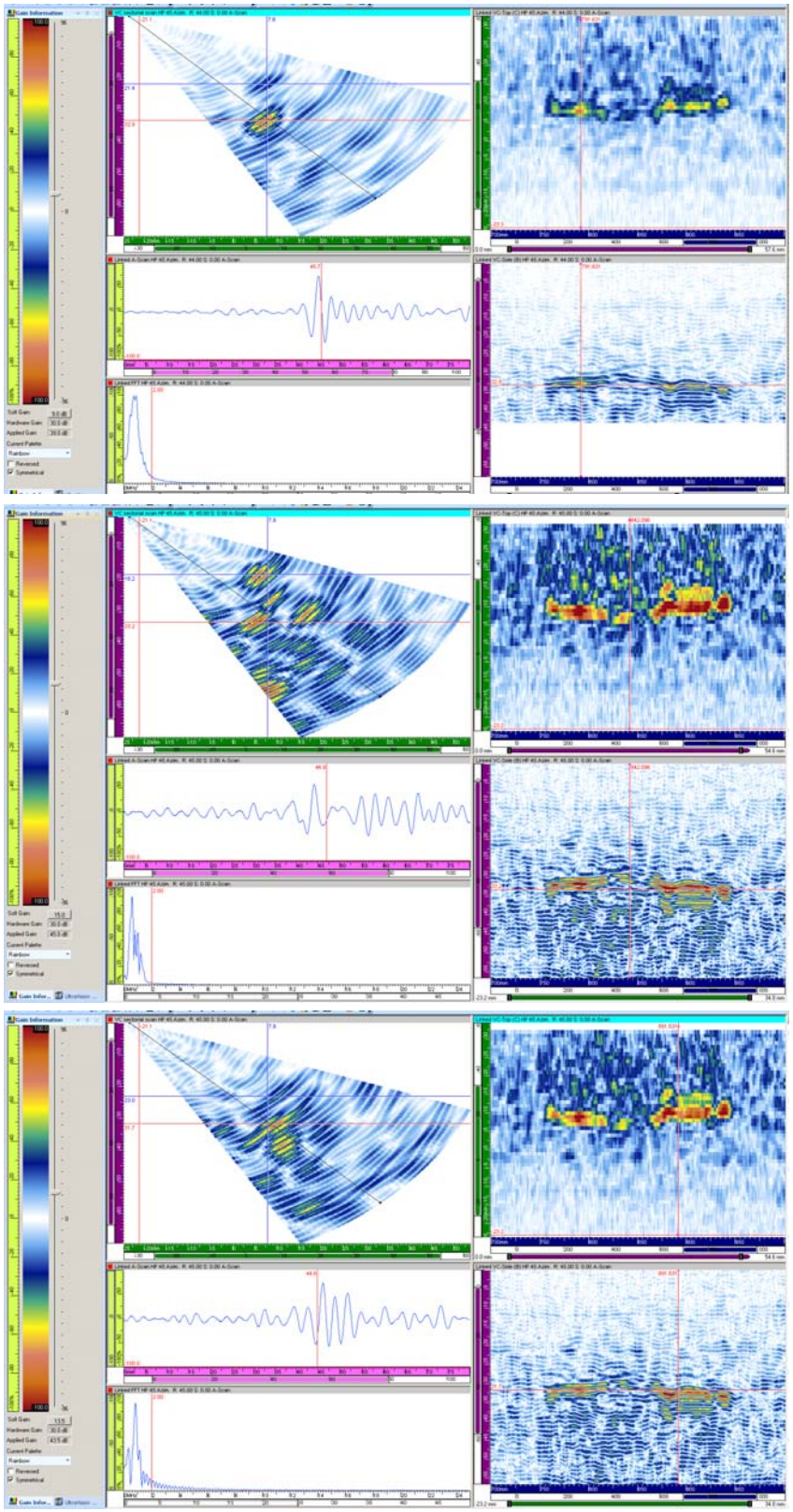

Figure B.15 1.0 MHz Data on Pipe Side of 7C-059, Flaw 4a, 4b, and 4c Top to Bottom for Depth Sizing

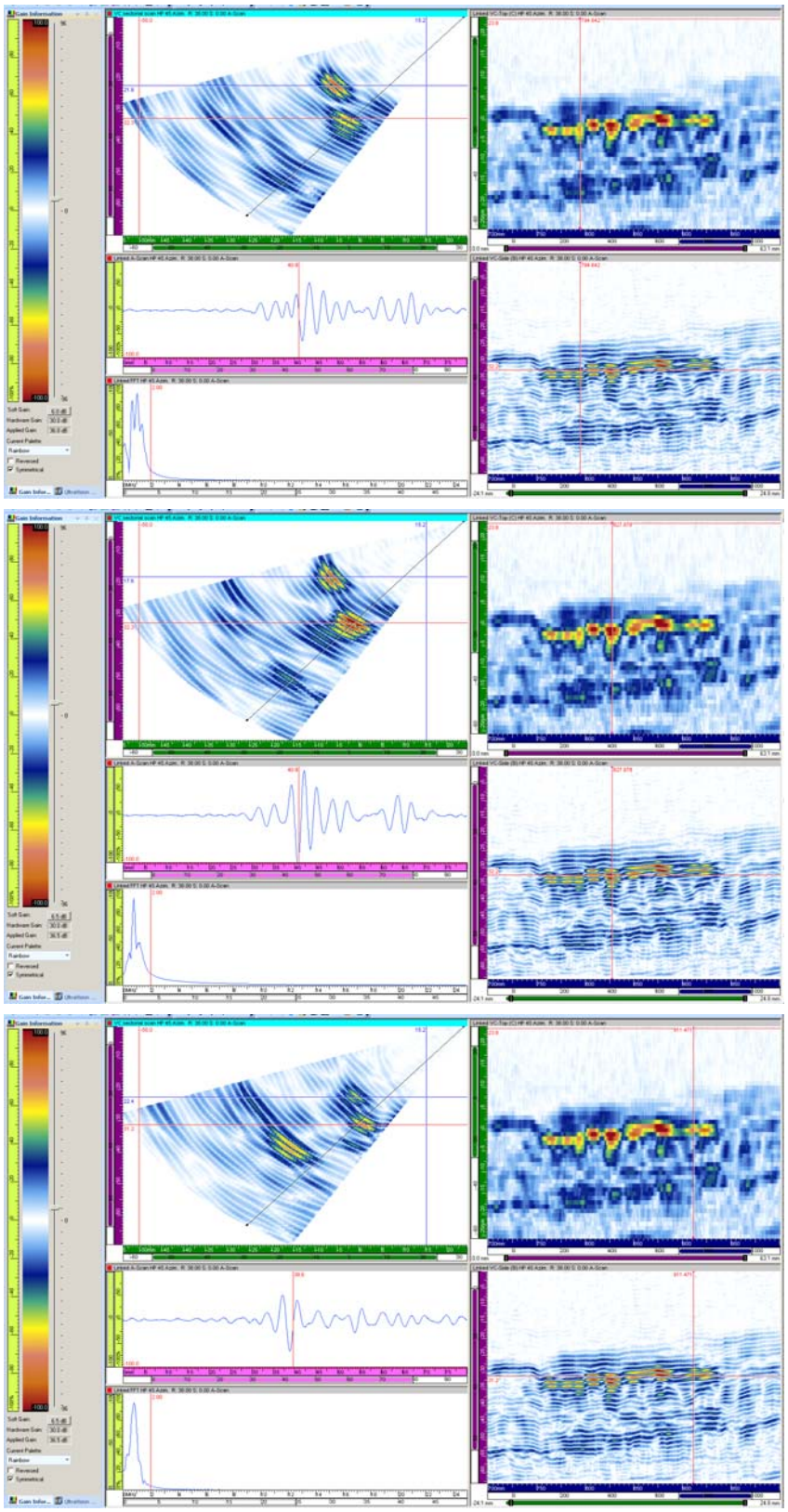

Figure B.16 1.0 MHz Data on Elbow Side of 7C-059, Flaw 4a, 4b, and 4c Top to Bottom for Depth Sizing

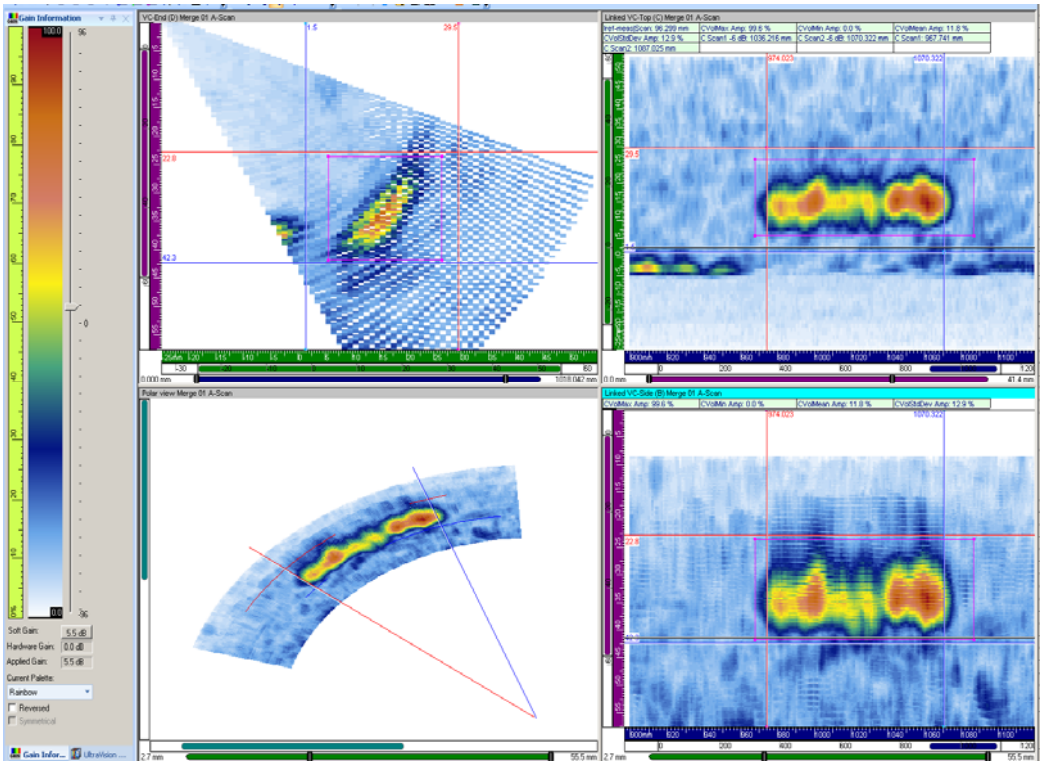

Figure B.17 1.0 MHz Data on Pipe Side of 9C-001, Flaw 1, Merged Image for Length Sizing

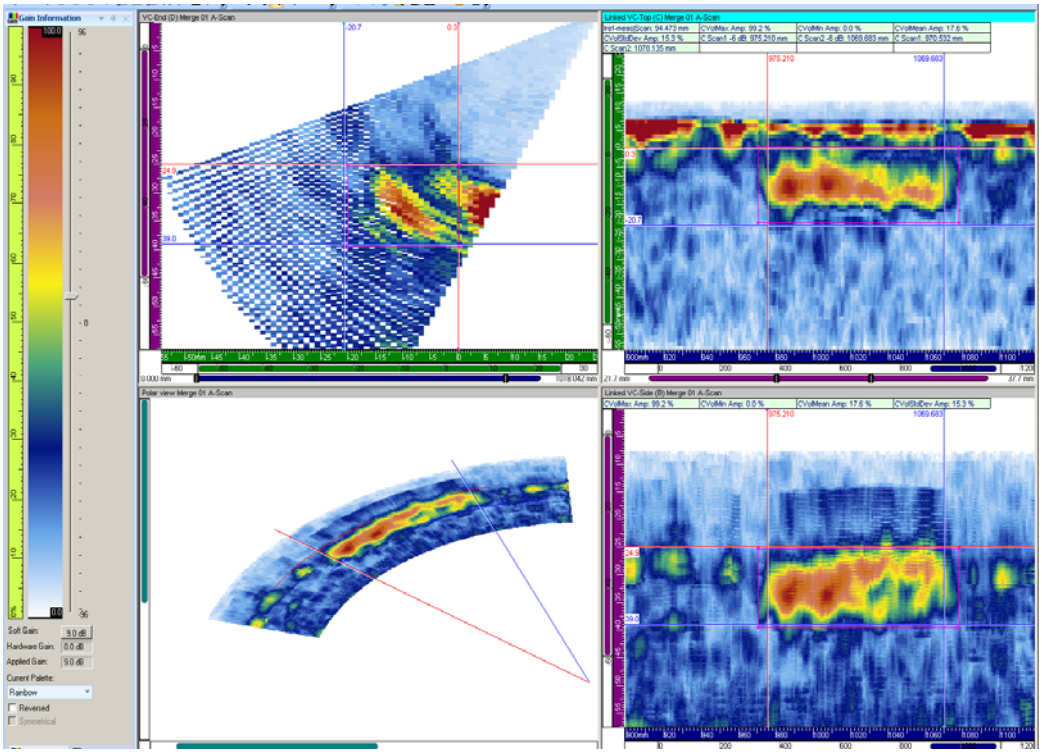

Figure B.18 1.0 MHz Data on Elbow Side of 9C-001, Flaw 1, Merged Image for Length Sizing

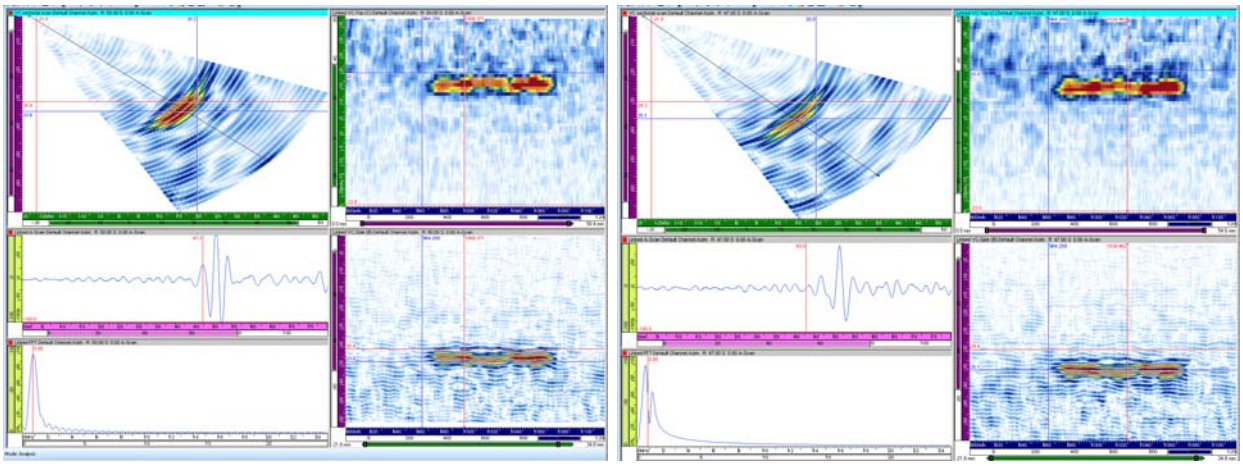

Figure B.19 1.0 MHz Data on Pipe Side of 9C-001, Flaw 1a and 1b, Left and Right, for Depth Sizing

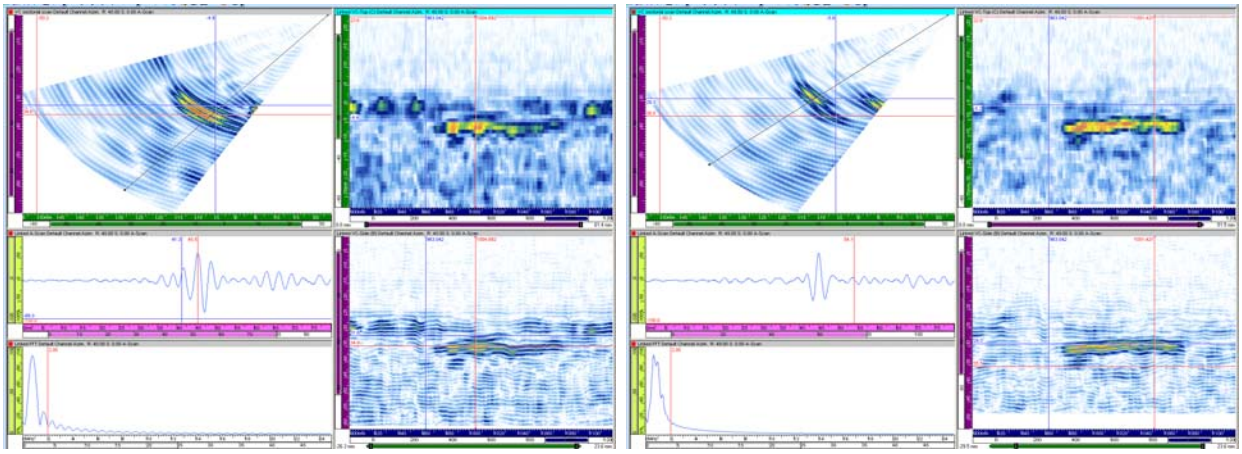

Figure B.20 1.0 MHz Data on Elbow Side of 9C-001, Flaw 1a and 1b, Left and Right, for Depth Sizing

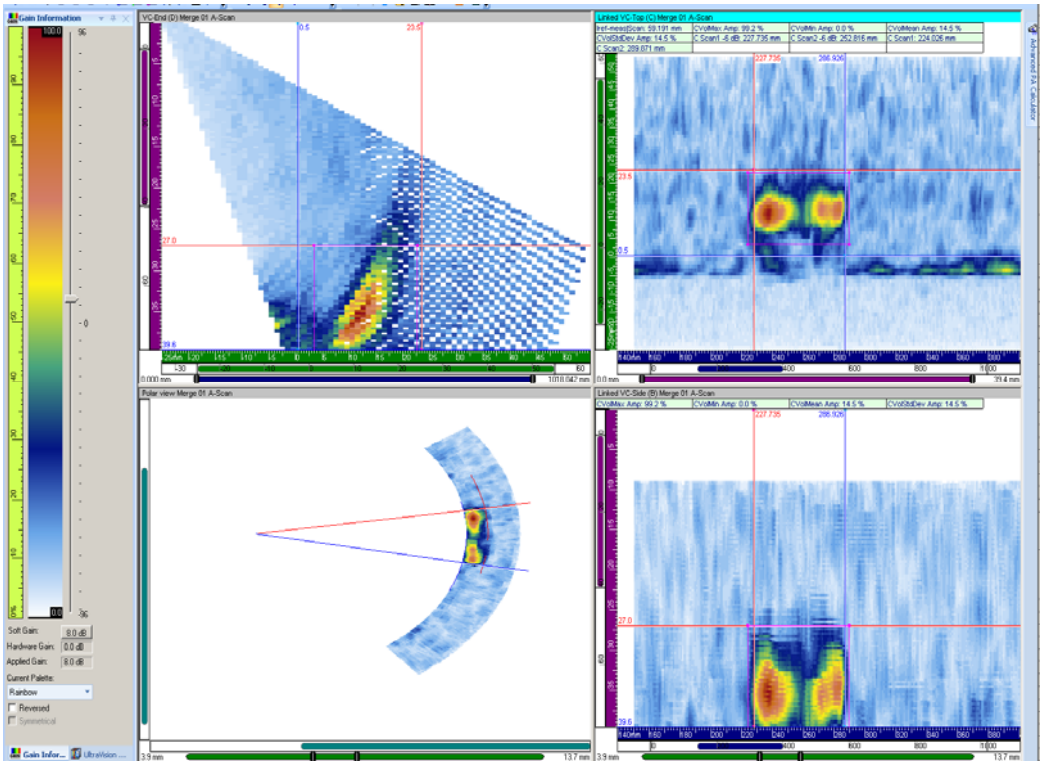

Figure B.21 1.0 MHz Data on Pipe Side of 9C-001, Flaw 2, Merged Image for Length Sizing

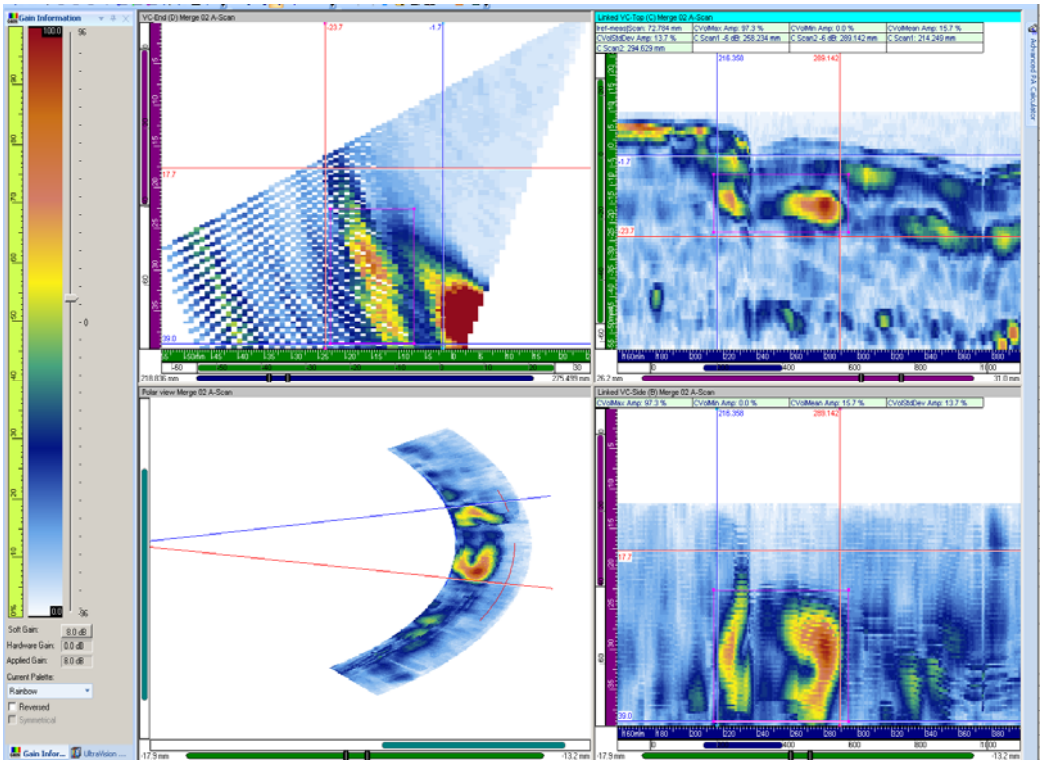

Figure B.22 1.0 MHz Data on Elbow Side of 9C-001, Flaw 2, Merged Image for Length Sizing

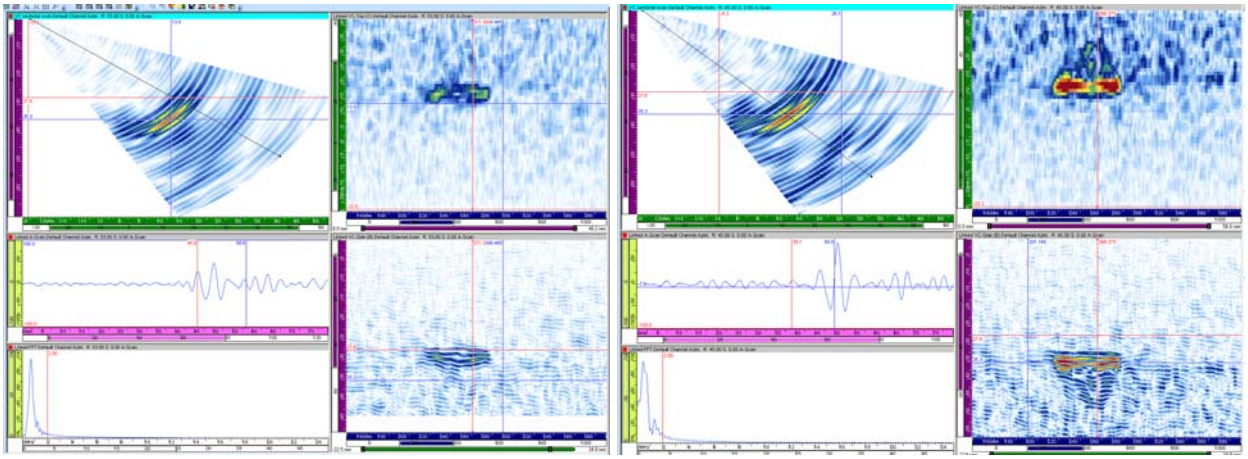

Figure B.23 1.0 MHz Data on Pipe Side of 9C-001, Flaw 2, for Depth Sizing

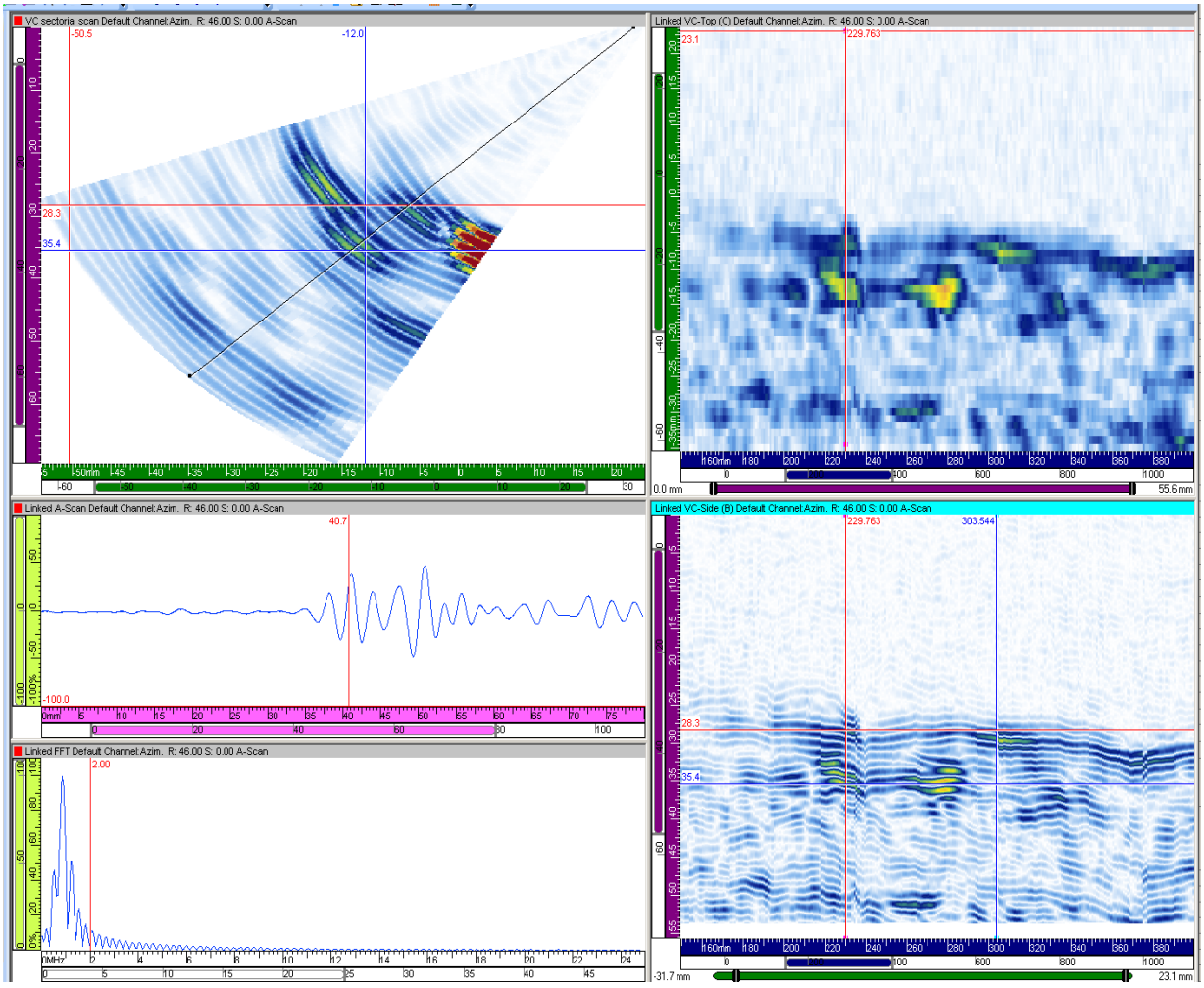

Figure B.24 1.0 MHz Data on Elbow Side of 9C-001, Flaw 2, for Depth Sizing

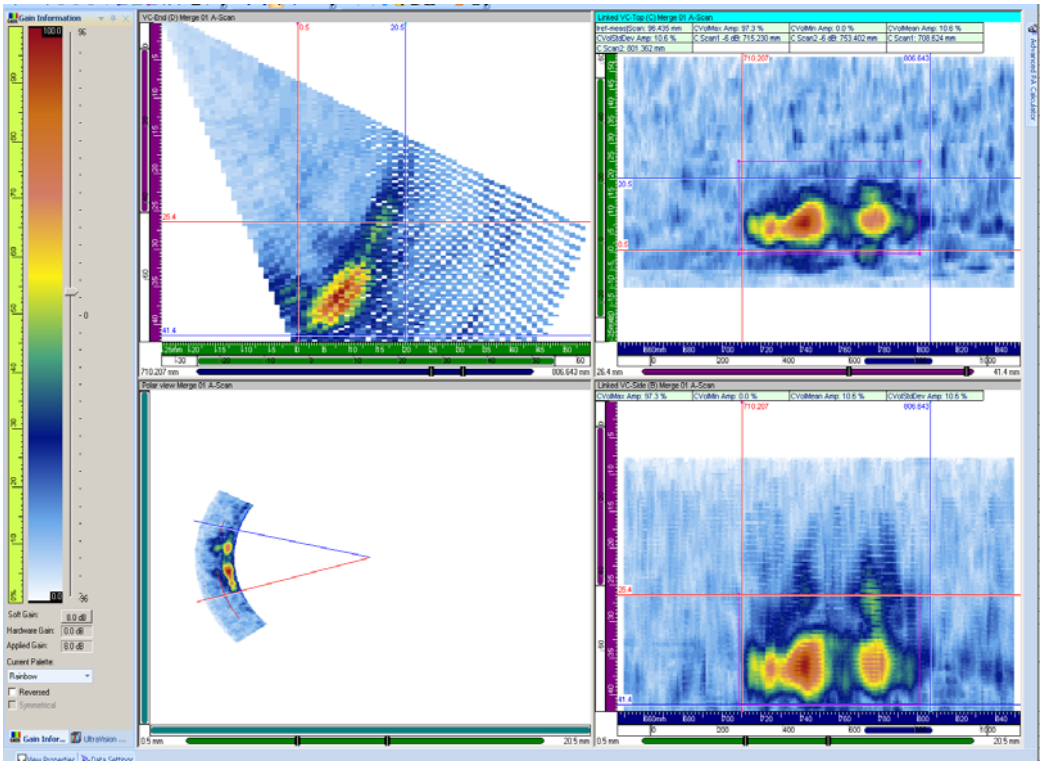

Figure B.25 1.0 MHz Data on Pipe Side of 9C-001, Flaw 3, Merged Image for Length Sizing

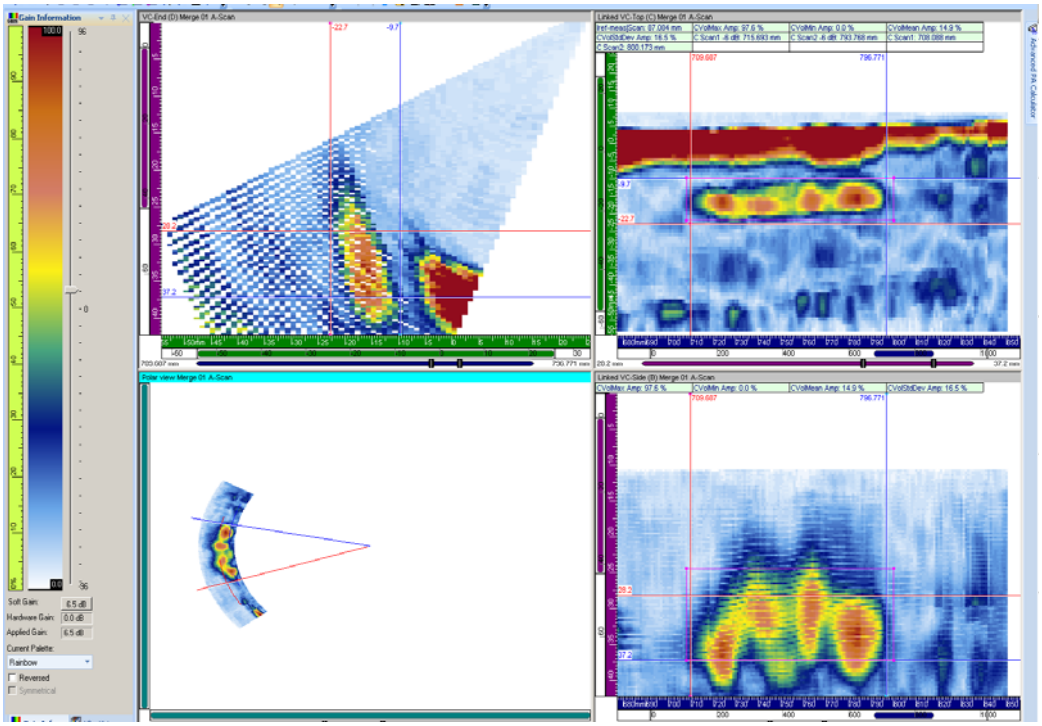

Figure B.26 1.0 MHz Data on Elbow Side of 9C-001, Flaw 3, Merged Image for Length Sizing

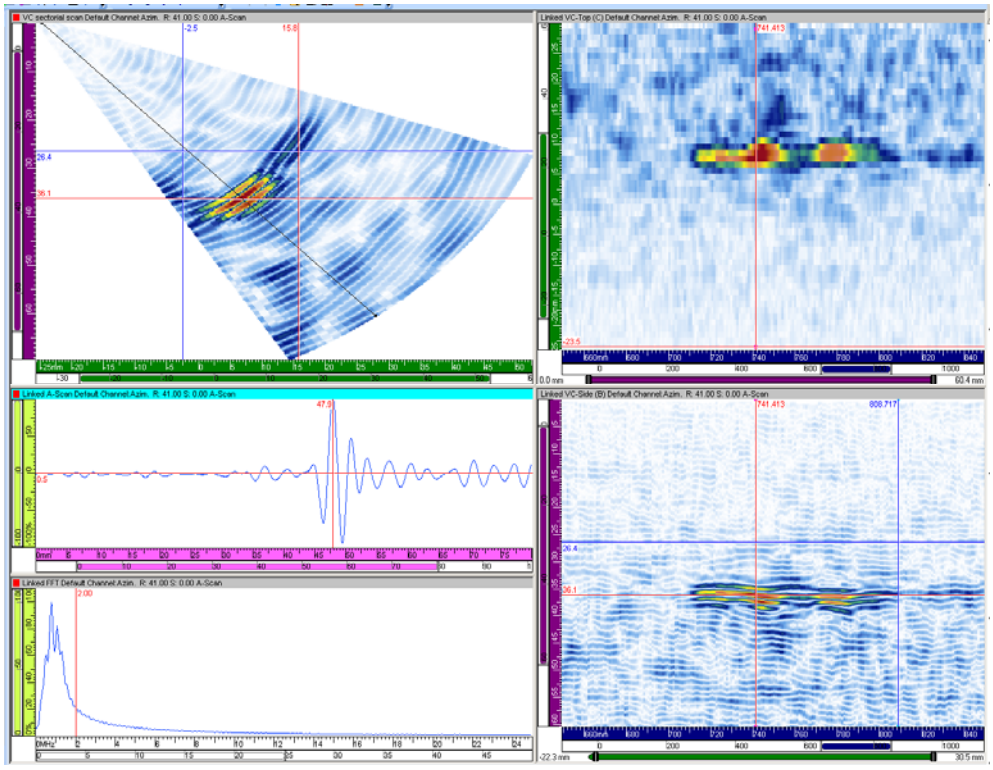

Figure B.27 1.0 MHz Data on Pipe Side of 9C-001, Flaw 3, for Depth Sizing

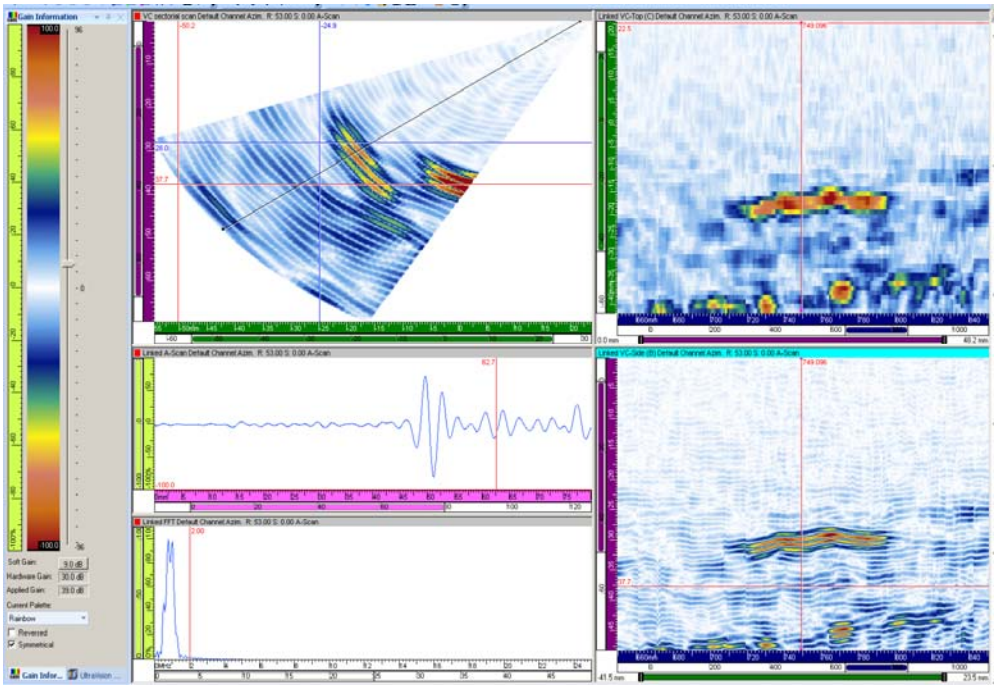

Figure B.28 1.0 MHz Data on Elbow Side of 9C-001, Flaw 3, for Depth Sizing

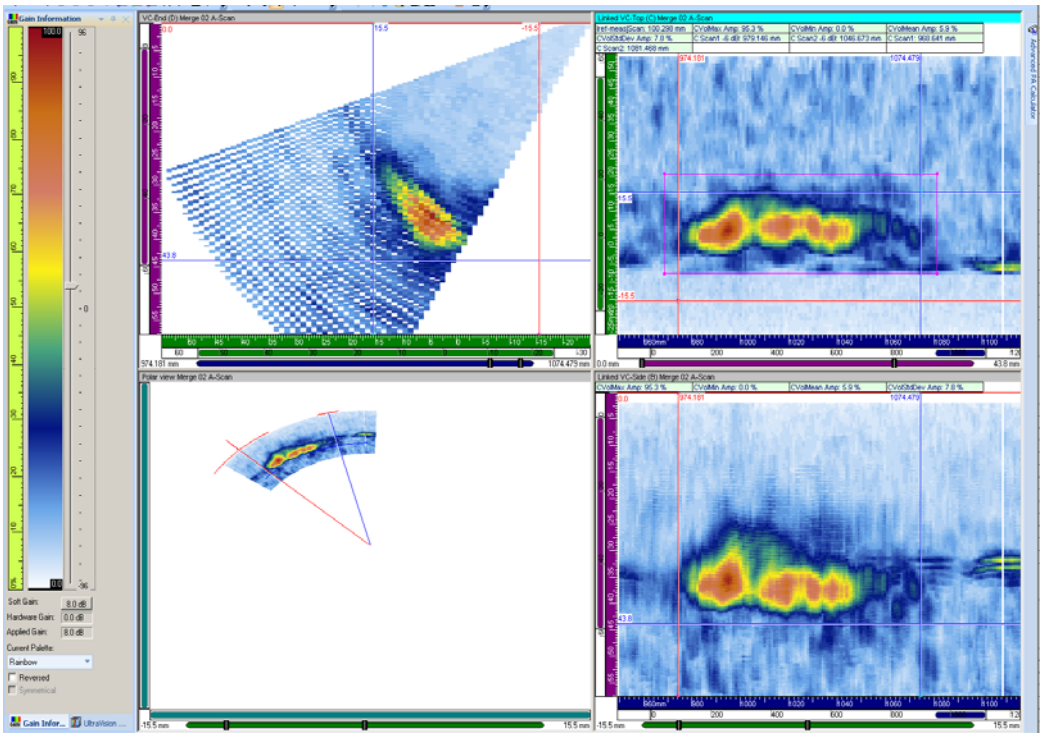

Figure B.29 1.0 MHz Data on Pipe Side of 9C-002, Flaw 1, Merged Image for Length Sizing

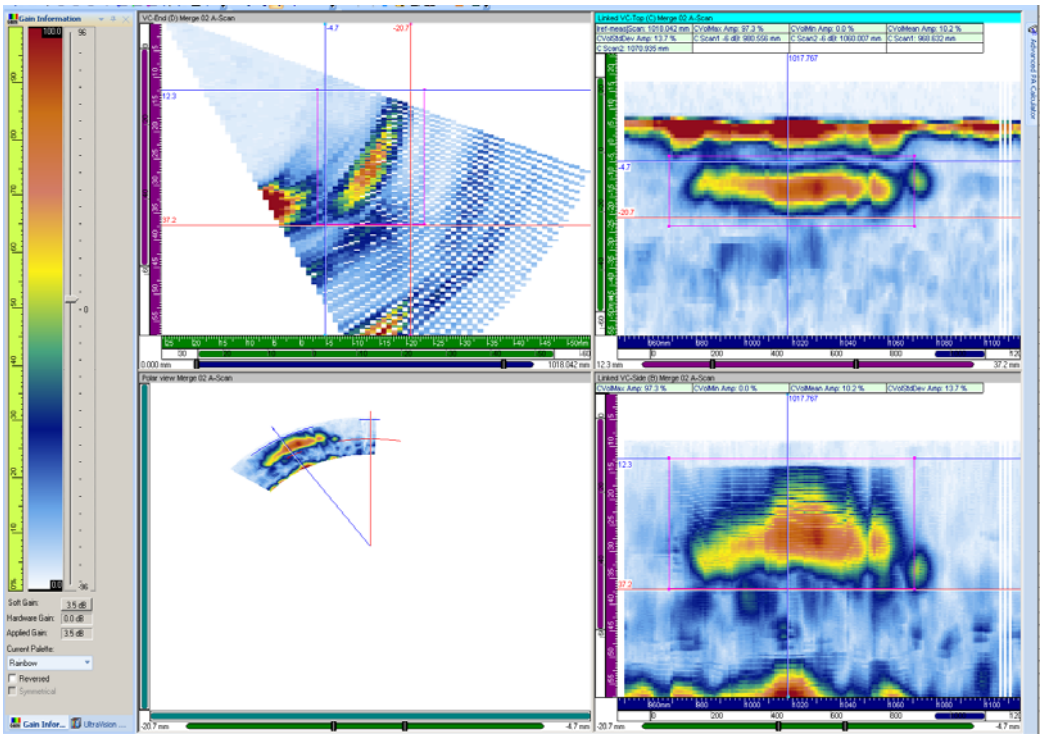

Figure B.30 1.0 MHz Data on Elbow Side of 9C-002, Flaw 1, Merged Image for Length Sizing

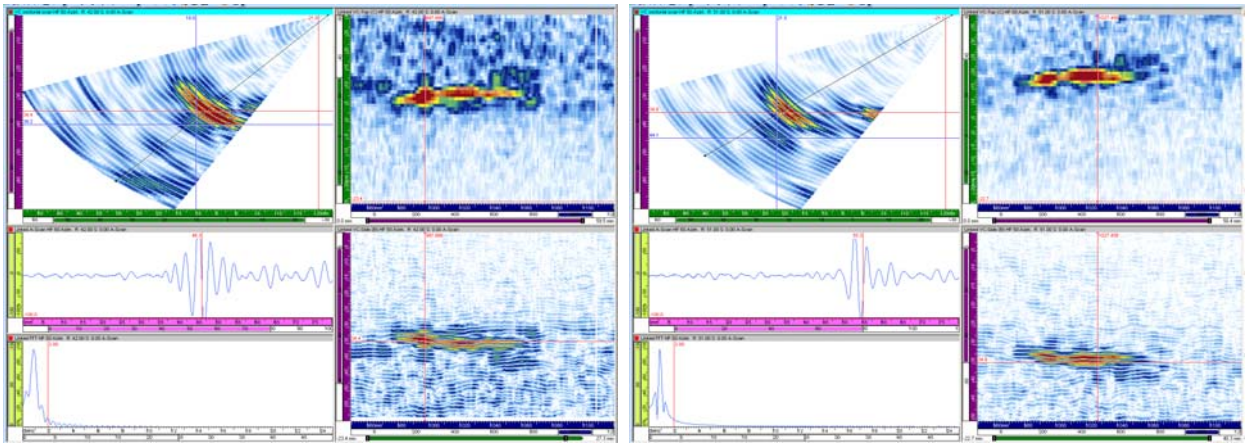

Figure B.31 1.0 MHz Data on Pipe Side of 9C-002, Flaw 1a on the Left and 1b on the Right for Depth Sizing

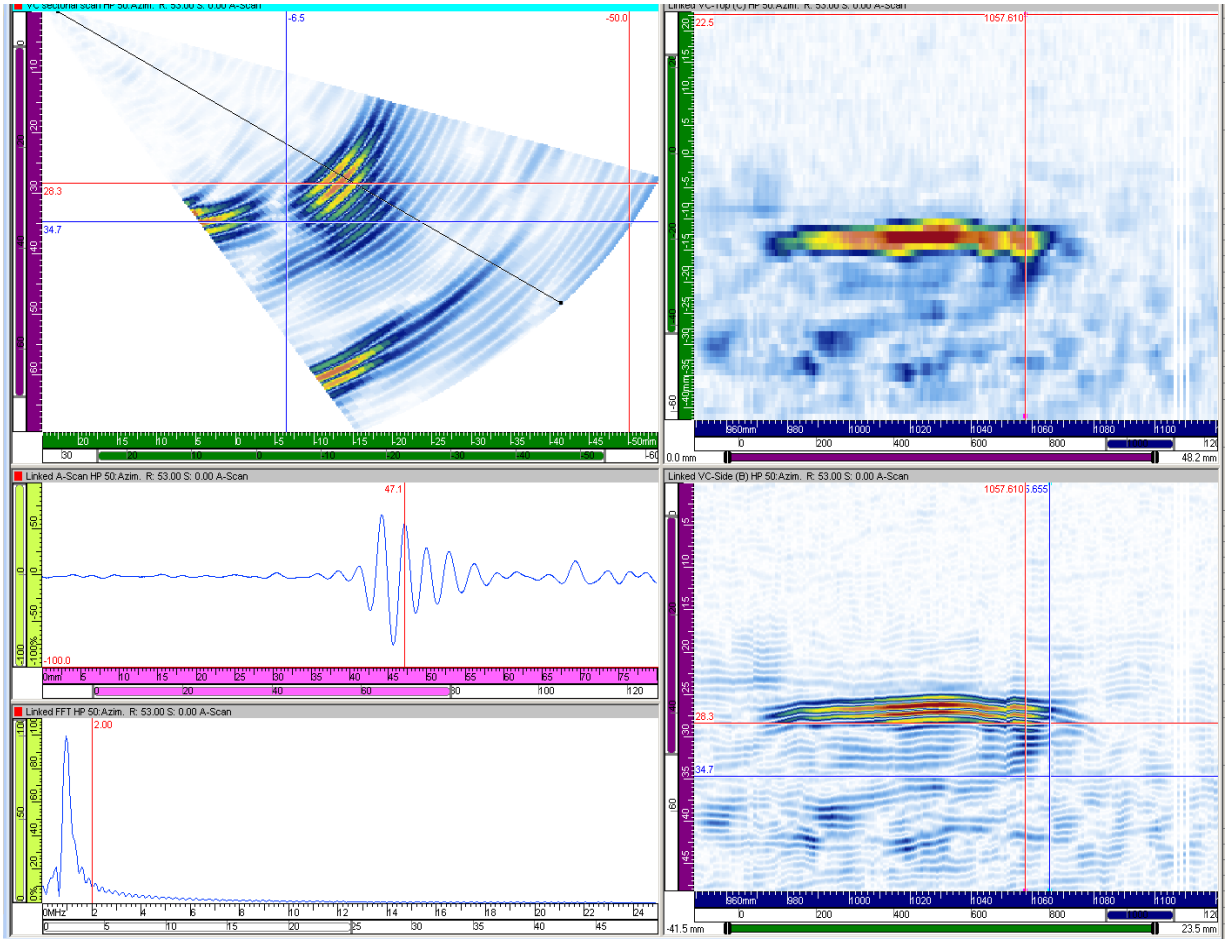

Figure B.32 1.0 MHz Data on Elbow Side of 9C-002, Flaw 1b, for Depth Sizing. The 1a portion of the flaw did not have any signal for depth sizing.

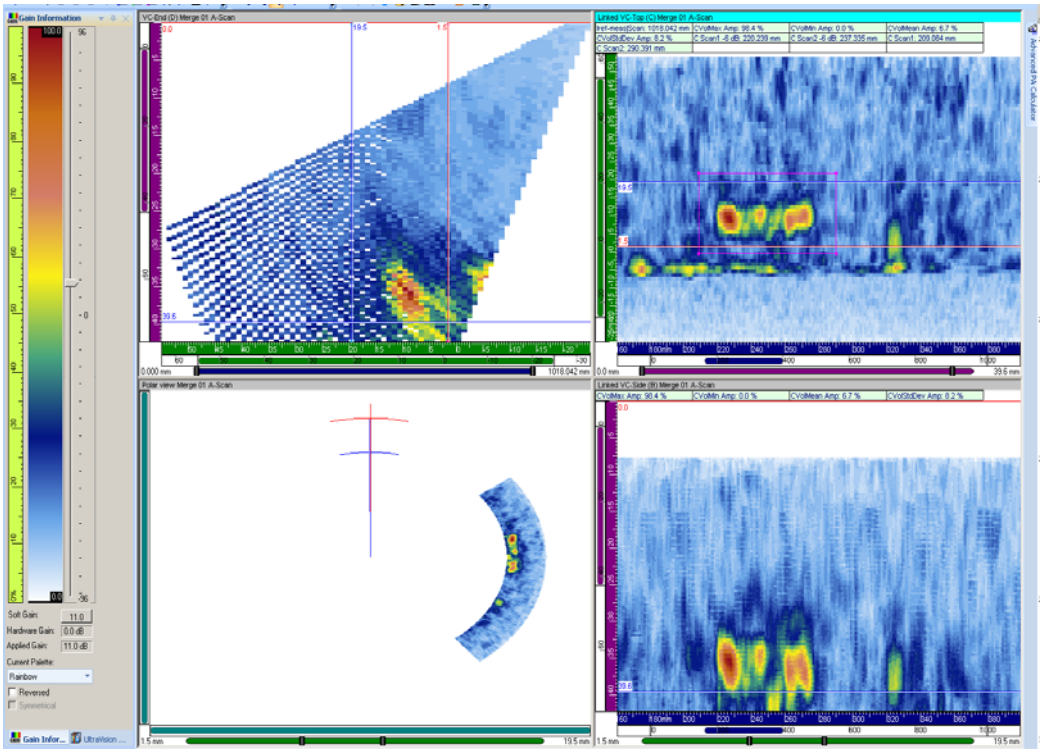

Figure B.33 1.0 MHz Data on Pipe Side of 9C-002, Flaw 2, Merged Image for Length Sizing

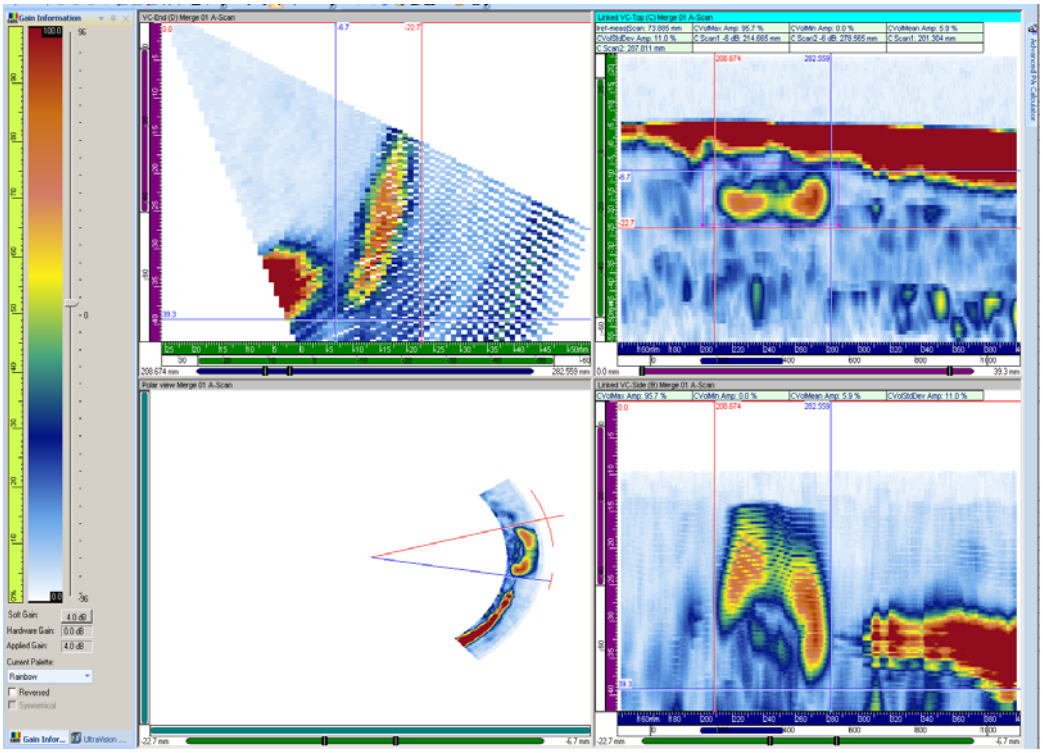

Figure B.34 1.0 MHz Data on Elbow Side of 9C-002, Flaw 2, Merged Image for Length Sizing

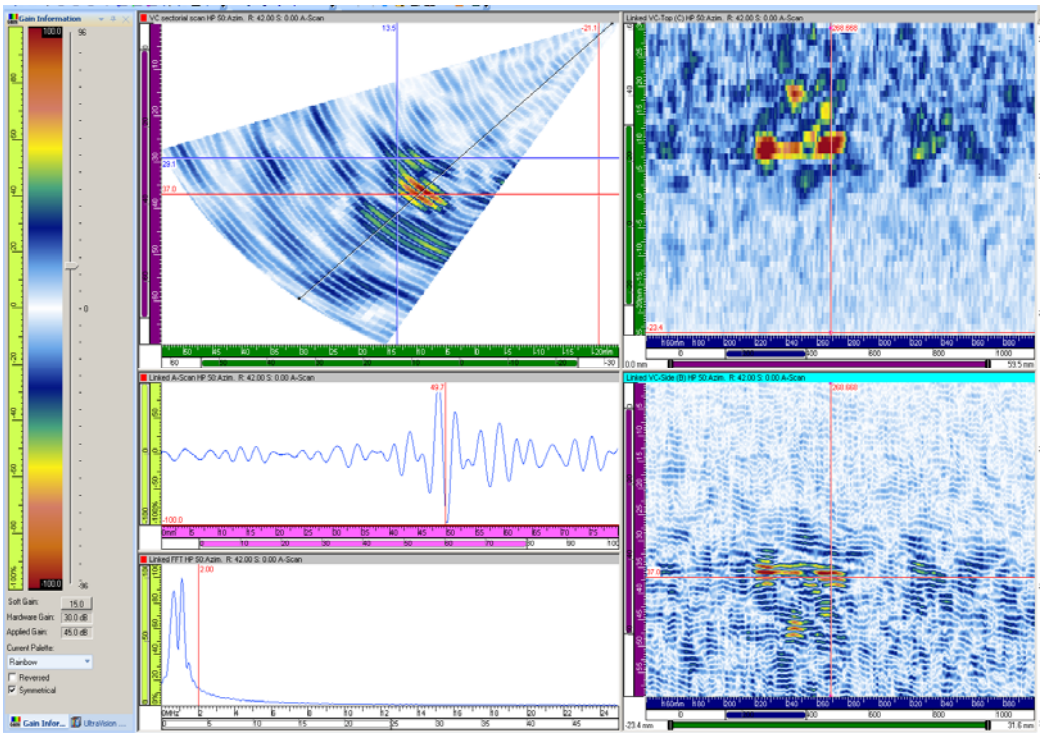

Figure B.35 1.0 MHz Data on Pipe Side of 9C-002, Flaw 2, for Depth Sizing

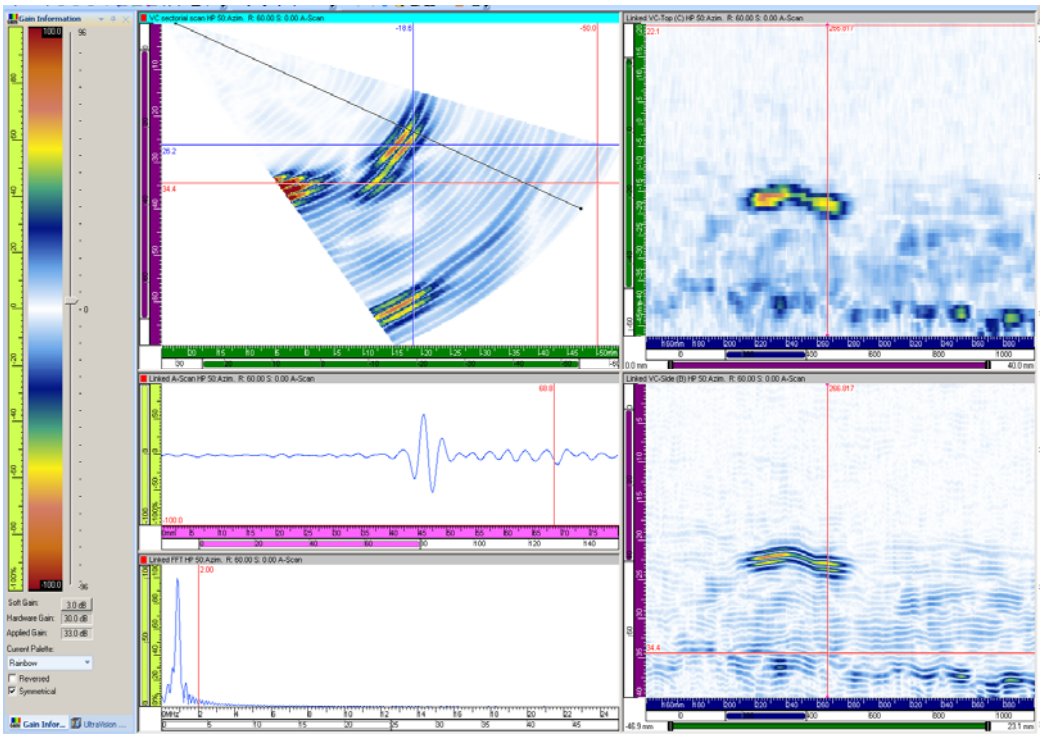

Figure B.36 1.0 MHz Data on Elbow Side of 9C-002, Flaw 2, for Depth Sizing

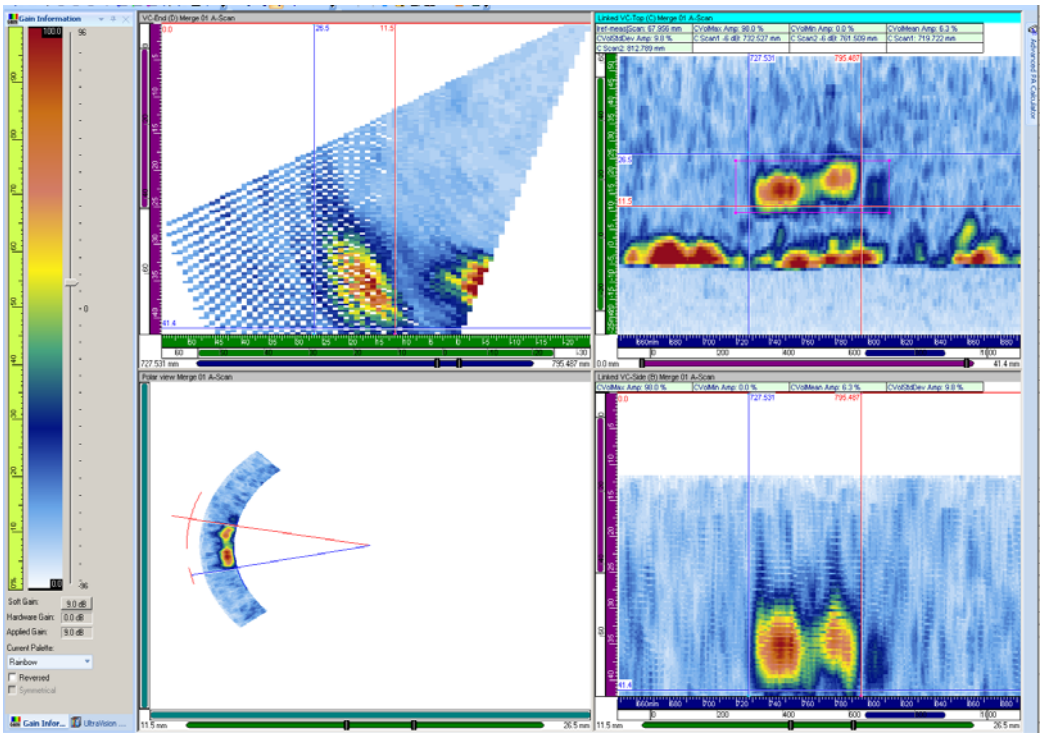

Figure B.37 1.0 MHz Data on Pipe Side of 9C-002, Flaw 3, Merged Image for Length Sizing

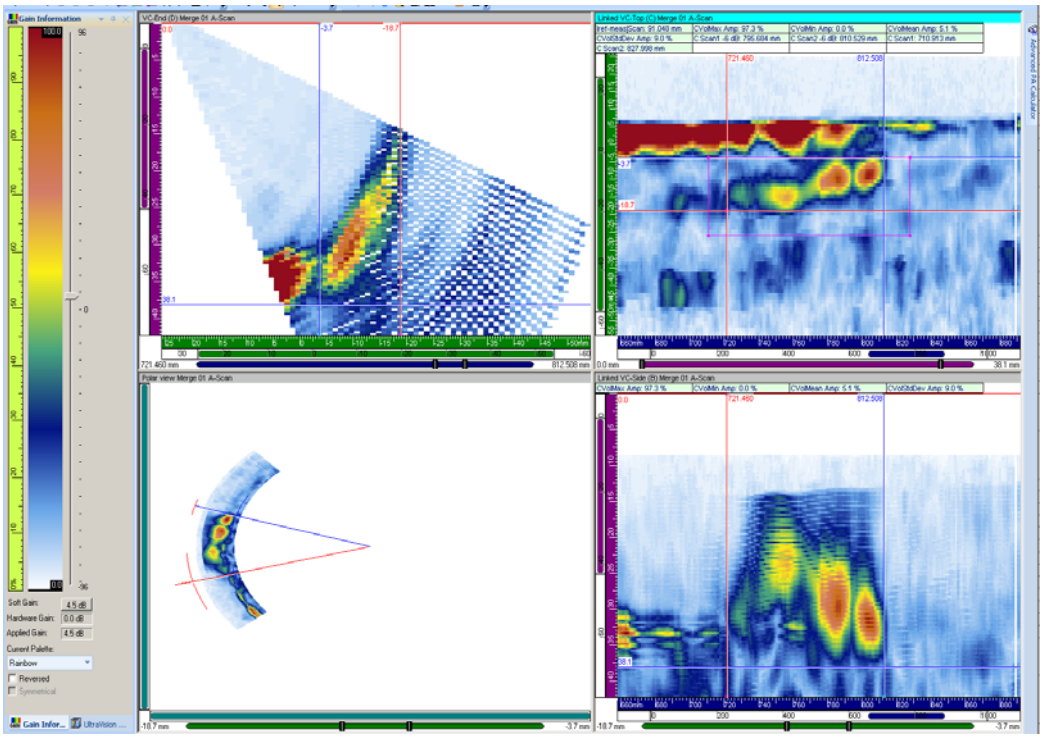

Figure B.38 1.0 MHz Data on Elbow Side of 9C-002, Flaw 3, Merged Image for Length Sizing

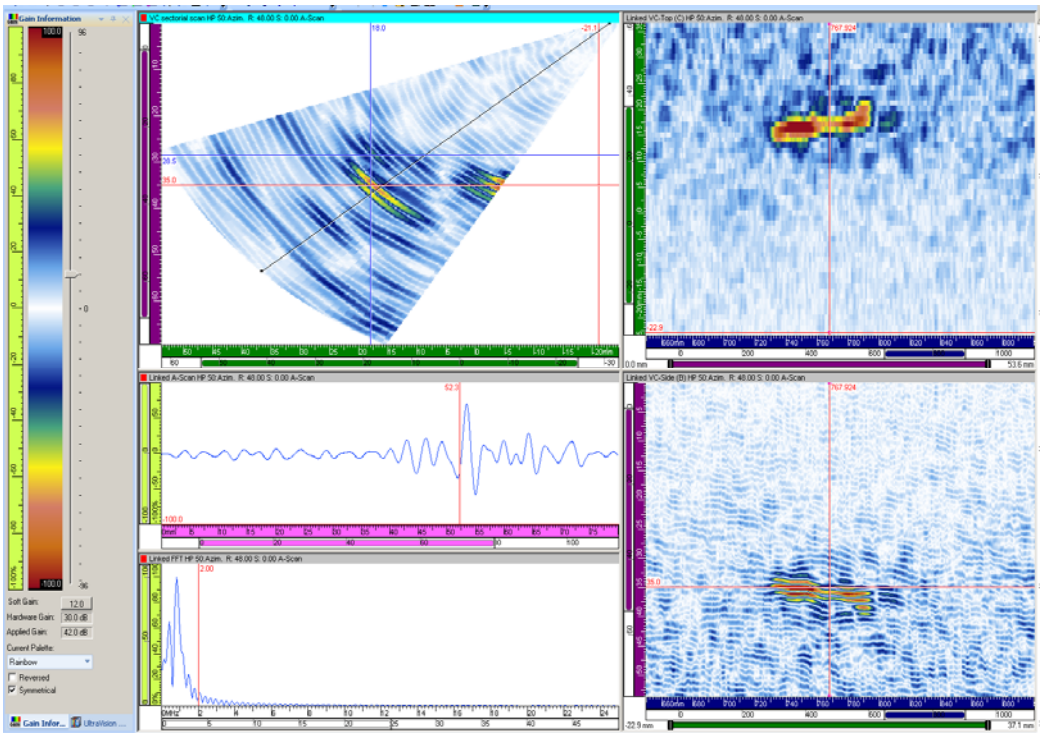

Figure B.39 1.0 MHz Data on Pipe Side of 9C-002, Flaw 3, for Depth Sizing

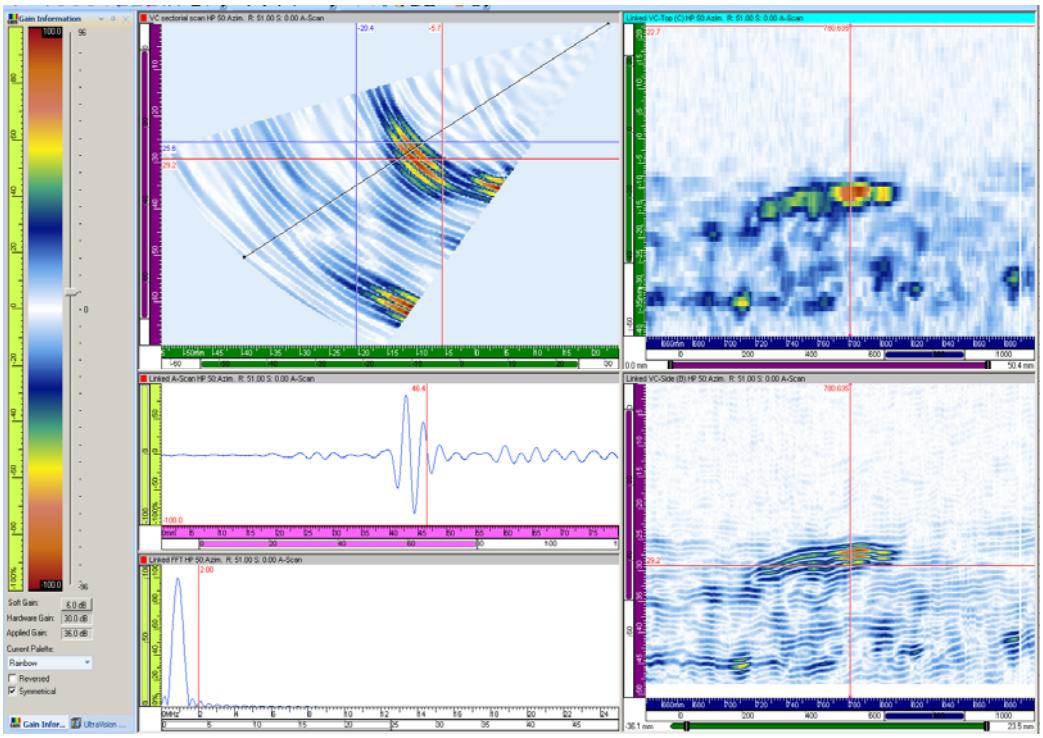

Figure B.40 1.0 MHz Data on Elbow Side of 9C-002, Flaw 3, for Depth Sizing